Coupled Modelling of Naturally Occurring Radionuclides in a Cementitious Engineered Barrier

Yousef Ahmad Baqer

Submitted in accordance with the requirements for the degree of Doctor of Philosophy

The University of Leeds

School of Civil Engineering

June 2022

Declaration and publication

The candidate confirms that the work submitted is his own, except where work which has formed part of jointly-authored publications has been included. The contribution of the candidate and the other authors to this work has been explicitly indicated below. The candidate confirms that appropriate credit has been given within the thesis where reference has been made to the work of others.

- The work of chapter 2 in the thesis has been published in a joint authors contribution publication.

"BAQER, Y., CHEN, X., 2022. A review on reactive transport model and porosity evolution in the porous media. Environmental Science and Pollution Research"

The contribution of each co-author in this publication was:

Yousef Baqer: Leading writing the paper, including conducting the research and investigation process along with the preparation and creation of the published critical review from the original literatures including pre-and post-publication stages. CHEN, X: supervise the work for the research activity planning and execution.

- The work of chapter 3 in the thesis has been published in a joint authors contribution publication.

"BAQER, Y., CHEN, X. & THORNTON, S. 2019. Geochemical modelling of multimineral evolution for a 15-month experiment. Environmental Geotechnics, 40, 1-9."

The contribution of each co-author in this publication was:

Yousef Baqer: Leading writing the paper, including setting up the geo-chemical code for the studied system, perform computer modelling and simulation, interpreted the behaviour of the modelling resulting compared with the experimental data, prepare the manuscript. CHEN, X: supported in understanding and building the geo-chemical model. THORNTON, S: assisted in the interpretation of the modelling results and contribute to the manuscript editing.

- The work of chapter 4 in the thesis has been published in a joint authors contribution publication.

"BAQER, Y., CHEN, X., ROCHELLE, C. & THORNTON, S. 2020. Modelling of multi-minerals kinetic evolution in hyper-alkaline leachate for a 15-year experiment. Environmental Science and Pollution Research, 27, 35604-35617."

The contribution of each co-author in this publication was:

Yousef Baqer: Leading writing the paper, including setting up the geo-chemical code for the studied system, perform computer modelling and simulation, interpreted the behaviour of the modelling resulting compared with the experimental data, prepare the manuscript. CHEN, X: supported in understanding and building the geo-chemical model. ROCHELLE, C: support in understanding the original experiment, refine the manuscript and provide deeper insight into the results. THORNTON, S: assisted in the interpretation of the modelling results and contribute to the manuscript editing.

- The work of chapter 5 in the thesis has been published in a joint authors contribution publication.

"BAQER, Y., BATEMAN, K., TAN, V., STEWART, D. I., CHEN, X. & THORNTON, S. F. 2021. The Influence of Hyper-Alkaline Leachate on a Generic Host Rock Composition for a Nuclear Waste Repository: Experimental Assessment and Modelling of Novel Variable Porosity and Surface Area. Transport in Porous Media, 140, 559-580."

The contribution of each co-author in this publication was:

Yousef Baqer: Leading writing the paper, including setting up the geo-chemical code for the studied system, perform computer modelling and simulation, interpreted the behaviour of the modelling resulting compared with the experimental data, prepare the manuscript. BATEMAN, K: provide technical details about the original experiment and advice on the procedure, assist in results interpretation and manuscript improvement. TAN, V: work on the original experiment and provided some technical conclusion. STEWART, D. I: assisted in the interpretation of the modelling results and contribute to the manuscript editing. CHEN, X: supported in understanding and building the geo-chemical model. ROCHELLE, C: support in understanding the original experiment, refine the manuscript and provide deeper insight into the results. THORNTON, S: assisted in the interpretation of the modelling results and contribute to the manuscript editing.

- The work of chapter 6 in the thesis has been submitted in a joint authors contribution publication.

"BAQER, Y., NORRIS, S., THORNTON, S., STEWART, D. I. & CHEN, X., Analysis of uranium sorption in a laboratory column experiment using a reactive transport and surface complexation model"

The contribution of each co-author in this publication was:

Yousef Baqer: Leading writing the paper, including setting up the geo-chemical code for the studied system, perform computer modelling and simulation, interpreted the behaviour of the modelling resulting compared with the experimental data, prepare the manuscript. NORRIS, S: refine the manuscript and provide deeper insight into the results. THORNTON, S: assisted in the interpretation of the modelling results and contribute to the manuscript editing. STEWART, D. I: assisted in the interpretation of the modelling results and contribute to the manuscript editing. CHEN, X: supported in understanding and building the geo-chemical model.

Abstract

Constructing a robust numerical model that captures multi-mineral transformations, multiple chemical reactions, and secondary phase pathways in geological repositories is challenging due to uncertainties in parameters and a limited available database describing the kinetics of dissolution/precipitation reactions. In this work, combined with experiments, a comprehensive reactive transport model is used to study the chemical and physical interactions among radionuclides, cement leachate and the host rock in a nuclear waste repository. Hence, the modelling efforts will enhance the understanding of the transport of radionuclides in complex soil/rock systems and highlight the critical factors driving their migration in soils/rocks. To achieve these aims, the modelling of the radionuclide migration process was first investigated, considering all possible reactions that could take place. Then, the PHREEQC software was used for the numerical simulation, and experimental data were used to validate the model. The experiment studied a system for 15 months and 15 years with young cement leachate (pH=13) and intermediate cement leachate (pH = 10.8), respectively. Then, with the dissolution/precipitation kinetics implemented and verified, the transport process was incorporated with the aim of building a geochemical model that will describe the multimineral mass transfer under different conditions. Furthermore, the geochemical model was constructed to ensure the porosity evolution of the porous medium. Finally, radionuclide migration was incorporated into the model to characterise the effect of the sorption process.

These studies showed that fluid chemistry controls the dissolution/precipitation of the primary minerals, which will control the long-term chemical equilibria and mineralogical composition of the host rock impacted by the alkaline leachate. Meanwhile, the chemical

interaction between hyper-alkaline leachate and the host rock results in a series of mineralogical reactions, including cycles of minerals dissolution and precipitation (calcium silicate hydrate gel, C-S-H phases, C-A-S-H phases, hydrated silicate, and Na-Ca zeolites). Furthermore, by coupling the mineral volume changes and porosity evolution to the dissolution/precipitation reaction model, the results showed a better fit in ion concentration compared to the fixed porosity model, as it led to a more reactive surface area with the cement leachate. Moreover, the model shows that the dissolution of primary minerals in the host rock is the initial driving mechanism for the chemical evolution of the system. At the same time, the subsequent precipitation of several secondary phases controls the host rock's long-term chemical equilibria and mineralogical composition. Lastly, the sorption of uranyl (UO_2^{2+} (U_{VI})) was found to strongly depend on the surface complexation model assumed, with no significant removal of U_{VI} by precipitation or ion exchange process. Furthermore, uranyl adsorption by the C-S-H phase was found to be minimum, which could be related to the lack of surface complexation parameters for C-S-H minerals.

Contents

Acknowledgment

My deepest appreciation goes to my advisor Dr. Xiaohui Chen who offered limitless guidance and support. He has been an ideal mentor and thesis supervisor. I am very proud and grateful for all my time working with Dr. Chen. I will never forget his persistence and encouragement from the initial steps and throughout my research.

Thanks to my second supervisor Prof. Stewart for his great feedback, excellent encouragement, and support.

Thanks to Kuwait petroleum company for sponsoring my scholarship and provide an opportunity for me to grow professionally.

Chapter 1: Introduction

Knowledge concerning chemical species' reactions and reactive transport in natural porous media is of great importance in the application of geological remediation and stabilisation of industrial wastes, such as radioactive waste repositories (Van Der Lee and De Windt, 2001, De Windt et al., 2004, Metz et al., 2003, Soler and Mäder, 2005, De Windt et al., 2006, De Windt et al., 2007). Both the transport and the final state of pollutants are largely affected by chemical reactions that change the properties and characteristics of the host porous media. In the abovementioned applications, interactions between water (high pH plume in cementitious barrier) and rock will result in alternation of the geological media at the interface of the engineered barrier and the host rock (Lasaga and Rye, 1993, Steefel and Lasaga, 1994, Le Gallo et al., 1998, Bolton et al., 1999, Marty et al., 2009, KOSAKOWSKI et al., 2009). This chemical interaction induces the dissolution of minerals in the host rock, which then precipitate in new solid phases.

In practice, the chemical reactions of dissolution/precipitation can be divided into two groups, fast (equilibrium) and slow (kinetic) reactions (Rubin, 1983), based on whether or not their reaction time (which usually involves mineral and aqueous species) is slower than that of other mass transport processes (e.g. diffusion, advection; (Sanchez-Vila et al., 2010). Over the long term, these kinetic reactions will be key players in defining porosity evolution and the degree of alteration in the near-field rock's disturbed zone. In a system of a multicomponent species with spatial distribution, discrepancies in chemical reaction times can lead to a much more complex geochemical system as it encounters nonlinearities (Molins et al., 2004, Steefel et al., 2005).

In addition, the dissolution/precipitation cycle tends to change the solid phase volume and restructure pore sizes, thus altering fluid flow and transport characteristics of the host media. The amount and distribution of pores will eventually define the porosity and permeability of the geological media, which are key parameters in determining how migrating fluids will behave in the soil (Uchida, 1987, Bryant and Raikes, 1995, Bear, 2013). Pore size can also play a significant role in mediating the rates of mineral dissolution and precipitation by offering different ratios of reacting surface area to fluid volume (Emmanuel et al., 2010). Between mineral dissolution and crystal growth, a dynamic porosity will occur and change the transport properties in the host media (Saripalli et al., 2001).

The relationship between those three hydrological properties of the studied system (porosity, permeability, and reactive surface area) is of major importance in simulating continuum-scale models (Chen et al., 2012). For example, reactive surface area is a key parameter that affects the rate of crystal growth, which in turn alters the porosity pattern and mineral deposition. Although there has been some progress in understanding the coupled interaction between porosity and permeability (Chen et al., 2014a, Chen et al., 2015a, Kang et al., 2002, Tartakovsky et al., 2007b), literature that explains the relationship between porosity and reactive surface area remains scarce, as it is challenging to monitor and quantify this alteration in the mineral surface area during experiments (Mu et al., 2016, Chen et al., 2013).

1.1 Geochemical Modelling Software

The change in porosity combined with a kinetic reactions approach, create an overly complex geochemical system that is challenging to model. One way to model this complex and nonlinear system is a mathematical approach with a set of partial differential equations.

Such a model would encompass multiple coupled chemical and physical processes, such as mass transport, chemical reaction, fluid flow and changes in the porous structure (porosity and permeability), all of which are related to reactive fluid being transported through the porous media via dissolution and precipitation reactions (Molins et al., 2012, Tartakovsky et al., 2007b, Liu et al., 2015, Ovaysi and Piri, 2014, Bekri et al., 1995, Huber et al., 2014, Kang et al., 2014, Ryan et al., 2011, Chen et al., 2014b).

Several geochemical modelling software has been developed based on the constant equilibrium approach or Gibbs free energy method. Some of these models are WATEQ developed by (Truesdell and Jones, 1974), MINTEQA2 by (Allison et al., 1991), CHESS by (Van der Lee and De Windt, 2002), CHEMSAGE by (Eriksson and Hack, 1990), THERIAC by (de Capitani and Brown, 1987) and GEM-Selektor by (Karpov et al., 1997, Karpov et al., 2001, Karpov et al., 2002, Kulik et al., 2013). Unfortunately, some of these models have limitations such as high computational cost, incomplete Newton scheme, and instability of the equilibrium phase. In this study, PHREEQC, which was developed by (Parkhurst and Appelo, 1999, Parkhurst and Appelo, 2013, Appelo and Postma, 2005), has been implemented.

PHREEQC is a geochemical software developed by the United States Geological Survey. It includes multiple databases users can use or modify and apply to various aqueous models, including geochemical and industrial applications (Parkhurst and Appelo, 2013). Adding to its geochemical modelling tool, it can simulate 1D transport in porous media, making it applicable for the resolution of this research. The software comprises a vast database and geochemical equations describing the equilibria or kinetic interactions of aqueous solutions

with solids, gases, and minerals, with the advantage of easily adding or modifying necessary reactions if needed.

In PHREEQC, chemical reactions are integrated based on a built-in or user-defined rate expression, with the possibility of simulating time-dependent geochemical reactions that depend on solute temperature, pH and saturation ratios of minerals. Regarding kinetics reactions, the built-in interpreter contains rate expression (which can also be user-defined) with a Runge-Kutta scheme that solves the differential equations and change the solution speciation within a specific time interval. In addition, the user can define an error tolerance which allows the software to reduce the time interval of the simulation. This scheme effectively achieves equilibrium when multiple kinetic reaction rates are defined, and the rate of each reactant is changed during the reaction.

Moreover, the software has an open access to its code and geochemical library, which allows the interpretation of any new chemical species, phases, and reactions. This enables the simulation of extra secondary phases such as CSH, CASH, and cement hydrates minerals with complex chemical composition. Likewise, surface complexation and cation exchange reaction and parameters (based on our experiment conditions) were allowed to be entered manually (Chapter 6). Moreover, the modular design of PHREEQC code allows the synthesis with other software (Comsol, PHAST, and PHT3D), which has a much more powerful tool for performing the physical changes of the studied system (Charlton and Parkhurst, 2011, Parkhurst and Wissmeier, 2015). Finally, PHREEQC also allows the user to write his own set of equations such that the changes in the chemical and physical properties of the studied mineral are performed under a specific set of conditions. This advantage, for instance, has been used in this research, especially in chapter 5, where the

variable porosity has been included in the system by manually calculating the changes in the mineral volume. The reader can refer to (Parkhurst and Appelo, 2013) for more details about PHREEQC.

1.1.1 Mixed Kinetic-Equilibrium Approach (MKE)

In PHREEQC, the algorithm works on the principle of equilibrium chemistry between the aqueous solution and the interacting minerals, solid solution, gases, Etc, which are brought to equilibrium with reactants. The reactions are usually defined by specifying one or multiple solutions that are in contact with a solid-solution, pure-phase, or surface assemblage. One of the major drawbacks of equilibrium modelling is that reactants do not react to equilibrium within the time frame of any experiment or simulation period of any model. Therefore, PHREEQC allows the capability to work on the concept of kinetic reactions that is integrated with a time-step algorithm and generates a change in the concentration of the solution's aqueous species. However, kinetic modelling can have a high computational cost in multi-component flow and reactive transport in porous media (since it depends on calculating the equilibrium following a set of reversible/irreversible reactions for each reactant at each time step). Moreover, the user-defined rate equation can have several mineral-specific parameters which are not always available. Thus, PHREEQC allows the kinetic and equilibrium chemical reactions to be interconnected in a mixed kinetic-equilibrium approach (Parkhurst and Appelo, 2013).

This approach was initially developed to overcome the shortage of kinetic data for minerals that dissolve and precipitate (Soetaert et al. 1996), assuming a faster reaction by means of the equilibrium concept and a slower reaction controlled by the kinetic process (Atkinson et

al. 1988; Hoch et al. 2012). The concept is based upon the timescale of each mineral reaction rate (i.e., which reaction is faster and which slower). For each mineral, either a kinetic or equilibrium approach, or a mix of both (if the difference between rates was more than 10^2) is applied. In overall, MKE approach enables faster reactions using the equilibrium concept with slower kinetically-limited reactions. It combines kinetic and equilibrium laws' advantages and allows the modelling of complex reaction systems (Chen and Thornton, 2018, Van der Lee, 1998, Bethke, 1996). This concept has been widely implemented in subsurface geochemical applications, as it allows both kinetic and equilibrium reactions to model a multiphase and multi-component system (Brun and Engesgaard 2002; Lichtner 1996; Mayer et al. 2002; Prommer et al. 2003).

1.2 Engineered Barriers for Geological Disposal

The overall concept of the waste management process for geological disposal is to design a multi-barrier system for direct immobilisation of radionuclide movement that can last for hundreds of years without any impact on the environment or human health. The containment matrix is placed in a certified site for the disposal, and is designed based on the radioactive level of the waste. One common multi-barrier system is known as Nirex Reference Vault Backfill (NRVB; (Crossland, 2007). The concept starts with locating a disposal site that is hundreds of metres, sometimes up to several kilometres, underground. The waste containers (usually made of stainless steel) are then placed in a host rock and backfilled with a high-pH cement or clay, which will provide an extra chemical barrier to radionuclide mobility.

Geochemical and hydrological factors of the repository, including salinity level, underground water minerals, thermal cycling and temperature rises due to cement hydration

and waste material decay, can also affect the integrity of the engineered barrier (Koťátková et al., 2017). All the possible interaction scenarios between those factors and the host rock should therefore be studied to prevent long-term failure of radionuclide repositories. Porosity and permeability of cement are also essential characteristics that influence groundwater and radionuclide migration through the cement barrier, so they should be considered cautiously while designing geological disposal facilities. A high porosity value will allow greater access for groundwater and more dissolution of cement hydrate phases, resulting in greater alkalinity (Vasconcelos et al., 2018). Cement permeability should therefore be very low; however, it must also be sufficient to allow the gases produced from the waste to discharge without building pressure and cracking the cement (Francis et al., 1997).

1.2.1 Cement Barrier

In a multi-barrier system, a wall of cement may be placed as engineered secondary protection for direct immobilisation of transported radionuclides. The adoption of cement as a barrier resulted due to its relatively low cost in combination with its unique chemical and physical bond properties, which both contribute to radionuclide immobilisation. The practice of cementitious backfilling has been widely used around the world in different mining and waste disposal applications (Fall and Nasir, 2009, Ghirian and Fall, 2014, Sivakugan et al., 2006, Yilmaz et al., 2004). Cement's large surface area allows higher sorption and uptake capacity for different radionuclide species. Moreover, when groundwater reacts with cement, an ideal alkaline environment with high buffering capacity is created via the dissolution process in the cement hydrate phases (Figure 1.1). Alkalinity then helps stop the migration process through sorption and low solubility, which only allows the diffusion process to take place in radionuclide transport (García-Gutiérrez et al., 2018).
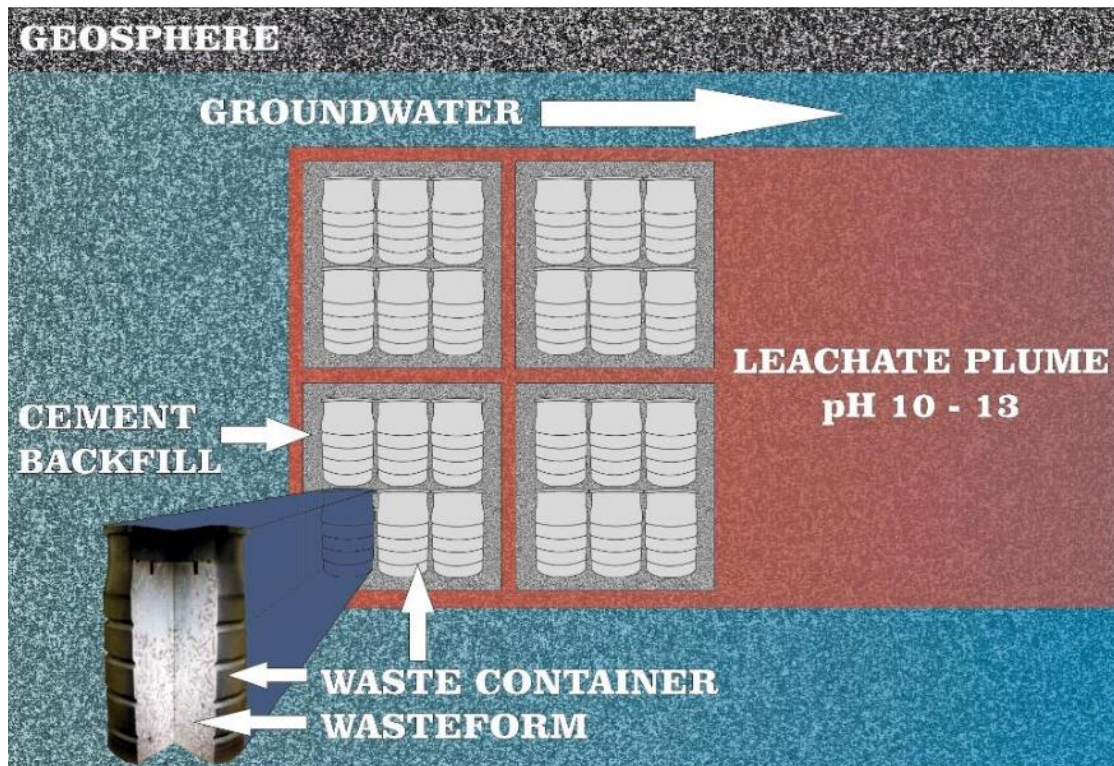
Figure 1.1: Schematic diagram showing the development of high cement leachate due to the interaction with the cement backfill in nuclear disposal facility (Moyce, 2014).

The technology of cement paste backfills (CPB) consists of a mixture of chemicals, water and additives such as Portland cement. As an engineered barrier, the structural design of CPB should fulfil several criteria, such as cost, durability and environmental impact performance for reliability and environmental assessments (Pierce, 1999, Denton et al., Ghirian and Fall, 2013). Thus, predicting the behaviour of the CPB structure is of great practical importance from early placement until advanced stages. Once it is underground, the CPB is continuously subjected to complex multi-physics conditions (thermal, hydraulic, mechanical and chemical) that influence its physical (transport, mechanical) properties (Cui and Fall, 2015). These reactive chemical and physical processes develop over a large scale of time and space, making them inaccessible through experimental methods. Thus, numerical modelling methods are needed to assess geochemical changes.

When groundwater equilibrates with minerals in the cement barrier of geological radioactive waste disposal facilities, there is a potential risk of the formation of an alkaline leachate. Previous research has considered three cement leachate evolution stages based on the progression of pH values (Small et al. 2016), which can be summarised as young cement leachate (YCL), intermediate cement leachate (ICL) and old cement leachate (OCL). Such leachates can trigger dissolution or precipitation reactions in the host rock and, thus, change its hydraulic, chemical and sorption properties long before any penetration of radionuclides. The time scale of each cement leachate phase can depend on the hydrogeological characteristics of the surrounding host rock. Typically, the first stage of cement leachate is highly alkaline (pH 13) and lasts a relatively short period of time. The second stage occurs over a long-time scale with a pH that has been buffered by the precipitation of solid CSH phases to lower than 12.5. In the final stage, the cement leachate equilibrates with groundwater to a pH of approximately 9. These changes in the pH value over time trigger different dissolution/precipitation reactions of secondary phases in the chemical disturbed zone (CDZ), which can eventually affect the surface sorption of radionuclides.

In the last two decades, efforts have been focused on developing a numerical code to model the coupled multi-physics processes (thermo-hydro-mechanical-chemical) in porous media. The aim is to develop a single code that can handle and simulate separate coupled non-linear partial differential equations of saturated flow that describe the coupling between fluid flow and multispecies solute transport in geochemical reactions in porous media. Among those efforts are PHREEQC (Parkhurst and Appelo, 2013), PHAST (Parkhurst et al., 2010), PHT3D (Prommer et al., 1999), PHWAT (Mao et al., 2006), TOUGHREACT (Xu et al., 2011) and OpenGeoSys (Kolditz et al., 2012). Despite the complexity of the integrated code

in some of the software programs, all are still designed for specific coupled processes and lack the capacity to model a wider application.

1.3 Radionuclides and Naturally Occurring Radioactive Material (NORM)

Radionuclides and their daughter products are long-lived radioactive and toxic materials that are the dominant nuclear wastes disposed into the environment. For example, U^{238} is the source of most uranium isotopes found in nature (Gavrilescu et al., 2009). In any disposal site with wet radioactive soil, uranium and its decay products will begin reacting with the soil content and migrate into other zones. The radionuclides can participate in an ion exchange reaction, complex with soil organic and inorganic material, and finally dissolve in solution. The solubility of radionuclide molecules depends on several factors, such as soil pH, porosity, moisture level, sorption characteristics, redox reaction, temperature, soil particle size and the existence of organic and inorganic materials (Allard et al., 1982, Bachmaf and Merkel, 2010a). The form of the uranium molecules (complexed, precipitated and sorbed) can also affect their mobility characteristics. Uranium is usually found in its oxidised state in soil, whereas in water, it is found in the form of uranyl hydroxyl (UO_2^{+2}) and carbonate complexes such as $(UO_2)_2CO_3(OH)_3$ (Roh et al., 2000, Vochten et al., 1990). The oxidised form of uranium, U(VI), generally has higher solubility and mobility than U(IV), which is insoluble (Tokunaga et al., 2004).

Uranium penetrates a cementitious geological repository through active diffusion that is governed by slow dissolution-precipitation kinetics. The solubility of uranium in a bespoke backfill (NRVB) is similar to that in a 95%-saturated Ca(OH)₂ solution. The extent of

uranium migration in the saturated zones of a nuclear waste repository depends primarily on the rate and direction of groundwater flow and the capacity of the host rock to absorb it.

In the natural environment, uranium usually occurs in igneous acid rock, from which it is then removed by the weathering process to an oxidising 6^+ state, forming UO_2^{2+} with oxygen. This bond between uranium and oxygen is characterised as uranyl/U_{VI}, which is very soluble and mobile in an oxidising environment. In this environment, the solubility and adsorption of U_{VI} is influenced by the pH of the water, ionic strength, uranyl mineralogy, carbonate concentration and the CO_2 partial pressure, all of which can modify the surface and aqueous speciation. As an example, U_{VI} becomes the dominant species at pH values between 4 and 6 and sorption increases up to the neutral point, whereas the presence of CO_2 can vastly reduce the adsorption of U_{VI}-carbonate aqueous species, which are dominant in many alkaline groundwaters. This reflects the fact that neutral (UO_2CO_3) and negatively charged $(UO_2(CO_3)_2^{2-})$ complex ions are unlikely to be sorbed on negatively charged mineral surfaces. The recent development of the sorption model shows that uranium retardation is still challenging to predict with all the variables included in the process, such as characterisation of the sorbent material (mineral type and composition, density of sorption sites, surface area), solid-solution ratio, solution composition, carbon dioxide concentration, and pH value.

Some of the most abundant industrial wastes today are naturally occurring radioactive materials (NORM). Although the issue of NORM production was first identified nearly 100 years ago, the importance of these materials did not become clear until the past few decades, when the radioactivity of concentrated NORM was placed in the category of life-threatening substances (Shawky et al., 2001, Rood and Kendrick, 1996, Parmaksiz et al., 2015, AL

Nabhani et al., 2016). Concerns regarding these wastes were raised among global societies, and a considerable effort has been made to elucidate and identify the chemistry of these radionuclides, how they form, the effects of geological and geotechnical factors on these nuclides and the health risks associated with their presence.

1.4 Capturing Mineral Dissolution and Precipitation Effects in Reactive Transport Modelling

In this section, a summary of works on precipitation and/or dissolution processes in reactive transport modelling is presented. Precipitation and dissolution reactions have significant effects on the evolution of the porous media matrix. The examination of the pore network shows that the pore sizes, pore diameters, and pore connectivity strongly affect the fluid transport in a porous medium. A low degree of tortuosity (which occurs with large pores and direct connectivity) easily enhances the flow and diffusive/advective transport.

In an evolving porous medium, the evolution of porosity and connectivity are both influenced by mineral dissolution and precipitation processes. The incremental change in porosity is proportional to the dissolution of the solid phase. Although the dissolution of the minerals increases the total porosity, it does not suggest the exact incremental change in the effective porosity of the system. For example, with increased dissolution, the effect can be significant, and it will open up more throats or dissolution paths, as observed by (Moreira and Coury, 2004, Knackstedt and Zhang, 1994). Still, if the dissolution is more uniformly distributed, the effect will be limited (Algive et al., 2010). In the same vein, if the precipitated minerals form on existing surfaces without the clogging of the pore throats, it can still limit the system's connectivity.

The most common and general equation which describe the dissolution/precipitation rate of minerals is (Morse and Berner, 1972):

$$r_m = -\frac{dm_{mineral}}{dt} = \left(\frac{S}{V_s}k_r\right)(1 - \Omega_j) \quad (1.1)$$

where r_m is the rate of precipitation or dissolution, m is moles of mineral, t is time, S_0 is reactive surface of the mineral exposed to the fluid reactants, V_s is solution volume, k_r is reaction rate constant and Ω_j is saturation ratio (Morse and Berner, 1972).

To implement the above equation, many pieces of information are required such as surface area, reaction rate and the number of moles. It is not an easy task to obtain those value for all minerals. Therefore, an equilibrium approach was implemented along with the kinetic one and a combined kinetic-equilibrium approach was generated. This method will allow the modelling of several minerals in complex reaction system (Van der Lee, 1998, Bethke, 1996).

1.4.1 Mineral Dissolution

Accounting for the dissolution effect on the material properties of the media is critical because such reactions can have a significant impact on solute transport through the pores of the media. Predicting the media's properties evolution due to the dissolution process requires the understanding of underlying processes that govern the development of patterns. Some of the past attempts which investigated the dissolution of minerals reported that there

is a possibility of developing stable fronts (Walsh et al., 2013, Barlet-Gouedard et al., 2006), while in some instances (for example, karst development), unstable dissolution fronts that can lead to worm holing can also occur (Golfier et al., 2002, Daccord et al., 1989, Hoefner and Fogler, 1988, Steefel and Lasaga, 1990).

The dissolution regime is affected by the characteristic times of advection, diffusion and reaction as observed by (Luhmann et al., 2014, Algive et al., 2012). Meanwhile, the Peclet and Damkohler numbers define the existing correlations between the characteristic times for transport and reaction processes. When describing the relative significance of the advective and diffusive transport, the Peclet is often used. At the same time, the Damkohler numbers help to describe the ratio of the characteristic times of reaction relative to transport (Tartakovsky et al., 2007b, Min et al., 2016). In an experiment conducted by (Fredd, 2000), the response of carbonates to the influx of acid water showed the possibility of having different dissolution patterns with increasing injection rates. When the injection rates become low, the dissolution near the injection point will be uniform, while all the injected acids are consumed at this point. However, an increase in the Peclet number will introduce a deeper reach of the acid water through the main path where reactions occur. This form of dissolution creates a conical wormhole. In a study conducted by (Detwiler et al., 2003), he demonstrated distinguishing conical and ramified dissolution patterns. When the injection rates are high, and the acid waters propagate throughout the porous media, uniform or ramified dissolution will be observed with little or no reaction with the medium.

Below are examples of dissolution chain-reaction for some minerals based on experiments done by different researchers (Arakaki and Mucci, 1995, Plummer et al., 1978, Chou et al., 1989, Van Cappellen et al., 1993, Morse and Arvidson, 2002).

$$CO_3^- + 2H^+ \leftrightarrows Ca^+ + H_2CO_3 \qquad (1.2)$$

$$Ca^+ + H_2CO_3 \leftrightarrows CO_3H^0 + CaHCO_3^+ \qquad (1.3)$$

$$CO_3H^0 + CaHCO_3^+ \leftrightarrows Ca^+ + H_2CO_3 + CaCO_3^0 \qquad (1.4)$$

$$CaMg(CO_3)_2 + H^+ \rightarrow MgCO_3 + Ca^{2+} + HCO_3^- \qquad (1.5)$$

$$CaMg(CO_3)_2 + H_2CO_3^0 \rightarrow MgCO_3 + Ca^{2+} + 2HCO_3^- \qquad (1.6)$$

$$CaMg(CO_3)_2 + H_2O \rightarrow MgCO_3 + Ca^{2+} + HCO_3^- + OH^- \quad (1.7)$$
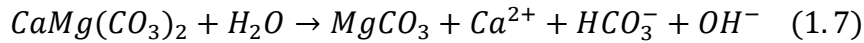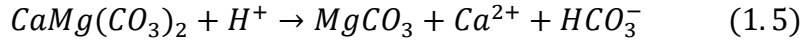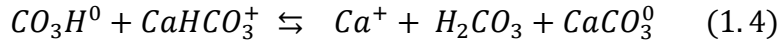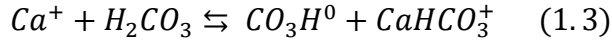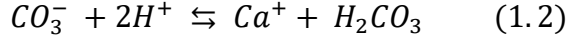
1.4.2 Mineral Precipitation

The secondary precipitation process can significantly affect the fluid flow and transport process in a porous media matrix. For instance, precipitation can result in self-healing of the fractures (Gherardi et al., 2007, Dobson et al., 2003, Steefel and Lasaga, 1994, MacQuarrie and Mayer, 2005) or strengthening of the porous matrix (Jacquemet et al., 2012, Bickmore et al., 2001, Pfingsten, 2002). In the works of (Dauzeres et al., 2010, Seigneur et al., 2017), they observed that when cementitious materials are carbonated underwater, this can form calcites on the material surface, which can make the materials impervious. Similarly, (Dewanckele et al., 2012) found that gypsum precipitation resulted in the formation of crust on some historical monuments. Alternatively, The formation of secondary minerals may generate mechanical stresses internally and induce fractures, which will further cause the porous media to deteriorate (Chagneau et al., 2015, Li et al., 2017). In cementitious materials, internal fractures can be generated due to the delayed formation of atmospheric carbonation, which can be dangerous in keeping the integrity of the repositories for CO_2 sequestration or radioactive waste management. From these cited examples, it is evident that

clogging can occur from precipitation and significantly affect flow and transport. Therefore, it is critical to understand the significance of precipitation on the transport properties of the media and their evolution.

1.5 Radionuclide Migration in Engineered Barriers by Convection and Diffusion

In geological disposal facilities, radionuclides could leak and thereby affect the geosphere if engineered barriers fail. The fear of environmental hazards involving radioactive materials is associated with the contamination of underground water and agricultural soils, which poses a risk to ecological systems and human health. Understanding this movement can help define the risk of external radiation in a contaminated area to a population. In general, the migration rate in engineered barriers depends on several key factors, including half-life of the radionuclides, mineralogy structure, water infiltration velocity and moisture content, as well as sorption kinetics, which are considered in most research to be the dominant factor (Kumar et al., 2013).

When radionuclide elements are solutes, their mobility depends not only on their concentration but also on other factors such as pH level, alkalinity, the presence of organic and inorganic materials, and the chemical behaviour of the complexes they form with other elements such as carbonates and phosphates (Baird and Cann, 2008, Brümmer, 1986). Radionuclides are generally trapped in their geological source by the engineered barrier, which prevents their escape. Groundwater/gas may carry the radionuclides, however, and transport them to the geosphere. This process is the main factor in radionuclide movement and depends on the characteristics of the engineered barrier and the surrounding boundary conditions. For this reason, the process is complicated, and it is not easy to characterise all

of the involved parameters. Nevertheless, researchers have included this phenomenon in their mathematical models and have described the transfer of radionuclides by the 1D advection-reaction-dispersion equation (Arnold et al., 2003).

1.5.1 Advection-Reaction-Dispersion Equation

Advection is usually defined as the process of transferring radionuclides by the movement of groundwater, where the radionuclides are a dissolved material in the water. The motion of the radionuclides can be along the flow of the groundwater and have different speeds, depending on the rock pore size. Radionuclides can also flow in a lateral direction in a process called negative dispersion. The convection process can be described by Darcy's Law, following the equation:

$$q_l = -\frac{\kappa}{\mu_l} \left(\nabla p_l - \rho_l g \right) \qquad (1.8)$$

where q_l is the Darcy flux (m^3 m^{-2} s^{-1}) for the liquid, κ is permeability tensor (m^2), μ_l is liquid dynamic viscosity (Pa s), p_l is fluid pressure (Pa), ρ_l is liquid density (kg m^{-3}) and g is gravity vector (m s^{-2}) (Pulkkanen, 2009).

Meanwhile, the diffusion process describes the movement of radionuclides from high-concentration to low-concentration areas. This means radionuclide diffusion will occur even if groundwater is not flowing (concentration gradient dependent). The diffusion process is considered random because it is impossible to know the position of a specific radionuclide in a future moment (Moreno et al., 2006). Mass transfer can occur mainly by this process for

low permeability geological media. For one-dimensional diffusion, the mass of the fluid

diffused is proportional to the concentration gradient, such that:

$$J_x = -D\frac{\partial C}{\partial x} \qquad (1.9)$$

where J is the mass flux (kg m^{-2} s^{-1}), D is the diffusion coefficient (m^2 s^{-1}), x is distance (m) ,

and C is the contaminant concentration (kg m^{-3}; (Bucur et al., 2006). In the geochemical

modelling code of PHREEQC, both processes are modelled simultaneously with the

incorporation of the chemical reaction by using the advection-reaction-dispersion equation

as below:

$$\frac{\partial C_i}{\partial t} = \underbrace{-q_l \frac{\partial C_i}{\partial x}}_{Advection} + \underbrace{D_L \frac{\partial^2 C_i}{\partial x^2}}_{Dispersion} - \sum_{m=1}^{l} v_{im} R_m \qquad (1.10)$$

where C_i is the total concentration of component i in water (mol kgw^{-1}), t is time (s), x is

the distance (m), D_L is hydrodynamic dispersion coefficient (m^2 s^{-1}), v_{im} is the

stoichiometric coefficient of component i in kinetic reactant m (dimensionless), R_m is the

overall dissolution/precipitation rate of kinetic reactant m (mol kgw^{-1} s^{-1}), and l is the

number of kinetic reactants. An explicit finite difference algorithm will solve the equation

for each time step using a split-operator scheme, where the chemical interaction term

($v_{im} R_m$) for each mineral is calculated separately after the advection and dispersion step

for all equilibrium and kinetic reactions.

1.6 Research Questions and Gaps in Modelling Evolved Porous Media with Reactive Transport

- The heterogeneities in mineral types and pore structure create a challenge in obtaining a relationship for transport and reactivity parameters in the porous media under continuous evolving conditions.

- Existing relationships which connect the effective transport parameters back to evolved porosity are inconsistent in results for the transport properties.

- The transport regime and time scale of reaction and transport can result in different evolution of the porous media, even for identical systems.

- The evolution of the porous media is usually related to processes at the pore scale. Therefore, studying transport and reactivity parameters evolution at the continuum scale is still limited.

- For some processes and materials, some generalisations can be drawn in terms of the relationships that describe the evolution of transport and reactivity parameters. However, those relationships should be built based on each case's observational data.

- In past numerical modelling attempts, when analysing nuclear waste repositories, most authors assumed the host rock's key properties to be constant. Though, in this research, an adequate approach was used to study the effects of variable porosity, reactive surface area and pore volume on improving the modelling of rock alteration in the system.

1.7 Aim and Objectives

Cement materials, which are often used as an engineering barrier in low/intermediate nuclear geological repositories, will be selected as a key element in this research. This research aims to develop a comprehensive reactive transport numerical model against

experiment to study chemical and physical interactions among radionuclides, cement leachate and the host rock of a nuclear waste repository. The purpose to improve our understanding of radionuclide transport in complex soil/rock systems and indicate critical factors in predicting radionuclide soil migration processes. To achieve this aim, several objectives have been set.

- **The process of modelling mineral dissolution/precipitation reactions**

Analysing all potential reactions that might occur with subsurface water or the aqueous phase is the initial step in modelling the radionuclides migration process. The process entails the dissolution and precipitation of pure phases to re-establish balance, which can impact radionuclide migration via convection. The modelling of these reactions is usually based on experimental data using geochemical software (PHREEQC) that can ascertain all potential phases manifested in the chemical processes.

- **The process of chemical transport in a column experiment**

The transport process of radionuclides is characterised by the movement of chemicals within the groundwater flow. The concept is based on the phenomenon of multi-mineral mass transfer under different geochemical conditions. In PHREEQC, the process is modelled by a one-dimensional advection-dispersion transport process for various porous media.

- **Dynamic porosity and surface area combined with the kinetics of mineral's dissolution/precipitation**

The movement and reaction of radionuclides entail fluid hydraulics, chemical reactions, and physical modifications. Over time, the coupled interactions between chemical and physical elements can evolve the chemical properties (e.g., sorption capacity, reactive surface area) and physical properties (e.g., porosity, permeability) of the host rock in the near field barrier. During the evolution of porous media, the transport and chemical properties vary in space and time. PHREEQC's chemical capacity ought to enable the modelling of various multi-physics and chemical situations, as well as show how each process affects the others and how porosity changes within the system.

- **Uranium Integration into the reactive transport model**

The migration of radionuclides in the engineered barriers depends on several key factors, including the half-life of the radionuclides, mineralogy structure, water infiltration velocity and moisture content, as well as sorption kinetics. In addition, the interaction between dissolved radionuclides and minerals in the host rock (sorption at solid/solution interface) is critical when evaluating the immobilisation of radionuclides. Uranium transport and sorption methodologies shed light on the critical variables that have the most significant bearing on reducing uranyl mobility in a geological repository. It also lists the information needed to build a consistent and trustworthy model for the geochemical application's reactive transport and sorption process of radionuclide migration.

1.8 Thesis Structure

The second chapter of this report starts with a comprehensive review of the equations governing multicomponent flow and reactive transport in porous media, along with a summary of the common methods used to describe the transport process, fluid flow, reactive surface area and reaction parameters such as porosity, permeability and tortuosity. Furthermore, past and recent attempts at using reactive transport models to address several challenges in nuclear waste disposal are also presented.

Modelling of multi-mineral transformations, multi-chemical reactions and multiple secondary phase pathways remains a challenge due to uncertainties in parameters and a limited available database describing the kinetics of dissolution/precipitation reactions. Thus, Chapter 3 discusses the modelling approach, Mixed Kinetic-Equilibrium (MKE), which has been employed to study the complex reactions occurring in an experimental system consisting of Borrowdale Volcanic Group rocks permeated with a hyper-alkaline leachate over 15 months.

Chapter 4 presents a modelling study for a 15-year experiment that simulated the reaction of crystalline basement rock with evolved near-field groundwater (pH = 10.8). An MKE modelling approach was employed to study a dolomite-rich fracture-filling assemblage reacting with intermediate cement leachate. Similarly, Chapter 5 describes an experimental and modelling study that evaluated the geochemical interaction between young cement leachate (YCL, pH = 13) and a generic hard rock (in this case, Hollington sandstone, representing a 'hard' host rock) while permeation with the leachate drove mineralogical changes in the system. One-dimensional reactive transport was modelled using a mixing cell approach within the PHREEQC geochemical code to identify the essential parameters,

and understand and scale up the effect of variations in these parameters on the observed geochemical processes. This study also focused on the effects of variable porosity, reactive surface area and pore volume on improving the modelling of rock alteration in the system in comparison to conventional models that assume constant values for these properties.

The sixth chapter presents a study in which the transport and attenuation of uranium in a column experiment was modelled by considering kinetic reactions, advection-dispersion and chemical/physical retardation processes. The modelling was first performed for column experiments with three-alluvium samples from Yucca Mountain under circumneutral pH conditions to understand the effects of different mineralogy and solution alkalinity on uranium breakthrough in the presence of retention mechanisms that involve mineral phase precipitation, ion exchange and surface complexation processes. After validating the reactive transport model with the sorption processes, the model was then used to interpret uranium transport in a laboratory column filled with Hollington sandstone under hyper-alkaline (pH 13) conditions. Finally, the overall conclusion, current challenges associated with reactive transport modelling and future research opportunities are discussed in Chapter 7.

References

1. AL NABHANI, K., KHAN, F. & YANG, M. 2016. Technologically Enhanced Naturally Occurring Radioactive Materials in oil and gas production: A silent killer. *Process Safety and Environmental Protection,* 99**,** 237-247.

2. ALGIVE, L., BÉKRI, S., NADER, F. H., LERAT, O. & VIZIKA, O. 2012. Impact of diagenetic alterations on the petrophysical and multiphase flow properties of carbonate rocks using a reactive pore network modeling approach. *Oil & Gas Science and Technology–Revue d'IFP Energies nouvelles,* 67**,** 147-160.

3. ALGIVE, L., BEKRI, S. & VIZIKA, O. 2010. Pore-network modeling dedicated to the determination of the petrophysical-property changes in the presence of reactive fluid. *SPE Journal,* 15**,** 618-633.

4. ALLARD, B., OLOFSSON, U., TORSTENFELT, B., KIPATSI, H. & ANDERSSON, K. 1982. Sorption of actinides in well-defined oxidation states on geologic media. *Mater. Res. Soc. Symp. Proc.,* 11**,** 775–782.

5. ALLISON, J., KEVIN, J., GRADAC, N. & BROWN, D. S. 1991. *MINTEQA2: A Geochemical Assessment Model for Environmental Systems: Version 3.0 User's Manual*, National Technical Information Service.

6. APPELO, C. & POSTMA, D. J. B., ROTERDAM 2005. Geochemistry, groundwater and pollution, CRC.

7. ARAKAKI, T. & MUCCI, A. J. A. G. 1995. A continuous and mechanistic representation of calcite reaction-controlled kinetics in dilute solutions at 25 C and 1 atm total pressure. 1**,** 105-130.

8. ARNOLD, B. W., KUZIO, S. P. & ROBINSON, B. A. 2003. Radionuclide transport simulation and uncertainty analyses with the saturated-zone site-scale model at Yucca Mountain, Nevada. *J. Contam. Hydrol.,* 62-63**,** 401–419.

9. BACHMAF, S. & MERKEL, B. J. 2010. Sorption of uranium(VI) at the clay mineral–water interface. *Environ. Earth Sci.,* 63**,** 925–934.

10. BAIRD, C. & CANN, M. 2008. *Environmental Chemistry Solutions Manual,* London, UK, Macmillan.

11. BARLET-GOUEDARD, V., RIMMELE, G., GOFFE, B. & PORCHERIE, O. Mitigation strategies for the risk of CO2 migration through wellbores. IADC/SPE drilling conference, 2006. Society of Petroleum Engineers.

12. BEAR, J. 2013. *Dynamics of fluids in porous media*, Courier Corporation.

13. BEKRI, S., THOVERT, J. & ADLER, P. 1995. Dissolution of porous media. *Chemical Engineering Science,* 50**,** 2765-2791.

14. BETHKE, C. 1996. *Geochemical reaction modeling: Concepts and applications*, Oxford University Press on Demand.

15. BICKMORE, B. R., NAGY, K. L., YOUNG, J. S. & DREXLER, J. W. 2001. Nitrate-cancrinite precipitation on quartz sand in simulated Hanford tank solutions. *Environmental science & technology,* 35**,** 4481-4486.

16. BOLTON, E. W., LASAGA, A. C. & RYE, D. M. 1999. Long-term flow/chemistry feedback in a porous medium with heterogenous permeability; kinetic control of dissolution and precipitation. *American Journal of Science,* 299**,** 1-68.

17. BRÜMMER, G. 1986. Heavy metal species, mobility and availability in soils. *In:* BERNHARD, M., BRINCKMAN, F. E. & SADLER, P. J. (eds.) *The Importance of Chemical "Speciation" in Environmental Processes.* Berlin, Heidelberg: Springer.

18. BRYANT, S. & RAIKES, S. 1995. Prediction of elastic-wave velocities in sandstones using structural models. *Geophysics,* 60**,** 437-446.

19. BUCUR, C., OLTEANU, M. & PAVELESCU, M. 2006. Radionuclide diffusion in geological media. *Rom. J. Phys.,* 51**,** 469–478.

20. CHAGNEAU, A., CLARET, F., ENZMANN, F., KERSTEN, M., HECK, S., MADÉ, B. & SCHÄFER, T. 2015. Mineral precipitation-induced porosity reduction and its effect on transport parameters in diffusion-controlled porous media. *Geochemical transactions,* 16**,** 1-16.

21. CHARLTON, S. R. & PARKHURST, D. L. 2011. Modules based on the geochemical model PHREEQC for use in scripting and programming languages. *Computers & Geosciences,* 37**,** 1653-1663.

22. CHEN, L., HE, Y.-L., KANG, Q. & TAO, W.-Q. 2013. Coupled numerical approach combining finite volume and lattice Boltzmann methods for multi-scale multi-physicochemical processes. *Journal of Computational Physics,* 255**,** 83-105.

23. CHEN, L., KANG, Q., MU, Y., HE, Y.-L & TAO, W.-Q. 2014a. A critical review of the pseudopotential multiphase lattice Boltzmann model: Methods and applications. *International journal of heat and mass transfer,* 76**,** 210-236.

24. CHEN, L., KANG, Q., VISWANATHAN, H. S. & TAO, W. Q. 2014b. Pore-scale study of dissolution-induced changes in hydrologic properties of rocks with binary minerals. *Water resources research,* 50**,** 9343-9365.

25. CHEN, L., LUAN, H.-B., HE, Y.-L. & TAO, W.-Q. 2012. Pore-scale flow and mass transport in gas diffusion layer of proton exchange membrane fuel cell with interdigitated flow fields. *International Journal of Thermal Sciences,* 51**,** 132-144.

26. CHEN, L., WU, G., HOLBY, E. F., ZELENAY, P., TAO, W.-Q. & KANG, Q. 2015. Lattice Boltzmann pore-scale investigation of coupled physical-electrochemical processes in C/Pt and non-precious metal cathode catalyst layers in proton exchange membrane fuel cells. *Electrochimica Acta,* 158**,** 175-186.

27. CHOU, L., GARRELS, R. M. & WOLLAST, R. J. C. G. 1989. Comparative study of the kinetics and mechanisms of dissolution of carbonate minerals. 78**,** 269-282.

28. CROSSLAND, I. G. J. C. C. R. 2007. Cracking of the Nirex Reference Vault Backfill: a review of its likely occurrence and significance. 250**,** 1.

29. CUI, L. & FALL, M. 2015. A coupled thermo–hydro-mechanical–chemical model for underground cemented tailings backfill. *Tunnelling and Underground Space Technology,* 50**,** 396-414.

30. DACCORD, G., TOUBOUL, E. & LENORMAND, R. 1989. Carbonate acidizing: toward a quantitative model of the wormholing phenomenon. *SPE production engineering,* 4**,** 63-68.

31. DAUZERES, A., LE BESCOP, P., SARDINI, P. & COUMES, C. C. D. 2010. Physico-chemical investigation of clayey/cement-based materials interaction in the context of geological waste disposal: Experimental approach and results. *Cement and Concrete Research,* 40**,** 1327-1340.

32. DE CAPITANI, C. & BROWN, T. H. 1987. The computation of chemical equilibrium in complex systems containing non-ideal solutions. *Geochimica et Cosmochimica Acta,* 51**,** 2639-2652.

33. DE WINDT, L., BADREDDINE, R. & LAGNEAU, V. 2007. Long-term reactive transport modelling of stabilized/solidified waste: from dynamic leaching tests to disposal scenarios. *Journal of hazardous materials,* 139**,** 529-536.

34. DE WINDT, L., PELLEGRINI, D. & VAN DER LEE, J. 2004. Reactive transport modelling of a spent fuel repository in a stiff clay formation considering excavation damaged zones. *Radiochimica Acta,* 92**,** 841-848.

35. DE WINDT, L., SCHNEIDER, H., FERRY, C., CATALETTE, H., LAGNEAU, V., POINSSOT, C., POULESQUEN, A. & JEGOU, C. 2006. Modeling radionuclide sourceterms and release in a spent nuclear fuel disposal. *Radiochimica Acta,* 94**,** 787-794.

36. DENTON, D. K., LARSON, M. K., RAINS, R., SEYMOUR, J., TESARIK, D. R. & WILLIAMS, T. Geomechanics of reinforced cemented backfill in an underhand stope at the Lucky Friday Mine, Mullan, Idaho.

37. DETWILER, R. L., GLASS, R. J. & BOURCIER, W. L. 2003. Experimental observations of fracture dissolution: The role of Peclet number on evolving aperture variability. *Geophysical Research Letters,* 30.

38. DEWANCKELE, J., DE KOCK, T., BOONE, M., CNUDDE, V., BRABANT, L., BOONE, M., FRONTEAU, G., VAN HOOREBEKE, L. & JACOBS, P. 2012. 4D imaging and quantification of pore structure modifications inside natural building stones by means of high resolution X-ray CT. *Science of the total environment,* 416**,** 436-448.

39. DOBSON, P. F., KNEAFSEY, T. J., SONNENTHAL, E. L., SPYCHER, N. & APPS, J. A. 2003. Experimental and numerical simulation of dissolution and precipitation: implications for fracture sealing at Yucca Mountain, Nevada. *Journal of Contaminant Hydrology,* 62**,** 459-476.

40. EMMANUEL, S., AGUE, J. J. & WALDERHAUG, O. 2010. Interfacial energy effects and the evolution of pore size distributions during quartz precipitation in sandstone. *Geochimica et Cosmochimica Acta,* 74**,** 3539-3552.

41. ERIKSSON, G. & HACK, K. 1990. ChemSage—a computer program for the calculation of complex chemical equilibria. *Metallurgical transactions B,* 21**,** 1013-1023.

42. FALL, M. & NASIR, O. Numerical modeling of the coupled thermo-chemo-mechanical response of cemented paste backfill structures in deep mine temperature conditions. Proceedings of the 3rd CANUS Rock Mechanics Symposium, Toronto, CD room, 2009. Citeseer.

43. FRANCIS, A., CATHER, R. & CROSSLAND, I. J. N. S. R. S., UNITED KINGDON NIREX LIMITED, 57P 1997. Development of the Nirex Reference Vault Backfill; report on current status in 1994.

44. FREDD, C. Dynamic model of wormhole formation demonstrates conditions for effective skin reduction during carbonate matrix acidizing. SPE Permian Basin Oil and Gas Recovery Conference, 2000. Society of Petroleum Engineers.

45. GARCÍA-GUTIÉRREZ, M., MISSANA, T., MINGARRO, M., MOREJÓN, J. & CORMENZANA, J. L. 2018. Cesium diffusion in mortars from different cements used in radioactive waste repositories. *Applied Geochemistry,* 98**,** 10-16.

45

46. GAVRILESCU, M., PAVEL, L. V. & CRETESCU, I. 2009. Characterization and remediation of soils contaminated with uranium. *J. Hazard. Mater.,* 163**,** 475–510.

47. GHERARDI, F., XU, T. & PRUESS, K. 2007. Numerical modeling of self-limiting and self-enhancing caprock alteration induced by CO2 storage in a depleted gas reservoir. *Chemical Geology,* 244**,** 103-129.

48. GHIRIAN, A. & FALL, M. 2013. Coupled thermo-hydro-mechanical–chemical behaviour of cemented paste backfill in column experiments. Part I: physical, hydraulic and thermal processes and characteristics. *Engineering Geology,* 164**,** 195-207.

49. GHIRIAN, A. & FALL, M. 2014. Coupled thermo-hydro-mechanical–chemical behaviour of cemented paste backfill in column experiments: Part II: Mechanical, chemical and microstructural processes and characteristics. *Engineering Geology,* 170**,** 11-23.

50. GOLFIER, F., ZARCONE, C., BAZIN, B., LENORMAND, R., LASSEUX, D. & QUINTARD, M. 2002. On the ability of a Darcy-scale model to capture wormhole formation during the dissolution of a porous medium. *Journal of fluid Mechanics,* 457**,** 213.

51. HOEFNER, M. & FOGLER, H. S. 1988. Pore evolution and channel formation during flow and reaction in porous media. *AIChE Journal,* 34**,** 45-54.

52. HUBER, C., SHAFEI, B. & PARMIGIANI, A. 2014. A new pore-scale model for linear and non-linear heterogeneous dissolution and precipitation. *Geochimica et Cosmochimica Acta,* 124**,** 109-130.

53. JACQUEMET, N., PIRONON, J., LAGNEAU, V. & SAINT-MARC, J. 2012. Armouring of well cement in H2S–CO2 saturated brine by calcite coating–Experiments and numerical modelling. *Applied geochemistry,* 27**,** 782-795.

54. KANG, Q., CHEN, L., VALOCCHI, A. J. & VISWANATHAN, H. S. 2014. Pore-scale study of dissolution-induced changes in permeability and porosity of porous media. *Journal of Hydrology,* 517**,** 1049-1055.

55. KANG, Q., ZHANG, D., CHEN, S. & HE, X. 2002. Lattice Boltzmann simulation of chemical dissolution in porous media. *Physical Review E,* 65**,** 036318.

56. KARPOV, I., CHUDNENKO, K., BYCHINSKII, V., KULIK, D. & AVCHENKO, O. 2001. Minimization of Gibbs free energy in geochemical systems by convex programming.

57. KARPOV, I. K., CHUDNENKO, K. V. & KULIK, D. A. 1997. Modeling chemical mass transfer in geochemical processes; thermodynamic relations, conditions of equilibria and numerical algorithms. *American Journal of Science,* 297**,** 767-806.

58. KARPOV, I. K., CHUDNENKO, K. V., KULIK, D. A. & BYCHINSKII, V. A. 2002. The convex programming minimization of five thermodynamic potentials other than Gibbs energy in geochemical modeling. *American Journal of Science,* 302**,** 281-311.

59. KNACKSTEDT, M. & ZHANG, X. 1994. Direct evaluation of length scales and structural parameters associated with flow in porous media. *Physical Review E,* 50**,** 2134.

60. KOLDITZ, O., BAUER, S., BILKE, L., BÖTTCHER, N., DELFS, J.-O., FISCHER, T., GÖRKE, U. J., KALBACHER, T., KOSAKOWSKI, G. & MCDERMOTT, C. 2012. OpenGeoSys: an open-source initiative for numerical simulation of thermo-hydro-mechanical/chemical (THM/C) processes in porous media. *Environmental Earth Sciences,* 67**,** 589-599.

61. KOSAKOWSKI, G., BLUM, P., KULIK, D., PFINGSTEN, W., SHAO, H. & SINGH, A. 2009. Evolution of a generic clay/cement interface: first reactive transport calculations utilizing a Gibbs energy minimization based approach for geochemical calculations. *Journal of Environmental Science for Sustainable Society,* 3**,** 41-49.

62. KOŤÁTKOVÁ, J., ZATLOUKAL, J., REITERMAN, P. & KOLÁŘ, K. J. J. O. E. R. 2017. Concrete and cement composites used for radioactive waste deposition. 178**,** 147-155.

63. KULIK, D. A., WAGNER, T., DMYTRIEVA, S. V., KOSAKOWSKI, G., HINGERL, F. F., CHUDNENKO, K. V. & BERNER, U. R. 2013. GEM-Selektor geochemical modeling package: revised algorithm and GEMS3K numerical kernel for coupled simulation codes. *Computational Geosciences,* 17**,** 1-24.

64. KUMAR, A., ROUT, S., GHOSH, M., SINGHAL, R. K. & RAVI, P. M. 2013. Thermodynamic parameters of U (VI) sorption onto soils in aquatic systems. *SpringerPlus,* 2**,** 530.

65. LASAGA, A. C. & RYE, D. M. 1993. Fluid flow and chemical reaction kinetics in metamorphic systems. *American Journal of Science,* 293**,** 361-404.

66. LE GALLO, Y., BILDSTEIN, O. & BROSSE, E. 1998. Coupled reaction-flow modeling of diagenetic changes in reservoir permeability, porosity and mineral compositions. *Journal of Hydrology,* 209**,** 366-388.

67. LI, Q., STEEFEL, C. I. & JUN, Y.-S. 2017. Incorporating nanoscale effects into a continuum-scale reactive transport model for CO2-deteriorated cement. *Environmental science & technology,* 51**,** 10861-10871.

68. LIU, Y., LIU, C., ZHANG, C., YANG, X. & ZACHARA, J. M. 2015. Pore and continuum scale study of the effect of subgrid transport heterogeneity on redox reaction rates. *Geochimica et Cosmochimica Acta,* 163**,** 140-155.

69. LUHMANN, A. J., KONG, X.-Z., TUTOLO, B. M., GARAPATI, N., BAGLEY, B. C., SAAR, M. O. & SEYFRIED JR, W. E. 2014. Experimental dissolution of dolomite by CO2-charged brine at 100 C and 150 bar: Evolution of porosity, permeability, and reactive surface area. *Chemical Geology,* 380**,** 145-160.

70. MACQUARRIE, K. T. & MAYER, K. U. 2005. Reactive transport modeling in fractured rock: A state-of-the-science review. *Earth-Science Reviews,* 72**,** 189-227.

71. MAO, X., PROMMER, H., BARRY, D., LANGEVIN, C. D., PANTELEIT, B. & LI, L. 2006. Three-dimensional model for multi-component reactive transport with variable density groundwater flow. *Environmental Modelling & Software,* 21**,** 615-628.

72. MARTY, N. C., TOURNASSAT, C., BURNOL, A., GIFFAUT, E. & GAUCHER, E. C. 2009. Influence of reaction kinetics and mesh refinement on the numerical modelling of concrete/clay interactions. *Journal of Hydrology,* 364**,** 58-72.

73. METZ, V., KIENZLER, B. & SCHÜßLER, W. 2003. Geochemical evaluation of different groundwater–host rock systems for radioactive waste disposal. *Journal of contaminant hydrology,* 61**,** 265-279.

74. MIN, T., GAO, Y., CHEN, L., KANG, Q. & TAO, W.-W. 2016. Changes in porosity, permeability and surface area during rock dissolution: effects of mineralogical heterogeneity. *International Journal of Heat and Mass Transfer,* 103**,** 900-913.

75. MOLINS, S., CARRERA, J., AYORA, C. & SAALTINK, M. W. 2004. A formulation for decoupling components in reactive transport problems. *Water Resources Research,* 40.

76. MOLINS, S., TREBOTICH, D., STEEFEL, C. I. & SHEN, C. 2012. An investigation of the effect of pore scale flow on average geochemical reaction rates using direct numerical simulation. *Water Resources Research,* 48.

77. MOREIRA, E. & COURY, J. 2004. The influence of structural parameters on the permeability of ceramic foams. *Brazilian Journal of Chemical Engineering,* 21**,** 23-33.

78. MORENO, L., CRAWFORD, J. & NERETNIEKS, I. 2006. Modelling radionuclide transport for time varying flow in a channel network. *J. Contam. Hydrol.,* 86**,** 215–38.

79. MORSE, J. W. & ARVIDSON, R. S. J. E.-S. R. 2002. The dissolution kinetics of major sedimentary carbonate minerals. 58**,** 51-84.

80. MORSE, J. W. & BERNER, R. A. J. A. J. O. S. 1972. Dissolution kinetics of calcium carbonate in sea water; I, A kinetic origin for the lysocline. 272**,** 840-851.

81. MOYCE, E. B. A. 2014. *Rock alteration at high pH relevant to the geological disposal of radioactive waste.* University of Leeds.

82. MU, Y.-T., CHEN, L., HE, Y.-L. & TAO, W.-Q. 2016. Pore-scale modelling of dynamic interaction between SVOCs and airborne particles with lattice Boltzmann method. *Building and Environment,* 104**,** 152-161.

83. OVAYSI, S. & PIRI, M. 2014. Pore-space alteration induced by brine acidification in subsurface geologic formations. *Water Resources Research,* 50**,** 440-452.

84. PARKHURST, D. L. & APPELO, C. 1999. User's guide to PHREEQC (Version 2): A computer program for speciation, batch-reaction, one-dimensional transport, and inverse geochemical calculations.

85. PARKHURST, D. L. & APPELO, C. 2013. Description of input and examples for PHREEQC version 3: a computer program for speciation, batch-reaction, one-dimensional transport, and inverse geochemical calculations. US Geological Survey.

86. PARKHURST, D. L., KIPP, K. L. & CHARLTON, S. R. 2010. PHAST Version 2—A program for simulating groundwater flow, solute transport, and multicomponent geochemical reactions. *US Geological Survey Techniques and Methods,* 6**,** A35.

87. PARKHURST, D. L. & WISSMEIER, L. 2015. PhreeqcRM: A reaction module for transport simulators based on the geochemical model PHREEQC. *Advances in Water Resources,* 83**,** 176-189.

88. PARMAKSIZ, A., AGUS, Y., BULGURLU, F., BULUR, E., ONCU, T. & OZKOK, Y. O. 2015. Measurement of enhanced radium isotopes in oil production wastes in Turkey. *Journal of Environmental Radioactivity,* 141**,** 82-89.

89. PFINGSTEN, W. 2002. Experimental and modeling indications for self-sealing of a cementitious low-and intermediate-level waste repository by calcite precipitation. *Nuclear Technology,* 140**,** 63-82.

90. PIERCE, M. E. 1999. *Laboratory and numerical analysis of the strength and deformation behaviour of paste backfill*, Queen's University at Kingston.

91. PLUMMER, L., WIGLEY, T. & PARKHURST, D. J. A. J. O. S. 1978. The kinetics of calcite dissolution in CO 2-water systems at 5 degrees to 60 degrees C and 0.0 to 1.0 atm CO 2. 278**,** 179-216.

92. PROMMER, H., DAVIS, G. & BARRY, D. PHT3D-A three-dimensional biogeochemical transport model for modelling natural and enhanced remediation. PHT3D-A three-dimensional

biogeochemical transport model for modelling natural and enhanced remediation, 1999. Centre for Groundwater Studies, CSIRO, Wembley, 351-358.

93. PULKKANEN, V.-M. Radionuclide Transport through Different Routes near a Deposition Hole for Spent Nuclear Fuel. COMSOL Conference. Milan, Italy, 2009. 2009.

94. ROH, Y., LEE, S. R., CHOI, S. K., ELLESS, M. P. & LEE, S. Y. 2000. Physicochemical and mineralogical characterization of uranium-contaminated soils. *J. Soil Contam.,* 9**,** 463–486.

95. ROOD, A. S. & KENDRICK, D. 1996. Measurement of 222 Rn flux, 222 Rn emanation and 226 Ra concentration from injection well pipe scale. Lockheed Idaho Technologies Co.

96. RUBIN, J. 1983. Transport of reacting solutes in porous media: Relation between mathematical nature of problem formulation and chemical nature of reactions. *Water resources research,* 19**,** 1231-1252.

97. RYAN, E. M., TARTAKOVSKY, A. M. & AMON, C. 2011. Pore-scale modeling of competitive adsorption in porous media. *Journal of contaminant hydrology,* 120**,** 56-78.

98. SANCHEZ-VILA, X., DONADO, L. D., GUADAGNINI, A. & CARRERA, J. 2010. A solution for multicomponent reactive transport under equilibrium and kinetic reactions. *Water Resources Research,* 46.

99. SARIPALLI, K. P., MEYER, P. D., BACON, D. H. & FREEDMAN, V. L. 2001. Changes in hydrologic properties of aquifer media due to chemical reactions: A review. *Critical reviews in environmental science and technology,* 31**,** 311-349.

100. SEIGNEUR, N., L'HÔPITAL, E., DAUZÈRES, A., SAMMALJÄRVI, J., VOUTILAINEN, M., LABEAU, P., DUBUS, A. & DETILLEUX, V. 2017. Transport properties evolution of cement model system under degradation-Incorporation of a pore-scale approach into reactive transport modelling. *Physics and Chemistry of the Earth, Parts A/B/C,* 99**,** 95-109.

101. SHAWKY, S., AMER, H., NADA, A. A., ABD EL-MAKSOUD, T. M. & IBRAHIEM, N. M. 2001. Characteristics of NORM in the oil industry from Eastern and Western deserts of Egypt. *Applied Radiation and Isotopes,* 55**,** 135-139.

102. SIVAKUGAN, N., RANKINE, R., RANKINE, K. & RANKINE, K. 2006. Geotechnical considerations in mine backfilling in Australia. *Journal of Cleaner Production,* 14**,** 1168-1175.

103. SOLER, J. M. & MÄDER, U. K. 2005. Interaction between hyperalkaline fluids and rocks hosting repositories for radioactive waste: reactive transport simulations. *Nuclear science and engineering,* 151**,** 128-133.

104.	STEEFEL, C. I., DEPAOLO, D. J. & LICHTNER, P. C. 2005. Reactive transport modeling: An essential tool and a new research approach for the Earth sciences. *Earth and Planetary Science Letters,* 240**,** 539-558.

105.	STEEFEL, C. I. & LASAGA, A. C. 1990. Evolution of dissolution patterns: Permeability change due to coupled flow and reaction.

106.	STEEFEL, C. I. & LASAGA, A. C. 1994. A coupled model for transport of multiple chemical species and kinetic precipitation/dissolution reactions with application to reactive flow in single phase hydrothermal systems. *American Journal of science,* 294**,** 529-592.

107.	TARTAKOVSKY, A. M., MEAKIN, P., SCHEIBE, T. D. & WOOD, B. D. 2007. A smoothed particle hydrodynamics model for reactive transport and mineral precipitation in porous and fractured porous media. *Water resources research,* 43.

108.	TOKUNAGA, T. K., WAN, J., PENA, J., SUTTON, S. R. & NEWVILLE, M. 2004. Hexavalent uranium diffusion into soils from concentrated acidic and alkaline solutions. *Environ. Sci. Technol.,* 38**,** 3056–3062.

109.	TRUESDELL, A. H. & JONES, B. F. 1974. WATEQ, a computer program for calculating chemical equilibria of natural waters. *J. Res. US Geol. Surv,* 2**,** 233-248.

110.	UCHIDA, T. 1987. Pore-size distributions and the evaluation of permeability in reservoir rocks–a proposal of empirical expressions with regard to petrological properties of pores. *J. Jpn. Assoc. Petrol. Technol,* 52**,** 1-11.

111.	VAN CAPPELLEN, P., CHARLET, L., STUMM, W. & WERSIN, P. J. G. E. C. A. 1993. A surface complexation model of the carbonate mineral-aqueous solution interface. 57**,** 3505-3518.

112.	VAN DER LEE, J. 1998. Thermodynamic and mathematical concepts of CHESS.

113.	VAN DER LEE, J. & DE WINDT, L. 2001. Present state and future directions of modeling of geochemistry in hydrogeological systems. *Journal of contaminant hydrology,* 47**,** 265-282.

114.	VAN DER LEE, J. & DE WINDT, L. 2002. CHESS Tutorial and Cookbook/Version 3.0, users manual LHM. RD/02/13, Ecole des mines de Paris, Fontainebleau.

115.	VASCONCELOS, R. G. W., BEAUDOIN, N., HAMILTON, A., HYATT, N. C., PROVIS, J. L. & CORKHILL, C. L. 2018. Characterisation of a high pH cement backfill for the geological disposal of nuclear waste: The Nirex Reference Vault Backfill. *Applied Geochemistry,* 89**,** 180-189.

116.	VOCHTEN, R., DEGRAVE, E. & LAUWERS, H. 1990. Transformation of synthetic u3o8 into different uranium oxide hydrates. *Mineral. Petrol.,* 41**,** 247–255.

117.	WALSH, S. D., DU FRANE, W. L., MASON, H. E. & CARROLL, S. A. 2013. Permeability of wellbore-cement fractures following degradation by carbonated brine. *Rock Mechanics and Rock Engineering,* 46**,** 455-464.

118.	XU, T., SPYCHER, N., SONNENTHAL, E., ZHANG, G., ZHENG, L. & PRUESS, K. 2011. TOUGHREACT Version 2.0: A simulator for subsurface reactive transport under non-isothermal multiphase flow conditions. *Computers & Geosciences,* 37**,** 763-774.

119.	YILMAZ, E., KESIMAL, A. & ERCIDI, B. Strength development of paste backfill simples at Long term using different binders. Proceedings of 8th symposium MineFill04, China, 2004. 281-285.

Chapter 2: Literature Review (A Review on Reactive Transport Model and Porosity Evolution in the Porous Media of Radioactive Waste Disposal)

Abstract

This work comprehensively reviews the equations governing multicomponent flow and reactive transport in porous media on the pore-scale, mesoscale, and continuum scale. For each of these approaches, the different numerical schemes for solving the coupled advection-diffusion-reactions equations are presented. The parameters influenced by coupled biological and chemical reactions in evolving porous media are emphasised and defined from a pore-scale perspective. Recent pore-scale studies, which have enhanced the basic understanding of processes that affect and control porous media parameters are discussed. Subsequently, a summary of the common methods used to describe the transport process, fluid flow, reactive surface area, and reaction parameters such as porosity, permeability, tortuosity are reviewed. Furthermore, past and recent attempts at using reactive transport models for addressing several challenges in nuclear waste disposal are also presented.

List of Notations

c	Volumetric solute concentration	r_i	Position vector of particle i
$\bar{c}$	Mean concentration	r_m	Rate of precipitation or dissolution of mineral m
c^*	Concentration of the solute at equilibrium	R_{surf}^j	Surface reaction source-sink term for j component
c'	Normalised solute concentration	S	Reactive surface of the mineral exposed to the fluid reactants
C^l	Mass fraction	S_0	Initial reactive surface area
$D, \mathcal{D}$	Solute molecular diffusion	Δt	Discrete-time step
D^*	Dispersion tensor	v	Fluid velocity vector
D_l^0	Diffusion coefficient of pure water	V	Representative volume element
D_l^{min}	Matrix effective diffusion coefficient	V_s	Solution volume
Da	Damkohler number	V_i	Interface velocity
Da_{ls}	Damkohler number for precipitation or dissolution process	w_i	Weights for the distribution function along the ith direction
D_{eff}	Effective diffusivity tensor	W	SPH smoothing kernel
e_i	The ith direction dependent on the lattice type	$W_{x,r_0}(y_b)$	Weighting function
f_i	Probability distribution function	x	Position vector of the interface
f_i^{eq}	Equilibrium distribution function.	Δx	Distance between two lattice nodes
h	Small increment in distance	y_b	Position vector of particle b
J^j	Flux of j component	ε	Length-scale parameter
k_r	Reaction rate constant	ρ_F	Fluid density
k	Permeability tensor	ρ_s	Solid density
k_0	Initial permeability	ρ_l	Liquid density
K	Dimensionless quantity	κ	Local reaction rate constant
K_c	Stoichiometric coefficient of the reaction	μ	Fluid dynamic viscosity
K_e	Effective reaction rate	θ, η	Empirical parameters in Eq. (2.13)
k_{eq}	Effective equilibrium constant	$\| \; \|$	Sign showing the magnitude of the corresponding vector
K_{sp}	Solubility product	φ_i	Mineral volume fraction
L_c	Macroscopic length scale	φ_{NR}	Volume fraction of the non-reactive minerals
l_l	Pore-geometry length scale	Ω_j	Saturation ratio
m	Moles of mineral	Ω^{BGK}	Lattice Boltzmann BGK collision operator
m_i	Mass of particle i	$\mho$	Averaging volume
n	Unit normal vector	τ	Lattice Boltzmann relaxation time
n_c	Cementation factor	τ_l	Tortuosity
n_i	Particle density of particle i	Ξ^l	dimensionless surface concentration of species l formed on the surface
$N(x)$	Number of liquid SPH particles contained in the representative volume	$\phi(\mathrm{x},t)$	Contour function
N_c	Number of primary species	ϕ	Total porosity
$N_{m,r}$	Number of reactive minerals	ϕ_e	Effective porosity
N_m	Number of minerals under kinetics conditions	ϕ_{crit}	Critical porosity
N_x	Number of secondary species	ϕ_0	Initial porosity
p, p_0	Fluid pressure	χ	Closure variable
Pe	Peclet number	$\mathcal{K}$	reaction rate constant for a surface reaction
Q	Activity products relating to the concentrations of species	Γ_{sl}^T	Solid-fluid interface
q_n	Flow rate	λ_j	Species j mobility

2.1 Introduction

Reactive transport in porous media appears in many areas in nature and industrial applications, including subsurface nuclear waste repository, acid fracturing of oil and gas reservoirs, geological carbon storage, geothermal energy systems, sea water intrusion, amongst others. To model a reactive transport process, it is worth noting that coupled biogeochemist-mechanical multiphysics including advection, diffusion, dispersion, and deformation can define the process. This has been mentioned by (Tenthorey and Gerald, 2006); these reactions affect the properties of the host porous media. In the same vein, (Le Gallo et al., 1998, Jin et al., 2013, Kaszuba et al., 2005) referenced that, with significant alteration of the reaction processes, the feedback mechanisms that influence flow or diffusion through the media can be triggered. More so, (Hao et al., 2012a, Harrison et al., 2017) observed that the reaction process could induce changes in the solid grains and thus affect the reaction rate; dissolution of minerals in an evolving porous media is a typical example. Also, with a substantial dissolution of the minerals, the porosity of the medium will increase. With such an increase in porosity in the porous medium, there are usually secondary effects, especially alteration of its connectivity (Navarre-Sitchler et al., 2009). The combined alterations can subsequently affect the transport processes by changing the primary transport properties, including permeability, tortuosity, transport mode and pathways.

In the same vein, the system's reactivity can also be impacted because the dissolution of the mineral can reshape the surface of the dissolving phases or cause the smaller particles in the porous media to completely dissolved, as observed by (Noiriel et al., 2009). The dissolution

of these minerals is one of the examples of an evolving porous media. During and after its evolution, processes such as precipitation (Gaucher and Blanc, 2006, Chagneau et al., 2015, Brovelli et al., 2009), pore-size alteration (Emmanuel et al., 2010, Emmanuel et al., 2015), bio clogging (Kim and Fogler, 2000, Thullner et al., 2002, Ezeuko et al., 2011), clay swelling (Wang et al., 2014, Herbert et al., 2008), and variations of surface loading and temperature, which can cause the expansion or contraction of the media (MacQuarrie and Mayer, 2005, Tian et al., 2014, Pfingsten, 2002) and affect the transport properties of porous media. As observed by (Houben, 2003) biogeochemical reactions account for over 90% of ageing wells. In similar studies, (Dauzeres et al., 2010, Dauzères et al., 2019) observed that the formation of the impermeable calcite layer or any other secondary minerals could be triggered through geochemical interactions at the interfaces of the cementitious materials and clay, and the resulting layer can impede the transport of solute across these interfaces. Understanding these processes is very important, especially for long-term storage of nuclear wastes and mine waste deposits (Soler and Mäder, 2005, Atkinson et al., 1987, Yang et al., 2008, Spycher et al., 2003).

As indicated by (Gouze and Coudrain-Ribstein, 2002, Jin et al., 2013, Opolot and Finke, 2015), during the evolution of porous media, the transport and chemical properties vary in space and time. Typical examples of this process include soil formation due to weathering and karst formation. In the works of (Birk et al., 2003, Birk et al., 2005), the rates of flow and weathering were identified to affect the evolution of heterogeneity patterns strongly. The interactions between reactive process and flow engineer the development of the karst, and the dissolution process is further enhanced as the flow rate increases. With increased dissolution, the medium's porosity and permeability will increase, increasing flow rates, and

the cycle continues (Hartmann et al., 2014, Xiao and Jones, 2007). In addition, reactions due to precipitation in natural systems have significant effects on the evolution of these media. With the cementation process reducing the porosity and permeability of the medium while strengthening its mechanical properties, the precipitation reactions can impact the reactivity of the primary minerals and trigger skarn or calcrete formation (Meinert et al., 2003, Wang et al., 1994).

Despite the significant changes to the porous media properties during reactive transport processes, many authors have assumed them to be time-invariant when modelling. However, when considering the impact of changes in water content, this simplifying assumption is exempted (Millington and Quirk, 1961). This simplifying assumption that there is no variation in the reactivity and transport parameters in model development is partly because the description of the temporal development of these parameters as a result of changes in the structure and composition of the porous media is quite difficult. Usually, reactive transport processes are performed using the upscaled parameters on a representative elementary volume (REV) or continuum scale. The relationships between transport and reactivity parameters (e.g., porosity, permeability, and evolving surface area) are established either empirically or based on theoretical aspects and are case specific (Akanni et al., 1987, Hommel et al., 2018, Low, 1981, Tomadakis and Sotirchos, 1993, Petersen, 1958). Though, some recent studies successfully applied the finite element method to descript the multiphysics coupling at the REV scale. For example, (Mou and Chen, 2020) have solved the transport properties and shrinkage volume of the deformed porous media. Meanwhile, (Lesueur et al., 2020) have descript permeability evolution due to fluid injection in deep carbonate reservoirs using a three-scale finite element framework.

Studies on evolving porosity and permeability due to reaction in porous media date back to the 1990s, with (Steefel and Lasaga, 1992), who presented the first numerical paper on the reactive infiltration instability. In a subsequent article, (Steefel and Lasaga, 1994) found that quartz precipitation impacts the diffusing flow paths over an increasingly wider volume, unlike the reactive worm holing effect caused by the matrix dissolution. In another study by (Steefel and Lichtner, 1994), they illustrated the impacts of the reactions in the rock matrix on the fracture volume from the surrounding matrix, leading to armouring of the fracture or isolation. (Steefel and Lichtner, 1998) showed that the balance between the rock cementation and the fracture is delicately balanced, and subsequent evolution of the fracture-rock system hang on it. (Navarre-Sitchler et al., 2011) considered the evolution of the pore connectivity and tortuosity on diffusivity. The evolution of the process reactivity has not been addressed in prior reactive modelling efforts. Still, the case involving the dissolution approaches zero reactive surface area has been addressed in the past. However, in a study by (Noiriel et al., 2012) on reactive flow with calcite, they concluded that considering the formation of high surface area precipitation when capturing the evolution of the system's reactivity is very important.

When developing the model framework for simulating reactive transport in porous media, it is imperative to consider the effect of climatic changes on the system of interest. For instance, when assessing the performance of deep repositories in fully saturated crystalline rock for long-term operations, an understanding of far-field geochemical conditions and the evolution of the repository is necessary. Within the required spatiotemporal scale to demonstrate the repository's safety, the patterns of the groundwater flow, flow rates, and geochemical properties within the far-field surrounding the nuclear waste repository may be

affected by climate change. Based on the properties and characteristics of the site, the change's rate and magnitude can affect the state of the redox reactions at the far-field, the performance of the engineered barrier systems, and radio-nuclide mobility.

Climate change-induced events such as glaciation/deglaciation cycles, permafrost conditions, coastlines movement due to sea-level changes, and isostatic compression and uplift can cause hydrogeologic changes, which can result in two main types of geochemical changes that can affect the performance of a subsurface repository (Puigdomenech et al., 2001). These changes relate to: (a) the pore water redox potential and presence of redox-active species; and (b) salinity and composition of pore water. The simultaneous consideration of hydrogeological and geochemical transport processes requires knowing the transient changes in the groundwater flow field over a long period. To evaluate hydro-chemical conditions in the radioactive waste disposal and geochemical changes associated with mines, multicomponent reactive transport modelling has been demonstrated to be very useful (De Windt et al., 2003, Guimerà et al., 1999, Dobson et al., 2003, Spycher et al., 2003, Xu et al., 2003). (MacQuarrie and Mayer, 2005) used multicomponent reactive transport models to investigate the evolution of redox conditions to address the impact of climatic changes on subsurface storage potential. Conceptual modelling of the influx of oxygen and redox buffering within a space-time shield environment was developed, which can be applicable to a nuclear waste repository. In this model, geochemical and biological processes relevant to understanding the buffering capacity of the redox reactions and the far-field mobility of the radionuclide were adequately described. In Sweden, The Redox experiment conducted at Aspo underground laboratory from 1998 to 2001 (REX experiment) was to

investigate the capacity of the host rock to shield redox conditions against oxidation, determine how oxygen is taken in and provide quantitative descriptions of the processes that could assess the stability of the redox process for the post-closure phase. To conduct the experiment, a closed recirculating system was used and placed at the access tunnel in the borehole at a depth of 380m in the laboratory.

Microbial actions are very important in the control of geochemical conditions in the subsurface systems. The advancement in coupled modelling of hydrodynamic, thermal, microbial, and geochemical processes in the porous media is critical in furthering our understanding of how the physical, biological, and geochemical processes interact and how they affect groundwater-chemistry evolution. To understand these coupled processes, numerical models have increasingly been used. Unfortunately, efforts have not been adequately directed at the inverse coupled models of non-isothermal, hydrodynamic, geochemical, and microbial processes (Yang et al., 2008). The inverse model provides a way to measure the system's state and determine the unknown model parameters by fitting the model to the measure data (Sun, 1994). Microbial parameters such as yield coefficient, half-saturation, specific growth rate, and the decay constants for synthetic and real experiments have been simultaneously determined with geochemical parameters through the inverse model proposed by (Yang et al., 2008). The observations from experiments suggested that the impact of dissolved organic carbon-oxygen composition is more significant than methane oxidation.

Microbial processes should also be considered when designing deep geological radioactive waste repositories (Pedersen, 1999, McKinley et al., 1997, Wang and Papenguth, 2001).

Several experiments have been implemented to study the significance of microbial processes on the safety of nuclear waste repositories (Trotignon et al., 2002, Samper and Yang, 2006, Yang et al., 2008). However, in complex systems in which there are couplings between microbial processes and transport, flow, and geochemical processes, the joint estimation of parameters for flow, transport, geochemical, and microbial parameters may be more complicated to determine than that illustrated with the REX experiment. Unfortunately, the drawback to this approach is that there is the possibility of having an ill-posed problem in the inverse problems of complex systems with strongly correlated parameters. In such situations, a multistage procedure for estimating the flow, transport, and geochemical parameters was recommended by (Dai and Samper, 2004). The procedure advises that the flow parameters should be estimated first, followed by transport parameters from data on conservative species. And both the parameters for geochemical and microbial processes can be determined from the reactive species.

The geochemical reactions and transport processes that control how the porous media evolve occur at the microscale. Moreover, knowing how complex and heterogeneous the pore structure and the multiphysics-nature of the problem is, acquiring a representative progression of the effective properties of the media in a macroscale-based approach is challenging. However, with the recently developed imaging techniques such as X-ray microtomography and improved pore-scale model formulations and higher computing power, the exploration of these processes at the pore-scale is now more possible than before from both experimental and numerical simulation. With these developments, recent studies on reactive transport modelling have focused on describing the processes at the micro-scale.

However, one major downside of the pore-scale approach is the difficulty in simulating reactive transport on larger scales. To handle this limitation, hybrid multiscale approaches have been developed.

This article presents a comprehensive review of past and current efforts to understand the underlying physics of reactive flow in porous media. A brief look into the different modelling scales –pore-scale, mesoscale, continuum, and hybrid multiscale approaches are addressed. More so, an extensive study was conducted on the other solution strategies for solving coupled multiphysics problems associated with reactive transport and porosity evolution in porous media. Finally, several practical applications, both natural occurrences and man-induced processes are presented.

2.2 Reactive Transport in Porous Media

Reactive transport modelling provides both space and time descriptions of the evolution of the species undergoing both transport process and chemical reactions. The flow process through a porous medium can be described through different modelling scales. The flow through the medium occurs through the void-space, which is bounded by the solid skeleton. Changes in the structure of the pore surface or its morphological makeup can happen because of several coupled and interacting processes. While changes in the pore surface properties and its pore's geometry occur on the micro-scale or molecular scale, the scale of engineering application is typically larger. Hence, the impacts of the morphological modification of the flow field are often described by the effective hydraulic properties to overcome the computational demand. Based on the continuum modelling approach, the medium's permeability is often used to measure resistance to flow, while the geometry of the pore is

left unresolved. Using permeability as a parameter intrinsically prevents the necessity of describing the interface of the solid and fluid at the cost of losing the microscopic description. To integrate the changes in the structure and morphology of the pore, the permeability is updated using permeability-porosity relations.

2.2.1 Modelling Scales

The hydraulic properties of porous media are linked to the interface between the solid skeleton and the pore space. Although the behaviour of the matrix-pore system is strongly dependent on the interfaces at the pore-scale, the computational cost at this level is too high when simulating domains with large sizes. Using the representative volume element approach helps to characterise spatial scale dependencies. Depending on the property of interest, the required dimensions of the representative volume element may vary (between millimetre and meter range) throughout the porous medium. In Fig. (2.1), a recursive look at a porous medium with bio clogging is shown. In this figure, each cut-out is a representation of a possible different modelling scale. The choice of the spatial dimension for each scale is arbitrary, and the transiting from one scale to another is done gradually. One benefit of this figure is to show that the details decrease with increasing scale. Although with increasing domain simulation, the computing power required to simulate reactive transport flow is large, and most scientists prefer to adopt the continuum approach, many scientists today are beginning to use the pore-scale approach with the help of supercomputers. Some of these applications are presented in subsequent sections of this paper.
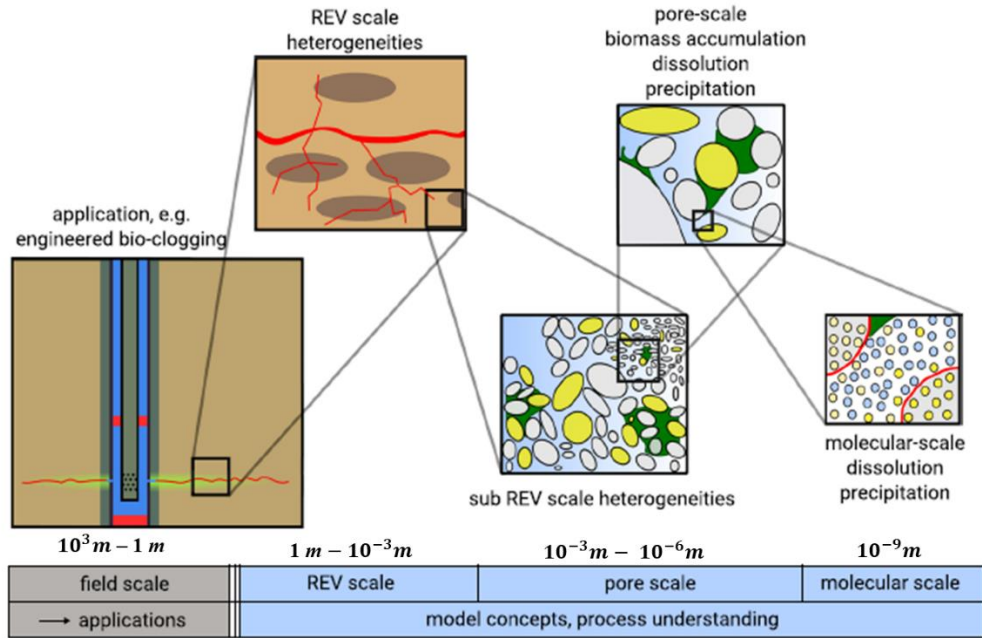
Figure 2.1: Modelling scales for reactive transport in porous media (Hommel et al., 2018). REV (Representative Elementary Volume).

The pore-scale simulation is based on a strong physical foundation. Still, the knowledge of pore geometry is required, which can be challenging to determine, and impractical at scales of higher magnitude than the pore-scale. Although the upscale approaches overcome this limitation, they fail to capture several transport features observed during experiments, including breakthrough curves with long asymmetrical tails (Neuman and Tartakovsky, 2009) and the extent of reactions in mixing-controlled chemical transformations (Knutson et al., 2007, Li et al., 2006). Also, the instability inflows with variable density and the disparity in fractal dimensions of diffusion and dispersion fronts (Måløy et al., 1988). These limitations occur as a result of violations of the closure assumptions on which the continuum approaches are based. Regardless of the upscaling approach such as volume averaging, pore-network models, method of moments, inadequacy in the macroscopic descriptions of pore-

scale processes may occur because of homogenisation through multiple-scale expansions and its variations and thermodynamically constrained averaging (Battiato et al., 2009), the nonlinearities of pore-scale governing equations with the boundary conditions require linearisation and other approximations.

Majority of works on upscaling approaches address deriving models for effective properties that show the relationship of microscopic characteristics of the porous medium with macroscopic properties. Such techniques show any existing connections between the physicochemical processes on different scales, provided the governing assumptions are still valid. However, they cannot be applied in identifying the validity of the governing assumptions and the regions of the computation domain where the continuum model fails. This is essential for hybrid models that apply microscale and macroscale descriptions of the same physics in different regions of a computation domain (Tartakovsky et al., 2008b). On the other hand, continuum approaches that depend on characteristic dimensionless numbers can provide quantitative measures to validate various upscaling approximations. For example, the Peclet number determines how well an advection-dispersion equation adequately represents the pore-scale dispersion; the Damkohler number is useful in predicting the breakdown of macroscopic-based models with concurrent pore-scale diffusion and nonlinear homogeneous and linear heterogeneous reactions (Battiato et al., 2009). Moreover, both Damkholer and Peclet numbers can determine if the advection, diffusion, and linear heterogeneous reactions in a capillary tube are homogenised.

2.2.1.1 Pore-scale Approach

Understanding the processes occurring at the pore-scale is essential for developing predictive models that couple flow, transport, the evolution of the reaction parameters and helps to understand the relationships among these processes and parameters and their influences on the reactive transport at the pore-scale and continuum scale.

Pore-scale simulations have been useful in enhancing the understanding of large-scale natural and man-induced processes. Their significance is due to their capabilities in providing predictions for local transport that is computationally inexpensive and accurate. Simultaneously, they allow for variations of the system's parameters, such as the geometry of the pore space, fluid properties, and boundary conditions, for assessing their impact, which is difficult to achieve in experiments (Meakin and Tartakovsky, 2009). Furthermore, using pore-scale simulations improved continuum transport properties assessments by varying the parameters of the pore space structure. Thus, offering an understanding of the scale of dependence of transport parameters, which macroscale approaches cannot capture. The most common pore-scale modelling methods include lattice Boltzman and smoothed particle hydrodynamics.

With the use of modern and non-invasive imaging techniques, visualising the structure of porous media at pore-scale is now possible. (Werth et al., 2010) provided a review of several of these techniques, including Nuclear Magnetic Resonance Imaging, X-Ray microtomography, and optical imaging methods, for hydrogeology and reactive transport applications. 3D X-ray microtomography, especially, is widely used because of its high

resolution. The use of these imaging methods allows for visualising pore structures at the submicron resolution, enhancing the view into the complexity of the structure of porous media.
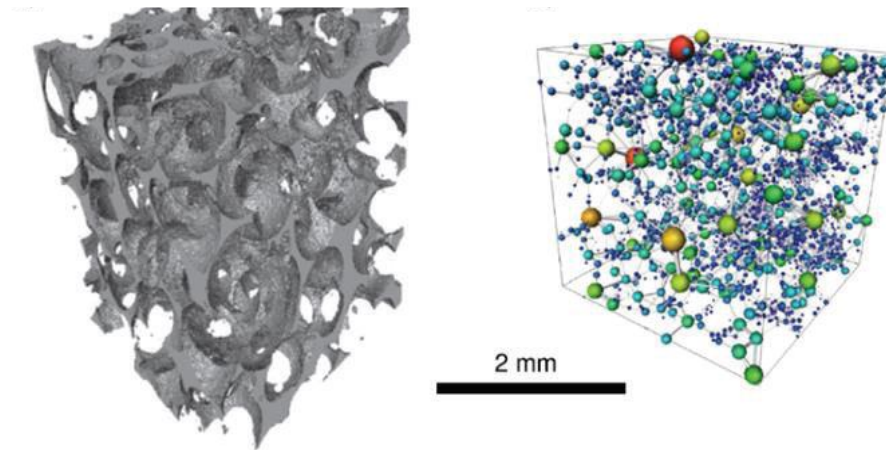
Figure 2.2: (a) Pore-space image of carbonate, and (b) shows the developed pore network model (Blunt et al., 2013).

Fig. (2.2) illustrates a 3D micro-CT (Computed Tomography) image of a limestone pore space, characterised by large, well-connected pores. These images make constructing the pore network models possible by representing the pores as spheres while the throats of the pores as the connecting cylinders to the pores of the medium (Blunt et al., 2013). However, as mentioned by (Navarre-Sitchler et al., 2009), in some cases, a fraction of the pores are isolated such that connectivity to other surrounding pores is blocked, creating dead ends and no contribution to the effective porosity of the system.

- **Solution Strategies for Pore-scale Approaches**

In the pore-scale model, first presented by (Bekri et al., 1995), the porous medium is described by void and solid voxels, named the "voxel method". The local governing equations for the solute concentration are numerically solved through the finite difference method. The evolution of the rock-fluid interfaces is then calculated, and the changes in porosity or permeability are determined. The voxel method is sometimes replaced with a more efficient interface that accurately tracks the algorithms to simulate complex surface motions. The pore-scale model is centred on resolving the Stokes equation and the convection-diffusion equation, accompanied by conditions on the deposition or dissolution flux at the pore walls.

Governing equations:

For a steady-state flow through a porous medium Ω with a fluid phase Ω_F and a solid phase Ω_S separated by an interface Γ, the Stokes equation in the fluid phase is (Varloteaux et al., 2013):

$$\left. \begin{array}{c} \mu\nabla^2 v + \nabla p = 0 \\ \\ \nabla . v = 0 \end{array} \right\} \qquad (2.1)$$

where μ is the fluid dynamic viscosity, assumed to be constant, p is the fluid pressure, and v is the fluid velocity vector. For no-slip conditions at the fluid-solid interface, $v = 0$. The solute flux is

$$J = cv - D\nabla c \qquad (2.2)$$

D is the solute molecular diffusion and c is the volumetric solute concentration.

For no bulk chemical reaction, the local convection-diffusion equation in the fluid phase becomes:

$$\frac{\partial c}{\partial t} + \nabla.(cv - D\nabla c) = 0 \qquad (2.3)$$

And the boundary condition for the solute concentration at the interface is assumed to be a first-order surface reaction, given as

$$n.J = \kappa(c - c^*) \qquad (2.4)$$

where κ is the local reaction rate constant, n is the unit normal vector, and c^* is the concentration of the solute at equilibrium. The normal displacement to the wall, caused by the reaction, which is proportional to the solute flux at the wall.

$$\frac{\partial W}{\partial t} = -K_c\rho_F\kappa(c - c^*) \qquad (2.5)$$

where ρ_F is the fluid density and K_c is the stoichiometric coefficient of the reaction. The velocity of this displacement is taken to be infinitesimal.

A. Level Set Method (LSM)

(Varloteaux et al., 2013) implemented the level set method (LSM) to simulate the complex surface motions, replacing the voxel method in (Bekri et al., 1995). The benefit of the level-set method is its ability to deal with curves and surfaces on a fixed cartesian grid without parametrising the domains. Also, the LSM can track the locus of shapes with changing topology, even when the shapes split into two or more, or developing holes (Sethian and Smereka, 2003). Combining the pore-scale model with LSM yielded accurate result, though demands high computing time and limited pore volumes.

69

In the LSM, the solid-liquid interface is defined by a length function based on the usual cartesian grid system. A triangulated surface represents the interface at the zero level of the length/distance function. The interface is defined as the zero-level of the contour function $\phi(\mathbf{x}, t)$:

$$\Gamma = \{x | \phi(x, t) = 0\} \qquad (2.6)$$

Nevertheless, the level set function satisfies the properties $\phi > 0$ for phase 1 and $\phi < 0$ for phase 2. And the chain derivation rule for $\phi(\mathbf{x}, t)$ is:

$$\frac{\partial \phi}{\partial t} + \nabla \phi . \frac{dx'}{dt} = 0 \qquad (2.7)$$

With unit normal vector pointing outward of the solid phase from the interface. The velocity of the interface is determined according to this relation:

$$V_i = \frac{dx'}{dt} . \frac{\nabla \phi}{\|\nabla \phi\|} \qquad (2.8)$$

where, $\boldsymbol{x}$ is the position vector of the interface and $\| \; \|$ is a sign showing the magnitude of the corresponding vector. The propagation velocity is related to the dimensionless displacement and Peclet number by

$$V_i = \frac{\partial W'}{\partial t'} = \text{Pe Da } c' \qquad (2.9)$$

where $c' = \frac{c - c^*}{\langle c \rangle - c^*}$ is the normalised solute concentration, Pe is the Peclet number, and Da is the Damkohler number; noting that Peclet number is a measure of the ratio of advective transport to mass diffusion rate, and Damkohler number is the characteristic residence to the reaction time of a fluid. Hence, the evolution of the level set function is

$$\frac{\partial \phi}{\partial t} + V_i \|\nabla \phi\| = 0 \qquad (2.10)$$

for a given initial geometry $\phi(\mathrm{x}, t = 0)$.

Fig. (2.3) shows the solution algorithm implemented by (Varloteaux et al., 2013). In the simulation, the coupled Stokes and convection-diffusion equations are solved following the same procedure as (Bekri et al., 1995):

- The velocity field v^n and the concentration field c^n are estimated with the current interface level set function ϕ^n.
- The concentration at the interface is extrapolated from the field c^n to estimate the interface propagation velocity.
- The new interface ϕ^{n+1} is then calculated at time t^{n+1} using the interface velocity and Eq. (2.10).
- The new interface is then updated, and the porous medium is visualised.
- The process is repeated until convergence.
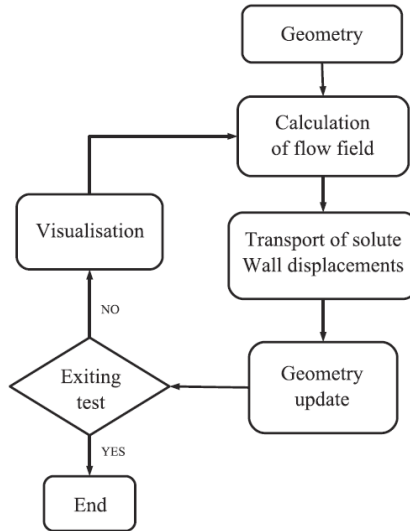
Figure 2.3: Solution scheme of the reactive transport using pore-scale method combined with LSM (Varloteaux et al., 2013).

B. Lattice Boltzmann Method

Many studies have used the Lattice Boltzmann method in the simulation of reactive and non-reactive transport in porous media, including dissolution and precipitation processes such as (Kang et al., 2006, Kang et al., 2007, Kang et al., 2010, He et al., 2000, Verhaeghe et al., 2006, Verhaeghe et al., 2007, Patel et al., 2014). Most of these works, except (Patel et al., 2014), considered heterogeneous reactions at the mineral grain boundary as flux from the boundary, making the separation of reaction and transport computations difficult, and consequently external geochemical codes are coupled. (Patel et al., 2014) approach is more efficient because its computation parallelisation is inherently localised and scalable for applications with high computation cost. The heterogeneous reactions were treated as pseudo homogeneous reactions in their work, and they are incorporated as additional source-sink terms in the fluid nodes close to the solid boundary. This technique makes it possible

for the sequential operation of transport and reaction step that enables the Lattice Boltzmann transport solver to be coupled with the external geochemical algorithm.

Following the model presented by (Patel et al., 2014), the fundamental governing equations were extended to multicomponent transport, neglecting the electro-kinetic effects from charged species. The heterogeneous surface reactions that occur at the solid-fluid interface was expressed in terms of the species' mass balance at the interface:

$$J^j . n|_{\Gamma = \Gamma_s} = R^j_{surf} \qquad (2.11)$$

where R^j_{surf} is the surface reaction source-sink term for j component. $n|_{\Gamma = \Gamma_s}$ is normal unit vector to the boundary. For all aqueous species, a similar coefficient of diffusion was assumed to limiting the number of transport equations to only primary species. The transport equation for each component was then expressed as the stoichiometric sum of the concentrations of each component's primary and secondary species.

In the work of (Gao et al., 2017b), the mineral reactions were described in a general form, and the rate of kinetic reaction on the reactive surface was proposed as

$$R^j_k = k_r S \left(\prod_j C^{nj}_{sj} \right) . \left[1 - \frac{Q}{k_{eq}} \right] \qquad (2.12)$$

where C_s is the concentrations of the fluid (gas or liquid) reactants on the mineral reactive surfaces, k_r is the reaction rate constant (particular to each reaction), S is the reactive surface of the mineral that is exposed to the fluid reactants, Q is the activity products relating to the concentrations of species, and k_{eq} is the effective equilibrium constant.

(Lasaga, 2014) proposed a general form of reaction rates, often used in geochemical simulation, as

$$R_k^j = k_r\, S\,.\left[1 - \Omega_j^\theta\right]^\eta \qquad (2.13)$$

where the empirical parameters, θ and η indicate the dependence of the reaction rate on saturation ratio, Ω_j. For more details on available models for dissolution and reaction rates, the reader is advised to check the works of (Marty et al., 2015), who provided a database of precipitation and dissolution rates of clay minerals, and (Bethke, 1996, De Simoni et al., 2005, Donado et al., 2009, Ajayi and Gupta, 2019) who provided several models for reaction rate constant, k_r.

Lattice Boltzmann method solves a discrete set of Boltzmann equations and recovers the advection-diffusion equation, for an incompressible flow, of the form in Eq. (2.3), but with a sink source. The collision term in the conventional Lattice Boltzmann – Bhatnagar Gross Krook (LB-BGK) approach is simplified by a linear term Ω^{BGK} (Bhathnagor et al., 1954), and neglecting the external force, the equation becomes

$$\left.\begin{aligned} \partial_t f_i + e_i\,.\,\nabla f_i &= \Omega^{BGK}(x,t) \\ \Omega^{BGK}(x,t) &= -\frac{1}{\tau}\left(f_i - f_i^{eq}\right) \end{aligned}\right\} \qquad (2.14)$$

f_i represents the probability distribution function for a given particle along a velocity direction with unit vector e_i in the ith direction dependent on the lattice type. τ is the relaxation time, and f_i^{eq} is the equilibrium distribution function. (He and Luo, 1997) further discretised Eq. (2.14) in space and time, and for passive scalar multicomponent mass transport. The applicable distribution function for each of the primary species is

$$f_i^j(x + e_i\Delta t, t + \Delta t) = f_i^j(x,t)\Omega^{BGK}(x,t)$$

$$\Omega^{BGK}(x,t) = -\frac{\Delta t}{\tau}\left(f_i^j(x,t) - f_i^{eq,j}(x,t)\right)$$

$$(2.15)$$

where Δt is the discrete-time step. The selection of the form of the equilibrium distribution function and the lattice type is dependent on the system of equations being solved. In the advection-diffusion equation being solved by (Patel et al., 2014), an orthogonal lattice D2Q5 (2-dimensional domain with 5 separate velocities) was sufficient to satisfy the isotropy requirement for a 2D geometry Fig. (2.4a). The corresponding discrete velocity vector for this lattice was given as

$$e_i = \begin{cases} o, & i = 0 \\ \left(\cos\frac{(i-1)\pi}{2}, \sin\frac{(i-1)\pi}{2}\right)c, & i = 1,2,3,4 \end{cases} \quad (2.16)$$

where $e = \Delta x/\Delta t$, and Δx is the distance between two lattice nodes. As referenced in Figs. (4b) and (4c), other forms of lattice mesh have been used by other authors. However, the D2Q9 lattice is widely used in the numerical solution of the advection-diffusion equation (Hiorth et al., 2013, Kang et al., 2006, He et al., 2000, Verhaeghe et al., 2006, Verhaeghe et al., 2007). Moreover, for low grid Peclet number (Pe < 10), a D2Q5 lattice can also be used. While, for a higher Peclet number (Pe > 10), the D2Q5 lattice is less accurate than D2Q9; nevertheless, its stability range is higher. Another key advantage of the D2Q5 lattice grid is that it requires less storage memory and computing time than the D2Q9 lattice, which can significantly gain performance for multicomponent transport simulations with large chemical species.
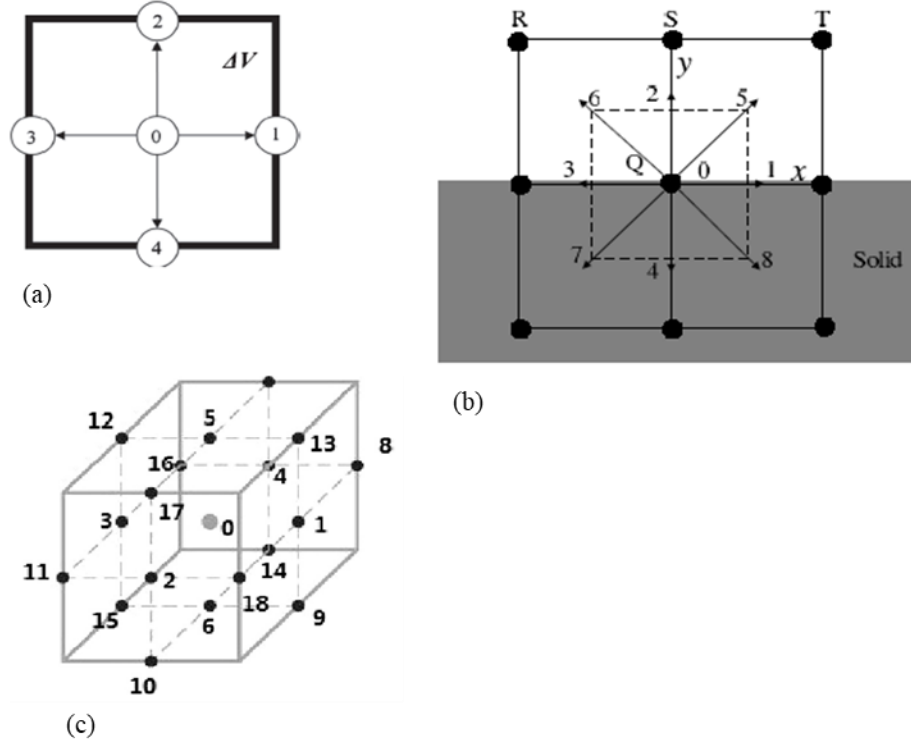
Figure 2.4: Lattice mesh and nodes (a) for a D2Q5 (Patel et al., 2014), (b) of D2Q4 and D2Q9 (Kang et al., 2007), and (c) for D3Q19 (Gao et al., 2017a).

The equilibrium distribution function for first-order approximation to solve advection-diffusion equation is sufficient, given by (Flekkøy, 1993, Patel et al., 2014) as

$$f_i^{eq,j}(x,t) = w_i C^j \left(1 + \frac{e_i \cdot u}{e_s^2}\right) \qquad (2.17)$$

where w_i are the weights for the distribution function along the ith direction and e_s is the lattice pseudo-speed. The reader can check the works of (Patel et al., 2014, d'Humieres and Lallemand, 1987, He and Luo, 1997, Ziegler, 1993, Kang et al., 2006, Kang et al., 2007, Kang et al., 2010, He et al., 2000, Verhaeghe et al., 2006, Verhaeghe et al., 2007, Hiorth et al., 2013) for more details on this implementation.

C. Finite Element Methods

In Discontinuous Galerkin (DG) finite element methods, the approximation of the solutions to differential equations is made through discontinuous piecewise polynomials, such that the boundary conditions are imposed weakly through bilinear forms. As explained by (Sun and Wheeler, 2006a) and demonstrated by other authors (Oden et al., 1998, Arnold, 1982, Rivière et al., 2001, Cockburn et al., 2000, Schötzau and Schwab, 2000, Schötzau et al., 2003, Chen and Chen, 2004, Larson and Niklasson, 2004, Karakashian and Pascal, 2003), the DG methods have gained popularity, despite having larger degrees of freedom than conforming approaches, because they: (1) are conservative element-wise; (2) support unstructured meshes, variable degrees of local approximations, and other nonconforming spaces; (3) easily adaptable, allow for sharp posterior error indicators, and local errors; (4) have insignificant numerical diffusion; (5) are applicable in addressing problems and discontinuities with rough coefficients in numerical simulations; (6) are robust and do not oscillate when there are high gradients; (7) are able to deliver exponential rates of convergence with the suitable meshing scheme; (8) are excellent in parallelisation because of the localised nature of their data communications; (9) provide substantial computational advantage when using explicit time integrations because their mass matrices are block diagonal for time-dependent problems. More so, by simply extending the flux average on the element faces, this method will provide a continuous flux field defined throughout the entire computation domain and efficiently allow coupling with conforming methods.

The simulation of reactive transport in porous media using adaptive DG has been observed to effectively track the moving concentration fronts (Sun and Wheeler, 2006a, Sun and Wheeler, 2006b, Sun, 2003). Four primal DG methods have been implemented: Oden

Babuska Baumann- DG (OBB-DG) approach by (Oden et al., 1998), Symmetric Interior

Penalty Galerkin formulation (SIPG) by (Wheeler, 1978), Non-symmetric Interior Penalty

Galerkin method (NIPG) by (Rivière et al., 2001, Riviere, 2000), and Incomplete Interior

Penalty Galerkin (IIPG) (Sun, 2003, Dawson et al., 2004). The general formulation of the

governing equation, with a source term, is presented below for completeness; the reader is

advised to see the referenced works for more details about these schemes.

$$\left(\frac{\partial \phi c}{\partial t}, N\right)_E - \int_E (vc - D(v)\nabla c) \cdot \nabla N + \int_{\partial E} (vc - D(v)\nabla c) \cdot n_{\partial E} N$$
$$= \int_E qc^* N + r(c) N \qquad (2.18)$$

where ϕ is porosity, v Darcy velocity, $n_{\partial E}$ is the unit normal vector on element E, N is the

weighting function, $r(c)$ is the reaction term, and qc^* is the source term.

Fig. (2.5) shows an unstructured FEM mesh for pore scale modelling of fluid flow in a

porous medium (Akanji and Matthai, 2010).
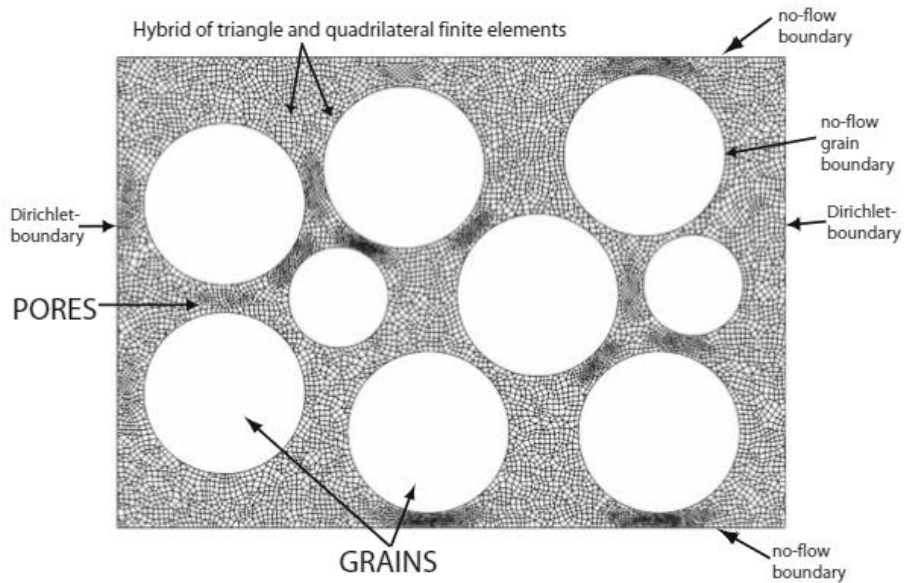
Figure 2.5: An unstructured FEM with adaptive refinement mesh having triangular and quadrilateral elements for 2D pore scale modelling of flow in porous media (Akanji and Matthai, 2010).

D. Smoothed Particle Hydrodynamics (SPH)

This is one of the Lagrangian methods, which is a meshless discretisation of partial differential equations. In this approach, the discretisation of the computational domain with a set of points and the corresponding discretisation scheme is used for discretising the scalar or vector fields as functions of their values at these discrete points. The meshless discretisation scheme permits the discretisation points to be moved with the fluid velocity, even for non-uniform flow. A recent study (Tartakovsky et al., 2016) discretised the Navier-Stokes (NS) and advection-diffusion equations for flow and reactive transport problems using the SPH discretisation scheme. In the Lagrangian coordinate system, the solution to the momentum conservation equation is simplified if the nonlinear inertia term is absent. Given a velocity field, discretising the advective term in the advection-diffusion equation will not cause numerical dispersion. Each discretised point with associated mass and density is assumed as the centre of the fluid particle. This discretisation scheme helps to reduce the Navier-Stokes equations to a system of ordinary differential equations for Newtonian particle dynamics. The sum of the forces between a particle and its neighbours is computed to determine the total force acting on each SPH particle. Hence, fluid-solid interactions can be easily achieved by adding a pair of molecular-like interaction forces to the force terms obtained after the SPH discretisation of the NS equations. For readers interested in using the SPH approach for modelling coupled flow and reactive transport problems, the work of (Tartakovsky et al., 2016) is worth reading.

The SPH discretisation of the advective-diffusion-reaction equation of M species, subject to an appropriate initial condition and the Robin boundary condition $D^l \mathbf{n} . \nabla c^l = g^l(c^1, \dots, c^M, \Xi^1, \dots, \Xi^L)$, presented by the authors are:

$$\frac{Dm_i c_i^l}{Dt} = \sum_{k\in\Omega_p} \frac{D^I(m_i n_i + m_k n_k)(c_i^l - c_k^l)}{n_i n_k (r_i - r_k)^2}(r_i - r_k) . \nabla W(r_{ik}, h)$$

$$- m_i \sum_{k\in\Omega_s} g^l \frac{2(n_i + n_k)}{n_i + n_k} . \nabla W(r_{ik}, h) \quad (2.19)$$

where r^l and g^l are the homogeneous and heterogeneous reaction rates of species l, respectively. m_i and n_i are mass and particle density of particle i, respectively. m_k and n_k are mass and particle density of particle k, respectively. W is the SPH smoothing kernel, and Ξ^l is the dimensionless surface concentration of species l formed on the surface. r_i is position vector of particle i, and r_k is the position vector of the particle k. h is a small increment in distance. $\sum_{k\in\Omega_p}$ and $\sum_{k\in\Omega_s}$ are summations over all the fluid and solid particles, respectively. The interface evolves through the precipitation/accumulation of the surface species with the normal velocity. The precipitation and dissolution of the reaction product can be determined by tracking the masses of the solid, changing according to this equation:

$$\frac{dm_i}{dt} = -m_i(C^{A,0} + C^{B,0}) \sum_{k\in\Omega_s} g^l \frac{2(n_i + n_k)}{n_i + n_k} . \nabla_i W(r_i - r_k, h) \quad (2.20)$$

For a reaction $A + B \rightarrow C_s$, resulting in the formation of a solid phase C. C^l is the mass fraction and $C^{l,0}$ is the initial mass fraction, for species $l = A, B$. To determine the new solid particle position during precipitation, the closest fluid particle to the solid particle is replaced with a solid particle. And for dissolution, the solid particles with mass less than or equal to zero is replaced with fluid particles. Finally, the velocity of the newly formed fluid particle is determined using the SPH interpolation scheme $v_i = \sum_{k\in f+s} \frac{v_k}{n_k} W(r_{ik}, h)$, and the

concentrations are set to $C_k^A = C_k^B = \sqrt{K_{sp}}$, where K_{sp} is the solubility product. (Tartakovsky et al., 2007a, Tartakovsky et al., 2007b, Tartakovsky et al., 2008a) used a similar formulation to model the precipitation of calcium carbonate for the reaction between calcium chloride and sodium carbonate.

In modelling complex transport processes, the use of the SPH method has some advantages. One of them is the triviality of treating interfacial problems compared with grid-based methods. This means that different fluid phases can be represented using different particle types. Also, within this context, the equations for the advection, diffusion, and reactions in the Lagrangian framework are reduced to diffusion and reaction equations, as the SPH fluid particles will advect the solute. Consequently, numerical diffusion is eliminated because of the discretisation of the advection term.

One of the limitations of the SPH method is its high computation cost compared to the grid-based methods. In discretising the spatial derivatives, more bordering particles participate in the computation than the grid-based methods. Another limitation is that SPH schemes may not be able to use higher-order discretisation schemes like the grid-based methods. Hence, the grid-based methods have higher accuracy and computational efficiency than SPH schemes for simple linear problems. However, for multiphase/multicomponent reactive transport problems, the SPH method may provide a superior advantage over the grid-based methods (finite element and finite volume). The use of adaptive resolution and consistent discretisation of the spatial derivatives can further enhance the accuracy of the SPH method.

2.2.1.2 Meso-Scale Approaches

The standard macroscopic equations are not yet needed at the mesoscale because the fluid flow and solute transport processes are simulated at the pore scale, and the exact dynamics of the particle dynamics are not considered. To do this, first, a dummy representation of the porous medium is constructed, which consists of the pore bodies and throats of differing but connected geometries. Then, the possibility of simulating fluid flow and/or reactive transport of interest at the mesoscale through the network, with the implementation of the pertinent physics pore-to-pore.

Pore Network Modelling (PNM)

The first network model was constructed by (Fatt, 1956), who used the analogue between flow in porous media and a random resistor network. Since his presentation, the modelling approach has been improved upon the work of other researchers, including (Balhoff and Wheeler, 2009, Lopez et al., 2003, Blunt et al., 2002, Ryazanov et al., 2009, Yiotis et al., 2006). It captures irregular lattices, arbitrary wettability, wetting layer-flow, and reactive transport.

PNM provides the description of the flow and transport on the mesoscale because of the need to upscale from small-imaged size to larger domains. In this approach, the void space is approximated by a bonds network and nodes with an idealised geometry. In this simplified representation, the pore bodies are spherical, while the pore throats are represented as circular, square, or triangular channels. The difference between the nodes and pore throats and their corresponding simplified geometries eases the complexity and allows analytical or semi-analytical solution methods.

The representation of the actual pore space using both topological and geometrical characteristics strongly influences the simulation accuracy for each application. Generally, the different experimental methods for characterising the pore space can limit constructing the representative pore network. However, previous attempts demonstrated the importance of having a good representation of the geometrical properties of the porous media, including the locations of the pores and throats and the size and shape distributions of the pores and throats (Knackstedt et al., 1998, Bryant and Blunt, 1992, Oren, 1994).

The computation of how the geometry evolves from the reaction is done through an iterative process based on porosity changes (Fig. 2.6). The flow field is first determined in step 1 for arbitrary differential pressure for a given initial pore network. Then, with the known mean interstitial velocity, the porosity and permeability of the pore network are determined. In step 2, the velocity field is adjusted through a linear correction applied to the differential pressure to the imposed Peclet number, Pe. The pore-scale transport coefficients are then determined for each pore body and throat. In step 4, the mass balance equation is solved over the whole network to specify each pore body's mean transverse profile parameter; see (Varloteaux et al., 2013) for more details. Finally, in step 5, how the geometry evolves is considered. For consistency with the PNM assumptions, the evolution of the wall is averaged over each pore network's element to retain the original shape of each element. Subsequently, the wall evolution is modified to have a porosity evolution that is controlled and small. Finally, the pore network is updated in an iterative process from steps 1 to 5 until convergence is reached as the geometry of the network becomes compatible with PNM.
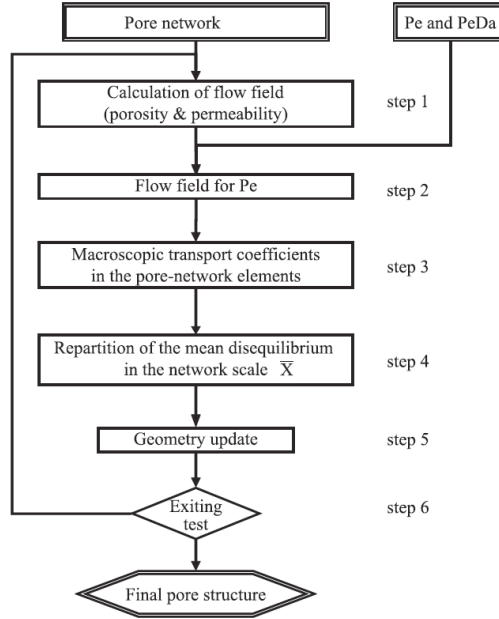
Figure 2.6: The general scheme of the reactive transport resolution using PNM (Varloteaux et al., 2013).

Constructing a PNM, representing a porous medium, is generally done in three ways: statistical reconstruction, grain-based method, and direct mapping model. In the statistical reconstruction technique, the construction of the 3D images can be achieved with information extracted from 2D pore space images. Then the 3D images of the actual pore space can be reconstructed with the knowledge of the pore's geometrical properties using the truncated Gaussian random field method (Adler and Thovert, 1998). The structure of the pore network can be regular or an irregular 3D lattice Fig. (2.7). For example, Fig. (2.7a) shows a pore with a cubic lattice structure, with each pore body connected to six pore throats, while Fig. (2.7b) is an extracted image from microtomography. Thus, the coordination number is six, and there is a constant ratio between the pore body and the throat diameter. The diameters of the pore throat are generated randomly using a defined probability density function, and the coordination number and aspect ratio can be varied.

When constructing a representative pore network of a porous medium, the selected probability density function should be able to reproduce geometrical properties required to replicate the medium's topology parameters, such as permeability and porosity. (Bekri and Vizika, 2006) recommended that the formation factor and the capillary pressure estimated through this modelling effort can be close in value to the actual porous media being considered since they are sensitive to its structure. This approach is possible if the pore networks can be directly constructed from a 3D image. If the experimental data comes from non-imaging techniques such as mercury intrusion porosimetry and gas adsorption, where the characteristics of the pore space are not available, the regular pore network construction technique is appropriate (Xiong et al., 2016). The reader can check the works of (Ioannidis and Chatzis, 2000, Adler and Thovert, 1998, Roberts and Torquato, 1999, Okabe and Blunt, 2004, Yeong and Torquato, 1998) for more details about this construction approach.
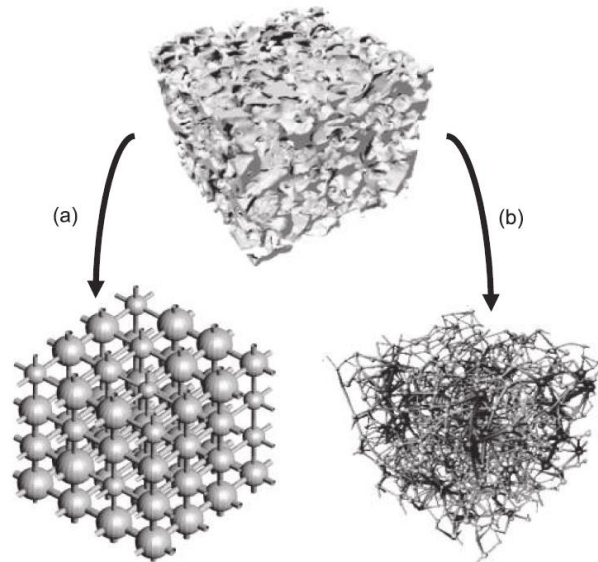
Figure 2.7: Pore network models (a) reconstructed with a regular lattice to reproduce the real petrophysical properties in the porous media (Bekri and Vizika, 2006), and (b) extracted from microtomography (Youssef et al., 2007).

The grain-based model was introduced by (Bryant and Blunt, 1992, Bryant et al., 1993a, Bryant et al., 1993b). The model is based on random close packing of equally sized spheres, with equivalent networks having four or fewer coordination numbers. In the modelling approach, the uniform swelling of the spheres and allowance for overlapping represents diagenesis. In contrast, the movement of the spheres' centres closer to each other in the vertical direction and allowing for overlap of the spheres represent compaction. This approach can predict the properties of cemented quartz sandstones and water-wet sand packs, such as the capillary pressure, absolute and relative permeabilities, and electrical and elastic properties. However, the main disadvantage of this method is that it is primarily applicable to porous media with spherical grains of the same size. Meanwhile (Bakke and Øren, 1997, Oren et al., 1998, Lerdahl et al., 2000, Øren and Bakke, 2002) extended the reconstruction method to simulate the packing of spheres with different sizes. In the same vein, attempts have also been made to integrate the extracted networks from images, at specific length scales, into a single two-scale network (Bultreys et al., 2015, Jiang et al., 2013, Mehmani and Prodanović, 2014).

The direct mapping of the real image of the pore networks will often yield an irregular lattice, which allows for verifying the imposed physical assumptions for the simulation of fluid flow. The results of the flow simulations can be compared with a 4D imaging of mass transport in the medium. In this model, medial axis and maximal ball algorithms are used for constructing the irregular lattice model. For more details, read the paper by (Dobson et al., 2016).

2.2.1.3 Macro-Scale Approaches

The macroscopic scale approaches assume the porous medium to be an averaged continuum. And in most of the studies on upscaling effective models that show the relationship between the pore-scale characteristics of the medium and/or other coupled processes to the upscaled equivalents are derived (Heße et al., 2009). Some of the upscaling approaches used included volume averaging, method of moments, homogenisation through multiscale expansions, and thermodynamically constrained averaging (Battiato et al., 2009). Hence, the fluctuations in the means of governing variables are often disregarded. Though these approaches establish links between physicochemical processes on different scales when the governing assumptions hold, they cannot validate these assumptions or provide the regions of a computational domain where the continuum model fails.

(Battiato et al., 2009) used the volume averaging method to upscale mixing-induced precipitation in identifying sufficient conditions for the continuum-based reaction-diffusion equations. In the analysis, they presented a phase diagram that showed the range at which the macroscopic models are applicable. The phase diagram Fig. (2.8) showed that highly localised processes in porous media, including mixing-induced precipitation, are not worth using macroscopic models. This is because using such reaction-diffusion equations relies on approximations whose accuracy cannot be determined apriori. The upscaled equations are as follows:

$$\phi \frac{\partial \langle c_i \rangle^l}{\partial t} = \frac{\varepsilon^2}{Da} \nabla . \left(\phi D_{eff} . \nabla \langle c_i \rangle^l \right) - \phi \langle c_1 \rangle^l \langle c_2 \rangle^l + \phi K \langle c_3 \rangle^l \quad (i = 1,2) \qquad (2.21)$$

$$\phi q \frac{\partial \langle c_3 \rangle^l}{\partial t} = \frac{q\varepsilon^2}{Da} \nabla.\left(\phi D_{eff}.\nabla \langle c_3 \rangle^l\right) + \phi \langle c_1 \rangle^l \langle c_2 \rangle^l - \phi K \langle c_3 \rangle^l$$
$$- q a_v l_l \frac{Da_{ls}}{Da}\left(\langle c_3 \rangle^l - 1\right) \qquad (2.22)$$

where ϕ is porosity, q is Darcy flow rate, $a_v = |A_{ls}|/|\mho|$ where $A_{ls} = \mho \cap V_1$ and $V_1 \in \mho$,

l_l is the pore-geometry length scale, $\varepsilon = l_1/L_c$ with L_c being the macroscopic length scale

associated with $\langle c \rangle = \phi \langle c \rangle^l$, D_{eff} is the effective diffusivity tensor, K is a dimensionless

quantity, Da_{ls} is the Damkohler number for precipitation or dissolution process, and $\mho$ is

size of the averaging volume.

Figure 2.8: A phase diagram showing the range of applicability of macroscopic models for a reaction-diffusion system in terms of the Da number. The macroscopic models are applicable in the blue region. In the red and orange regions, macroscale and microscale problems (Battiato et al., 2009).

Conversely, in upscaling the pore-scale construction of advection and diffusion equations,

where the reaction equations are formulated such that they are placed in the boundary

conditions of the fluid-solid interface, (Battiato and Tartakovsky, 2011) used multiple-scale

expansions to ensure the macroscopic description of the process accurately represents the pore-scale processes. They also provided a phase diagram to establish the range of applicability of macroscopic models, using a different set of process and media properties. Still, they arrived at the same conclusions as to the previous work. The homogenised form of the advection-diffusion-reaction equation using this upscaling approach was presented as

$$\phi \frac{\partial \langle c \rangle_B}{\partial t} = \nabla \cdot (D^* \nabla \langle c \rangle_B - Pe \langle c \rangle_B \langle v \rangle) - \varepsilon^{-1} \phi Da K^* (\langle c \rangle_B^a - 1) \qquad (2.23)$$

subject to the following conditions

1. $\varepsilon \, "1$

2. $Pe < \varepsilon^{-2}$

3. $Da/Pe < \varepsilon$

4. $Da < 1$

5. $\langle \chi \rangle_\Gamma \approx \langle \chi \rangle_{B*}$

the dispersion tensor D* in Eq. (2.23) was given as

$$D^* = \langle D(I + \nabla_y \chi) \rangle + \varepsilon Pe \langle \chi k \rangle \nabla_x p_0 \qquad (2.24)$$

while the closure variable with zero mean is defined as the solution to the local problem:

$$-\nabla_y \cdot D(\nabla_y \chi + I) + \varepsilon Pe v_0 \nabla_y \chi = \varepsilon Pe(\langle v_0 \rangle_B - v_0) \quad , y \in B \qquad (2.25)$$

$$-n \cdot D(\nabla_y \chi + I) = 0 \quad , y \in \Gamma \qquad (2.26)$$

where $v_0 = -k \nabla_x p_0$, p_0 is pressure, k is permeability, ε is a length-scale parameter, χ is the closure variable, and I is the identity matrix. The constraints listed above is critical in ensuring the separation of scales. The first constraint is a common observation in several

practical applications, and the remaining four are dependent on the relative importance of the transport's diffusive, reactive, and advective processes.

- **Solution Strategies for Macro-Scale Approaches**

In recent years, efforts to develop numerical solutions for reactive transport processes have focused on how to couple the reaction and transport terms (Yeh and Tripathi, 1991). In the effort to develop such algorithms, several methods have been proposed, dating back to those presented by (Rubin, 1983). The most rigorous of these algorithms is the attempt to solve the governing equations simultaneously. In this work, three commonly used numerical solution methods are discussed.

A. Finite Volume Scheme

(Hao et al., 2012b) presented an integrated finite difference solution for a multiphase, multicomponent heat and mass flow and reactive transport in both unsaturated and saturated porous media. Similar model and approach have been implemented before their works or are integrated into the robust codes NUFT (Nonisothermal Unsaturated-saturated Flow and Transport), such as the work of (Pruess, 1991, Nitao, 1998, Nitao, 2000, Yeh and Tripathi, 1991, Xu et al., 1999, Mills et al., 2007, Nichols et al., 1997, Xu, 1998).

One outstanding feature of the NUFT model is its capability to handle the disappearance and appearance of any of the three fluid phases that may occur during evaporation or condensation or immiscible fluid displacement processes. To approximate flow in fractured porous media effectively, NUFT considered using the effective continuum model, which has

been described extensively earlier, along with the dual-porosity model. The dual porosity/permeability model describes the fracture and matrix systems as two separate overlapping continua, where multiphase flow and heat transfer equations are conceptually addressed in both. In addition, each continuum will have a set of its mass and energy balance equations. For more details on this approach and other relevant equations, the reader is advised to check the following references: (Hao et al., 2012b, Buscheck et al., 2003, Buscheck et al., 2006, Buscheck et al., 2009).

The finite volume method was applied to discretise the partial differential equations, governing each sub-model's mass and energy balance equations, and an implicit scheme for the time integration because of its numerical stability. At each time step, the nonlinear system of equations, which results from the discretisation, are solved using the Newton-Raphson algorithm. Each nonlinear iteration step requires solving a set of linear algebraic equations. Therefore, multiple linear solvers and decomposition options, including Gauss elimination preconditioned conjugate method, block Gauss-Seidel preconditioning, and incomplete block LU (Lower-Upper) decomposition were implemented in NUFT. In addition, the numerical stability, robustness, and accuracy of the algorithm were further enhanced through some special numerical techniques, including primary variable switching, basis-species switching, artificial diffusion technique, and flux-correction methods to reduce numerical dispersion.

The critical issue in numerical simulations of reactive transport is the coupling of the transport and reaction models accurately and efficiently. Generally, most available

numerical algorithms proceed into forms: global implicit and operator splitting methods. The operator-splitting method separates the transport and chemical models and then sequentially solves them. The representative numerical implementations for this method include sequential iterative and sequential non-iterative approaches. The iterative approach includes iterations for convergence between two solution steps, which requires more CPU (Central Processing Unit) time but has more accurate solutions than the non-iterative method. In the global implicit method, there is a full coupling between the transport and chemical reaction equations, and they are solved simultaneously. Though the computation cost of the global implicit method is high, it effectively coupling physical and chemical processes without any inconsistency.

The coupling between the two models is often done with a time-marching sequential solution procedure to reduce the high computation cost in simulating flow and reactive transport processes. This approach avoids the computation of a large Jacobian matrix present in a fully coupled flow and transport procedure. Given a time step, the flow model's mass and energy balance equations are solved first, and the flow variables are then calculated and incorporated into the reactive transport equation. After that, the reactive transport simulation is then performed using the same flow variables for the time step. Because the chemical reactions time scale is often smaller than flow processes, multiple time steps are usually required for reactive transport calculations to reach the given flow time step. At the end of the computation, porosity and permeability changes caused by the chemical reactions are then updated in the flow equation for the next time step. It should be noted that this same algorithm can be applied to the finite element method as well.

B. Mixed Finite Element Method

(Arbogast et al., 1996) presented a flow and reactive transport simulator called PARSIM (Parallel Simulator). In this work, the simulation of the transport and reactions of dissolved chemical species in the groundwater was done. The time splitting method was used for the advection, diffusion, and reaction coupled equations. The method of characteristics and the higher-order Godunov method were provided as options to treat the advection problem. In contrast, the mixed finite element method was used to discretise the diffusion equation. Reactions were handled separately as a differential-algebraic system of equations. The Godunov scheme is applicable when the reactive time steps are of the order of a CFL (Courant Friedrichs Lewy) time step. The Godunov mixed finite element scheme and the characteristic-mixed method have also been implemented for other advection or diffusion problems by (Arbogast et al., 1994, Arbogast and Wheeler, 1995, Dawson, 1995, Dawson, 1993).

C. Upscaled Smoothed Particle Hydrodynamic Method

Mesh-free smoothed particle hydrodynamics approach was used by (Battiato et al., 2009, Tartakovsky et al., 2007a, Tartakovsky et al., 2007b) to solve the upscaled advection-diffusion-reaction equations of M species. The macroscopic quantities were computed from the micro-scale simulations by averaging them over a representative volume, whose characteristic dimension is such that the characteristic radius is far greater than the pore-geometry length scale. The representative volume was defined as the averaging volume with the minimum radius beyond which the porosity remains invariant with increasing averaging volume. The intrinsic average solute concentration was determined as

$$\langle c_1 \rangle^l (x) = \frac{1}{N(x)} \sum_{b \in V} c_1(y_b) W_{x,r_0}(y_b) \qquad (2.27)$$

where N is the number of liquid SPH particles contained in the representative volume V, y_b is the position vector of particle b, and $W_{x,r_0}(y_b)$ is a weighting function.

2.2.1.4 Hybrid Approach

Macroscopic models for flow and reactions in porous media sometimes fail to describe observed phenomena in experiments. At the same time, the corresponding pore-scale approaches can accurately capture the observed events, although they may be computationally expensive. Most multiscale models that seek to couple both upscale and microscopic approaches require empirical closure relations about the behaviour of the quantities at pore and continuum scales (Christie, 1996, Efendiev and Durlofsky, 2003, Langlo and Espedal, 1994). On the other hand, (Battiato et al., 2011) proposed a general framework for the iterative hybrid numerical method that couples the microscopic and macroscopic scales without any empirical closure. The formulation assumes the exchanged fluxes at the internal boundaries between the microscopic and macroscopic scale domains are unknown and permits iteratively determining the necessary boundary conditions at the microscopic scale to guarantee flux continuity.

One of the benefits of the hybrid simulation scheme is that it provides significant speed-up in simulations where pore-scale simulations are necessary locally in the computational domain. This is possible because of the low cost of the continuum scale simulations, which

is applied for most of the computational domain. Furthermore, as noted by (Alexander et al., 2002), choosing a hybrid algorithm provides a great benefit when the interfacial region of interest is very small compared to the entire computational domain. The hybrid formulation is applicable for Darcy flow in the medium (Battiato et al., 2009, Battiato et al., 2011).

The hybrid pore-scale/continuum-scale algorithm developed by (Battiato et al., 2011) has three dependent variables that satisfy a system of coupled partial-differential equations:

$$\phi \frac{\partial \bar{c}}{\partial t} + \phi \nabla . (V\bar{c}) = \nabla . (\boldsymbol{D}^* \nabla \bar{c}) - K_e \bar{c} \quad x \in \Omega^T \quad t > 0 \quad (2.28)$$

$$\phi \frac{\partial \bar{c}}{\partial t} = \frac{1}{\phi \|\Omega_p\|} \int_{\Gamma_{ll}} q_n dx - \frac{1}{\phi \|\Omega_p\|} \int_{\Gamma_{sl}} \mathcal{K} \, c dx \quad x = x^* \quad t > 0 \quad (2.29)$$

$$\frac{\partial c}{\partial t} + \nabla . (vc) = \boldsymbol{D}^* \nabla^2 c \quad x \in \Omega_p \quad t > 0 \quad (2.30)$$

$$-n. \boldsymbol{D}^* \nabla c = \mathcal{K} \, c \quad x \in \Gamma_{sl} \quad t > 0 \quad (2.31)$$

$$n. (\mathcal{D} \nabla c - vc) = q_n \quad x \in \Gamma_{ll} \quad t > 0 \quad (2.32)$$

where $c = c' + \bar{c}$ is the pore-scale concentration, $\bar{c}$ being the mean concentration and c' the fluctuation, $\mathcal{D}$ is the molecular diffusion, D^* is the dispersion tensor, $\mathcal{K}$ is the reaction rate constant for a surface reaction, n is the outward unit normal vector of the solid-fluid interface Γ_{sl}^T. q_n is the flow rate, K_e is the effective reaction rate, $\Omega_p \subset \Omega$ is the computational subdomain where pore-scale simulation is required, t is time.

The initial and boundary conditions on the computation domain are also added to these equations. It should be noted that porosity is assumed to be constant in this formulation. In

a case where porosity evolves, the equation can easily be modified to account for that, unlike other multiscale approaches that decouple the two descriptions (pore-scale and continuum scale) by using closure assumptions to show the undetermined pore-scale flux q_n based on its continuum scale correspondence. One form of strategy representing the pore-scale concentration is the sum of its average and the corresponding fluctuations. Other techniques are linearising the concentration function, postulating a numerical or analytical closure for the corresponding fluctuations, and imposing boundary conditions on the interface.

The hybrid strategy employed by (Battiato et al., 2011) computes the undetermined pore-scale flux with no assumption of the pore-scale behaviour and without linearising the general reactive term if present. Hence, the pore-scale concentration is obtained from Eq. (2.29) by solving the transport problem defined in the subdomain. And the boundary condition $n.D\nabla c = \mathcal{H}c$ ($\mathcal{H}$ is the reaction rate constant for a surface reaction) is now represented on the union of all the solid-liquid surfaces contained in the subdomain. While on the fluid-fluid segments, the mass conservation requires that $n.(D\nabla c - vc) = q_n$.

2.3 Evolution of Continuum-Scale Parameters

Parameterisation of an evolving porous medium can be challenging, especially in the continuum scale. To capture such a phenomenon, some tools have been proposed. This section presents a review of common methods available in the literature to parameterise evolving parameters for simulations of reactive transport such as porosity, transport parameters, and the existing relationships among the rate of flow and transport processes. These processes are discussed at the pore-scale, although with a significant impact at the macroscale.

2.3.1 Porosity Evolution in Porous Media

As mentioned in the previous section, as the minerals dissolve and/or are precipitated, it can lead to changes in the porosity of the porous media. Estimating the total change in porosity at the macro-scale is determined at any point in time, based on the volume fractions of the mineral that make up the grain matrix, as (Appelo and Postma, 2005, Hommel et al., 2018)

$$\phi = 1 - \sum_i^{N_m} \varphi_i \qquad (2.33)$$

It is worth noting that this equation defines total porosity, while effective porosity is not addressed. In a situation where the mineralogical composition of the media is unknown, and the dissolution of few phases contributes to porosity changes, the equation below can be applied.

$$\phi = 1 - \varphi_{NR} \sum_i^{N_{m,r}} \varphi_i \qquad (2.34)$$

φ_{NR} is the volume fraction of the non-reactive minerals, and $N_{m,r}$ is the number of reactive minerals, and φ_i is the mineral volume fraction of a mineral phase. Hence, the change in porosity with time can be determined from

$$\frac{d\phi}{dt} = - \sum_i^{N_{m,r}} \frac{d\varphi_i}{dt} \qquad (2.35)$$

The effective porosity of the medium can also be updated through a similar procedure. One of the limitations of the previous equation is that it fails to provide any detailed description of the structural evolution of the pore, although it accurately provides a description of the

foregoing processes. However, other attempts have developed macro-scaled relationships to describe the evolution of the pore structure indirectly.

2.3.2 Diffusivity and Tortuosity as Functions of Porosity

When there is an absence of the advective fluxes, diffusion dominates the transport of solute. Therefore, for deep geologic repositories, the dominant transport process must be diffusion. And to better understand the degradation process of cementitious materials at the interface of clay and cement in radioactive waste repositories, efforts have been applied using reactive transport modelling (Dauzères et al., 2019, Savage, 2013, Jenni et al., 2017, Gaucher and Blanc, 2006). However, it should be noted that the diffusion properties of the media are liable to vary as the porosity and tortuosity evolve because of dissolution and precipitation processes. As defined by (Bear, 1988), tortuosity is the ratio of the path taking by the solute in water to that followed through the rock.

Several reactive models have been established to describe the correlation between tortuosity and porosity and the direct influence of porosity on diffusion. In these relationships, which are mainly applicable to evolving porous media, the effective diffusion coefficients are determined from porosity, which is easy to measure. One of the relationships often used is Archie's law which shows the dependence of porosity on the pore diffusion coefficient. The simplest form of the relationship between tortuosity and porosity is

$$\tau_l = \phi^{n_c} \qquad (2.36)$$

where is τ_l tortuosity, ϕ is porosity and n_c is the cementation factor. Recall that the saturated aqueous phase effective diffusion coefficient is (Seigneur et al., 2019):

$$D_l^e = \phi \tau_l D_l^0 \qquad (2.37)$$

A generic form of relationship for the liquid-phase effective diffusion coefficient is presented in this paper in Eq. (2.38). This relation reduces to the form presented by (Seigneur et al., 2019) when $k = 2$ and (Oelkers, 2018) when $D_l^{min} = 0$:

$$D_l^e = \phi_e^k D_l^0 + D_l^{min} \qquad (2.38)$$

where D_l^0 is the pure water diffusion coefficient, D_l^{min} is the matrix effective diffusion coefficient, k is an empirical parameter, and ϕ_e is the effective porosity, defined as

$$\phi_e = \begin{cases} a(\phi - \phi_{crit})^\beta & \phi \geq \phi_{crit} \\ 0 & \phi < \phi_{crit} \end{cases} \qquad (2.39)$$

The constant a is a fitting parameter, β is the scaling exponent, as defined by (Stauffer and Aharony, 1985, Ellis and Wright, 2006), and ϕ_{crit} is a critical porosity. Another form of relationship for estimating effective porosity was presented by (Tarafdar and Roy, 1998) as:

$$\phi_e = \varepsilon \phi \qquad (2.40)$$

where ε is the pore connectivity fraction.

There are other forms of relationships for tortuosity, including an exponential relationship with porosity, which are not covered in this review. For an unsaturated condition, (Millington and Quirk, 1961) showed that phase saturation is a variable that affects tortuosity. They presented an empirical model of the form:

$$\tau_\alpha = S_\alpha^{7/3} \phi^{1/3} \qquad (2.41)$$

Eq. (2.41) shows that tortuosity has a strong nonlinear relationship with saturation, S_α, which (Millington, 1959) derived for gas diffusion in porous media. However, in most reactive transport simulations, the relation proposed by (Millington and Quirk, 1961) in modelling the diffusion through the liquid phase is adopted. On the other hand, the application of this model to unsaturated conditions is questionable. A review of several models for unsaturated conditions was presented by (Chou et al., 2012) and affirmed the inaccuracy of the Millington-Quirk model.

When applying reactive transport modelling, the deterioration of cementitious materials is enhanced by dissolution reactions, driven by the solute diffusion into these materials. The extent of degradation into these materials is dependent on the cementation factor or the type of feedback law used. This is because the diffusion of calcium into the affected areas strongly impacts the dissolution rates of the primary minerals. In other studies on reactive transport, the extent of the degradation in the material was estimated using either Archie's law (Georget et al., 2018, De Windt and Badreddine, 2007, Li et al., 2017, Galíndez et al., 2006, Chagneau et al., 2015) or an exponential correlation (Mainguy et al., 2000, Seigneur et al., 2017) for the description of the relationship between evolving porosity and tortuosity variation. However, the selection of the cementation factor used in these studies is strongly dependent on the materials being considered. Other relevant contributions on this topic include the works of (Maxwell, 1881, Petersen, 1958, Tomadakis and Sotirchos, 1993).

In most modelling studies, the initial porosity and tortuosity, representing the state and type of the material of interest, are imposed. These empirical relations are then used to compute

how the diffusion parameters evolve in the process. In these attempts, curve-fitting of the early time data or independent approaches is used to determine the media's initial diffusion properties. Knowing that dissolution within the regime-controlled by diffusion occurs uniformly in the domain can cause a slight increase in tortuosity. Using this technique has resulted in a close agreement between modelling and experimental data. However, it is often difficult to know the dynamic interactions between precipitation and dissolution processes and the consequent effects on tortuosity and diffusion parameters when both occur simultaneously. Others attempt to tune the empirical factors of the precipitation reaction artificially (Huet et al., 2010, Chagneau et al., 2015, Brunet et al., 2013), modify the parameters defining the reactivity (Jacquemet et al., 2012) or employ other empirical relations (Walsh et al., 2013) to mimic breakthrough curves and degradation extent in materials under carbonation process.

Following these modelling approaches, their results have been consistent with pore-scale simulations. Hence, it suggests that localised precipitation of minerals can significantly affect the paths of diffusion. Consequently, it is evident from the foregoing that the effect of precipitation reactions on diffusion is not easy to capture compared to the impact on dissolution. Also, it can be implied that the reactions of different pore materials to these reactive processes strongly depend on the state of their initial pore structures. In this light, porous media having high initial tortuosity and small pore throats are highly sensitive to actions of precipitation (Seigneur et al., 2017, Brunet et al., 2013, Kutchko et al., 2007, Huber et al., 2014). Furthermore, it suggests that using a specific correlation between tortuosity and porosity for all materials may not be advisable because different materials

respond to dissolution and precipitation reactions differently. However, understanding the impacts of these reactions on the diffusivity of materials remains unresolved because of the coupled nature of these reactions.

2.3.3 Permeability as a Function of Porosity

The advection driven transport regime is influenced by the evolution of the permeability of the porous media. In this regime, porosity alteration can affect permeability, and thus, the fluid flow patterns, which can impact the degree of chemical fluctuations that can alter the nature and structure of the medium. Hence, using relationships that can capture the impact of evolving porosity on permeability is often advised. One prominent power-law relation is the Kozeny-Carman model (Hommel et al., 2018, Appelo and Postma, 2005), which can simulate permeability evolution affected by the dissolution and precipitation of minerals. Its commonly used form is:

$$k = k_0 \frac{\phi^3}{(1 - \phi)^2} \frac{(1 - \phi_0)^2}{\phi_0^3} \qquad (2.42)$$

where k_0 and ϕ_0 are the initial permeability and porosity, respectively, other forms of power-law models have been used extensively to model permeability evolution (Hommel et al., 2018). In the modelling efforts, capturing the evolution of diffusivity is challenging. Within regions where diffusion dominates, there is a measure of stability in the reaction fronts. On the other hand, within the regimes dominated by advection, the distribution of flow rates is affected by pore-scale heterogeneities, which can cause the fronts to be unstable. Alternatively, it is common to use cubic relations for permeability evolution related to the local fracture aperture. This form of relationship has long been used, dating back to the work

of (Witherspoon et al., 1980). (Oron and Berkowitz, 1998) generalised the local cubic law for rough fractures. For more details on this topic, the reader is referred to the work of (Deng and Spycher, 2019).

Furthermore, as pointed out by (Hommel et al., 2018), it is worth noting that generally the use of the simple power law model, provides similar accurate permeability predictions as the more complex models. However, with increased porosity reduction, there is a great disparity between them and the simple power law model. Hence, it is recommended that the simple power laws be used as default for modelling an evolving medium. While more complex models be used to capture known processes alongside the porosity evolution of the medium.

2.3.4 Evolution of Reactive Surface Area

Mineral dissolution and precipitation not only result in modification of the transport properties, but they also alter reactivity, causing the reaction rates to be enhanced or decreased. Understanding the evolution of reaction rates is equally important as knowing how the transport parameters evolve. Therefore, it is critical to have an adequate description of the reaction rates to capture concentrations and loadings of the solutes for the long term. Also, having a proper definition of reactions is essential for pH-buffer reactions to capture the interactions with the flow and transport processes. To describe reactivity, the reactive surface area of the minerals is often used. As observed by (Emmanuel and Berkowitz, 2007, Liu et al., 2008, Landrot et al., 2012, Peters, 2009, Lai and Krevor, 2014, Deng et al., 2018), several factors affect the reactive surface area, including grain size, exposure of the mineral to pore fluid, degree of occlusion, surface roughness and etch-pits. However, the presence of multiple phases causes the surface fraction to differ significantly from its fractional

volume (Lai and Krevor, 2014). Furthermore, the flow state can increase the formation of more reactive zones, consequently contributing to alterations of reactive areas from the geometric surface area; thereby, the effective reactive surface area is controlled (Jung and Navarre-Sitchler, 2018).

Different mathematical modelling attempts have been made to describe how the surface evolves. One of the simplest models assumes the dissolution of a spherical grain is uniform, and the surface area has an inverse proportionality relationship to its radius. Based on this relationship, (Steefel and Lichtner, 1998) proposed that the exponent of the power-law relationship between surface area evolution (S) and porosity (ϕ) be two-third.

$$S = S_0 \left(\frac{\phi}{\phi_0}\right)^{2/3} \qquad (2.43)$$

where S_0 and ϕ_0 define the surface area and the porosity, respectively. This same relationship has been used on the continuum scale, although it was derived based on a single-grain assumption. In some instances, the reduction in reactivity and surface area as dissolution proceeds is intuitively assumed; unfortunately, this assumption fails in some cases. The reactive surface area can also be increased through the dissolution processes, as observed by (Noiriel et al., 2009). He noticed that dissolution reactions could have the same effect of etch pits on the mineral surface area, thus increasing the reactive surface area. Another power-law relationship for describing the evolution of the surface area with porosity was presented by (Luquot and Gouze, 2009):

$$S = S_0 \left(\frac{\phi}{\phi_0}\right)^{-w} \qquad (2.44)$$

where w is a fitting parameter. The reader is also advised to check the work of (Noiriel et al., 2012, Molins et al., 2014, Molins et al., 2019, Ritchie, 1994, Wunderly et al., 1996, Lefebvre et al., 2001, Mayer et al., 2002, Steefel and Lichtner, 1994, Steefel and Lichtner, 1998, Deng et al., 2016, Dentz et al., 2011a, Luhmann et al., 2014, Appelo and Postma, 2005) for more details.

The reactive surface area of the primary minerals can also be affected by the secondary minerals precipitated, which can cause the passivation to the reaction surface. Capturing this passivation can be challenging because of the complexity in the surface morphology of the secondary phases. Conceptually, it can be viewed that the reactivity of the phases of the primary minerals can be linked to the fractional volume of the secondary minerals. (Jeen et al., 2007) presented an exponential decay function to describe the evolution of the reactive surface of iron present in a permeable reactive barrier:

$$S = S_0 \, exp\big(-a\varphi_p\big) \qquad (2.45)$$

where φ_p represents the total volume fraction of precipitated secondary carbonate minerals, a is a fitting parameter, and S_0 is the initial surface area. (Harrison et al., 2016, Daval et al., 2009, Noiriel et al., 2012) are other relevant studies on the evolution of reactive surface area during mineral precipitation that the reader can check for more details.

2.3.5 Thermal, Hydrological, Mechanical and Chemical (THMC) Coupled Model

This is the most recent and developed model used to assess some subsurface applications such as oil/gas production, geothermal reservoir and repository of nuclear waste, where heat and fluid transfer take an essential role in the process. The original versions of this model

were THC and THM, which both imitate the interaction between two critical couplings processes such as heat transfer, hydraulic fluid flow, mechanical deformation, and chemical reactions in geological repositories. The "coupling" term indicates that it is a two-way process of interaction where one process will affect and initiate other processes (Lanru and Xiating). Some examples of those coupling are TM (temperature effect on mechanical deformation), TC (temperature effect on chemical reactions), HC (fluid transport effect on chemical reactions) and HM (fluid pressure effect on mechanical deformation) (Zheng et al., 2017). A full THMC coupled model was developed to illustrate the interaction between the mechanical and chemical processes over THM and THC models. The model is based on a numerical analysis which allows the imitation of complex couplings interactions.

In the engineered barrier system, clay minerals are generally used as a buffer because of their high retention capacity, low thermal conductivity, along with low permeability, and diffusion coefficient. Through time, the performance of the clay repository is affected by complex thermal, hydrological, mechanical and chemical (THMC) processes (Zheng et al., 2012). The clay will be subjected to several changes in temperature and hydration level as heat is released from the radioactive waste through the radionuclide decay phenomenon and water filtration from neighbour rocks. In addition, chemical reactions, formation damage and multiphase flow might also take place and disturb the integrity of the repository. To establish a mathematical formulation for the full THMC model, balance equations were developed based on the THM model and then a chemical formulation was added to it.

2.3.5.1 THM Theoretical Formulation

This model is done by (Olivella et al., 1994), and it is based on the theoretical model of multiphase and species, which describes the mechanics of fracture geomaterials. The model considers the porous medium as solid, liquid and gas phases. The precipitated minerals represent the solid phase; the liquid phase contains water and dissolved chemicals, while dry air and water vapour make up the gas phase (Gens et al., 2010). Two coupling processes are established in this model, the thermo-elasticity process (T-M), which imitates thermal stress and expansion of solids, and the poroelasticity process (H-M), which imitates the deformation of porous media (Lanru and Xiating). Hook's, Fourier's, and Darcy's laws were used to define elasticity deformation, heat transfer and fluid flow, respectively. Subsequently, balance equations are made as below:

$$\frac{\partial}{\partial t}[\rho_s(1 - \phi)] + \nabla.j_s = 0 \qquad\qquad (2.46)$$

$$\frac{\partial}{\partial t}(\rho_l\phi) + \nabla.j_l = f^w \qquad\qquad (2.47)$$

$$\frac{\partial}{\partial t}[E_s\rho_s(1 - \phi) + E_l\rho_lS_l\phi] + \nabla.(i_c + j_{E_s+}j_{E_l}) = f^Q \qquad\qquad (2.48)$$

$$\nabla.\sigma + b = 0 \qquad\qquad (2.49)$$

where ϕ is porosity, ρ_s is solid density, ρ_l is liquid density, $j_i(i = s, l)$ total mass flux, σ is stress tensor, b is body force vector, $E_i(i = s, l)$ is specific internal energy, $j_{E_i}(i = s, l)$ is energy flux due to mass motion, f^w and f^Q are sink/source terms for water mass and energy, respectively. i_c is conductive heat flux (Gens et al., 2010).

2.3.5.2 Chemical Formulation

This model is used to describe the equation of chemical species reactive transport, and it is formulated based on the mass continuity of those chemicals in the porous medium (Gens et al., 2010, Olivella et al., 1994). The chemical model will account for the chemical reactions of cation exchange, acid/base, aqueous complexation, surface complexation and minerals dissolution/precipitation (Zheng et al., 2008, Zheng et al., 2012)

$$\frac{\partial}{\partial t}\left(\phi S_l \rho_l U_j\right) + \nabla.\left[\rho_l (Ua)_j q_l - D_l \nabla (Ua)_j + \phi S_l \rho_l U_j \dot{u}\right] + \sum_{m=1}^{N_m} v_{jm} r_m$$
$$= 0 \qquad (j = 1,2,\dots,N_c) \qquad\qquad (2.50)$$

$$U_j = C_j + \sum_{i=1}^{N_x} v_{ij} X_i \qquad (i = 1,2,\dots,N_c) \qquad (2.51)$$

$$(Ua)_j = \lambda_j C_j + \sum_{i=1}^{N_x} v_{ij} \lambda_i X_i \qquad (i = 1,2,\dots,N_c) \qquad (2.52)$$

where U_j is total analytical concentration, $(Ua)_j$ is total aqueous concentration of the primary species j, C_j and X_i are concentrations of the primary and secondary species, respectively. λ_j and λ_i are mobility of primary and secondary species, respectively. r_m is rate of precipitation or dissolution of mineral m under kinetics conditions. N_m is number of minerals under kinetics conditions, v_{jm} is the mole number of primary species j in a mole of mineral m. N_c is a number of primary species, N_x is a number of secondary species (Gens et al., 2010).

2.4 Speciation Methods

Speciation is the process of identifying, estimating quantitatively, or describing the various species or phases present in a material. Several attempts and reviews have been made on speciation methods for radionuclides and metals in sediments and surface waters (Markich, 2002, Von Gunten and Beneš, 1995, Tessier and Turner, 1995, Salbu et al., 2001). Generally, there are two main approaches or methods in speciation, analytical and computational methods. In analytical methods, the nature of the material or medium to be investigated and its phases are very important. However, it is worth noting that no single method will provide indisputable information about the material. Often, more than two or more techniques are combined using a speciation scheme. The choice of a speciation scheme is strongly dependent on the nature of the medium. The different analytical techniques can be grouped into two sub-methods – invasive and non-invasive. In invasive techniques, the samples require to be pre-treated, while in non-invasive techniques, there is no need for pre-treatment. The reader can refer to (Markich, 2002) for a comprehensive list of different analytical methods.

Because analytical methods cannot adequately determine uranium speciation in natural surface waters, computational methods are often used. And most of the information on its speciation in natural waters are determined through thermodynamic modelling. Two separate approaches are usually used: the equilibrium constant and Gibbs free energy methods, although they are both subject to mass balance and chemical equilibrium conditions. In the equilibrium constant method, the expressions of the mass action are incorporated into the mass balance equations, which results in a system of nonlinear equations. On the other hand, the Gibbs free energy method involves transforming the

governing variables using their thermodynamic relations. For more details on the classification, the reader can refer to (Smith, 1982, Van Zeggeren and Storey, 2011, Zeleznik and Gordon, 1968).

There are several geochemical solvers based on the equilibrium constant approach, including WATEQ by (Truesdell and Jones, 1974), MINTEQA2 by (Allison et al., 1991), CHESS by (Van der Lee and De Windt, 2002), and PHREEQC by (Parkhurst and Appelo, 1999, Parkhurst and Appelo, 2013, Appelo and Postma, 2005). Although the determination of the stable equilibrium phase is challenging and computationally expensive in these codes, this issue has since been resolved using heuristic techniques (Bethke, 2022). However, there are other issues associated with some of these solvers, such as using an incomplete Newton scheme. The reader is advised to check the works of (Leal et al., 2013, Leal et al., 2014) for more details.

Similarly, there are geochemical codes based on the Gibbs free energy method, including CHEMSAGE by (Eriksson and Hack, 1990), THERIAC by (de Capitani and Brown, 1987) and GEM-Selektor by (Karpov et al., 1997, Karpov et al., 2001, Karpov et al., 2002, Kulik et al., 2013). Unfortunately, some of these packages also have limitations. For instance, in CHEMSAGE, the code cannot converge at a quadratic rate in the neighbourhood of the solution, GEM-Selektor does not use logarithmic barrier functions often used by other nonlinear programming software.

2.5 Mixing in Reactive Transport Modelling

Mixing is a form of potential interaction between pairs of molecules of reactants in a mixture, and it is affected by two main mechanisms. The first of these mechanisms is advective

transport. Without molecular diffusion, mixing depends on the initial and boundary conditions on which the reacting species enter the flow domain. Also, it depends on the configurations of the streamline that drive the reactants very close to enable reaction. The other mechanism is diffusion, which helps transfer reactants between streamlines, furthering interactions among the molecules.

In the macro-scale reactive transport modelling approach, it is assumed that there are well-mixed conditions at the pore scale, and changes in the concentration of the species based on chemical reactions occur on time scales greater than the mixing time. This implies that the diffusion time is faster than the reaction.

Incomplete small-scale mixing can significantly impact both heterogeneous and homogeneous reaction rates. (Meile and Tuncay, 2006) studied its impact and whether the continuum description can still be applied. (Li et al., 2008) similarly presented numerical and experimental studies challenging the necessity of the well-mixed condition for the Darcy-scale reactive transport modelling approach.

From the foregoing, it is evident that correctly quantifying the mixing and spreading of the reactants is very important for reactive transport modelling in heterogeneous media. In homogeneous media, mixing and spreading are the same but different in heterogeneous media. The heterogeneities of the porous medium and spatial fluctuations of the flow field can distort the plume of the solute. On a time scale smaller than the time for mass transfer, these mechanisms will increase the spread of the solute but not mixing (Kitanidis, 1994). Although these mechanisms are coupled, they are often separated in heterogeneous media.

For instance, as spread leads to the spatial concentration gradient, it thus enhances diffusion and local dispersion, further enhancing mixing.

(Dentz et al., 2011b) mentioned that mixing controls the chances of reactants meeting in a flowing fluid. In a macroscopic description, the transport equation for two aqueous species is

$$\phi \frac{\partial c_j(x,t)}{\partial t} + \nabla \cdot (q(x) - D\nabla)c_j(x,t) = r(x,t) \qquad (2.53)$$

and reaction rate $r(x,t)$ is

$$r(x,t) = k_r(1 - \Omega) \qquad (2.54)$$

$$\Omega = \frac{c_1(x,t)c_2(x,t)}{K} \qquad (2.55)$$

where ϕ is porosity, q is specific discharge, D is the dispersion tensor (the reader is referred to the work of (Dentz et al., 2011b) for more description of the dispersion coefficient), and k_r is the kinetic rate constant.

For the continuum description here to hold, the two reactants must mix at a very fast rate compared to the reaction time scale. For such to happen requires that the microscopic Damkohler number $Da_{mic} = \tau_D^{mic}/\tau_r \ll 1$ with $\tau_D^{mic} = l_p^2/D_{mic}$; note that τ_r is the reaction time scale. The implication is that the reaction is very slow compared to the transport on a microscopic scale. They assumed that the time for changes in concentration due to bulk transport, τ_t, is greater than the reaction time, thus requiring that $Da = \tau_t/\tau_r \gg 1$. When

the Damkohler number is large, the system approaches equilibrium, which implies, saturation $\Omega = 1$. This means the mass action law for the bulk species concentrations, i.e. $c_1(x,t)c_2(x,t) = K$. In this limit, the reaction involving the two reactants is controlled by mixing.

(Kitanidis, 1994) characterised mixing in terms of entropy, defining the entropy of a continuous distribution $c(x,t)$ as

$$H(t) = -\int c(\boldsymbol{x},t)lnc(\boldsymbol{x},t) \qquad (2.56)$$

This quantifies the degree of disorderliness in the transport process, while $E(t) = \exp[-H(t)]$ is called the dilution index. He showed that the rate of change of dilution in the system with time is

$$\frac{d\,lnE(t)}{dt} = -\int \nabla ln\boldsymbol{c}(x,t)D\nabla ln\boldsymbol{c}(x,t)\,c(x,t) \qquad (2.57)$$

(Dentz et al., 2011b) identified this function as a measure of mixing of the system. The implication is that in the absence of diffusion and dispersion, the entropy corresponds to the entropy of the initial system. Hence, in the absence of dispersion, there is no mixing, and the system's entropy is not increasing. There is a decrease in the maximum concentration with mixing, and the concentration gradient becomes gentle. Thus, leading to decreased variability in concentration in the system.

(De Simoni et al., 2007) proposed a mixing ration-based formulation for multicomponent reactive transport. The goal of the proposed strategy is to evaluate the concentrations of the solute and reaction rates when mixing drives the equilibrium aqueous reactions and precipitation or dissolution of minerals. Their approach decouples the solute transport and

the speciation problems to ensure mixing ratios are estimated by solving the conservative transport equation and then using it in the general speciation models to obtain the concentrations of the reactants. The four-step strategy includes (1) evaluation of the mixing ratios, (2) evaluation of components, (3) speciation calculations, and (4) calculation of reaction rates.

For further reading on mixing in reactive transport modelling, the reader is referred to (De Simoni et al., 2007, Tartakovsky et al., 2009, Dentz et al., 2011b, Soler-Sagarra et al., 2022, Appelo and Postma, 2005), and other cited references by these authors for more details.

2.6 Reactive Transport Simulation in Nuclear Waste Disposal

One of the most challenging problems in the fields of geoscience and geological engineering is the disposal of radioactive wastes in the subsurface. In most disposal techniques, the multiple-barrier system, which consists of both natural and engineered materials, is employed. The goal of this system design is to prevent contact between the radioactive materials with the groundwater. Furthermore, reactive transport modelling is often used to understand and assess the existing coupling in the thermal, hydrological, and geochemical process present in this problem.

In some countries, burying the radioactive waste in the subsurface is the best long-term solution to prevent contact with humans or wildlife (Ewing et al., 2016). However, the barriers are often located close to where the wastes are generated, and a rock formation with very tight permeability is often sought after. As shown in Fig. (2.9), the waste is put into a sealed metallic container, usually made of copper or iron, surrounded by bentonite buffers to prevent or delay contact with the groundwater.
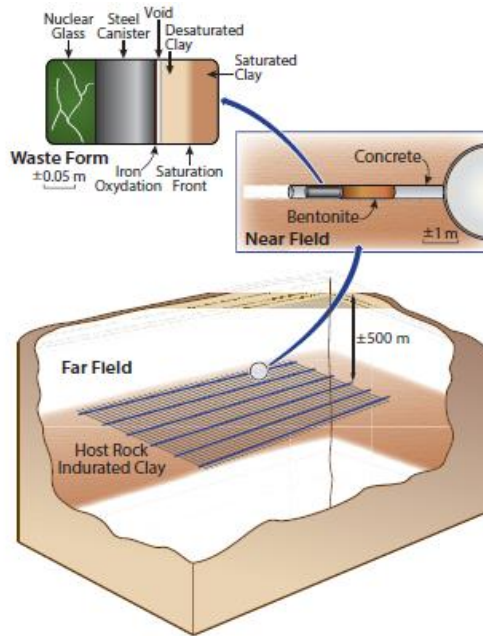
Figure 2.9: An illustration of the multiple-barrier system prototype typically adopted in geologic nuclear waste repositories (De Windt and Spycher, 2019).

The adjoining geological barrier helps prevent the movement of the contaminated wastes from the repository when there is a failure in the metallic barrier. Similarly, the geological barrier also inhibits the influx of harmful elements that can affect the system's integrity. These multi-layered barrier systems are often designed with very low permeability materials. In some cases, the metallic containers are plated or coated to prevent any chemically induced deterioration. The deployment of these strict measures prevents the mobilisation of the dangerous radioactive wastes and allows the radioactive isotopes to decay faster. It should be noted that the lifespans of these barriers depend primarily on the disposal concept. These barriers are designed to last for thousands of years, while the transport through the geological barrier may take hundreds of thousands of years.

High thermal loading can also affect the integrity of the barrier. Using a reactive transport model, (Spycher et al., 2003) investigated the waster tunnel in the volcanic tuffs at Yucca mountain, considering both thermal and hydrological mechanisms that can affect the barrier's integrity. This is a site located above the aquifer with fractured volcanic tuffs. Conducting reactive transport modelling, the fluid chemistry evolution and alteration of the minerals in the tunnel were investigated, considering cases above and below the water boiling point. The simulations were for hundred years and below the life expectancy of the repository. The simulation predicted that the fractures in the tunnels would be sealed by the precipitated minerals and consequently prevent the influx of liquid waste. Also, the simulations showed that the heat generated by the radioactive waste as it decays enhances the dissolution of the rock minerals. This led to the dissolution of the silica minerals at an elevated rate.

Considering the experiment conducted by (Salas et al., 2014) to investigate the evolution of the hydro-chemical process of the bentonite buffer in the radioactive waste repository, managed by the Apo Hard Rock Laboratory in Sweden, the same conditions in the KBS-3 repository, Fig. (2.10) were imposed. In this work, a vertical well was drilled, and a central heater is placed inside a tube made of copper and surrounded with compacted bentonite Fig. (2.10). The heater was used for representing the heat generated during the decay of the radioactive waste. Though 90 ^{0}C was the highest temperature reached in the KBS-3 repository, in the experiment at Apo laboratory, the heater was set to 130 ^{0}C at 2 m from bottom of the borehole. This high temperature was reached to assess the impact of extreme temperature on the repository. The equipment for the experiment was placed in a core-drilled borehole at a depth of 450 m below ground surface and lasted for six years. The compacted

bentonite was placed 100 mm between the copper tube and granite rock. In the course of the

first year, there was an increase in the temperature of the bentonite buffer and reached a

constant thermal gradient for the last five years of the experiment. During the heating

process, measurements of key variables such as temperature, water content, water pressure,

and the total pressure exerted were made every hour using sensors linked to a standard

computer system. All the sensors monitoring the humidity during the experiment indicated

a significant increase in moisture over 90% within the first year of the simulation, suggesting

that the bentonite was fully saturated with water during most of the experiment. The

temperature profile observed in this experiment is similar to that predicted by (Spycher et

al., 2003).
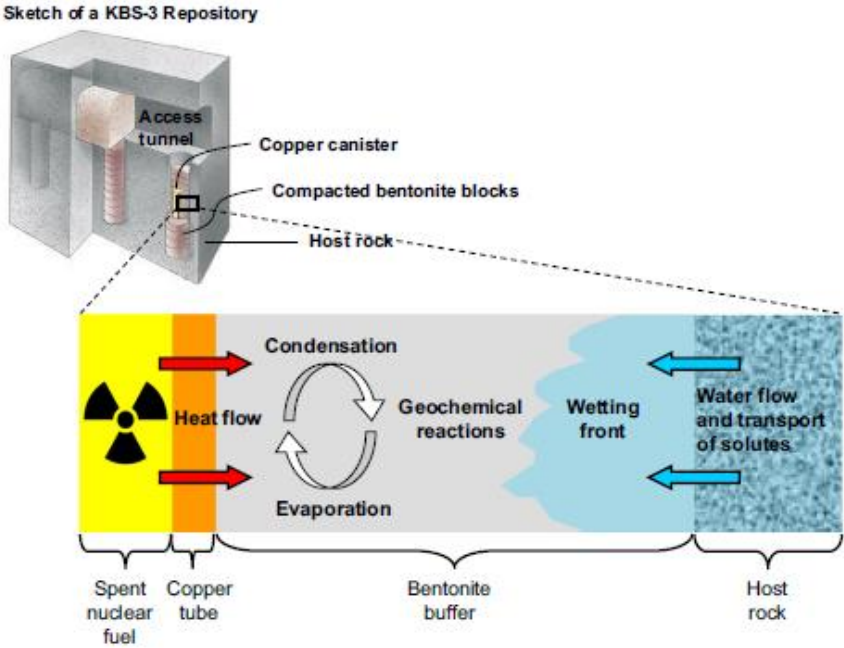
Figure 2.10: A sketch of the thermo-hydraulic geochemical and transport processes expected in the bentonite buffer of a KBS-3 repository (Salas et al., 2014).

The influences of temperature elevation and iron ions may also change the clay barrier's initial physical and chemical properties. In prior attempts (Perronnet, 2004, Guillaume, 2002) had conducted a laboratory experiment trying to investigate how the clay minerals are altered when in contact with steel. Using the information from these studies (and others) as the background, they simulated 100,000 years of simulated mass transport-reaction. The study predicted the variations of the minerals of the engineered barrier system, which was in contact with the fluid in the subsurface and iron-2 ions presented by the steel overpacks corrosion.

(Marty et al., 2010) investigated the potential long-term modification of the engineered bentonite barrier in France's underground radioactive waste repository using reactive transport modelling. In the design, a multiple-barrier system was used to separate the radioactive waste from the Callovo-Oxfordian clay host rock. It was expected that after the closure of this facility, the dry barrier would be saturated with groundwater, which may alter the physical and chemical properties of the chosen clay material (MX-80 bentonite).

(Montarnal et al., 2007) assessed the safety conditions of the nuclear waste repositories through the predictions of the migrations of radionuclides and chemical species through the barrier and rock. In the experiment, water was at equilibrium with the atmospheric oxygen and was allowed to infiltrate an aquifer with a 2.5 m/year constant vertical flow velocity and leached a zone with enriched uraninite subsystems. Based on the data collected, the initial chemical compositions of the aquifer and soil were different, having high contents of sulphide and ammonium in the underground porewater. To validate the simulation results, an inert tracer was first used. All calculations were also performed in NaCl 10^{-3} M media for

constant ionic strength. Moreover, an inert tracer that was taken as tritiated water was injected from the surface to estimate the depth of penetration of the dissolved oxygen. Finally, using the reactive transport modelling approach, the transport phenomenon through the porous rock and the chemical mechanisms driving the movement of the radionuclides were integrated. Through these coupled processes, the uranium migration through a porous medium with different redox conditions became the crux of the study.

Measurements conducted in a site polluted with uraninite showed an increase in the dissolved uranium concentration in winter and a decrease in summer due to porewater composition and variations of redox conditions. Similar deviations were also observed with sulphur and nitrogen speciation – sulphide and ammonium ions were found in summer, while thiosulphate, sulphate, and nitrate ions were seen in winter. Furthermore, when ammonium or sulphide ions were present initially, the oxygen was consumed instantaneously by the nitrate-producing reaction, sulphate, and thiosulfate ions. And the acidification process accompanied the oxidation reactions also. When ammonium and sulphide ions were both present initially, the sulphur reacted first with oxygen to form thiosulfate and sulphate, which led to the presence of two separate Eh zones. When uranium only was considered, the maximum uranium concentration was close to 10^{-7} mol/L. However, when nitrogen and sulphur were induced, the maximum uranium content increased to 10^{-5} mol/L.

(Shao et al., 2013) investigated the clogging process at the Maqarin natural analogue site in Jordan using reactive transport modelling. The site has been used as a natural analogue for 30 years to investigate the evolution of materials in contact with hyper alkaline solutions.

The numerical simulation studied the localised geochemical alterations and porosity evolution as the hyper-alkaline solution contacted the Maqarin marl rock. In the geochemical setup, the mineralogy of the rock and pore water were calibrated to the field measurements. In the experiment, zeolite minerals, a material that can simulate ion exchange processes, were used. It was observed in the experiment that clogging of the pores occurred at 5-10 mm from the location of contact with the alkaline solution after several hundreds of years. The formation of the precipitates ettringite and C-S-H minerals was responsible for this clogging. They further conducted sensitivity studies on the diffusion coefficient, Archie's exponent, and the available surfaces for mineral dissolution and precipitation. In these studies, they also discovered that the availability of Al required for the precipitation of ettringite and C-S-H phase is strongly dependent on the clay minerals dissolution. Therefore, it was concluded that the clay minerals dissolution controls how porosity evolves. And the cation exchange or formation of zeolite minerals has little or no influence on the geochemical development of the system.

Other relevant studies demonstrating the application of reactive transport modelling in radioactive waste storage include (Idiart et al., 2020, Nasir et al., 2014, Trotignon et al., 2007). The reader can check these references for more details.

2.7 Conclusion

The homogeneous and heterogeneous reactions of biochemical species in dissolution in the liquid phase are partly responsible for making complicated reactive transport simulations in porous media. Using Pe and Da, the relative significance of advection, reactions, and molecular diffusion can be quantified. Establishing sufficient conditions where macroscopic scale equations for coupled advection, dispersion, and reaction process adequately provides

a description of the processes at pore-scale has been done by using multiple-scale expansions in upscaling the pore-scale equations to the macroscopic scale while entering the reactions through a boundary condition on the interfaces between the fluid and solid phases. The volume averaging method has also been used to achieve the same results observed in the multiple-scale expansions approach. The phase diagrams developed through these techniques revealed that these transport processes occurring at the pore-scale are quite difficult to describe by macroscopic approaches. On these bases, the governing assumptions and approximations on which the macroscopic models are based cannot be ascertained a priori. In transport regimes, where continuum equations break down, the use of nonlocal or hybrid pore-scale/continuum-scale models is valid. These models present rigorous frameworks compared to the traditional upscaled models that are based on developing closure approximations.

Despite the inherent challenges of evolving relevant parameters that describe the properties of the evolving media in the macroscale approach, the quantitative analysis of the reactive transport has been successful. In addition, the use of hybrid approaches has provided the necessary tools to further understand reactive transport processes in porous media. However, it is worth noting that the empirical correlations are not for physically representing the exact pore-scale processes. Hence, these relationships would not lead to a comprehensive process-based assessment of the experimental observations. Nevertheless, there is sufficient understanding to model specific processes through these empirical correlations.

It should be noted that PNM can be applied to any length scale where the pore space structure has been experimentally observed and analysed. The key elements of the PNM approach, sites, and bonds can be abstract but are relatable to the measurable features in various ways,

depending on the available information. It is possible to extract individual pore networks at each length scale and integrate it into a single multiscale network by characterising the cross-scale link structure between these networks. In the upscaling of reactive transport processes from microscopic to macroscopic scales, pore network models have proven to be an effective research tool. Despite the attractiveness and successful applications of PNMs, successfully simulate transport processes demands adequate representation of the actual porous media, which is quite challenging in this modelling approach because these models simplify the pore geometry. Also, the representation of microscopic features is difficult to be described by pore network models explicitly.

In both naturally occurring or man-made systems, the pore structures can be significantly modified during dissolution and precipitation in porous media. Using reactive transport modelling on these occasions has been successful. Finally, a summary table of the different modelling approaches is presented below (Table 2.1) with their capabilities, applications, and limitations.

2.8 Summary for the Overall Design of this Research

Modelling reactive transport in an evolving porous medium is challenging and requires more innovative scientific methods. Because of the immense heterogeneities in the media, the application of continuum-scaled models for describing effective transport properties and reactive processes in evolving porous media poses a significant challenge.

Accurately describing the porous media's effective porosity with reaction and transport properties is essential in key simulations, such as breakthrough curves and concentration distributions of the minerals. Several relationships have been developed in correlating

transport properties with porosity, but predictions of the transport properties from these relationships differ, in some cases, by several orders of magnitude. Furthermore, the evolution of identical systems may occur, even when the evolution of the transport properties occurs differently. More so, it is often possible that as the pore structure evolves, there are evolutions in the relationships linking the transport parameters and porosity. Finally, it is worth noting that pore-scale processes primarily impact porous media evolution, and there are likely variations in mineralogical compositions and reactivities, limiting the predictive power of these models to describe the evolutions of porosity, permeability, tortuosity and reactivity. Therefore, it is critical to identify the limits of these models based on data observed in each case to allow possible extrapolation to cases beyond the limits of the observed data for each specific material and process. Although some theoretical frameworks have been developed to address some of these issues, models describing the evolution of reactivity and transport parameters are mostly empirical. Nevertheless, most of these empirical relationships are power law-like and have been helpful in quantitatively interpreting observations as porous media evolve.

Table 2.1: A summary of the different modelling methods.

Modelling scale	Methods	Capabilities	Limitations
Pore scale	Level set	1. Coupling flow, transport, and evolution of porous media properties. 2. Applicable to large-scale natural and man-induced processes. 3. Simulation of complex surface motions without domain parametrization.	1. Demands high computing time and limited pore volumes. 2. The interface is constrained by the defined length function.
	Lattice Boltzmann	1. Coupling flow, transport, and evolution of porous media properties. 2. Applicable to large-scale natural and man-induced processes. 3. Able to simulate multicomponent transport problems with large chemical species. 4. Simple calculation procedure 5. Efficient when implementing for parallel computation. Robust in handling complex geometries.	1. Schemes with higher dimensions with more velocity directions are computationally expensive. 2. There is no consistent thermo-hydrodynamic scheme. 3. High-Mach number flows are difficult to implement.
	Finite Element Method	1. Coupling flow, transport, and evolution of porous media properties. 2. Applicable to large-scale natural and man-induced processes. 3. Able to model complex geometries. 4. Provide high accurate results even for very complex geometries. 5. Ease of incorporating boundary conditions. 6. Material heterogeneity can be easily implemented. 7. Ability to implement higher order elements.	1. High computing time for complex geometries with fine meshes. 2. Accuracy of the results is highly dependent on mesh size.
	Smoothed Particle Hydrodynamics (SPH)	1. Coupling flow, transport, and evolution of porous media properties. 2. Applicable to large-scale natural and man-induced processes. 3. Triviality of treating interfacial problems. 4. Advection, diffusion, and reaction equations in the Lagrangian framework are reduced to diffusion and reaction equations. 5. Numerical diffusion is eliminated. 6. Provide superior advantage over grid-based methods when simulating multiphase or multicomponent transport problems.	1. High computation cost compared to grid-based methods. 2. Difficulty in using higher-order discretization schemes unlike mesh-based methods.
Meso scale	Pore Network Modelling (PNM)	1. Ease of implementing material heterogeneity. 2. Provides an affordable computational tool and a reduced impact on the numerical simulations as the pore volume is increased unlike other techniques. 3. Able to simulate multiphase and single-phase flow in porous media.	1. They are constructed with simplifying assumptions of the pore geometry. 2. The governing assumption can make the predictions less accurate. 3. The challenge of identifying the critical features relevant to the process of interest.

Scale	Method	Advantages	Limitations
REV scale	Finite Element Method	1. Coupling flow, transport, and evolution of porous media properties. 2. Applicable to large-scale natural and man-induced processes. 3. Able to model complex geometries. 4. Provide high accurate results even for very complex geometries. 5. Ease of incorporating boundary conditions. 6. Material heterogeneity can be easily implemented. 7. Ability to implement higher order elements.	1. High computing time for complex geometries with fine meshes. 2. Accuracy of the results is highly dependent on mesh size.
	Finite Volume Method	1. Applicable to simulating multiphase or multicomponent reactive transport in both saturated and unsaturated porous media. 2. Captures the appearance and disappearance of phases in multiphase flow problems. 3. The method enforces the conservation of the field variables after discretization. 4. It can be used on unstructured grids. 5. Uses arbitrary meshes for complex geometries. 6. The discontinuities of coefficients are overcome, provided the mesh is chosen such that the discontinuities occur on the boundaries of the control volume. 7. Computationally inexpensive and robust for highly nonlinear systems of hyperbolic equations.	1. Not applicable to highly localized processes in porous media. 2. Great effort is required when the geometry is not regular.
Macro scale	Mixed Finite Element	1. All capabilities of FEM mentioned above. 2. Applicable to problems where the primal-based methods are impractical.	1. It requires more degrees of freedom than the displacement FEM. 2. Its discrete system is indefinite since the mixed variational principal is a saddle point, as a result several matrix solution methods, direct and iterative methods, cannot be used with this technique. 3. Subject to numerical instabilities not observed with standard displacement methods.
	Upscaled SPH	Same as SPH above.	Same as SPH above
	Hybrid Methods	1. Provides significant speed-up in simulations where pore-scale simulations are localized in the computational domain. 2. Provides a great benefit when the interfacial region of interest is very small compared to the entire domain.	The limitations of the mixed methods apply.

References

1. ADLER, P. & THOVERT, J.-F. 1998. Real porous media: Local geometry and macroscopic properties.

2. AJAYI, T. & GUPTA, I. 2019. A review of reactive transport modeling in wellbore integrity problems. *Journal of Petroleum Science and Engineering,* 175**,** 785-803.

3. AKANJI, L. T. & MATTHAI, S. K. 2010. Finite element-based characterization of pore-scale geometry and its impact on fluid flow. *Transport in porous media,* 81**,** 241-259.

4. AKANNI, K., EVANS, J. & ABRAMSON, I. 1987. Effective transport coefficients in heterogeneous media. *Chemical engineering science,* 42**,** 1945-1954.

5. ALEXANDER, F. J., GARCIA, A. L. & TARTAKOVSKY, D. M. 2002. Algorithm refinement for stochastic partial differential equations: I. Linear diffusion. *Journal of Computational Physics,* 182**,** 47-66.

6. ALLISON, J., KEVIN, J., GRADAC, N. & BROWN, D. S. 1991. *MINTEQA2: A Geochemical Assessment Model for Environmental Systems: Version 3.0 User's Manual*, National Technical Information Service.

7. APPELO, C. & POSTMA, D. J. B., ROTERDAM 2005. Geochemistry, groundwater and pollution, CRC.

8. ARBOGAST, T., BRYANT, S., DAWSON, C., SAAF, F., WANG, C. & WHEELER, M. 1996. Computational methods for multiphase flow and reactive transport problems arising in subsurface contaminant remediation. *Journal of Computational and Applied Mathematics,* 74**,** 19-32.

9. ARBOGAST, T. & WHEELER, M. F. 1995. A characteristics-mixed finite element method for advection-dominated transport problems. *SIAM Journal on Numerical analysis,* 32**,** 404-424.

10. ARBOGAST, T., WHEELER, M. F. & YOTOV, I. Logically rectangular mixed methods for groundwater flow and transport on general geometry. in Computational Methods in Water Resources X, 1994. Citeseer.

11. ARNOLD, D. N. 1982. An interior penalty finite element method with discontinuous elements. *SIAM journal on numerical analysis,* 19**,** 742-760.

12. ATKINSON, A., EVERITT, N. & GUPPY, R. 1987. Evolution of pH in a radwaste repository: Experimental simulation of cement leaching. UKAEA Harwell Lab.(UK). Materials Development Div.

13. BAKKE, S. & ØREN, P.-E. 1997. 3-D pore-scale modelling of sandstones and flow simulations in the pore networks. *Spe Journal,* 2**,** 136-149.

14. BALHOFF, M. T. & WHEELER, M. F. 2009. A predictive pore-scale model for non-Darcy flow in porous media. *SPE Journal,* 14**,** 579-587.

15. BATTIATO, I. & TARTAKOVSKY, D. 2011. Applicability regimes for macroscopic models of reactive transport in porous media. *Journal of contaminant hydrology,* 120**,** 18-26.

16. BATTIATO, I., TARTAKOVSKY, D. M., TARTAKOVSKY, A. M. & SCHEIBE, T. 2009. On breakdown of macroscopic models of mixing-controlled heterogeneous reactions in porous media. *Advances in water resources,* 32**,** 1664-1673.

17. BATTIATO, I., TARTAKOVSKY, D. M., TARTAKOVSKY, A. M. & SCHEIBE, T. D. 2011. Hybrid models of reactive transport in porous and fractured media. *Advances in Water Resources,* 34**,** 1140-1150.

18. BEAR, J. 1988. *Dynamics of fluids in porous media*, Courier Corporation.

19. BEKRI, S., THOVERT, J. & ADLER, P. 1995. Dissolution of porous media. *Chemical Engineering Science,* 50**,** 2765-2791.

20. BEKRI, S. & VIZIKA, O. Proceeding of the International Symposium of the Society of Core Analysts. 2006. SCA.

21. BETHKE, C. 1996. *Geochemical reaction modeling: Concepts and applications*, Oxford University Press on Demand.

22. BETHKE, C. M. 2022. *Geochemical and biogeochemical reaction modeling*, Cambridge university press.

23. BHATHNAGOR, P., GROSS, E. & KROOK, M. 1954. A model for collision processes in gases. *Physical Review,* 94**,** 511.

24. BIRK, S., LIEDL, R., SAUTER, M. & TEUTSCH, G. 2003. Hydraulic boundary conditions as a controlling factor in karst genesis: A numerical modeling study on artesian conduit development in gypsum. *Water Resources Research,* 39**,** SBH 2-1-SBH 2-14.

25. BIRK, S., LIEDL, R., SAUTER, M. & TEUTSCH, G. 2005. Simulation of the development of gypsum maze caves. *Environmental Geology,* 48**,** 296-306.

26. BLUNT, M. J., BIJELJIC, B., DONG, H., GHARBI, O., IGLAUER, S., MOSTAGHIMI, P., PALUSZNY, A. & PENTLAND, C. 2013. Pore-scale imaging and modelling. *Advances in Water resources,* 51**,** 197-216.

27. BLUNT, M. J., JACKSON, M. D., PIRI, M. & VALVATNE, P. H. 2002. Detailed physics, predictive capabilities and macroscopic consequences for pore-network models of multiphase flow. *Advances in Water Resources,* 25**,** 1069-1089.

28. BROVELLI, A., MALAGUERRA, F. & BARRY, D. A. 2009. Bioclogging in porous media: Model development and sensitivity to initial conditions. *Environmental Modelling & Software,* 24**,** 611-626.

29. BRUNET, J.-P. L., LI, L., KARPYN, Z. T., KUTCHKO, B. G., STRAZISAR, B. & BROMHAL, G. 2013. Dynamic evolution of cement composition and transport properties under conditions relevant to geological carbon sequestration. *Energy & Fuels,* 27**,** 4208-4220.

30. BRYANT, S. & BLUNT, M. 1992. Prediction of relative permeability in simple porous media. *Physical review A,* 46**,** 2004.

31. BRYANT, S. L., KING, P. R. & MELLOR, D. W. 1993a. Network model evaluation of permeability and spatial correlation in a real random sphere packing. *Transport in porous media,* 11**,** 53-70.

32. BRYANT, S. L., MELLOR, D. W. & CADE, C. A. 1993b. Physically representative network models of transport in porous media. *AIChE Journal,* 39**,** 387-396.

33. BULTREYS, T., VAN HOOREBEKE, L. & CNUDDE, V. 2015. Multi-scale, micro-computed tomography-based pore network models to simulate drainage in heterogeneous rocks. *Advances in Water Resources,* 78**,** 36-49.

34. BUSCHECK, T., GLASCOE, L., LEE, K., GANSEMER, J., SUN, Y. & MANSOOR, K. 2003. Validation of the multiscale thermohydrologic model used for analysis of a proposed repository at Yucca Mountain. *Journal of contaminant hydrology,* 62**,** 421-440.

35. BUSCHECK, T., HAO, Y., MORRIS, J. & BURTON, E. 2009. Thermal-hydrological sensitivity analysis of underground coal gasification. Lawrence Livermore National Lab.(LLNL), Livermore, CA (United States).

36. BUSCHECK, T. A., SUN, Y. & HAO, Y. 2006. Multiscale Thermohydrologic Model Supporting the Licence Application for the Yucca Mountain Repository. Yucca Mountain Project, Las Vegas, Nevada.

37. CHAGNEAU, A., CLARET, F., ENZMANN, F., KERSTEN, M., HECK, S., MADÉ, B. & SCHÄFER, T. 2015. Mineral precipitation-induced porosity reduction and its effect on transport parameters in diffusion-controlled porous media. *Geochemical transactions,* 16**,** 1-16.

38. CHEN, Z. & CHEN, H. 2004. Pointwise error estimates of discontinuous Galerkin methods with penalty for second-order elliptic problems. *SIAM Journal on Numerical Analysis,* 42**,** 1146-1166.

39. CHOU, H., WU, L., ZENG, L. & CHANG, A. 2012. Evaluation of solute diffusion tortuosity factor models for variously saturated soils. *Water Resources Research,* 48.

40. CHRISTIE, M. A. 1996. Upscaling for reservoir simulation. *Journal of petroleum technology,* 48**,** 1,004-1,010.

41. COCKBURN, B., KARNIADAKIS, G. E. & SHU, C.-W. 2000. The development of discontinuous Galerkin methods. *Discontinuous Galerkin Methods.* Springer.

42. D'HUMIERES, D. & LALLEMAND, P. 1987. Numerical simulations of hydrodynamics with lattice gas automata in two dimensions. *Complex Systems,* 1**,** 599-632.

43. DAI, Z. & SAMPER, J. 2004. Inverse problem of multicomponent reactive chemical transport in porous media: Formulation and applications. *Water Resources Research,* 40.

44. DAUZÈRES, A., DE WINDT, L., SAMMALJÄRVI, J., BARTIER, D., TECHER, I., DETILLEUX, V. & SIITARI-KAUPPI, M. 2019. Mineralogical and microstructural evolution of Portland cement paste/argillite interfaces at 70° C–Considerations for diffusion and porosity properties. *Cement and Concrete Research,* 115**,** 414-425.

45. DAUZERES, A., LE BESCOP, P., SARDINI, P. & COUMES, C. C. D. 2010. Physico-chemical investigation of clayey/cement-based materials interaction in the context of geological waste disposal: Experimental approach and results. *Cement and Concrete Research,* 40**,** 1327-1340.

46. DAVAL, D., MARTINEZ, I., CORVISIER, J., FINDLING, N., GOFFÉ, B. & GUYOT, F. 2009. Carbonation of Ca-bearing silicates, the case of wollastonite: Experimental investigations and kinetic modeling. *Chemical Geology,* 265**,** 63-78.

47. DAWSON, C. 1993. Godunov-mixed methods for advection-diffusion equations in multidimensions. *SIAM Journal on Numerical Analysis,* 30**,** 1315-1332.

48. DAWSON, C. 1995. High resolution upwind-mixed finite element methods for advection-diffusion equations with variable time-stepping. *Numerical Methods for Partial Differential Equations,* 11**,** 525-538.

49. DAWSON, C., SUN, S. & WHEELER, M. F. 2004. Compatible algorithms for coupled flow and transport. *Computer Methods in Applied Mechanics and Engineering,* 193**,** 2565-2580.

50. DE CAPITANI, C. & BROWN, T. H. 1987. The computation of chemical equilibrium in complex systems containing non-ideal solutions. *Geochimica et Cosmochimica Acta,* 51**,** 2639-2652.

51. DE SIMONI, M., CARRERA, J., SANCHEZ-VILA, X. & GUADAGNINI, A. 2005. A procedure for the solution of multicomponent reactive transport problems. *Water resources research,* 41.

52. DE SIMONI, M., SANCHEZ-VILA, X., CARRERA, J. & SAALTINK, M. 2007. A mixing ratios-based formulation for multicomponent reactive transport. *Water Resources Research,* 43.

53. DE WINDT, L. & BADREDDINE, R. 2007. Modelling of long-term dynamic leaching tests applied to solidified/stabilised waste. *Waste management,* 27**,** 1638-1647.

54. DE WINDT, L., BURNOL, A., MONTARNAL, P. & VAN DER LEE, J. 2003. Intercomparison of reactive transport models applied to UO2 oxidative dissolution and uranium migration. *Journal of contaminant hydrology,* 61**,** 303-312.

55. DE WINDT, L. & SPYCHER, N. F. 2019. Reactive transport modeling: a key performance assessment tool for the geologic disposal of nuclear waste. *Elements: An International Magazine of Mineralogy, Geochemistry, and Petrology,* 15**,** 99-102.

56. DENG, H., MOLINS, S., STEEFEL, C., DEPAOLO, D., VOLTOLINI, M., YANG, L. & AJO-FRANKLIN, J. 2016. A 2.5 D reactive transport model for fracture alteration simulation. *Environmental science & technology,* 50**,** 7564-7571.

57. DENG, H., MOLINS, S., TREBOTICH, D., STEEFEL, C. & DEPAOLO, D. 2018. Pore-scale numerical investigation of the impacts of surface roughness: Upscaling of reaction rates in rough fractures. *Geochimica et Cosmochimica Acta,* 239**,** 374-389.

58. DENG, H. & SPYCHER, N. 2019. Modeling reactive transport processes in fractures. *Reviews in Mineralogy and Geochemistry,* 85**,** 49-74.

59. DENTZ, M., GOUZE, P. & CARRERA, J. 2011a. Effective non-local reaction kinetics for transport in physically and chemically heterogeneous media. *Journal of contaminant hydrology,* 120**,** 222-236.

60. DENTZ, M., LE BORGNE, T., ENGLERT, A. & BIJELJIC, B. 2011b. Mixing, spreading and reaction in heterogeneous media: A brief review. *Journal of contaminant hydrology,* 120**,** 1-17.

61. DOBSON, K. J., COBAN, S. B., MCDONALD, S. A., WALSH, J. N., ATWOOD, R. C. & WITHERS, P. J. 2016. 4-D imaging of sub-second dynamics in pore-scale processes using real-time synchrotron X-ray tomography. *Solid Earth,* 7**,** 1059-1073.

62. DOBSON, P. F., KNEAFSEY, T. J., SONNENTHAL, E. L., SPYCHER, N. & APPS, J. A. 2003. Experimental and numerical simulation of dissolution and precipitation: implications for fracture sealing at Yucca Mountain, Nevada. *Journal of Contaminant Hydrology,* 62**,** 459-476.

63. DONADO, L. D., SANCHEZ-VILA, X., DENTZ, M., CARRERA, J. & BOLSTER, D. 2009. Multicomponent reactive transport in multicontinuum media. *Water resources research,* 45.

64. EFENDIEV, Y. & DURLOFSKY, L. J. 2003. A generalized convection-diffusion model for subgrid transport in porous media. *Multiscale Modeling & Simulation,* 1**,** 504-526.

65. ELLIS, S. R. & WRIGHT, J. L. 2006. Modeling of aqueous transport in rigid porous matrices near the percolation threshold. *Pharmaceutical research,* 23**,** 2441-2453.

66. EMMANUEL, S., AGUE, J. J. & WALDERHAUG, O. 2010. Interfacial energy effects and the evolution of pore size distributions during quartz precipitation in sandstone. *Geochimica et Cosmochimica Acta,* 74**,** 3539-3552.

67. EMMANUEL, S., ANOVITZ, L. M. & DAY-STIRRAT, R. J. 2015. Effects of coupled chemo-mechanical processes on the evolution of pore-size distributions in geological media. *Reviews in Mineralogy and Geochemistry,* 80**,** 45-60.

68. EMMANUEL, S. & BERKOWITZ, B. 2007. Effects of pore-size controlled solubility on reactive transport in heterogeneous rock. *Geophysical Research Letters,* 34.

69. ERIKSSON, G. & HACK, K. 1990. ChemSage—a computer program for the calculation of complex chemical equilibria. *Metallurgical transactions B,* 21**,** 1013-1023.

70. EWING, R. C., WHITTLESTON, R. A. & YARDLEY, B. W. 2016. Geological disposal of nuclear waste: a primer. *Elements,* 12**,** 233-237.

71. EZEUKO, C., SEN, A., GRIGORYAN, A. & GATES, I. 2011. Pore-network modeling of biofilm evolution in porous media. *Biotechnology and bioengineering,* 108**,** 2413-2423.

72. FATT, I. 1956. The network model of porous media. *Transactions of the AIME,* 207**,** 144-181.

73. FLEKKØY, E. 1993. Lattice Bhatnagar-Gross-Krook models for miscible fluids. *Physical Review E,* 47**,** 4247.

74. GALÍNDEZ, J., MOLINERO, J., SAMPER, J. & YANG, C. Simulating concrete degradation processes by reactive transport models. Journal de Physique IV (Proceedings), 2006. EDP sciences, 177-188.

75. GAO, D., TIAN, F.-B., CHEN, Z. & ZHANG, D. 2017a. An improved lattice Boltzmann method for solid-liquid phase change in porous media under local thermal non-equilibrium conditions. *International Journal of Heat and Mass Transfer,* 110**,** 58-62.

76. GAO, J., XING, H., TIAN, Z., PEARCE, J. K., SEDEK, M., GOLDING, S. D. & RUDOLPH, V. 2017b. Reactive transport in porous media for CO2 sequestration: Pore scale modeling using the lattice Boltzmann method. *Computers & Geosciences,* 98**,** 9-20.

77. GAUCHER, E. C. & BLANC, P. 2006. Cement/clay interactions – A review: Experiments, natural analogues, and modeling. *Waste Management,* 26**,** 776-788.

78. GENS, A., GUIMARÄES, L. D. N., OLIVELLA, S., SÁNCHEZ, M. J. J. O. R. M. & ENGINEERING, G. 2010. Modelling thermo-hydro-mechano-chemical interactions for nuclear waste disposal. 2**,** 97-102.

79. GEORGET, F., PRÉVOST, J. H. & HUET, B. 2018. Impact of the microstructure model on coupled simulation of drying and accelerated carbonation. *Cement and concrete research,* 104**,** 1-12.

80. GOUZE, P. & COUDRAIN-RIBSTEIN, A. 2002. Chemical reactions and porosity changes during sedimentary diagenesis. *Applied geochemistry,* 17**,** 39-47.

81. GUILLAUME, D. 2002. Experimental study of the iron-smectite system in the presence of a solution at 80 at 300 deg. Nancy-1 Univ. Henri Poincare.

82. GUIMERÀ, J., DURO, L., JORDANA, S. & BRUNO, J. 1999. Effects of ice melting and redox front migration in fractured rocks of low permeability.

83. HAO, L., ZHANG, S., DONG, J. & KE, W. 2012a. Evolution of corrosion of MnCuP weathering steel submitted to wet/dry cyclic tests in a simulated coastal atmosphere. *Corrosion science,* 58**,** 175-180.

84. HAO, Y., SUN, Y. & NITAO, J. 2012b. Overview of NUFT: A versatile numerical model for simulating flow and reactive transport in porous media. *Groundwater Reactive Transport Models***,** 212-239.

85. HARRISON, A., DIPPLE, G., SONG, W., POWER, I., MAYER, K., BEINLICH, A. & SINTON, D. 2017. Changes in mineral reactivity driven by pore fluid mobility in partially wetted porous media. *Chemical Geology,* 463**,** 1-11.

86. HARRISON, A. L., DIPPLE, G. M., POWER, I. M. & MAYER, K. U. 2016. The impact of evolving mineral–water–gas interfacial areas on mineral–fluid reaction rates in unsaturated porous media. *Chemical Geology,* 421**,** 65-80.

87. HARTMANN, A., GOLDSCHEIDER, N., WAGENER, T., LANGE, J. & WEILER, M. 2014. Karst water resources in a changing world: Review of hydrological modeling approaches. *Reviews of Geophysics,* 52**,** 218-242.

88. HE, X., LI, N. & GOLDSTEIN, B. 2000. Lattice Boltzmann simulation of diffusion-convection systems with surface chemical reaction. *Molecular Simulation,* 25**,** 145-156.

89. HE, X. & LUO, L.-S. 1997. Theory of the lattice Boltzmann method: From the Boltzmann equation to the lattice Boltzmann equation. *Physical review E,* 56**,** 6811.

90. HERBERT, H.-J., KASBOHM, J., SPRENGER, H., FERNÁNDEZ, A. M. & REICHELT, C. 2008. Swelling pressures of MX-80 bentonite in solutions of different ionic strength. *Physics and Chemistry of the Earth, Parts A/B/C,* 33**,** S327-S342.

91. HEßE, F., RADU, F. A., THULLNER, M. & ATTINGER, S. 2009. Upscaling of the advection–diffusion–reaction equation with Monod reaction. *Advances in water resources,* 32**,** 1336-1351.

92. HIORTH, A., JETTESTUEN, E., CATHLES, L. & MADLAND, M. 2013. Precipitation, dissolution, and ion exchange processes coupled with a lattice Boltzmann advection diffusion solver. *Geochimica et Cosmochimica Acta,* 104**,** 99-110.

93. HOMMEL, J., COLTMAN, E. & CLASS, H. 2018. Porosity–permeability relations for evolving pore space: a review with a focus on (bio-) geochemically altered porous media. *Transport in Porous Media,* 124**,** 589-629.

94. HOUBEN, G. 2003. Iron oxide incrustations in wells. Part 1: genesis, mineralogy and geochemistry. *Applied Geochemistry,* 18**,** 927-939.

95. HUBER, C., SHAFEI, B. & PARMIGIANI, A. 2014. A new pore-scale model for linear and non-linear heterogeneous dissolution and precipitation. *Geochimica et Cosmochimica Acta,* 124**,** 109-130.

96. HUET, B. M., PREVOST, J. H. & SCHERER, G. W. 2010. Quantitative reactive transport modeling of Portland cement in CO2-saturated water. *International Journal of Greenhouse Gas Control,* 4**,** 561-574.

97. IDIART, A., LAVIÑA, M., KOSAKOWSKI, G., COCHEPIN, B., MEEUSSEN, J. C., SAMPER, J., MON, A., MONTOYA, V., MUNIER, I. & POONOOSAMY, J. 2020. Reactive transport modelling of a low-pH concrete/clay interface. *Applied Geochemistry,* 115**,** 104562.

98. IOANNIDIS, M. & CHATZIS, I. 2000. On the geometry and topology of 3D stochastic porous media. *Journal of colloid and interface science,* 229**,** 323-334.

99. JACQUEMET, N., PIRONON, J., LAGNEAU, V. & SAINT-MARC, J. 2012. Armouring of well cement in H2S–CO2 saturated brine by calcite coating–Experiments and numerical modelling. *Applied geochemistry,* 27**,** 782-795.

100.   JEEN, S.-W., MAYER, K. U., GILLHAM, R. W. & BLOWES, D. W. 2007. Reactive transport modeling of trichloroethene treatment with declining reactivity of iron. *Environmental science & technology,* 41**,** 1432-1438.

101.   JENNI, A., GIMMI, T., ALT-EPPING, P., MÄDER, U. & CLOET, V. 2017. Interaction of ordinary Portland cement and Opalinus Clay: Dual porosity modelling compared to experimental data. *Physics and Chemistry of the Earth, Parts A/B/C,* 99**,** 22-37.

102.   JIANG, Z., VAN DIJKE, M., SORBIE, K. S. & COUPLES, G. D. 2013. Representation of multiscale heterogeneity via multiscale pore networks. *Water resources research,* 49**,** 5437-5449.

103.   JIN, L., MATHUR, R., ROTHER, G., COLE, D., BAZILEVSKAYA, E., WILLIAMS, J., CARONE, A. & BRANTLEY, S. 2013. Evolution of porosity and geochemistry in Marcellus Formation black shale during weathering. *Chemical Geology,* 356**,** 50-63.

104.   JUNG, H. & NAVARRE-SITCHLER, A. 2018. Physical heterogeneity control on effective mineral dissolution rates. *Geochimica et cosmochimica Acta,* 227**,** 246-263.

105.   KANG, Q., LICHTNER, P. C. & JANECKY, D. R. 2010. Lattice Boltzmann method for reacting flows in porous media. *Adv. Appl. Math. Mech,* 2**,** 545-563.

106.   KANG, Q., LICHTNER, P. C. & ZHANG, D. 2006. Lattice Boltzmann pore-scale model for multicomponent reactive transport in porous media. *Journal of Geophysical Research: Solid Earth,* 111.

107.   KANG, Q., LICHTNER, P. C. & ZHANG, D. 2007. An improved lattice Boltzmann model for multicomponent reactive transport in porous media at the pore scale. *Water Resources Research,* 43.

108.   KARAKASHIAN, O. A. & PASCAL, F. 2003. A posteriori error estimates for a discontinuous Galerkin approximation of second-order elliptic problems. *SIAM Journal on Numerical Analysis,* 41**,** 2374-2399.

109.   KARPOV, I., CHUDNENKO, K., BYCHINSKII, V., KULIK, D. & AVCHENKO, O. 2001. Minimization of Gibbs free energy in geochemical systems by convex programming.

110.   KARPOV, I. K., CHUDNENKO, K. V. & KULIK, D. A. 1997. Modeling chemical mass transfer in geochemical processes; thermodynamic relations, conditions of equilibria and numerical algorithms. *American Journal of Science,* 297**,** 767-806.

111.   KARPOV, I. K., CHUDNENKO, K. V., KULIK, D. A. & BYCHINSKII, V. A. 2002. The convex programming minimization of five thermodynamic potentials other than Gibbs energy in geochemical modeling. *American Journal of Science,* 302**,** 281-311.

112.   KASZUBA, J. P., JANECKY, D. R. & SNOW, M. G. 2005. Experimental evaluation of mixed fluid reactions between supercritical carbon dioxide and NaCl brine: Relevance to the integrity of a geologic carbon repository. *Chemical Geology,* 217**,** 277-293.

113.   KIM, D. S. & FOGLER, H. S. 2000. Biomass evolution in porous media and its effects on permeability under starvation conditions. *Biotechnology and Bioengineering,* 69**,** 47-56.

114.   KITANIDIS, P. K. 1994. The concept of the dilution index. *Water resources research,* 30**,** 2011-2026.

115.   KNACKSTEDT, M. A., SHEPPARD, A. P. & PINCZEWSKI, W. 1998. Simulation of mercury porosimetry on correlated grids: Evidence for extended correlated heterogeneity at the pore scale in rocks. *Physical review E,* 58**,** R6923.

116.   KNUTSON, C., VALOCCHI, A. & WERTH, C. 2007. Comparison of continuum and pore-scale models of nutrient biodegradation under transverse mixing conditions. *Advances in Water Resources,* 30**,** 1421-1431.

117.   KULIK, D. A., WAGNER, T., DMYTRIEVA, S. V., KOSAKOWSKI, G., HINGERL, F. F., CHUDNENKO, K. V. & BERNER, U. R. 2013. GEM-Selektor geochemical modeling package: revised algorithm and GEMS3K numerical kernel for coupled simulation codes. *Computational Geosciences,* 17**,** 1-24.

118.   KUTCHKO, B. G., STRAZISAR, B. R., DZOMBAK, D. A., LOWRY, G. V. & THAULOW, N. 2007. Degradation of well cement by CO2 under geologic sequestration conditions. *Environmental science & technology,* 41**,** 4787-4792.

119.   LAI, P. & KREVOR, S. 2014. Pore scale heterogeneity in the mineral distribution and surface area of Berea sandstone. *Energy Procedia,* 63**,** 3582-3588.

120.   LANDROT, G., AJO-FRANKLIN, J. B., YANG, L., CABRINI, S. & STEEFEL, C. I. 2012. Measurement of accessible reactive surface area in a sandstone, with application to CO2 mineralization. *Chemical Geology,* 318**,** 113-125.

121.   LANGLO, P. & ESPEDAL, M. S. 1994. Macrodispersion for two-phase, immiscible flow in porous media. *Advances in Water Resources,* 17**,** 297-316.

122.   LANRU, J. & XIATING, F. J. 岩. NUMERICAL MODELING FOR COUPLED THERMO-HYDRO-MECHANICAL AND CHEMICAL PROCESSES (THMC) OF GEOLOGICAL MEDIA——INTERNATIONAL AND CHINESE EXPERIENCES. 10.

123.   LARSON, M. G. & NIKLASSON, A. J. 2004. Analysis of a nonsymmetric discontinuous Galerkin method for elliptic problems: stability and energy error estimates. *SIAM journal on numerical analysis,* 42**,** 252-264.

124.   LASAGA, A. C. 2014. *Kinetic theory in the earth sciences*, Princeton university press.

125.   LE GALLO, Y., BILDSTEIN, O. & BROSSE, E. 1998. Coupled reaction-flow modeling of diagenetic changes in reservoir permeability, porosity and mineral compositions. *Journal of Hydrology,* 209**,** 366-388.

126.   LEAL, A. M., BLUNT, M. J. & LAFORCE, T. C. 2013. A robust and efficient numerical method for multiphase equilibrium calculations: Application to CO2–brine–rock systems at high temperatures, pressures and salinities. *Advances in water resources,* 62**,** 409-430.

127.   LEAL, A. M., BLUNT, M. J. & LAFORCE, T. C. 2014. Efficient chemical equilibrium calculations for geochemical speciation and reactive transport modelling. *Geochimica et Cosmochimica Acta,* 131**,** 301-322.

128.   LEFEBVRE, R., HOCKLEY, D., SMOLENSKY, J. & GÉLINAS, P. 2001. Multiphase transfer processes in waste rock piles producing acid mine drainage: 1: Conceptual model and system characterization. *Journal of Contaminant Hydrology,* 52**,** 137-164.

129.   LERDAHL, T. R., OREN, P.-E. & BAKKE, S. A predictive network model for three-phase flow in porous media. SPE/DOE Improved Oil Recovery Symposium, 2000. Society of Petroleum Engineers.

130.   LESUEUR, M., POULET, T. & VEVEAKIS, M. 2020. Three-scale multiphysics finite element framework (FE3) modelling fault reactivation. *Computer Methods in Applied Mechanics and Engineering,* 365**,** 112988.

131.   LI, L., PETERS, C. A. & CELIA, M. A. 2006. Upscaling geochemical reaction rates using pore-scale network modeling. *Advances in water resources,* 29**,** 1351-1370.

132.   LI, L., STEEFEL, C. I. & YANG, L. 2008. Scale dependence of mineral dissolution rates within single pores and fractures. *Geochimica et Cosmochimica Acta,* 72**,** 360-377.

133.   LI, Q., STEEFEL, C. I. & JUN, Y.-S. 2017. Incorporating nanoscale effects into a continuum-scale reactive transport model for CO2-deteriorated cement. *Environmental science & technology,* 51**,** 10861-10871.

134.   LIU, J., ARUGUETE, D. M., JINSCHEK, J. R., RIMSTIDT, J. D. & HOCHELLA JR, M. F. 2008. The non-oxidative dissolution of galena nanocrystals: Insights into mineral dissolution rates as a function of grain size, shape, and aggregation state. *Geochimica et Cosmochimica Acta,* 72**,** 5984-5996.

135.   LOPEZ, X., VALVATNE, P. H. & BLUNT, M. J. 2003. Predictive network modeling of single-phase non-Newtonian flow in porous media. *Journal of colloid and interface science,* 264**,** 256-265.

136.   LOW, P. F. 1981. Principles of ion diffusion in clays. *Chemistry in the soil environment,* 40**,** 31-45.

137.   LUHMANN, A. J., KONG, X.-Z., TUTOLO, B. M., GARAPATI, N., BAGLEY, B. C., SAAR, M. O. & SEYFRIED JR, W. E. 2014. Experimental dissolution of dolomite by CO2-charged brine at 100 C and 150 bar: Evolution of porosity, permeability, and reactive surface area. *Chemical Geology,* 380**,** 145-160.

138.   LUQUOT, L. & GOUZE, P. 2009. Experimental determination of porosity and permeability changes induced by injection of CO2 into carbonate rocks. *Chemical Geology,* 265**,** 148-159.

139.   MACQUARRIE, K. T. & MAYER, K. U. 2005. Reactive transport modeling in fractured rock: A state-of-the-science review. *Earth-Science Reviews,* 72**,** 189-227.

140.   MAINGUY, M., TOGNAZZI, C., TORRENTI, J.-M. & ADENOT, F. 2000. Modelling of leaching in pure cement paste and mortar. *Cement and Concrete Research,* 30**,** 83-90.

141.   MÅLØY, K. J., FEDER, J., BOGER, F. & JØSSANG, T. 1988. Fractal structure of hydrodynamic dispersion in porous media. *Physical review letters,* 61**,** 2925.

142.   MARKICH, S. J. 2002. Uranium speciation and bioavailability in aquatic systems: an overview. *TheScientificWorldJOURNAL,* 2**,** 707-729.

143.   MARTY, N. C., CLARET, F., LASSIN, A., TREMOSA, J., BLANC, P., MADÉ, B., GIFFAUT, E., COCHEPIN, B. & TOURNASSAT, C. 2015. A database of dissolution and precipitation rates for clay-rocks minerals. *Applied Geochemistry,* 55**,** 108-118.

144.   MARTY, N. C., FRITZ, B., CLÉMENT, A. & MICHAU, N. 2010. Modelling the long term alteration of the engineered bentonite barrier in an underground radioactive waste repository. *Applied Clay Science,* 47**,** 82-90.

145.   MAXWELL, J. C. 1881. *A Treatise on Electricity and Magnetism: pt. III. Magnetism. pt. IV. Electromagnetism*, Clarendon press.

146.   MAYER, K. U., FRIND, E. O. & BLOWES, D. W. 2002. Multicomponent reactive transport modeling in variably saturated porous media using a generalized formulation for kinetically controlled reactions. *Water Resources Research,* 38**,** 13-1-13-21.

147.   MCKINLEY, I. G., HAGENLOCHER, I., ALEXANDER, W. R. & SCHWYN, B. 1997. Microbiology in nuclear waste disposal: interfaces and reaction fronts. *FEMS microbiology reviews,* 20**,** 545-556.

148.   MEAKIN, P. & TARTAKOVSKY, A. M. 2009. Modeling and simulation of pore-scale multiphase fluid flow and reactive transport in fractured and porous media. *Reviews of Geophysics,* 47.

149.	MEHMANI, A. & PRODANOVIĆ, M. 2014. The effect of microporosity on transport properties in porous media. *Advances in Water Resources,* 63**,** 104-119.

150.	MEILE, C. & TUNCAY, K. 2006. Scale dependence of reaction rates in porous media. *Advances in Water Resources,* 29**,** 62-71.

151.	MEINERT, L., HEDENQUIST, J., SATOH, H. & MATSUHISA, Y. 2003. Formation of anhydrous and hydrous skarn in Cu-Au ore deposits by magmatic fluids. *Economic Geology,* 98**,** 147-156.

152.	MILLINGTON, R. 1959. Gas diffusion in porous media. *Science,* 130**,** 100-102.

153.	MILLINGTON, R. & QUIRK, J. 1961. Permeability of porous solids. *Transactions of the Faraday Society,* 57**,** 1200-1207.

154.	MILLS, R. T., LU, C., LICHTNER, P. C. & HAMMOND, G. E. Simulating subsurface flow and transport on ultrascale computers using PFLOTRAN. Journal of physics: conference series, 2007. IOP Publishing, 012051.

155.	MOLINS, S., TREBOTICH, D., ARORA, B., STEEFEL, C. I. & DENG, H. 2019. Multi-scale model of reactive transport in fractured media: diffusion limitations on rates. *Transport in Porous Media,* 128**,** 701-721.

156.	MOLINS, S., TREBOTICH, D., YANG, L., AJO-FRANKLIN, J. B., LIGOCKI, T. J., SHEN, C. & STEEFEL, C. I. 2014. Pore-scale controls on calcite dissolution rates from flow-through laboratory and numerical experiments. *Environmental science & technology,* 48**,** 7453-7460.

157.	MONTARNAL, P., MÜGLER, C., COLIN, J., DESCOSTES, M., DIMIER, A. & JACQUOT, E. 2007. Presentation and use of a reactive transport code in porous media. *Physics and Chemistry of the Earth, Parts A/B/C,* 32**,** 507-517.

158.	MOU, X. & CHEN, Z. 2020. Pore-scale simulation of heat and mass transfer in deformable porous media. *International Journal of Heat and Mass Transfer,* 158**,** 119878.

159.	NASIR, O., FALL, M. & EVGIN, E. 2014. A simulator for modeling of porosity and permeability changes in near field sedimentary host rocks for nuclear waste under climate change influences. *Tunnelling and underground space technology,* 42**,** 122-135.

160.	NAVARRE-SITCHLER, A., STEEFEL, C. I., SAK, P. B. & BRANTLEY, S. L. 2011. A reactive-transport model for weathering rind formation on basalt. *Geochimica et Cosmochimica Acta,* 75**,** 7644-7667.

161.		NAVARRE-SITCHLER, A., STEEFEL, C. I., YANG, L., TOMUTSA, L. & BRANTLEY, S. L. 2009. Evolution of porosity and diffusivity associated with chemical weathering of a basalt clast. *Journal of Geophysical Research: Earth Surface,* 114.

162.		NEUMAN, S. P. & TARTAKOVSKY, D. M. 2009. Perspective on theories of non-Fickian transport in heterogeneous media. *Advances in Water Resources,* 32**,** 670-680.

163.		NICHOLS, W., AIMO, N., OOSTROM, M. & WHITE, M. 1997. STOMP subsurface transport over multiple phases: Application guide. Pacific Northwest Lab.

164.		NITAO, J. 2000. Documentation of the thermal energy balance equation used in the USNT module of the NUFT flow and transport code. *Rep. UCRL-ID,* 139836.

165.		NITAO, J. J. 1998. User's manual for the USNT module of the NUFT Code, Version 2.0 (NP-Phase, NC-component, Thermal). *Lawrence Livermore National Laboratory, Nitao, Livermore, CA*.

166.		NOIRIEL, C., LUQUOT, L., MADÉ, B., RAIMBAULT, L., GOUZE, P. & VAN DER LEE, J. 2009. Changes in reactive surface area during limestone dissolution: An experimental and modelling study. *Chemical Geology,* 265**,** 160-170.

167.		NOIRIEL, C., STEEFEL, C. I., YANG, L. & AJO-FRANKLIN, J. 2012. Upscaling calcium carbonate precipitation rates from pore to continuum scale. *Chemical Geology,* 318**,** 60-74.

168.		ODEN, J. T., BABUŜKA, I. & BAUMANN, C. E. 1998. A discontinuoushpfinite element method for diffusion problems. *Journal of computational physics,* 146**,** 491-519.

169.		OELKERS, E. H. 2018. Physical and chemical properties of rocks and fluids for chemical mass transport calculations. *Reactive transport in porous media.* De Gruyter.

170.		OKABE, H. & BLUNT, M. J. 2004. Prediction of permeability for porous media reconstructed using multiple-point statistics. *Physical Review E,* 70**,** 066135.

171.		OLIVELLA, S., CARRERA, J., GENS, A. & ALONSO, E. J. T. I. P. M. 1994. Nonisothermal multiphase flow of brine and gas through saline media. 15**,** 271-293.

172.		OPOLOT, E. & FINKE, P. 2015. Evaluating sensitivity of silicate mineral dissolution rates to physical weathering using a soil evolution model (SoilGen2. 25). *Biogeosciences,* 12**,** 6791-6808.

173.		ØREN, P.-E. & BAKKE, S. 2002. Process based reconstruction of sandstones and prediction of transport properties. *Transport in porous media,* 46**,** 311-343.

174.		OREN, P.-E., BAKKE, S. & ARNTZEN, O. J. 1998. Extending predictive capabilities to network models. *SPE journal,* 3**,** 324-336.

175.   OREN, P. Pore-scale network modelling of waterflood residual oil recovery by immiscible gas flooding. SPE/DOE Improved Oil Recovery Symposium, 1994. Society of Petroleum Engineers.

176.   ORON, A. P. & BERKOWITZ, B. 1998. Flow in rock fractures: The local cubic law assumption reexamined. *Water Resources Research,* 34**,** 2811-2825.

177.   PARKHURST, D. L. & APPELO, C. 1999. User's guide to PHREEQC (Version 2): A computer program for speciation, batch-reaction, one-dimensional transport, and inverse geochemical calculations.

178.   PARKHURST, D. L. & APPELO, C. 2013. Description of input and examples for PHREEQC version 3: a computer program for speciation, batch-reaction, one-dimensional transport, and inverse geochemical calculations. US Geological Survey.

179.   PATEL, R. A., PERKO, J., JACQUES, D., DE SCHUTTER, G., VAN BREUGEL, K. & YE, G. 2014. A versatile pore-scale multicomponent reactive transport approach based on lattice Boltzmann method: Application to portlandite dissolution. *Physics and Chemistry of the Earth, Parts A/B/C,* 70**,** 127-137.

180.   PEDERSEN, K. 1999. Subterranean microorganisms and radioactive waste disposal in Sweden. *Engineering Geology,* 52**,** 163-176.

181.   PERRONNET, M. 2004. Réactivité des matériaux argileux dans un contexte de corrosion métallique. *Application au stockage des déchets radioactifs en site argileux. These INPL Nancy*.

182.   PETERS, C. A. 2009. Accessibilities of reactive minerals in consolidated sedimentary rock: An imaging study of three sandstones. *Chemical Geology,* 265**,** 198-208.

183.   PETERSEN, E. 1958. Diffusion in a pore of varying cross section. *AIChE Journal,* 4**,** 343-345.

184.   PFINGSTEN, W. 2002. Experimental and modeling indications for self-sealing of a cementitious low-and intermediate-level waste repository by calcite precipitation. *Nuclear Technology,* 140**,** 63-82.

185.   PRUESS, K. 1991. TOUGH2-A general-purpose numerical simulator for multiphase fluid and heat flow.

186.   PUIGDOMENECH, I., AMBROSI, J., EISENLOHR, L., LARTIGUE, J., BANWART, S., BATEMAN, K., MILODOWSKI, A., WEST, J., GRIFFAULT, L. & GUSTAFSSON, E. 2001. O 2 depletion in granitic media. The Rex project. Swedish Nuclear Fuel and Waste Management Co.

187.   RITCHIE, A. 1994. Sulfide oxidation mechanisms: controls and rates of oxygen transport. *The environmental geochemistry of sulfide mine wastes*, 201-245.

188.   RIVIERE, B. 2000. *Discontinuous Galerkin methods for solving the miscible displacement problem in porous media*, The University of Texas at Austin.

189.   RIVIÈRE, B., WHEELER, M. F. & GIRAULT, V. 2001. A priori error estimates for finite element methods based on discontinuous approximation spaces for elliptic problems. *SIAM Journal on Numerical Analysis,* 39, 902-931.

190.   ROBERTS, A. & TORQUATO, S. 1999. Chord-distribution functions of three-dimensional random media: approximate first-passage times of gaussian processes. *Physical Review E,* 59, 4953.

191.   RUBIN, J. 1983. Transport of reacting solutes in porous media: Relation between mathematical nature of problem formulation and chemical nature of reactions. *Water resources research,* 19, 1231-1252.

192.   RYAZANOV, A. V., VAN DIJKE, M. I. J. & SORBIE, K. S. 2009. Two-phase pore-network modelling: existence of oil layers during water invasion. *Transport in Porous Media,* 80, 79-99.

193.   SALAS, J., SENA, C. & ARCOS, D. 2014. Hydrogeochemical evolution of the bentonite buffer in a KBS-3 repository for radioactive waste. Reactive transport modelling of the LOT A2 experiment. *Applied Clay Science,* 101, 521-532.

194.   SALBU, B., LIND, O., BORRETZEN, P., OUGHTON, D., BRECHIGNAC, F. & HOWARD, B. 2001. Advanced speciation techniques for radionuclides associated with colloids and particles. *Radioactive Pollutants: Impact on the Environment*.

195.   SAMPER, J. & YANG, C. 2006. Stochastic analysis of transport and multicomponent competitive monovalent cation exchange in aquifers. *Geosphere,* 2, 102-112.

196.   SAVAGE, D. 2013. Constraints on cement-clay interaction. *Procedia Earth and Planetary Science,* 7, 770-773.

197.   SCHÖTZAU, D. & SCHWAB, C. 2000. Time discretization of parabolic problems by the hp-version of the discontinuous Galerkin finite element method. *SIAM Journal on Numerical Analysis,* 38, 837-875.

198.   SCHÖTZAU, D., SCHWAB, C. & TOSELLI, A. 2003. Stabilized hp-DGFEM for incompressible flow. *Mathematical Models and Methods in Applied Sciences,* 13, 1413-1436.

199.   SEIGNEUR, N., L'HÔPITAL, E., DAUZÈRES, A., SAMMALJÄRVI, J., VOUTILAINEN, M., LABEAU, P., DUBUS, A. & DETILLEUX, V. 2017. Transport properties evolution of cement model

system under degradation-Incorporation of a pore-scale approach into reactive transport modelling. *Physics and Chemistry of the Earth, Parts A/B/C,* 99**,** 95-109.

200.   SEIGNEUR, N., MAYER, K. U. & STEEFEL, C. I. 2019. Reactive transport in evolving porous media. *Reviews in Mineralogy and Geochemistry,* 85**,** 197-238.

201.   SETHIAN, J. A. & SMEREKA, P. 2003. Level set methods for fluid interfaces. *Annual review of fluid mechanics,* 35**,** 341-372.

202.   SHAO, H., KOSAKOWSKI, G., BERNER, U., KULIK, D. A., MÄDER, U. & KOLDITZ, O. 2013. Reactive transport modeling of the clogging process at Maqarin natural analogue site. *Physics and Chemistry of the Earth, Parts A/B/C,* 64**,** 21-31.

203.   SMITH, W. R. 1982. Missen. RW Chemical reaction. Equilibrium analisis: Theory and algorithms. Wiley-Interscience: New York.

204.   SOLER-SAGARRA, J., SAALTINK, M., NARDI, A., DE GASPARI, F. & CARRERA, J. 2022. Water Mixing Approach (WMA) for reactive transport modeling. *Advances in Water Resources***,** 104131.

205.   SOLER, J. M. & MÄDER, U. K. 2005. Interaction between hyperalkaline fluids and rocks hosting repositories for radioactive waste: reactive transport simulations. *Nuclear science and engineering,* 151**,** 128-133.

206.   SPYCHER, N., SONNENTHAL, E. & APPS, J. 2003. Fluid flow and reactive transport around potential nuclear waste emplacement tunnels at Yucca Mountain, Nevada. *Journal of Contaminant Hydrology,* 62**,** 653-673.

207.   STAUFFER, D. & AHARONY, A. 1985. Introduction to Percolation Theory. Taylor and Fransis. London.

208.   STEEFEL, C. & LICHTNER, P. 1998. Multicomponent reactive transport in discrete fractures: II: Infiltration of hyperalkaline groundwater at Maqarin, Jordan, a natural analogue site. *Journal of Hydrology,* 209**,** 200-224.

209.   STEEFEL, C. I. & LASAGA, A. C. 1992. Putting transport into water-rock interaction models. *Geology,* 20**,** 680-684.

210.   STEEFEL, C. I. & LASAGA, A. C. 1994. A coupled model for transport of multiple chemical species and kinetic precipitation/dissolution reactions with application to reactive flow in single phase hydrothermal systems. *American Journal of science,* 294**,** 529-592.

211.   STEEFEL, C. I. & LICHTNER, P. C. 1994. Diffusion and reaction in rock matrix bordering a hyperalkaline fluid-filled fracture. *Geochimica et Cosmochimica Acta,* 58**,** 3595-3612.

212.   SUN, N. 1994. Inverse Problems in Groundwater Modeling. Kluwer Acad.

213.   SUN, S. 2003. *Discontinuous Galerkin methods for reactive transport in porous media*, The University of Texas at Austin.

214.   SUN, S. & WHEELER, M. F. 2006a. Anisotropic and dynamic mesh adaptation for discontinuous Galerkin methods applied to reactive transport. *Computer methods in applied mechanics and engineering,* 195**,** 3382-3405.

215.   SUN, S. & WHEELER, M. F. 2006b. A posteriori error estimation and dynamic adaptivity for symmetric discontinuous Galerkin approximations of reactive transport problems. *Computer methods in applied mechanics and engineering,* 195**,** 632-652.

216.   TARAFDAR, S. & ROY, S. 1998. A growth model for porous sedimentary rocks. *Physica B: Condensed Matter,* 254**,** 28-36.

217.   TARTAKOVSKY, A. M., MEAKIN, P., SCHEIBE, T. D. & WEST, R. M. E. 2007a. Simulations of reactive transport and precipitation with smoothed particle hydrodynamics. *Journal of Computational Physics,* 222**,** 654-672.

218.   TARTAKOVSKY, A. M., MEAKIN, P., SCHEIBE, T. D. & WOOD, B. D. 2007b. A smoothed particle hydrodynamics model for reactive transport and mineral precipitation in porous and fractured porous media. *Water resources research,* 43.

219.   TARTAKOVSKY, A. M., REDDEN, G., LICHTNER, P. C., SCHEIBE, T. D. & MEAKIN, P. 2008a. Mixing-induced precipitation: Experimental study and multiscale numerical analysis. *Water Resources Research,* 44.

220.   TARTAKOVSKY, A. M., TARTAKOVSKY, D. M., SCHEIBE, T. D. & MEAKIN, P. 2008b. Hybrid simulations of reaction-diffusion systems in porous media. *SIAM Journal on Scientific Computing,* 30**,** 2799-2816.

221.   TARTAKOVSKY, A. M., TARTAKOVSKY, G. D. & SCHEIBE, T. D. 2009. Effects of incomplete mixing on multicomponent reactive transport. *Advances in Water Resources,* 32**,** 1674-1679.

222.   TARTAKOVSKY, A. M., TRASK, N., PAN, K., JONES, B., PAN, W. & WILLIAMS, J. R. 2016. Smoothed particle hydrodynamics and its applications for multiphase flow and reactive transport in porous media. *Computational Geosciences,* 20**,** 807-834.

223.   TENTHOREY, E. & GERALD, J. D. F. 2006. Feedbacks between deformation, hydrothermal reaction and permeability evolution in the crust: Experimental insights. *Earth and Planetary Science Letters,* 247**,** 117-129.

224.   TESSIER, A. & TURNER, D. R. 1995. *Metal speciation and bioavailability in aquatic systems*, Wiley Chichester.

225.   THULLNER, M., ZEYER, J. & KINZELBACH, W. 2002. Influence of microbial growth on hydraulic properties of pore networks. *Transport in porous media,* 49**,** 99-122.

226.   TIAN, H., XU, T., WANG, F., PATIL, V. V., SUN, Y. & YUE, G. 2014. A numerical study of mineral alteration and self-sealing efficiency of a caprock for CO_2 geological storage. *Acta Geotechnica,* 9**,** 87-100.

227.   TOMADAKIS, M. M. & SOTIRCHOS, S. V. 1993. Transport properties of random arrays of freely overlapping cylinders with various orientation distributions. *The Journal of chemical physics,* 98**,** 616-626.

228.   TROTIGNON, L., DEVALLOIS, V., PEYCELON, H., TIFFREAU, C. & BOURBON, X. 2007. Predicting the long term durability of concrete engineered barriers in a geological repository for radioactive waste. *Physics and Chemistry of the Earth, Parts A/B/C,* 32**,** 259-274.

229.   TROTIGNON, L., MICHAUD, V., LARTIGUE, J.-E., AMBROSI, J.-P., EISENLOHR, L., GRIFFAULT, L., DE COMBARIEU, M. & DAUMAS, S. 2002. Laboratory simulation of an oxidizing perturbation in a deep granite environment. *Geochimica et cosmochimica acta,* 66**,** 2583-2601.

230.   TRUESDELL, A. H. & JONES, B. F. 1974. WATEQ, a computer program for calculating chemical equilibria of natural waters. *J. Res. US Geol. Surv,* 2**,** 233-248.

231.   VAN DER LEE, J. & DE WINDT, L. 2002. CHESS Tutorial and Cookbook/Version 3.0, users manual LHM. RD/02/13, Ecole des mines de Paris, Fontainebleau.

232.   VAN ZEGGEREN, F. & STOREY, S. H. 2011. *The computation of chemical equilibria*, Cambridge University Press.

233.   VARLOTEAUX, C., VU, M. T., BEKRI, S. & ADLER, P. M. 2013. Reactive transport in porous media: pore-network model approach compared to pore-scale model. *Physical Review E,* 87**,** 023010.

234.   VERHAEGHE, F., ARNOUT, S., BLANPAIN, B. & WOLLANTS, P. 2006. Lattice-Boltzmann modeling of dissolution phenomena. *Physical Review E,* 73**,** 036316.

235.   VERHAEGHE, F., LIU, J., GUO, M., ARNOUT, S., BLANPAIN, B. & WOLLANTS, P. 2007. Dissolution and diffusion behavior of Al_2O_3 in a $CaO–Al_2O_3–SiO_2$ liquid: An experimental-numerical approach. *Applied Physics Letters,* 91**,** 124104.

236.   VON GUNTEN, H. & BENEŠ, P. 1995. Speciation of radionuclides in the environment. *Radiochimica Acta,* 69**,** 1-30.

237.   WALSH, S. D., DU FRANE, W. L., MASON, H. E. & CARROLL, S. A. 2013. Permeability of wellbore-cement fractures following degradation by carbonated brine. *Rock Mechanics and Rock Engineering,* 46**,** 455-464.

238.   WANG, Q., CUI, Y.-J., TANG, A. M., DELAGE, P., GATMIRI, B. & YE, W.-M. 2014. Long-term effect of water chemistry on the swelling pressure of a bentonite-based material. *Applied clay science,* 87**,** 157-162.

239.   WANG, Y., NAHON, D. & MERINO, E. 1994. Dynamic model of the genesis of calcretes replacing silicate rocks in semi-arid regions. *Geochimica et Cosmochimica Acta,* 58**,** 5131-5145.

240.   WANG, Y. & PAPENGUTH, H. W. 2001. Kinetic modeling of microbially-driven redox chemistry of radionuclides in subsurface environments: coupling transport, microbial metabolism and geochemistry. *Journal of contaminant hydrology,* 47**,** 297-309.

241.   WERTH, C. J., ZHANG, C., BRUSSEAU, M. L., OOSTROM, M. & BAUMANN, T. 2010. A review of non-invasive imaging methods and applications in contaminant hydrogeology research. *Journal of contaminant hydrology,* 113**,** 1-24.

242.   WHEELER, M. F. 1978. An elliptic collocation-finite element method with interior penalties. *SIAM Journal on Numerical Analysis,* 15**,** 152-161.

243.   WITHERSPOON, P. A., WANG, J. S., IWAI, K. & GALE, J. E. 1980. Validity of cubic law for fluid flow in a deformable rock fracture. *Water resources research,* 16**,** 1016-1024.

244.   WUNDERLY, M., BLOWES, D., FRIND, E. & PTACEK, C. 1996. Sulfide mineral oxidation and subsequent reactive transport of oxidation products in mine tailings impoundments: A numerical model. *Water Resources Research,* 32**,** 3173-3187.

245.   XIAO, Y. & JONES, G. D. Reactive transport models of limestone-dolomite transitions: implications for reservoir connectivity. International Petroleum Technology Conference, 2007. International Petroleum Technology Conference.

246.   XIONG, Q., JIVKOV, A. P. & AHMAD, S. M. 2016. Modelling reactive diffusion in clays with two-phase-informed pore networks. *Applied Clay Science,* 119**,** 222-228.

247.   XU, T. 1998. Coupled modeling of non-isothermal multiphase flow, solute transport and reactive chemistry in porous and fractured media: 2. Model Applications.

248.   XU, T., SAMPER, J., AYORA, C., MANZANO, M. & CUSTODIO, E. 1999. Modeling of non-isothermal multi-component reactive transport in field scale porous media flow systems. *Journal of Hydrology,* 214**,** 144-164.

249.   XU, T., SONNENTHAL, E. & BODVARSSON, G. 2003. A reaction-transport model for calcite precipitation and evaluation of infiltration fluxes in unsaturated fractured rock. *Journal of contaminant hydrology,* 64**,** 113-127.

250.   YANG, C., SAMPER, J. & MONTENEGRO, L. 2008. A coupled non-isothermal reactive transport model for long-term geochemical evolution of a HLW repository in clay. *Environmental Geology,* 53**,** 1627-1638.

251.   YEH, G. T. & TRIPATHI, V. S. 1991. A model for simulating transport of reactive multispecies components: model development and demonstration. *Water Resources Research,* 27**,** 3075-3094.

252.   YEONG, C. & TORQUATO, S. 1998. Reconstructing random media. *Physical review E,* 57**,** 495.

253.   YIOTIS, A. G., TSIMPANOGIANNIS, I. N., STUBOS, A. K. & YORTSOS, Y. C. 2006. Pore-network study of the characteristic periods in the drying of porous materials. *Journal of colloid and interface science,* 297**,** 738-748.

254.   YOUSSEF, S., ROSENBERG, E., GLAND, N., BEKRI, S. & VIZIKA, O. 2007. Quantitative 3D characterisation of the pore space of real rocks: improved μ-CT resolution and pore extraction methodology. *Int. Sym. of the Society of Core Analysts*.

255.   ZELEZNIK, F. J. & GORDON, S. 1968. Calculation of complex chemical equilibria. *Industrial & Engineering Chemistry,* 60**,** 27-57.

256.   ZHENG, L., LI, L., RUTQVIST, J., LIU, H.-H. & BIRKHOLZER, J. 2012. Modeling radionuclide transport in clays.

257.   ZHENG, L., RUTQVIST, J., XU, H. & BIRKHOLZER, J. T. 2017. Coupled THMC models for bentonite in an argillite repository for nuclear waste: Illitization and its effect on swelling stress under high temperature. *Engineering Geology,* 230**,** 118-129.

258.   ZHENG, L., SAMPER, J. J. P. & CHEMISTRY OF THE EARTH, P. A. B. C. 2008. A coupled THMC model of FEBEX mock-up test. 33**,** S486-S498.

259.   ZIEGLER, D. P. 1993. Boundary conditions for lattice Boltzmann simulations. *Journal of statistical physics,* 71**,** 1171-1177.

Chapter 3: A Geochemical Modelling of Multi-minerals Evolution for a 15 Months Experiment

Abstract

The impact of hyper alkaline leachate released from the cementitious barrier of a geological disposal facility (GDF) on the host rock is a significant issue for the safety assessment of long-term nuclear disposal. However, modelling of multi-mineral transformations, multiple chemical reactions and multiple secondary phase pathways remains a challenge due to uncertainties in parameters and a limited available database describing the kinetics of dissolution/precipitation reactions. In this study, a modelling approach, Mixed Kinetic-Equilibrium (MKE), has been employed to study the complex reactions occurring in an experimental system consisting of Borrowdale Volcanic Group rocks permeated with a hyper-alkaline leachate over 15 months. The modelling suggests that dissolution of primary dolomite, quartz, calcite and K-feldspar in the host rock initially drives the chemical evolution of this system. The subsequent precipitation of several secondary phases, including calcite, brucite, talc and calcium-silicate-hydrate (CSH) phases, is predicted to control the long-term chemical equilibria and mineralogical composition of the host rock impacted by the alkaline leachate. The results from the modelling provides a deeper understanding of the long-term interactions between the host rock and high pH leachate, with dolomite predicted to be a major controlling phase on the geochemical evolution of the system.

List of Notations:

A_0	Initial Surface area
$f_{H^+}, f_{H_2O}, f_{OH}, f_{CO_2}$	Inhibition factors
$\dfrac{IAP}{K}$	Ion activity divided by equilibrium constant, equal to the saturation ratio (SR) of the reactant
k_k	Reactant empirical constant
$k_{H^+}, k_{H_2O}, k_{OH^-}, k_{CO_2}$	Solutes rate coefficients
k_1, k_2, k_3, k_4	Rate constants
m_k	Moles of reactant at a given time
m_{0k}	Initial moles of reactant
n	Order of reaction constant (Crystal grain size distribution)
P_{CO_2}	Partial pressure of carbon dioxide
R_k	Reactant overall dissolution rate
r_k	Reactant specific reaction rate
r_f	Forward reaction
V	Solution volume
$[X]$	Ion activity of the element X

3.1 Introduction

In the UK the concept of multilayer barrier developed by Nirex (Francis et al., 1997) has been adopted for intermediate/low level waste disposal. A location hundreds of meters below the biosphere is to be selected for a deep geological waste repository, with wastes interred within stainless-steel containers encapsulated within a cementitious engineered barrier at the site. A hyper-alkaline plume may be generated by groundwater in contact with the cement barrier, creating a chemical disturbed zone (CDZ) (Chen et al., 2015, Chen et al., 2016, Chen and Thornton, 2018, Corkhill et al., 2013). The influence of the CDZ on the host rock for an intermediate/low level waste disposal facility in the UK has been summarized in the BIGRAD report (Small et al., 2016). In addition, significant effort has been made by the wider waste management community in the past two decades, in terms of experimental analysis (at lab scale, field scale and on natural analogues), as well as in terms of modelling, to investigate the long-term interaction between cement materials and potential host rock. The mechanisms and modelling of waste-cement and cement-host rock interactions have been summarized in a special issue of Physics and Chemistry of the Earth (Jacques et al., 2014).

In the field of geochemical modelling considerable research has been conducted based on the concept of thermodynamic equilibrium (Bethke, 1994, Bethke, 1996, Van der Lee, 1997). However, in a disposal site with natural water dominant, this assumption may not be valid for slow reaction processes. Therefore, an improved modelling approach incorporating non-equilibrium and kinetically controlled precipitation and dissolution was developed by (Soetaert et al., 1996) to illustrate kinetics processes in terms of first or

second order formulations. However, even with this model, values of kinetic parameters such as surface area, initial and final moles of reactants, reaction and precipitation rates cannot easily be obtained from experimental study. For example, (Parkhurst and Appelo, 1999) have attempted to address this using the geochemical model of PHREEQC as the framework for the complex geo-reaction system, however the database only covers a rates for a limited number of minerals such as calcite and K-feldspar, for example.

Recently, a Mixed Kinetic-Equilibrium approach (MKE) was introduced to combine the advantages of both kinetic and equilibrium laws and enable modelling of complex multi-mineral and multi-component reaction systems (Chen and Thornton, 2018, Van der Lee, 1998, Bethke, 1996). This approach enables faster reactions using the equilibrium concept with slower kinetically-limited reactions. In addition, it allows existing models developed on the thermodynamic equilibrium approach to be re-evaluated. Nevertheless, this requires a full understanding of the chemical reaction system (e.g. which reaction is faster and slower, etc.) and the availability of appropriate kinetic data. This paper aims to illustrate the MKE approach's application in the interpretation of multi-mineral reactions that may occur in Borrowdale Volcanic Group rocks during experimental permeation with hyper-alkaline leachate originating from the cementitious barrier of a geological disposal facility for intermediate-level nuclear waste (ILW).

3.2 Experimental study

A 15 year experiment, starting in 1995, was conducted by the British Geological Survey (Rochelle et al., 2001, Moyce et al., 2014, Rochelle et al., 2016) to examine the chemical behaviour of the Borrowdale Volcanic Group (BVG) rock sample in contact with young

near-field porewater (YNFP) or evolved near-field groundwater (ENFG) intended to represent model fluid compositions released from cementitious barrier materials used for ILW disposal. The rock sample used in the experiment was taken from a hydrological fracture zone in Ordovician volcanic rocks in the UK. A 150 ml and 100 ml pressure vessels were used for the solution with, and without, BVG rock, respectively (Figure 3.1).
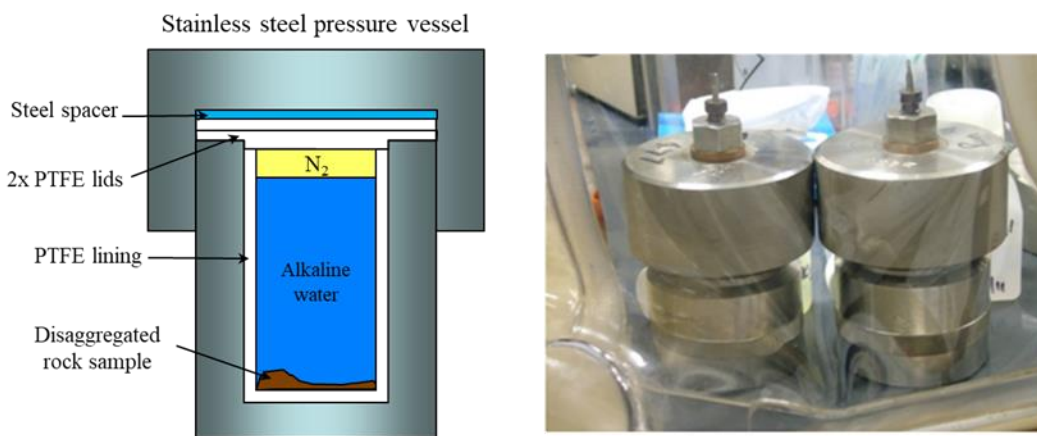
Figure 3.1: Actual and schematic diagram of stainless steel pressure vessels lined with Teflon® used to contain the BVG and synthetic CDZ-type fluid experiments.

The original 15 year experiment was divided into two time periods with different targets. The first period, from 0-15 months, investigated short term mineral evolution, whereas the second period, from month 15 to year 15, investigated the long-term mineral evolution. The modelling study described in this paper considers the first period of the experiment from 0 to 15 months, and is focused on chemical interactions occurring between the YNFP and BVG rock only (YNFP characteristics are given in Table 3.1).

Fluid and rock samples were collected from these vessels at 4, 9 and 15 months for chemical and mineralogical analysis. Before analysis, the rock samples were washed in isopropanol, milled and micro ionised in acetone with the addition of 10% corundum

(Al_2O_3) as an internal standard. The rock samples were then placed in a stainless-steel holder and analysed using a PANalytical X'Pert Pro diffractometer. The final analysis process was then performed using the PANalytical X'Pert Highscore Plus software (Moyce et al., 2014, Rochelle et al., 2016). Other than the analysed samples, the experiment was continued in parallel for a much longer reaction period of 15 years (Moyce et al., 2014, Chen and Thornton, 2018).

Table 3.1: Recipes for young near-field porewater (YNFP) prepared by the British Geological Survey (Rochelle et al., 2016).

Chemical component	Concentration (mg/L)
Br	0.5
Ba	0.01
CO_3	166
Ca	51.8
Cl	63.7
F	19
Fe	0.1
K	3230
Mg	0.089
Mn	0.01
Na	1890
SO_4	1
NO_3	1
Si	9.2
Sr	0.018
pH (at 70ºC) *	11.67

* Adjusted using NaOH, 1.5137 g required for the YNFP

3.3 Mineralogical analysis and kinetic information for BVG rock

The mineralogical composition of BVG rock is given in Table (3.2). Note here that the fracture fill and clay phases have not been considered despite that the starting material has indicated their presence. Six minerals are presented in BVG rock, all of which can dissolve

and react with YNFP. Based on the mineral weight percentage values, the initial mass for each reactant is calculated for 35g of rock sample, based on the original experiment (Rochelle et al., 2016).

Table 3.2: Quantitative XRD analysis of unreacted BVG rock starting material conducted by the British Geological Survey (Rochelle et al., 2001, Rochelle et al., 2016). m_0 is calculated based on a 35g rock sample.

Mineral	Weight %	m_0 (g)
Orthoclase	12	4.2
Quartz	41	14.35
Dolomite	29	10.15
Muscovite	13	4.55
Hematite	2	0.7
Calcite	3	1.05

The overall dissolution rates of minerals may be described by (Appelo and Postma, 2005):

$$R_k = r_k \frac{A_0}{V} \left(\frac{m_k}{m_{0k}} \right)^n \qquad (3.1)$$

In which $\frac{A_0}{V}$ is initial surface area (m^2) / volume of solution (L), $\left(\frac{m_k}{m_{0k}} \right)^n$ is moles of solid at a given time / initial moles of solid, n=2/3 (for uniformly dissolving spheres and cubes, generally obtained from experiments), r_k is a specific reaction rate (mol/m^2/s) with various forms. The general formulation below is proposed by (Rimstidt and Barnes, 1980):

$$r_k = k_k \left(1 - \left(\frac{IAP}{K} \right)_k \right) \qquad (3.2)$$

where k_k is an empirical constant for a reactant and $\left(\frac{IAP}{K} \right)$ (ion activity divided by equilibrium constant) is equal to the saturation ratio (*SR*) of the reactant. The kinetic

information for the minerals in BVG rock obtained from the literature is summarised

below, and the rates and surface areas used for the modelling are provided in Table (3.3).

Table 3.3: Modelling parameters for the BVG rock.

Mineral	Weight %	Solution Volume (L)	Surface area (m²/g)	Rate constant
Orthoclase	12		0.02 (De Windt et al., 2008)	k (using equation 3.6) (Appelo and Postma, 2005)
Quartz	41		0.02 (De Windt et al., 2008)	k = 1x10$^{-12.2}$ (70°C) (Worley, 1994)
Dolomite	29	0.15 (Rochelle et al., 2016)	0.02 (De Windt et al., 2008)	k= 1.2x10^{-10} (Appelo and Postma, 2005, Appelo et al., 1984). This value was lowered one order of magnitude to fit well with the experimental data (k= 1.2x10^{-11})
Muscovite	13		NA	NA
Hematite	2		NA	NA
Calcite	3		0.02 (De Windt et al., 2008)	k1 = 10^(0.198 - 444.0 / (273.16 + T)) k2 = 10^(2.84 - 2177.0 / (273.16 + T)) k3 = 10^(-1.1 - 1737.0 / (273.16 + T)) in which T denotes temperature. (Appelo and Postma, 2005, Plummer et al., 1978)

3.3.1 Quartz (SiO_2)

The dissolution function of quartz may be described by (Merkel et al., 2005):

$$SiO_2 + 2H_2O \leftrightarrow H_2SiO_4 \qquad (3.3)$$

and, as per equation (3.1) and (3.2), the overall dissolution kinetic equation for quartz will be:

$$R_{Quartz} = k_{Quartz} \left(\frac{A_0}{V}\right)\left(\frac{m}{m_0}\right)^{0.67}\left(1 - \left(\frac{IAP}{K}\right)_{Quartz}\right) \qquad (3.4)$$

where R is overall quartz dissolution rate (mol L^{-1} s^{-1}), A$_0$ is the initial surface area of quartz

(m²), V is the solution volume (L), m is the moles of quartz at a given time, m$_0$ is the initial

moles of quartz ; k is the specific dissolution rate = $10^{-12.2}$ mol/m²/s at 70°C (Worley, 1994), $\left(\frac{IAP}{K}\right)$ is equal to the SR value of quartz.

3.3.2 Orthoclase ($KAlSi_3O_8$) K-feldspar

K-feldspar ($KAlSi_3O_8$), also known as orthoclase, is 12% of the BVG rock. Preliminary rate expressions for K-feldspar may be found in the literature (Sverdrup, 1990, Brantley et al., 1993). The general form of the overall dissolution rate proposed by (Appelo and Postma, 2005) is used to simulate K-feldspar reaction at specific temperatures and pH value:

$$R_{K-feldspar} = k_{K-feldspar} \left(\frac{A_0}{V}\right)\left(\frac{m}{m_0}\right)^{0.67}\left(1 - \left(\frac{IAP}{K}\right)_{K-feldspar}\right) \tag{3.5}$$

where

$$k_{K-feldspar} = k_{H^+}\frac{[H^+]^{0.5}}{f_H} + k_{H_2O}\frac{1}{f_{H_2O}} + k_{OH^-}\frac{[OH^-]^{0.3}}{f_{OH}}$$
$$+ k_{CO_2}\frac{[P_{CO_2}]^{0.6}}{f_{CO_2}} \tag{3.6}$$

where $k_{K-feldspar}$ is the specific reaction rate (mol m⁻² s⁻¹), k_i are the solute rate coefficients (mol m⁻² s⁻¹), and f_i are inhibition factors.

3.3.3 Calcite ($CaCO_3$)

(Appelo and Postma, 2005, Parkhurst and Appelo, 1999, Plummer et al., 1978) have described the dissolution rate of calcite in a solution using the following expression which is suitable for both dissolution and precipitation reaction:

$$r_{calcite} = \underbrace{k_1[H^+] + k_2[H_2CO_3] + k_3[H_2O]}_{r_f} - k_4[Ca^{2+}][HCO_3^-] \qquad (3.7)$$

and then simplified in a calcite-water system as:

$$r_{calcite} = r_f \left[1 - \left(\frac{IAP}{K}\right)_{Calcite}^{2/3}\right] \qquad (3.8)$$

The overall dissolution rate of calcite will then be:

$$
\begin{aligned}
R_{calcite} &= r_{calcite} \left(\frac{A_0}{V}\right)\left(\frac{m}{m_0}\right)^{0.67} \\
&= r_f \left(\frac{A_0}{V}\right)\left(\frac{m}{m_0}\right)^{0.67}\left[1 - \left(\frac{IAP}{K}\right)_{Calcite}^{2/3}\right] \qquad (3.9)
\end{aligned}
$$

The value of the coefficients k_1, k_2 and k_3 in equation (3.7) are obtained from the literature (Plummer et al., 1978).

3.3.4 Dolomite $CaMg(CO_3)_2$

The dissolution kinetics of dolomite has been analysed by (Busenberg and Plummer, 1982) and found to be much slower than that for calcite. The rate expression for dolomite dissolution may also be found from the saturation index $\left(SI = log\left(\frac{IAP}{K}\right)\right)$, as below (Appelo and Postma, 2005, Parkhurst and Appelo, 1999, Appelo et al., 1984):

$$R_{Dolomite} = -k_{Dolomite}\left(\frac{A_0}{V}\right)\left(\frac{m}{m_0}\right)^{0.67} log\left(\frac{IAP}{K}\right)_{Dolomite} \qquad (3.10)$$

3.3.5 Hematite (Fe_2O_3) and Muscovite $[KAl_3Si_3O_{10}(OH)_2]$

The dissolution behaviour of hematite (Fe_2O_3) has been investigated intensively in low pH conditions (Sidhu et al., 1981, Schwertmann, 1984, Torrent et al., 1987). However, few studies have been done at high pH. The dissolution kinetics of muscovite has been discussed by (Knauss, 1989) as a function of pH and time. Since the percentage of hematite in the rock sample is very low (2%) and it does not present significant influence on the mineral evolution process in the experiment (Rochelle et al., 2016), and muscovite (a clay mineral presented in the fracture of the BVG rock) has not been the attention of the initial experiment (Rochelle et al., 2001, Moyce et al., 2014), therefore both phases are not modelled to simply the discussion.

3.4 Modelling methodology

3.4.1 Conceptual model

PHREEQC, a geochemical modelling tool developed by the USGS (U.S. Geological Survey) (Parkhurst et al., 1980) with functions such as aqueous, mineral, surface-complexion, and ion-exchange equilibrium, etc, was used with a modified database (entitled as llnl-BGS) that included additional kinetic information based on the LLNL (Lawrence Livermore National Laboratory) aqueous model parameters database. Thermodynamic information (reactions and equilibrium constants) for the major minerals is included in Table (3.4) (Chen and Thornton, 2018). Note here that there are other databases available, such as Thermoddem and Thermoddem DB (Blanc et al., 2012) for low temperature water/rock interactions and waste materials, and CEMDATA DB (Lothenbach et al., 2019) specifically for cement materials supporting state-of-the-art

models for C-A-S-H phases as solid solution (with variable C/S ratio). As this paper is focused on the mixed equilibrium and kinetics approach, and the control mineral function of dolomite, the modified PHREEQC database was used for convenience. The complex potential interactions between primary and secondary phases are described in Figure (3.2).

K-feldspar $(KAlSi_3O_8)$

Quartz (SiO_2)

Dolomite $[CaMg(CO_3)_2]$

Calcite $(CaCO_3)$

Muscovite $[KAl_3Si_3O_{10}(OH)_2]$

Hematite (Fe_2O_3)

Dissolution   Precipitation

Mg Si Fe CO_3 Ca OH Al K

CSH Phases $CaO.SiO_2.H_2O$

Calcite $CaCO_3$

Talc $Mg_3Si_4O_{10}(OH)_2$

Brucite $Mg(OH)_2$
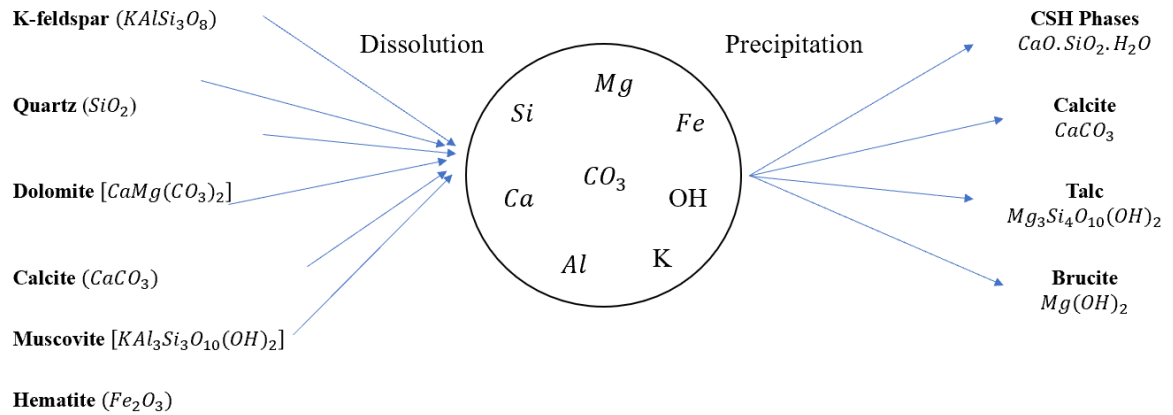
Figure 3.2: Conceptual model for geochemical modelling of BVG reaction with YNFP.

Figure (3.3) shows the modelling process developed in this study. Initially, a conceptual model was established based on information from both theoretical and experimental analysis. The kinetic information was obtained from published databases or literature. During this process reaction rates were compared in terms of the timescale, to identify the quickest or slowest rates of minerals and to provide supporting information for the modelling approach (e.g. either kinetics or equilibrium, or a mix of both). In the case where the kinetics of any minerals are not available, or there is a large difference between rates (e.g. more than 10^2), then the mixed kinetics and equilibrium approach may be preferred. Finally, potential secondary phases, obtained by using information from either the

experiment or published literature, were used to refine the model. In this study, the kinetic data for the primary minerals were available from literature. Thus, kinetic dissolution/precipitation was applied (Table 3.3). Meanwhile, the precipitation of secondary CSH phases was included in the equilibrium reaction due to the unavailability of kinetic data.
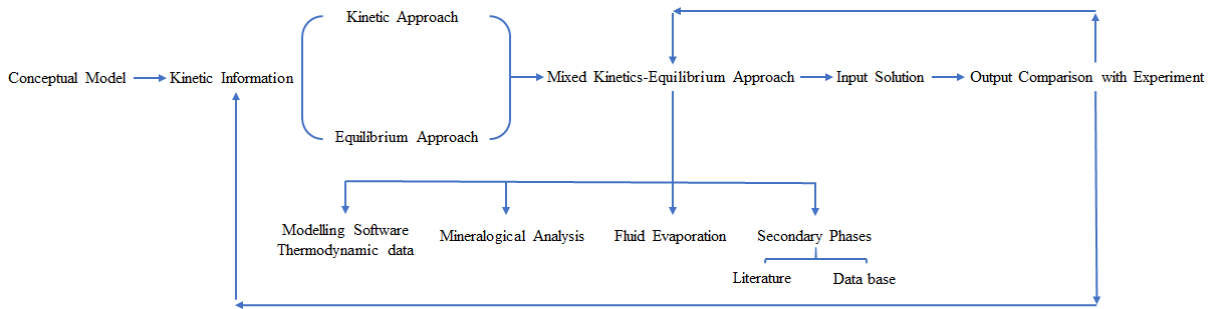
Figure 3.3: Modelling process adopted.

3.4.2 Secondary phases

Over a long period several dissolution and precipitation reactions may occur as the chemical system evolves. The potential secondary phases selected in this study include brucite, talc, calcite and CSH phases, according to experimental observations and theoretical considerations of interactions between the host rock and cement leachate (Small et al., 2016). Although PHREEQC can represent the thermodynamics of brucite, talc and calcite equilibria, the relevant data required to simulate CSH reactions is lacking. For this reason, more investigation needs to be performed on this topic.

$xCaO.ySiO_2.zH_2O$ can be used to describe the general CSH phase in which silicate in Portland cement reacts with water. The chemical reaction which will generate CSH phases is usually described as (Peterson et al., 2005):

$$2Ca_2SiO_4 + 5H_2O \rightarrow 3CaO.2SiO_2.4H_2O + Ca(OH)_2 + 58.6\ kJ \qquad (3.11)$$
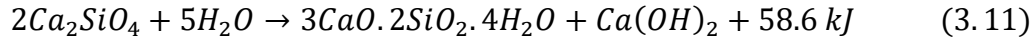
More than 30 calcium silicate hydrate phases exist (also known as C-S-H or CSH) (Taylor, 1997). The structural complexity of this silicate makes it difficult to know the exact precipitated phase since the reactions will create several secondary phase compositions (Chen et al., 2004). For simplicity, tobermorite was selected to represent CSH phases since the ratio of Ca:Si was observed to be variable during the reaction in the experiment. The formation and precipitation of CSH phase are outside the scope of this study; for this the reader is referred to the original 15 years experiment study (Moyce et al., 2014, Chen and Thornton, 2018).

Table 3.4: Reactions and equilibrium constants for minerals used in the calculations.

Mineral	Reaction	Log Keq
Calcite	$CaCO_3 + H^+ = Ca^{++} + HCO_3^-$	1.8487
Muscovite	$KAl_3Si_3O_{10}(OH)_2 + 10H^+ = K^+ + 3Al^{+++} + 3SiO_2 + 6H_2O$	13.5858
Kaolinite	$Al_2Si_2O_5(OH)_4 + 6H^+ = +2Al^{+++} + 2SiO_2 + 5H_2O$	6.8101
Chalcedony	$SiO_2 = +1.0\ SiO_2$	-3.7281
Sepiolite	$Mg_4Si_6O_{15}(OH)_2:6H_2O + 8H^+ = +4Mg^{++} + 6SiO_2 + 11H_2O$	30.4439
Brucite	$Mg(OH)_2 + 2H^+ = +1.0\ Mg^{++} + 2H_2O$	16.2980
Ettringite	$Ca_6Al_2(SO_4)_3(OH)_{12}:26H_2O + 12H^+ = +2Al^{+++} + 3SO_4^{--} + 6Ca^{++} + 38H_2O$	62.5362
Tobermorite-11A	$Ca_5Si_6H_{11}O_{22.5} + 10H^+ = +5Ca^{++} + 6SiO_2 + 10.5H_2O$	65.6121
Tobermorite-14A	$Ca_5Si_6H_{21}O_{27.5} + 10H^+ = +5Ca^{++} + 6SiO_2 + 15.5H_2O$	63.8445
Tobermorite-9A	$Ca5Si6H6O20 + 10\ H+ = +5Ca++ + 6SiO2 + 8H2O$	69.0798
Portlandite	$Ca(OH)_2 + 2H^+ = +1.0Ca^{++} + 2H_2O$	22.5552
Gypsum	$CaSO_4:2H_2O = +1.0\ Ca^{++} + 1.0\ SO_4^{--} + 2H_2O$	-4.4823
Hillebrandite	$Ca_2SiO_3(OH)_2:0.17H_2O + 4H^+ = SiO_2 + 2Ca^{++} + 3.17\ H_2O$	36.8190
Foshagite	$Ca_4Si_3O_9(OH)_2:0.5H_2O + 8H^+ = +3SiO_2 + 4Ca^{++} + 5.5H_2O$	65.9210

3.5 Results and discussion

3.5.1 Modelling of short-term experiment (0 months to 15 months)

Calcite, quartz, K-feldspar and dolomite have all been modelled in the first 15 months using the mixed equilibrium and kinetics approach. Changes in the concentration of Ca, Mg, Na, Si, CO_3 and pH, as measured from the experiment, were analysed in the modelling simulations.

Since all the 6 minerals involved in the dissolution do not contain Na^+, and the potential secondary phases do not also consume Na^+, then Na^+ remains constant over time, in good agreement with the experimental results (Figure 3.4). Ca^{2+} decreases significantly in the initial few months due to precipitation of $CaCO_3$ (Figure 3.5), which has a SI above zero (Figure 3.10). Silicon (Si) (Figure 3.6) increases due to dissolution of both quartz and K-feldspar (both have SI below zero as in Figure 3.10) and then decreases due to precipitation of talc and some CSH phases. The magnesium (Mg) in the original solution decreases before the fourth month (nearly matching the timing of peak Si values due to quartz dissolution) as a result of precipitation of secondary talc $[Mg_3Si_4O_{10}(OH)_2]$ and brucite $[Mg(OH)_2]$ phases (both have above zero SI at the beginning of the reaction, Figure 3.7 and 3.10). Carbonate (CO_3^{2-}) concentration increases in the solution as a result of dolomite dissolution (Figure 3.8). The pH decreases due to the precipitation of secondary phases (Figure 3.9) and may also subsequently influence the dissolution or precipitation of some secondary phases.

Figure 3.10 shows the evolution of some primary phases and selected secondary phases. As there was an initial concentration of Ca, CO_3 and Mg in the YNFP at time zero (Rochelle et al., 2016), dolomite $CaMg(CO_3)_2$, calcite ($CaCO_3$) and talc are oversaturated in the solution and hence start to precipitate during the initial few weeks. After some time, dolomite reaches a SI of 0 but then starts to dissolve, allowing other minerals to reach equilibrium. Since dolomite forms 29% of the BVG rock and can provides a pool of Ca, Mg and CO_3, calcite and talc both reach equilibrium, whereas dolomite will keep dissolving with a positive slope to reach equilibrium as well. Since the dissolution rate of dolomite is very small, its SI is below 0 until month 15 (Figure 3.10). As a CSH phase, tobermorite-11A is unlikely to precipitate due to a deficiency in Ca related to calcite precipitation. K-feldspar initially has a negative SI and then follows the dissolution kinetics to reach equilibrium.

From the analysis, dolomite is proved to be a major controlling phase on the geochemical evolution of BVG rock minerals interaction with the young cement leachate. The findings from the numerical modelling and theoretical analysis have provided an in-depth understanding of the long-term interactions between the host rock and alkaline leachate. The modelling results in line with experimental further support the concept of Mixed Kinetic-Equilibrium (MKE) approach to interpret the evolution of multiple mineral phases.
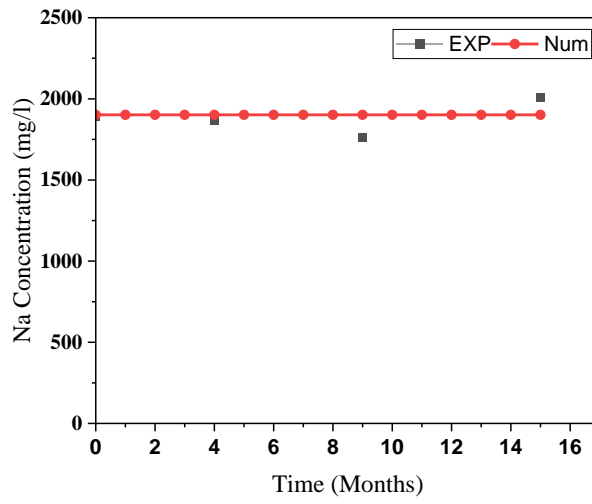
Figure 3.4: Na concentration variation over time.
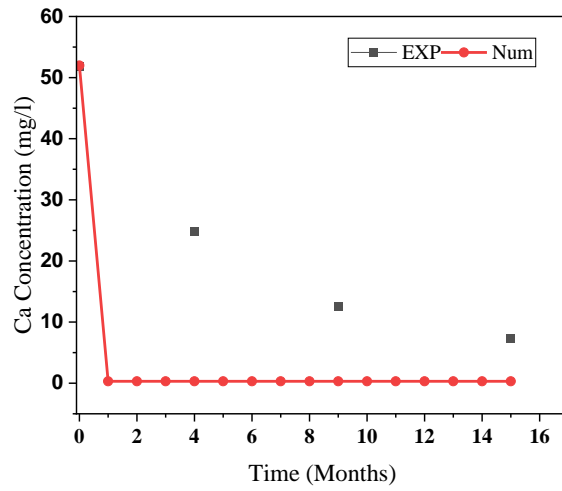
Figure 3.5: Ca concentration variation over time.
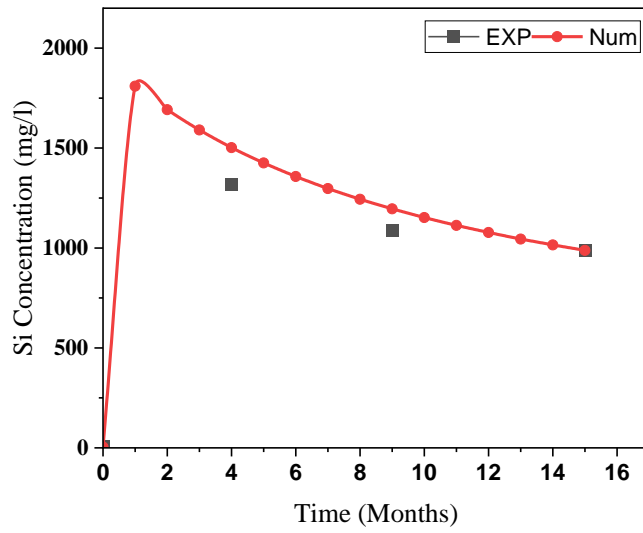
Figure 3.6: Si concentration variation over time.
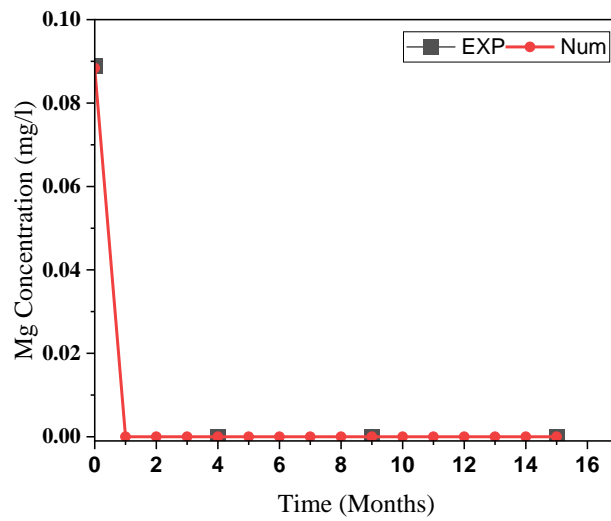
Figure 3.7: Mg concentration variation over time.
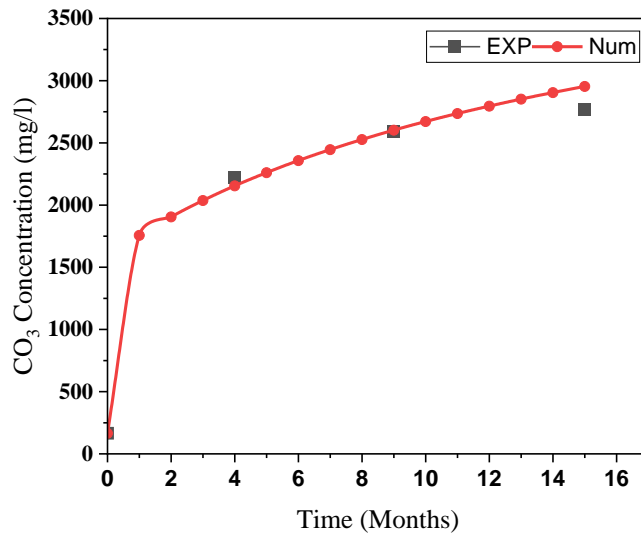
Figure 3.8: CO_3 concentration variation over time.
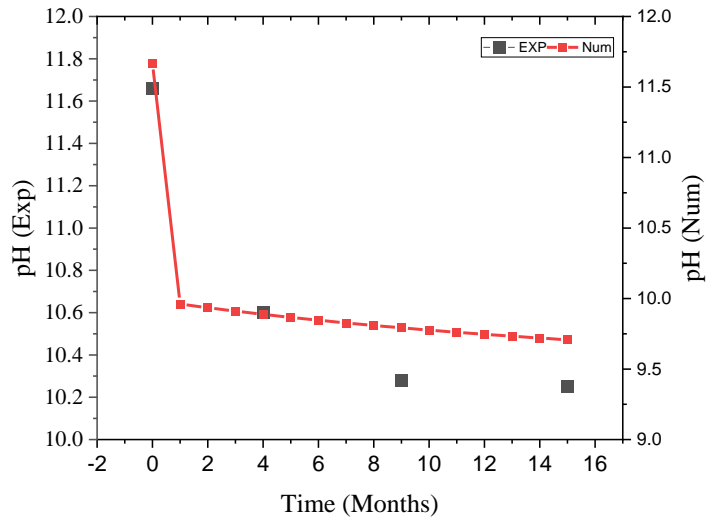
Figure 3.9: pH variation over time.
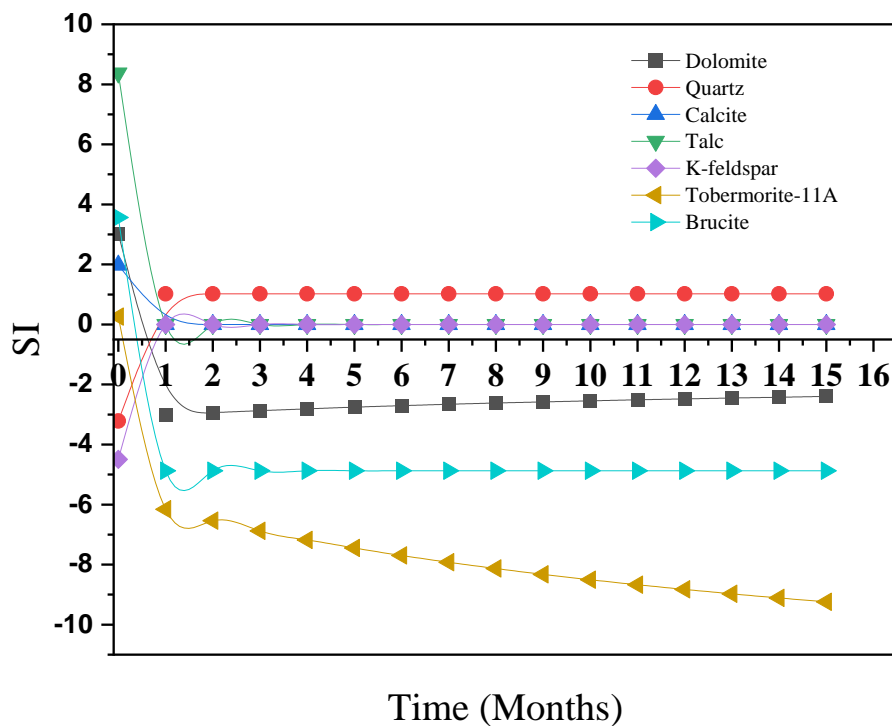
Figure 3.10: Variation in minerals saturation indices (SI) over time.

3.6 Conclusion

A "mixed kinetic and equilibrium" modelling approach, has been implemented to model the reaction of Borrowdale Volcanic Group (BVG) rock in contact with Young Near-Field Porewater (YNFP) over 15 months. The aim was to study the influence of high pH alkaline leachate on the chemical dissolution of the host rock in a geological disposal facility. The results indicate that (1) dolomite equilibria will be the most significant control during the reaction of this pore fluid with the BVG rock, (2) Na is not involved in mineral alteration

reactions, and (3) Ca^{2+} from dissolution of dolomite will be precipitated in the reaction, forming a variety of secondary mineral phases. Modelling multi-mineral evolution in the CDZ surrounding a nuclear waste geological disposal facility, characterised by both equilibrium and kinetic reactions, remains a challenging field. However, the results of this study suggest that this approach adopted offers greater insight into the long-term interactions between the high pH alkaline leachate and host rock for this scenario.

References

1. APPELO, C., BEEKMAN, H. & OOSTERBAAN, A. J. I. P. 1984. Hydrochemistry of springs from dolomite reefs in the southern Alps of northern Italy. 150**,** 125-138.
2. APPELO, C. & POSTMA, D. J. B., ROTERDAM 2005. Geochemistry, groundwater and pollution, CRC.
3. BETHKE, C. 1994. *The Geochemist's Workbench, Version 2.0: A Users Guide to Rxn, Act2, Tact, React, and Gtplot*, Craig M. Bethke.
4. BETHKE, C. 1996. *Geochemical reaction modeling: Concepts and applications*, Oxford University Press on Demand.
5. BLANC, P., LASSIN, A., PIANTONE, P., AZAROUAL, M., JACQUEMET, N., FABBRI, A. & GAUCHER, E. C. 2012. Thermoddem: A geochemical database focused on low temperature water/rock interactions and waste materials. *Applied Geochemistry,* 27**,** 2107-2116.
6. BRANTLEY, S. L., BLAI, A. C., CREMEENS, D. L., MACINNIS, I. & DARMODY, R. G. J. A. S. 1993. Natural etching rates of feldspar and hornblende. 55**,** 262-272.
7. BUSENBERG, E. & PLUMMER, L. N. 1982. The kinetics of dissolution of dolomite in CO2-H2O systems at 1.5 to 65oC and 0 to 1 atm PCO2. *American Journal of Science,* 282**,** 45-78.

8. CHEN, J. J., THOMAS, J. J., TAYLOR, H. F. & JENNINGS, H. M. 2004. Solubility and structure of calcium silicate hydrate. *Cement and concrete research,* 34**,** 1499-1519.

9. CHEN, X., PAO, W., THORNTON, S. & SMALL, J. 2016. Unsaturated hydro-mechanical–chemical constitutive coupled model based on mixture coupling theory: Hydration swelling and chemical osmosis. *International Journal of Engineering Science,* 104**,** 97-109.

10. CHEN, X. & THORNTON, S. 2018. Multi-Mineral Reactions Controlling Secondary Phase Evolution in a Hyper-Alkaline Plume. *Environmental Geotechnics*.

11. CHEN, X., THORNTON, S. F. & SMALL, J. 2015. Influence of hyper-alkaline pH leachate on mineral and porosity evolution in the chemically disturbed zone developed in the near-field host rock for a nuclear waste repository. *Transport in Porous Media,* 107**,** 489-505.

12. CORKHILL, C. L., BRIDGE, J. W., CHEN, X. C., HILLEL, P., THORNTON, S. F., ROMERO-GONZALEZ, M. E., BANWART, S. A. & HYATT, N. C. 2013. Real-time gamma imaging of technetium transport through natural and engineered porous materials for radioactive waste disposal. *Environmental science & technology,* 47**,** 13857-13864.

13. DE WINDT, L., MARSAL, F., TINSEAU, E., PELLEGRINI, D. J. P. & CHEMISTRY OF THE EARTH, P. A. B. C. 2008. Reactive transport modeling of geochemical interactions at a concrete/argillite interface, Tournemire site (France). 33**,** S295-S305.

14. FRANCIS, A., CATHER, R. & CROSSLAND, I. J. N. S. R. S., UNITED KINGDON NIREX LIMITED, 57P 1997. Development of the Nirex Reference Vault Backfill; report on current status in 1994.

15. JACQUES, D., LOTHENBACH, B., WIELAND, E., VAN LOON, L. R., MÜLLER, W., THIEN, B. M., KULIK, D. A., CURTI, E., PEGADO, L. & MARSALEK, O. 2014. Mechanisms and modelling of waste-cement and cement-host rock interactions Preface. PERGAMON-ELSEVIER SCIENCE LTD THE BOULEVARD, LANGFORD LANE, KIDLINGTON ….

16. KNAUSS, K. G. J. G. E. C. A. 1989. Muscovite dissolution kinetics as a function of pH and time at 70 C. 53, 1493-1501.

17. LOTHENBACH, B., KULIK, D. A., MATSCHEI, T., BALONIS, M., BAQUERIZO, L., DILNESA, B., MIRON, G. D. & MYERS, R. J. 2019. Cemdata18: A chemical thermodynamic database for hydrated Portland cements and alkali-activated materials. *Cement and Concrete Research,* 115, 472-506.

18. MERKEL, B. J., PLANER-FRIEDRICH, B., NORDSTROM, D. K. J. A. P. G. T. M. O. N. & SYSTEMS, C. A. 2005. Groundwater geochemistry. 2.

19. MOYCE, E. B., ROCHELLE, C., MORRIS, K., MILODOWSKI, A. E., CHEN, X., THORNTON, S., SMALL, J. S. & SHAW, S. J. A. G. 2014. Rock alteration in alkaline cement waters over 15 years and its relevance to the geological disposal of nuclear waste. 50, 91-105.

20. PARKHURST, D., THORSTENSON, D. & PLUMMER, L. J. W. R. I., RESTON, VA., USA 1980. PHREEQE. A computer program for geochemical calculations. Report 80-96, United States Geological Survey.

21. PARKHURST, D. L. & APPELO, C. 1999. User's guide to PHREEQC (Version 2): A computer program for speciation, batch-reaction, one-dimensional transport, and inverse geochemical calculations.

22. PETERSON, V. K., NEUMANN, D. A. & LIVINGSTON, R. A. 2005. Hydration of Tricalcium and Dicalcium Silicate Mixtures Studied Using Quasielastic Neutron Scattering. *The Journal of Physical Chemistry B,* 109, 14449-14453.

23. PLUMMER, L., WIGLEY, T. & PARKHURST, D. J. A. J. O. S. 1978. The kinetics of calcite dissolution in CO 2-water systems at 5 degrees to 60 degrees C and 0.0 to 1.0 atm CO 2. 278, 179-216.

24. RIMSTIDT, J. D. & BARNES, H. J. G. E. C. A. 1980. The kinetics of silica-water reactions. 44, 1683-1699.

25. ROCHELLE, C., MILODOWSKI, A., BATEMAN, K., MOYCE, E. & HUDSON-EDWARDS, K. 2016. A long-term experimental study of the reactivity of basement rock with highly alkaline cement waters: Reactions over the first 15 months. *Mineralogical Magazine,* 80, 1089-1113.

26. ROCHELLE, C., PEARCE, J., BATEMAN, K., COOMBS, P. & WETTON, P. 2001. *The Evaluation of Chemical Mass Transfer in the Disturbed Zone of a Deep Geological Disposal Facility for Radioactive Wastes. X, Interaction Between Synthetic Cement Porefluids and BVG: observations from Experiments of 4, 9, and 15 Months Duration: British Geological Survey, Fluid Processes Series, Technical Report WE/97/016.*

27. SCHWERTMANN, U. J. C. M. 1984. The influence of aluminium on iron oxides. IX. Dissolution of Al-goethites in 6 M HCl. 19**,** 9-19.

28. SIDHU, P., GILKES, R., CORNELL, R. & POSNER, A. Dissolution of iron oxides and oxyhydroxides in hydrochloric and perchloric acids. Clays Clay Miner, 1981. Citeseer.

29. SMALL, J., BRYAN, N., LLOYD, J., MILODOWSKI, A., SHAW, S. & MORRIS, K. 2016. Summary of the BIGRAD project and its implications for a geological disposal facility. *National Nuclear Laboratory, Report NNL (16),* 13817.

30. SOETAERT, K., HERMAN, P. M. & MIDDELBURG, J. J. J. G. E. C. A. 1996. A model of early diagenetic processes from the shelf to abyssal depths. 60**,** 1019-1040.

31. SVERDRUP, H. U. 1990. *The kinetics of base cation release due to chemical weathering*, Krieger Publishing Company.

32. TAYLOR, H. F. 1997. *Cement chemistry*, Thomas Telford.

33. TORRENT, J., SCHWERTMANN, U. & BARRON, V. J. C. M. 1987. The reductive dissolution of synthetic goethite and hematite in dithionite. 22**,** 329-337.

34. VAN DER LEE, J. 1997. HYTEC, un modèle couplé hydro-géochimique de migration de polluants et de colloïdes. *Technical Report LHM/RD/97/02.* CIG, École des Mines de Paris Fontainbleau, France.

35. VAN DER LEE, J. 1998. Thermodynamic and mathematical concepts of CHESS.

36. WORLEY, W. G. 1994. *Dissolution kinetics and mechanisms in quartz-and grainite-water systems.* Massachusetts Institute of Technology.

Chapter 4: Modelling of multi-mineral kinetical evolution in hyper-alkaline leachate for 15 years experiment

Abstract

Cement has been widely used for low- to intermediate-level radioactive waste management; however, the long-term modelling of multiple mineral transfer between the cement leachate and the host rock of a geological disposal facility remains a challenge due to the strong physical-chemical interactions within the chemically-disturbed zone. This paper presents a modelling study for a 15-year experiment simulating the reaction of crystalline basement rock with evolved near-field groundwater (pH = 10.8). A mixed kinetic equilibrium (MKE) modelling approach was employed to study the dolomite-rich fracture-filling assemblage reacting with intermediate cement leachate. The study found that the mineralogical and geochemical transformation of the system was driven by the kinetically-controlled dissolution of the primary minerals (dolomite, calcite, quartz, k-feldspar and muscovite). The initial high concentration of calcium ions appeared to be the main driving force initiating the dedolomitization process, which played a significant role in the precipitation of secondary talc, brucite and Mg-aluminosilicate minerals. The modelling study also showed that most of the initially precipitated calcium silicon hydrate phases redissolved and formed more stable calcium silicon aluminium hydrate phases. The findings highlight the importance of a deep and insightful understanding of the geochemical transformations based on the type and characteristics of the host rock and, where the system is under out of equilibrium conditions, the rates of mineral reactions.

List of Notations:

A_0	Initial Surface area
$f_{H^+}, f_{H_2O}, f_{OH}, f_{CO_2}$	Inhibition factors
$\dfrac{IAP}{K}$	Ion activity divided by equilibrium constant, equal to the saturation ratio (SR) of the reactant
k_k	Reactant empirical constant
$k_{H^+}, k_{H_2O}, k_{OH^-}, k_{CO_2}$	Solutes rate coefficients
k_1, k_2, k_3, k_4	Rate constants
m_k	Moles of reactant at a given time
m_{0k}	Initial moles of reactant
n	Order of reaction constant (Crystal grain size distribution)
P_{CO_2}	Partial pressure of carbon dioxide
R_k	Reactant overall dissolution rate
r_k	Reactant specific reaction rate
V	Solution volume
$[X]$	Ion activity of the element X

4.1 Introduction

Underground geological facilities are the most secure places to store/dispose of radioactive wastes generated during the civil/military programmes, and also generated through scientific, engineering and medical usage. One concept for low- and intermediate-level radioactive waste involves constructing an underground facility in a host rock at a depth of several hundred metres, then backfilling with a cementitious material. Such a facility is designed to achieve two main safety objectives: 1) to isolate the radioactive waste from the biosphere, and 2) to provide multiple barriers (including a high pH environment) to minimise radionuclide mobility over long timescales.

The containment system involves multiple barriers in which the engineered barriers work alongside natural ones (e.g. stable and low permeability host rock) to prevent the release of radionuclides to the biosphere. The concept has been adopted by several countries, including the UK, Sweden and South Korea (Authority 2010a; Francis et al. 1997; Kim et al. 2007; Skogsberg and Ingvarsson 2006). The final design and performance assessment of the engineered barrier can be influenced by the waste inventory, the surrounding conditions that can be expected during the performance assessment timescale and the degree of reaction with the surrounding host geology. Usually, the near field plays a crucial role in providing long-term control over radionuclide migration, which limits their release to the surrounding environment. Over time, the chemical properties (e.g., sorption capacity, reactive surface area) and physical properties (e.g., porosity, permeability) of the host rock in the near field barrier evolve as a result of the interactions with their surroundings and with other barriers. As this will happen long before any potential migration of

radionuclides, it is useful to understand and to be able to predict these changes, as they are likely to influence potential radionuclide retardation.

One of the challenges in evaluating the effectiveness of an engineered barrier is understanding the extent to which the evolving process of the near field host rock may occur. This will help in assuring that the engineered barrier materials will fulfil their safety functions over performance assessment timescales. The evolution of near field properties will strongly be linked to the interaction of the host rock and high pH water leaching out of the cement (the 'alkaline disturbed zone', ADZ).

Cement leachate is usually formed when the facility is closed and becomes saturated with groundwater that then reacts and equilibrates with the cementitious engineered barrier. The reaction process results in a high-pH plume that inhibits corrosion and limits some radionuclide solubility. Eventually, some cement leachate will migrate into the surrounding rock and create a chemically disturbed zone (CDZ) at the interface between the cement barrier and the host rock, initiating a series of reactions (Chen et al. 2016; Chen and Thornton 2018; Chen et al. 2015). The dissolution of primary minerals in the host rock is likely to be accompanied by precipitation of new minerals with evolved chemical and physical properties that may contribute to decreased radionuclide mobility through processes such as the reduction in permeability, increased sorption, and coprecipitation.

For a cement-based geological disposal facility, several experimental studies and numerical models have been performed to demonstrate the reaction of highly-alkaline

cement leachate with minerals in the host rock (Berner 1990; Harris et al. 2001a; Harris et al. 2001b; Schwyn et al. 2003). Previous research has considered three cement leachate evolution stages based on the progression of pH values (Small et al. 2016), which can be summarised as: young cement leachate (YCL), intermediate cement leachate (ICL) and old cement leachate (OCL). The reaction of ICL with the near field host rock is the focus of this study, and this may result in the formation of a changing series of mineral assemblages, changes to mineral surfaces, variations in pH, as well as other changes (Moyce et al. 2014). These processes will eventually affect the sorption capability of radionuclides at the mineral surface (Authority 2010b).

The paper aims to model mineral evolution in a 15-year laboratory experiment, analysing interlinks among multiple minerals known to occur in Borrowdale Volcanic Group (BVG) rocks in reaction with ICL by applying the concept of mixed kinetic equilibrium (MKE) approach (the BVG is an important basement rock in north-west England, and which was previously investigated by UK Nirex Limited (Francis et al. 1997). Importantly, the rock sample comprised a hydraulically-conductive dolomite-rich fracture, and thought dolomite is only a minor phase in the rock overall; it is a major phase in direct contact with current groundwater. The modelling process implements the concept of (MKE), which combines the advantages of both equilibrium and kinetic formulations to enable the modelling of complex geochemical reactions (Bethke 1994; Bethke 1996; Chen and Thornton 2018; Van der Lee 1997; Van der Lee 1998; Westall 1986). This approach was initially developed to overcome the shortage of kinetic data for minerals that dissolve and precipitate (Soetaert et al. 1996), assuming a faster reaction by means of the equilibrium concept and a slower

reaction controlled by the kinetic process (Atkinson et al. 1988; Hoch et al. 2012). The model is used to develop a deeper understanding of the pH evolution along with quantification of the amount of host rock minerals dissolving or precipitating in the near field/alkaline disturbed zone.

4.2 Experimental study

The experiment was conducted by the British Geological Survey (Moyce et al. 2014; Rochelle et al. 2016; Rochelle et al. 1997) over the course of 15 years, starting in 1995, and being part of a larger series of experiments of different durations. The original intent of the experiment was to study the reaction of a sample of Ordovician age Borrowdale Volcanic Group (BVG) rock with both a pH 13 'young near-field porewater' (YNFP) and a pH 12 'evolved near-field groundwater' (ENFG) (rock type and fluid naming convention based on that used in the Nirex Safety Assessment research programme [NSARP] at the time). These fluids represent, respectively, 'young cement leachate (YCL) and 'intermediate cement leachate' (ICL) (naming convention used in the BIGRAD project) released from a representative cementitious barrier that could be used in a deep geological disposal facility for intermediate-level radioactive waste. Although the experiments significantly exceeded their originally planned durations and also that of the NSARP, it was useful to continue them as the BVG contains many mineral phases typical of crystalline basement rocks in general. In the experiment of relevance to the study presented here, a dolomite-rich fracture assemblage in the BVG was reacted with YNFP, and the resultant solid and fluid products initially examined after 15 months and also for up to 15 years. The focus of the current study was to better understand the mineralogical evolution

of this experimental system for the entire 15 years, in order to investigate longer-term geochemical processes.
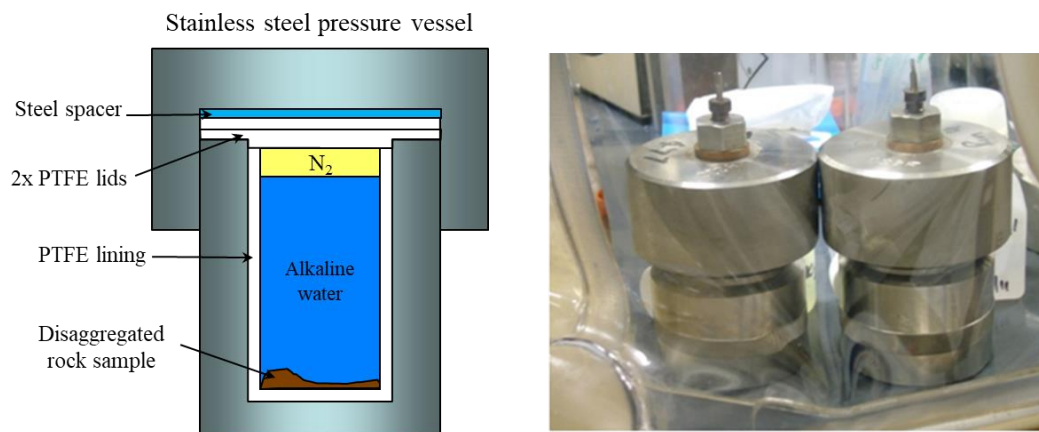
Figure 4.1: Actual and schematic diagram of stainless steel pressure vessels lined with Teflon® used to contain the BVG and synthetic CDZ-type fluid experiments.

Two PTFE-lined stainless steel vessels, of 150 mL and 100 mL, were used for the 'reacting' and blank experiments, respectively (Figure 4.1). The solid phase consisted of a piece of drill core containing altered wall rock and a dolomite-rich fracture fill from a hydrogeological conductive fracture zone in the BVG. The 2-kg rock sample was then disaggregated and sieved (Moyce et al. 2014; Rochelle et al. 1997). In the 'reacting' experiment, 35 g of disaggregated BVG was used with 140 g of groundwater-cement leachate, and the stainless-steel vessel was kept in a 70°C oven. The smaller blank experiment just contained the leachate. The ENFG leachate was presented by slightly saline water (Na/CaCl) saturated with $Ca(OH)_2$ (Table 4.1). All preparation processes were performed under a nitrogen atmosphere to prevent reaction of the alkaline water with atmospheric carbon dioxide. During the reaction, the rock underwent mineralogical changes that changed the concentration of the dissolved ions in the ENFG leachate.

Experiments were terminated and sampled after the fourth, ninth and fifteenth months (Rochelle et al. 2016; Rochelle et al. 1997), and importantly also at the end of the fifteenth year (Moyce et al. 2014). The solid experimental residues were washed in propan-2-ol and then dried prior to storage and analysis. For X-ray diffraction analysis, a subsample was milled and a 10% corundum (Al_2O_3) standard added. A diffractometer instrument (PANalytical X'Pert Pro) with PANalytical X'Pert Highscore Plus software was then used to carry out the final mineralogical analysis (Moyce et al. 2014; Rochelle et al. 2016).

Table 4.1: Composition of the Evolved Near-Field Groundwater (ENFG) prepared by the British Geological Survey (Rochelle et al. 2016; Rochelle et al. 1997).

Chemical component	Concentration (mg/L)
Al	4.17
B	0.335
Ba	0.017
Br	23.2
CO_3	20
Ca	1930
Cl	15100
F	0.03
Fe	0.120
K	185
Li	0.153
Mg	0.117
Mn	0.010
Na	9160
SO_4	1090
NO_3	20
Si	2.07
Sr	166
pH (at 70ºC)	10.84

4.3 Modelling Methodology

The conceptual model developed for this study is presented in Figure (4.2). The idea was developed based on theoretical and experimental analysis. The MKE approach is based upon the timescale of each mineral reaction rate (i.e., which reaction is faster and which

slower). For each mineral, either a kinetic or equilibrium approach, or a mix of both (if the difference between rates was more than 10^2), was used to provide the supporting information for the software. The concept of MKE has been widely implemented in subsurface geochemical applications, as it allows both kinetic and equilibrium reactions to model a multiphase and multi-component system (Brun and Engesgaard 2002; Lichtner 1996; Mayer et al. 2002; Prommer et al. 2003).
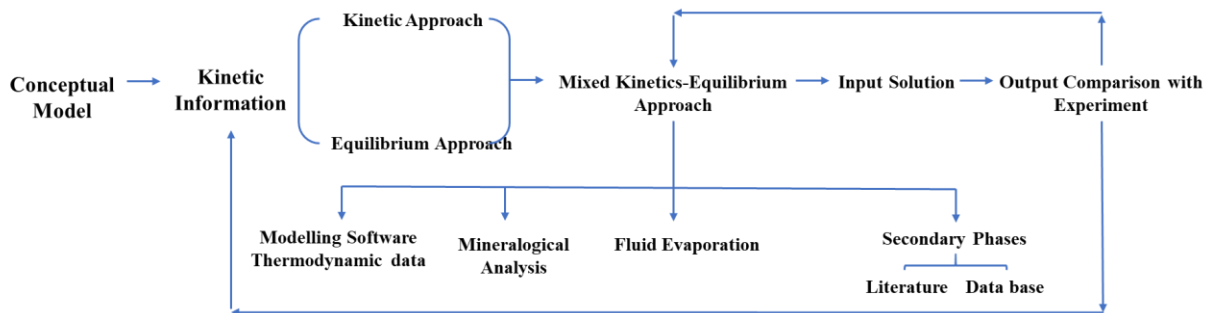
Figure 4.2: Conceptual Model for the Mixed Kinetic-Equilibrium approach.

4.3.1 Conceptual model software and thermodynamic data

The simulation carried out in this study was performed with the PHREEQC code (version 3.6.1). The software can compute a wide range of chemical reactions in aqueous geochemical systems, utilising both chemical thermodynamic and kinetic data. In recent years, several databases have been developed by various authors to optimise the use of this geochemical code. For a cement leachate–host rock reaction in an underground repository, the Lawrence Livermore National Laboratory (LLNL), Thermoddem, Thermoddem DB and CEMDATA DB databases were applied by previous researchers (Blanc et al. 2012; Lothenbach et al. 2019; Wolery 1992; Wolery and Daveler 1992). In this work, LLNL

database (Delany and Lundeen 1990) –was utilise though with some modifications, namely; the addition of kinetic information for calcium silicon hydrate (CSH) and calcium silicon aluminium hydrate phases (CASH). This database seemed to be the best option available since it has kinetic information for a variety of minerals and aqueous species, especially carbonate minerals that are required for the simulation of phases present in the BVG rock sample. The data of thermodynamic reactions (equilibrium constants) for the major minerals are shown in Table (4.2) (Chen and Thornton 2018). Note that the below values of $log\ K_{eq}$ are valid for the experiment condition.

Table 4.2: Reactions and equilibrium constants for minerals used in the calculations.

Mineral	Reaction	Log Keq
Calcite	$CaCO_3 + H^+ = Ca^{++} + HCO_3^-$	1.8487
Muscovite	$KAl_3Si_3O_{10}(OH)_2 + 10H^+ = K^+ + 3Al^{+++} + 3SiO_2 + 6H_2O$	13.5858
Kaolinite	$Al_2Si_2O_5(OH)_4 + 6H^+ = \ \ +2Al^{+++} + 2SiO_2 + 5H_2O$	6.8101
Quartz	$SiO_2 = +1.0\ SiO_2$	-3.9993
Dolomite	$CaMg(CO_3)_2 + 2H^+ = +1.0Ca^{++} + 1.0\ Mg^{++} + 2\ HCO_3^-$	2.5135
K-feldspar	$KAlSi3O8 + 4.0000\ H+ = + 1.0000\ Al+++ + 1.0000\ K+ + 2.0000\ H2O + 3.0000\ SiO2$	-0.2753
Brucite	$Mg(OH)_2 + 2H^+ \ = \ + 1.0\ Mg^{++} + 2H_2O$	16.2980
Tobermorite-11A	$Ca_5Si_6H_{11}O_{22.5} + 10H^+ = +5Ca^{++} + 6SiO_2 + 10.5H_2O$	65.6121
Saponite-Mg	$Mg3.165Al.33Si3.67O10(OH)2 + 7.3200\ H+ = + 0.3300\ Al+++ + 3.1650\ Mg++ + 3.6700\ SiO2 + 4.6600\ H2O$	26.2523
Nontronite-Mg	$Mg.165Fe2Al.33Si3.67H2O12 + 7.3200\ H+ = + 0.1650\ Mg++ + 0.3300\ Al+++ + 2.0000\ Fe+++ + 3.6700\ SiO2 + 4.6600\ H2O$	-11.6200
Talc	$Mg3Si4O10(OH)2 + 6.0000\ H+ \ = \ + 3.0000\ Mg++ + 4.0000\ H2O + 4.0000\ SiO2$	21.1383
Mesolite (Zeolite)	$Na.676Ca.657Al1.99Si3.01O10:2.647H2O + 7.9600\ H+ = + 0.6570\ Ca++ + 0.6760\ Na+ + 1.9900\ Al+++ + 3.0100\ SiO2 + 6.6270\ H2O$	13.6191
Stilbite (Zeolite)	$Ca1.019Na.136K.006Al2.18Si6.82O18:7.33H2O + 8.7200\ H+ = + 0.0060\ K+ + 0.1360\ Na+ + 1.0190\ Ca++ + 2.1800\ Al+++ + 6.8200\ SiO2 + 11.6900\ H2O$	1.0545

4.3.2 Mineralogical analysis and kinetic information

The mineralogical composition of the BVG rock used in the experiment is shown in Table (4.3). The concept of MKE was applied to the minerals existing in the rock that react with the ENFG leachate. The initial mass of each reactant was calculated based upon its abundance in the 35 g BVG sample (Rochelle et al. 2016; Rochelle et al. 1997). Note that the original rock sample showed some traces of other fracture filling phases such as clays, but these were not included in the model.

Table 4.3: BVG rock sample composition. Analysis conducted by the British Geological Survey (Rochelle et al. 2016; Rochelle et al. 1997). The mass of each phase (m_0) is calculated based on a 35g rock sample.

Mineral	Weight %	m_0 (g)
Orthoclase	12	4.2
Quartz	41	14.35
Dolomite	29	10.15
Muscovite	13	4.55
Hematite	2	0.7
Calcite	3	1.05

When cement leachate encounters the surrounding host rock, they will be out of chemical equilibrium, and local dissolution of existing 'primary' minerals will occur. The process releases new solutes into the reaction system, resulting in the precipitation of new 'secondary' minerals. Some secondary phases can have enhanced sorption and permeability-limiting properties relative to the primary phases, and are thus beneficial in term of limiting radionuclide migration. Thus, it is important to be able to describe/model the temporal evolution of these phases.

Commonly, the rate of mineral dissolution is measured experimentally by measuring the rate of change in solute concentration as a function of time under 'far from equilibrium'

conditions. To model the experimental values of dissolution and precipitation, a variety of factors must first be addressed, which include: the reactive surface area of the mineral, initial and final amounts, the specific dissolution rate constant, and slowing of reaction as equilibrium is approached. The availability of these data is one of the challenges in the field of modelling mineral dissolution and precipitation. The MKE approach is implemented to overcome that drawback with a proper representation of the geochemical system. Equation (4.1) is a general form that is usually used to calculate the overall dissolution rate of minerals (Appelo and Postma 2005; Parkhurst and Appelo 1999; Rimstidt and Barnes 1980).

$$R_k = r_k \frac{A_0}{V} \left(\frac{m_k}{m_{0k}}\right)^n \quad (4.1)$$

where

$$r_k = k_k \left(1 - \left(\frac{IAP}{K}\right)_k\right) \quad (4.2)$$

R is the overall dissolution rate into solution (mol L^{-1} s^{-1}), k_k is the specific dissolution rate (mol/m^2/s), A_0 is the initial surface area (m^2), V is the solution volume (L), m is the moles at a given time and m_0 is the initial moles. $(m_k/m_{0k})^n$ is an interpretation of the changes in the reactive surface area as a result of changes in the size of the mineral during the dissolution process. The value of $n = 2/3$ (Appelo and Postma 2005). (IAP/K) (i.e., ion activity divided by equilibrium constant) is equal to the saturation ratio *(SR)* of the reactant.

It is worth noting that clay minerals were not the focus of the original experiment, and that the exact mica/clay phase(s) present in the fracture of the BVG rock were not fully

identified (Moyce et al. 2014). However, muscovite was chosen to represent this phase(s) in the modelling process to control aluminium concentration in solution. Table (4.4) shows the kinetic information (reaction rate constant, reactive surface area, solution volume) obtained from the literature for the minerals in BVG that were modelled by the MKE approach (k-feldspar, quartz, dolomite, calcite, muscovite). Conversely, hematite was modelled by the equilibrium approach only, because of its low percentage in the rock sample (2%) and its assumed minimal influence on the mineralogical evolution process. In terms of the precipitation process, for most minerals the kinetics and specific rates of precipitation are unknown. Therefore, the precipitation of secondary phases was modelled assuming control by thermodynamic equilibrium.

Table 4.4: Modelling parameters for the BVG rock. MKE (mixed kinetic equilibrium)

Mineral	Modelling	Solution Volume (L)	Surface area (m²/g)	Rate constant (mol m⁻² s⁻¹)
Orthoclase	MKE		0.02 (De Windt et al. 2008)	k (using equation 4.5) (Appelo and Postma 2005)
Quartz	MKE		0.02 (De Windt et al. 2008)	$k = 1x10^{-12.2}$ (70°C) (Worley 1994)
Dolomite	MKE	0.14 (Rochelle et al. 2016)	0.02 (De Windt et al. 2008)	$k= 1.2x10^{-12}$ (Appelo and Postma 2005) This value was lowered two orders of magnitude ($k= 1.2x10^{-10}$)
Muscovite	MKE		1.1 (Knauss 1989)	$k=10^{-18.1}$ (Knauss 1989)
Calcite	MKE		0.02 (De Windt et al. 2008)	$k1 = 10^{(0.198 - 444.0 / (273.16 + T))}$ $k2 = 10^{(2.84 - 2177.0 / (273.16 + T))}$ $k3 = 10^{(-1.1 - 1737.0 / (273.16 + T))}$ in which T denotes temperature. (Appelo and Postma 2005; Plummer et al. 1978)
Hematite	Equilibrium	-	-	-

1) *Quartz* (SiO_2)

As per equation (4.1) and (4.2), the overall dissolution kinetic equation for quartz will be:

$$R_{Quartz} = k_{Quartz} \left(\frac{A_0}{V}\right) \left(\frac{m}{m_0}\right)^{0.67} \left(1 - \left(\frac{IAP}{K}\right)_{Quartz}\right) \qquad (4.3)$$

2) K-feldspar ($KAlSi_3O_8$)

The overall dissolution rate proposed by (Appelo and Postma 2005; Parkhurst and Appelo 1999) is used to simulate k-feldspar reaction at specific temperatures and pH value:

$$R_{K-feldspar} = k_{K-feldspar} \left(\frac{A_0}{V}\right) \left(\frac{m}{m_0}\right)^{0.67} \left(1 - \left(\frac{IAP}{K}\right)_{K-feldspar}\right) \quad (4.4)$$

where

$$k_{K-feldspar} = k_{H^+} \frac{[H^+]^{0.5}}{f_H} + k_{H_2O} \frac{1}{f_{H_2O}} + k_{OH^-} \frac{[OH^-]^{0.3}}{f_{OH}} + k_{CO_2} \frac{[P_{CO_2}]^{0.6}}{f_{CO_2}} \quad (4.5)$$

where $k_{K-feldspar}$ is the specific reaction rate (mol m^{-2} s^{-1}), k_i are the solute rate coefficients (mol m^{-2} s^{-1}), and f_i are inhibition factors.

3) Calcite ($CaCO_3$)

The specific dissolution rate for calcite was described by (Appelo and Postma 2005; Parkhurst and Appelo 1999; Plummer et al. 1978):

$$r_{calcite} = \left[k_1[H^+] + k_2[H_2CO_3] + k_3[H_2O]\right] * \left[1 - \left(\frac{IAP}{K}\right)^{\frac{2}{3}}_{Calcite}\right] \quad (4.6)$$

from equation (4.1), the overall dissolution rate of calcite will then be:

$$R_{calcite} = r_{calcite} \left(\frac{A_0}{V}\right) \left(\frac{m}{m_0}\right)^{0.67} \quad (4.7)$$

The value of the coefficients k_1, k_2 and k_3 in equations (4.6) are calculated by (Plummer et al. 1978) by fitting them to the experimental data as a function of temperature.

4) Dolomite $[CaMg(CO_3)_2]$

The specific dissolution rate of dolomite is described below by (Appelo et al. 1984; Appelo and Postma 2005; Parkhurst and Appelo 1999).

$$r_{Dolomite} = -k_{Dolomite} \, log \left(\frac{IAP}{K}\right)_{Dolomite} \qquad (4.8)$$

then, the overall dissolution rate of dolomite will be:

$$R_{Dolomite} = r_{Dolomite} \left(\frac{A_0}{V}\right)\left(\frac{m}{m_0}\right)^{0.67} \qquad (4.9)$$

5) Muscovite $[KAl_2(AlSi_3O_{10})(OH)_2]$

The specific dissolution rate for muscovite was calculated from the below equation, which was described by (Knauss 1989):

$$r_{Muscovite} = 10^{-18.1}[a_{H^+}]^{+0.22} \qquad (4.10)$$

then, as per equation (4.1), the overall dissolution rate of muscovite will be:

$$R_{Muscovite} = r_{Muscovite} \left(\frac{A_0}{V}\right)\left(\frac{m}{m_0}\right)^{0.67} \qquad (4.11)$$

4.3.3 Fluid evaporation

Over the 15-year experiment period, (Rochelle et al. 2016; Rochelle et al. 1997) note that some of the reacting fluid was lost, most likely through diffusion around the threads in the steel vessel. Measures were not taken to limit this process, because the experiments were only initially planned to only run for <18 months. The extent of this process could be estimated based on measured increases in the concentration of conservative (i.e. inactive) dissolved ions in the experiment. In both ENFG experiments (blank and reactive), the chloride ion was set as the inactive and conservative species over the entire experiment

period. It was observed that the rate of change in chloride ion concentration was the same in both solutions, and amounted to a 34% fluid loss (Moyce et al. 2014). It is crucial that modelling includes this fluid loss since this loss affects the concentration value (usually measured in mg/L) of all the ions released into the solution. In the modelling procedure, the simulated result of the chloride ion concentration indicated only a 22% fluid loss.

4.3.4 Secondary phases

During the reaction period of 15 years, the chemical characteristics of the system would significantly evolve and result in multiple cycles of mineral dissolution and precipitation reactions. The type of precipitated secondary mineral can vary over the entire experimental period. In this study, two time periods were defined: from 0 to 15 months (short-term mineral evolution) and from 15 months to 15 years (long-term mineral evolution). In numerical simulations, the specification of each expected secondary mineral was defined to allow its precipitation after saturation. In the modelling process, attention was paid to minerals that were actually observed in the experiments, together with ones that might precipitate (i.e. with saturation index close to zero), in order to achieve more accurate results. Moreover, the list of secondary minerals being tracked during the modelling should reasonably embrace the range of chemical ions represented in the experiment. Finally, the stability range of realistic secondary phases being modelled should be coincident with the experimental conditions (e.g. especially temperature and pH).

Several previous experimental studies have shown that when high-pH calcium-bearing cement leachate reacts with the host rock in the CDZ, the primary silicate dissolves, followed mostly by the precipitation of secondary CSH phases with different calcium-to-

silicon ratios (Bateman et al. 1999; Braney et al. 1993; Gaucher and Blanc 2006; Hodgkinson and Hughes 1999; Mäder et al. 2006; Savage and Rochelle 1993). Where the system also includes aluminosilicate minerals (Equations 4.12 and 4.13) and potassium (from minerals or the cement leachate), then secondary phases of aluminium- and potassium-bearing minerals (C-[Al]-[K]-S-H) also precipitate (Braney et al. 1993; Savage et al. 1992). Carbonate minerals, especially dolomite, can also play a significant role in the precipitation of other, secondary carbonates (e.g., calcite, Equation 4.14) when reacting with cement porewater leachate (Braithwaite and Heath 2013; Poole and Sotiropoulos 1980). Their relatively fast dissolution reaction compared to silicate minerals can control fluid chemistry during the early stages of the reaction (Bérubé et al. 1990; Choquette et al. 1991). Modelling studies have also shown that the reaction time and the composition of the primary solution (e.g., pH) are the two dominant factors in controlling the precipitating phases. Those studies also indicate that over time, CSH gel will evolve into zeolite, feldspar and CSH minerals (Bateman et al. 1999; Braney et al. 1993; Fernández et al. 2010; Pfingsten et al. 2006; Savage et al. 1992; Savage and Rochelle 1993; Soler and Mäder 2007).

$$KAlSi_3O_8 + 3OH^- + 2H_2O \rightarrow Al(OH)_4^- + 3HSiO_{3\ (aq)}^- + K^+{}_{(aq)} \quad (4.12)$$

$$HSiO_{3\ (aq)}^- + Ca^{2+}{}_{(aq)} + H_2O \rightarrow C - S - H_{gel} \quad (4.13)$$

$$MgCa(CO_3)_2 + 2OH^- \rightarrow Mg(OH)_2 + CaCO_3 + CO_3^{2-}{}_{(aq)} \quad (4.14)$$
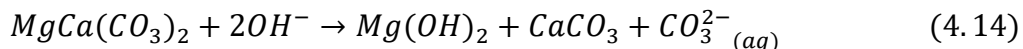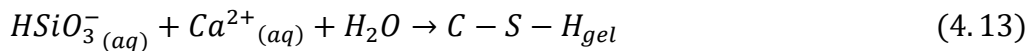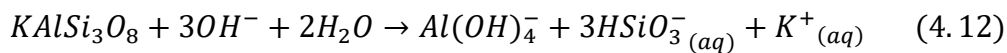
As the BVG rock sample was rich in dolomite, it was assumed that the dedolomitization process would result in an enormous number of magnesium and carbonate ions. This indicates that aqueous calcium ions can also be a driving force for the dissolution process

of dolomite, as well as the fluid pH level. At the beginning of the experiments (from 0 to 15 months), there was a low concentration of calcium ions in the YNFP, which led to undersaturation with respect to calcite and its dissolution. However, in the ENFG fluid, the system had a high concentration of calcium ions, which consumed all the aqueous ions of carbonate (CO_3^{2-}) to form the secondary calcite. Since the rock sample also included quartz and feldspar, the released magnesium ions were expected to react with both aqueous calcium and silica to form a secondary (Ca)-Mg-(Al)-(K)-silicate and ettringite (In case sulphate ions were in the solution), as demonstrated in the literature (Derkowski et al. 2013; Galí et al. 2001; Garcia et al. 2020; Schwarzenbach et al. 2013; Techer et al. 2012; Tinseau et al. 2006; Xie et al. 2013). Studies have also confirmed the formation of talc, smectite (Mg-saponite), illite and brucite as secondary Mg-rich phases during the dedolomitization process (Chen et al. 2018; Moyce et al. 2014; Rochelle et al. 2016). Figure (4.3) shows the conceptual model for mineral evolution during the dissolution and precipitation cycle of BVG rock reaction with ENFG fluid.
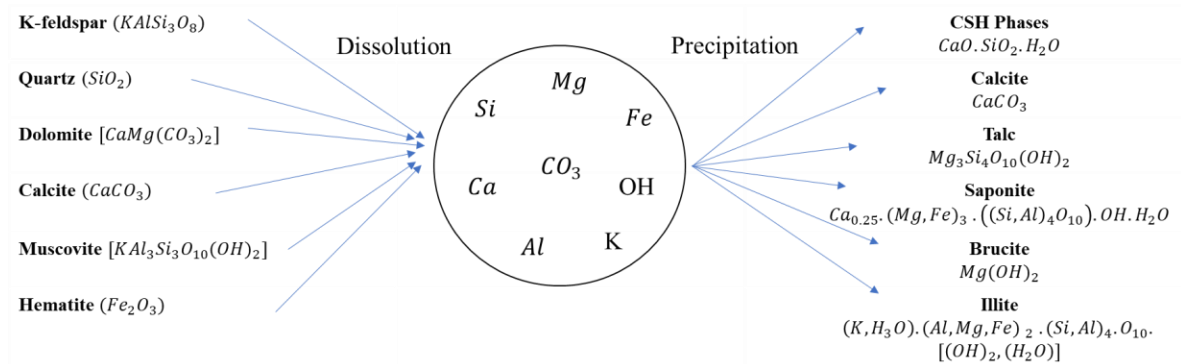
Figure 4.3: Conceptual model for minerals evolution during the dissolution and precipitation cycle of BVG reaction with ENFG.

4.4 Results and discussion

The reaction of BVG rock with ENFG was modelled over a simulated 15-year duration using the MKE approach. Changes in the concentration of Ca, Mg, Na, K, Al, Si, CO_3 and pH, as measured from the experiment, were analysed in the modelling simulations, and the comparison is shown in Figures (4.4–4.8). As an inactive ion, the chloride concentration (Figure 4.4, Plot A) increased in the solution as a result of the evaporation process, in line with the experimental data. Furthermore, since none of the primary minerals in the original rock sample included sodium and the potential secondary phases did not significantly consume sodium, the increase in sodium concentration (Plot A) also appears to be mainly a result of the evaporation process. This indicates that the sodium ion is also a conservative species in this geochemical system.

The dissolution process of quartz, which accounts for 41% of the BVG rock, released a significant amount of silicon into the highly alkaline solution in the first few months (Plot B). The availability of silicon ions along with the initial calcium concentration (plus calcium released from the dissolution of dolomite) then promoted the precipitation of secondary CSH and CASH phases, represented by a sharp drop in silicon concentration along with a decrease in calcium concentration (Plot C). The increase in potassium concentration (Plot D) was mostly linked to the evaporation plus the dissolution of k-feldspar and muscovite, which also released silicon and aluminium. This can be seen in the numerical results of Plot E, which show a small increase in aluminium concentration in the first few months. The concentration line then drops heavily and follows the experimental behaviour as a result of forming secondary aluminosilicate phases. The saturation index

lines in Figure (4.5) show that k-feldspar and muscovite both start with a higher dissolution rate than quartz, which defines the small peak in aluminium concentration in the beginning before it drops down as secondary calcium silicates start to precipitate. The figure also shows that muscovite was always undersaturated, and thus would have continued to dissolve, providing a source of aluminium for secondary phases. Moreover, the precipitation rates for talc, CSH gel and tobermorite (CSH) were all high in the first few months of the reaction (Figure 4.7). This high precipitation was mirrored by a substantial drop in silicon, aluminium and calcium concentrations at almost the same time. Note that in Figure (4.7), the positive value is for the dissolving process, whereas, negative for the precipitation process. Both CSH gel and tobermorite precipitated initially and redissolved after 18 months, with a similar kinetic rate. Talc started to precipitate from the beginning of the experiment and reached a stable amount after around 18 months. The initial concentration of magnesium in the leachate, plus that released during dedolomitization, drove brucite precipitation in the high pH conditions and created a sink for Mg (Bérubé et al. 1990; Cheng 1986), which also consumed hydroxyl ions and reduced the pH value. This rapid drop in pH in the first few months (Figure 4.4, Plot H) is also reflected in Figure (4.6), which shows a higher precipitation rate of brucite in the same period. Subsequently, the drop in the pH value progressively continued, but at a slower rate. From Figure 4.4 (Plot F), it is also clear that the initial magnesium ions were consumed in the first few months before the dedolomitization process took control. The saturation index of dolomite (Figure 4.5) shows that it was undersaturated (dissolving) in the geochemical system, but with a much slower rate as the pH value went below 9. This agrees with literature information (Min and Mingshu 1993), which suggests that dedolomitization does not occur

below pH 11. Despite that, dedolomitization still occurred in the geochemical system, but at a very slow rate. This is demonstrated by the high magnesium concentration (Evaporation can also play a part in this increase as well) at the end of the 15 years (Figure 4.4, Plot F), which was observed in the experiment as well (Moyce et al. 2014). The escalation of dedolomitization can be caused by the high concentration of Ca^{2+} in the ENFG, which promotes this process even at lower pH values. Dedolomitization provides calcium and aqueous CO_3^{2-}, which are removed effectively (Figure 4.4, Plot G) from the system by the precipitation of calcite (Bérubé et al. 1990). This can be seen in the saturation indices of calcite and brucite (Figure 4.6), which both precipitate in concurrence with the consumption of CO_3^{2-}. The extra amount of CO_3^{2-} in Equation (4.14) plus the amount released from the dissolution of calcite at later stages of the experiment is also reflected in Figure 4.4 (Plot G) which shows a small increase in (CO_3^{2-}) concentration. Thus, to incorporate the slow dedolomitisation process in the modelling, the specific dissolution rate of dolomite was lowered by two orders of magnitude. This compensates for the slower dolomitisation process below pH 11 but at the same time allows the process to take place, driven by the high concentration of calcium ions, especially at the early stage of the reaction. Another indication that supports the dedolomitization process is the high precipitation rate of Mg-silicate (talc and saponite-Mg), which was reflected by the higher dissolution rate of dolomite in the same period. Since brucite was close to saturation after the first few months (Figure 4.6), most of the released magnesium from the dedolomitization process was likely consumed during the formation of magnesium-silicate minerals, which is also recognised in other literature (Eglinton 1998; Glasser 2001).

After the large drop in the pH value, tobermorite and CSH gel starts to dissolve; at that time, a substitution between aluminium and silicon ions takes place to produce more stable calcium aluminosilicate hydrate (Myers et al. 2015; Richardson 2014; Richardson et al. 1993). This secondary CASH phase can then bind with the magnesium from the dedolomitization and create Mg-aluminosilicate (Galí et al. 2001; Moyce et al. 2014). This phenomenon highlights the importance of the modelling procedure for this kind of complex long-term geochemical reaction, as it allows a better understanding of the potential chemical and physical reactions that occur in the geosphere. It can also allow the extension of the timescale from relatively short-duration lab tests to the long timescales of performance assessments. Additionally, it can reveal the type of dissolved or precipitated secondary minerals that can contribute effectively to the retardation of radionuclide migration. For example, zeolites would be useful secondary phases as they have a high sorption capability to the radionuclide. Their considerable surface area and ion exchange capacity could play a key role in retarding radionuclide migration. Unfortunately, no evidence of zeolite precipitation was found in any of the NSARP experiments (Moyce et al. 2014; Rochelle et al. 2016). A plausible explanation for this is the rapid removal of silicon and aluminium by CSH and CASH phases that could suppress the formation of zeolites as they may have slower kinetic precipitation. Even though the modelling results obtained from the geochemical analysis showed potential for mesolite, stilbite and scolecite precipitation (based on the temperature of the experiment), which all are part of the zeolite family (Figure 4.8; (Bucher and Stober 2010; Bucher and Weisenberger 2013; Fridriksson et al. 1999; Weisenberger and Selbekk 2009)).

Even though those minerals did not precipitate in the experiment, this does not prove that the situation will be the same in the actual geosphere. The experimental design tried to mimic the actual environmental conditions as much as possible (rock type, temp, pH, etc.). However, there are still some variances, which can lead to different results. For example, as reported by (Adler et al. 1999), zeolite formation is preferred in the pore spaces in which leachate flux is minimal, and in these experiments the leachate: rock ratio was very high. The composition and nature of the rock type can also play a significant role, as it can affect the amount of CO_2 released into the leachate (e.g., depending on dolomite percentage), which can buffer the formation of zeolites (Mullis et al. 1994; Weisenberger and Bucher 2010). Taken together, the findings reveal the potentially important role of dolomite in the geochemical system. Moreover, they provide valuable insight into specific geochemical processes alongside the usefulness of iterating between modelling and experimental results to achieve a better understanding of the system under study.
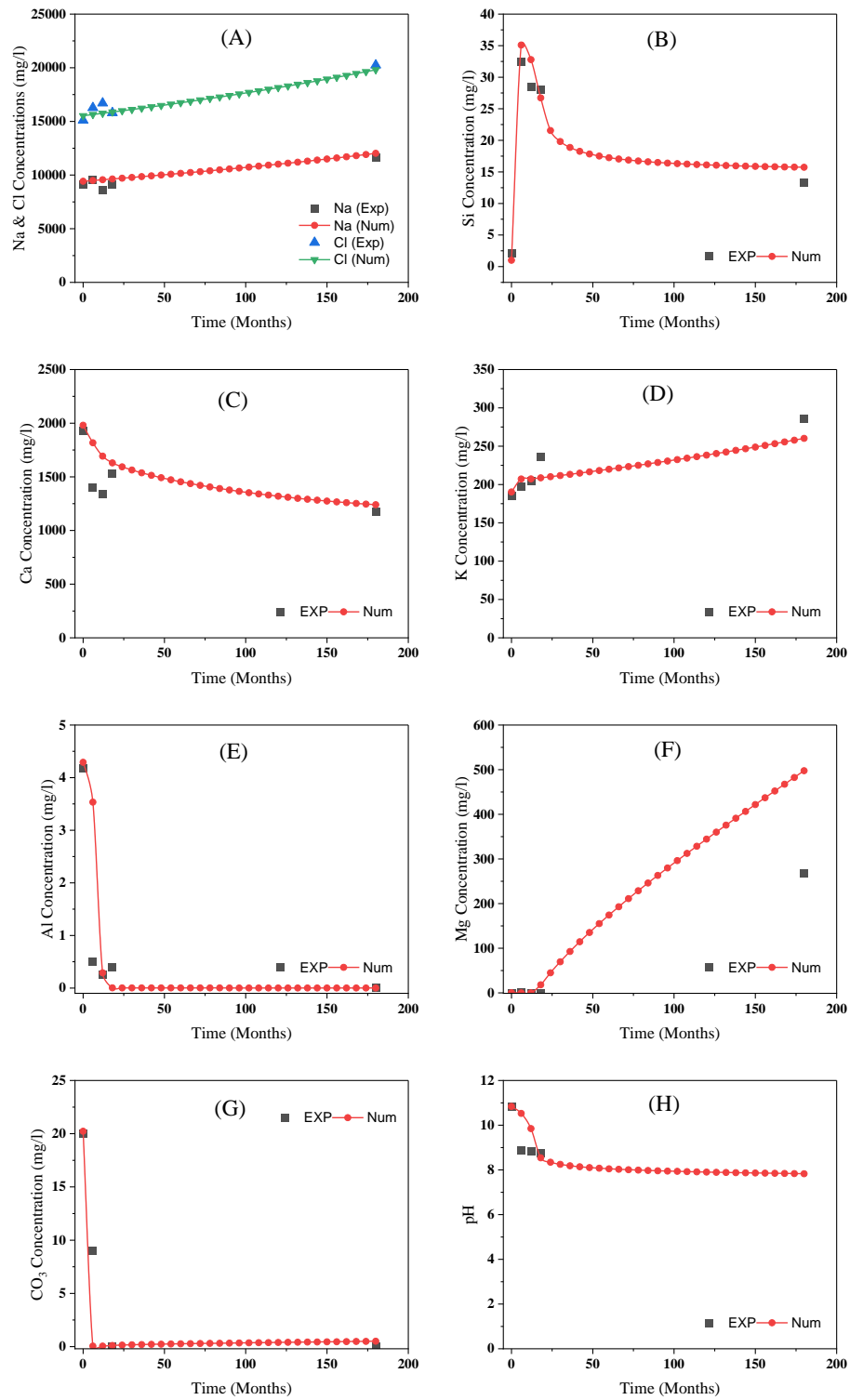
Figure 4.4: Modelled and experimental values for ions concentration and pH versus time.
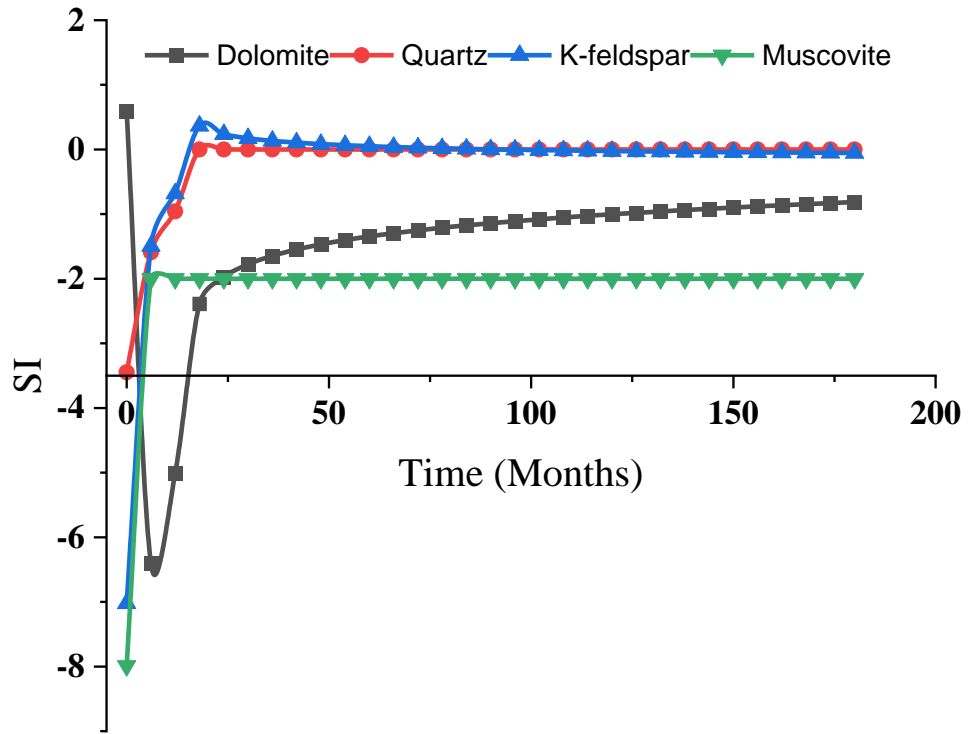
Figure 4.5: Saturation indices of primary mineral versus time.
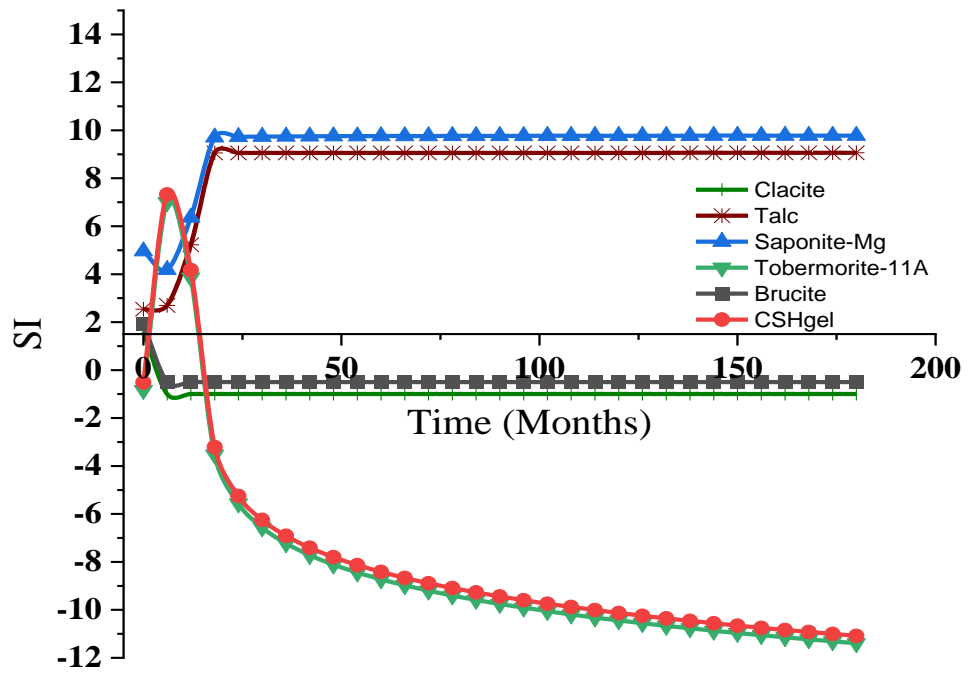
Figure 4.6: Saturation indices of secondary phases versus time.
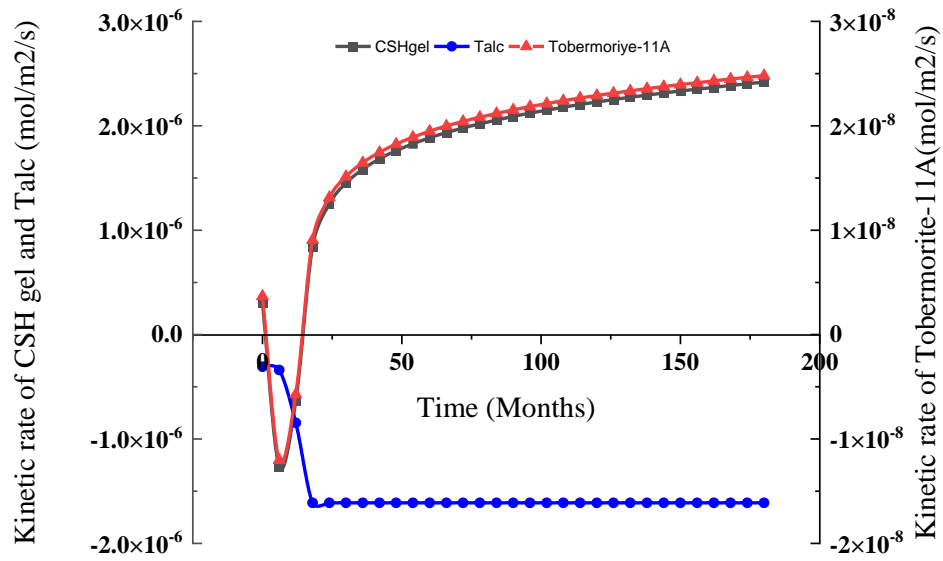
Figure 4.7: Kinetic rates for CSH gel, talc and tobermorite-11A versus time.
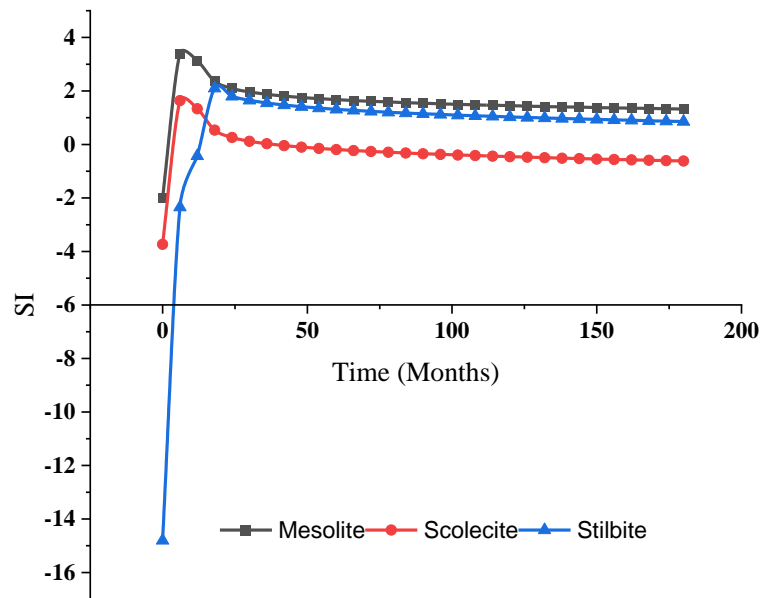
Figure 4.8: Zeolites minerals saturation indices versus time.

4.5 Conclusion

The construction of a cement-based, deep underground geological disposal facility for radioactive waste will result in an alkaline plume when groundwater equilibrates with minerals in the cement barrier. This will initiate a series of dissolution/precipitation reactions in the surrounding host rock, and consequent changes in physical, hydraulic, chemical and sorption properties long before any potential migration of radionuclides. It is useful to understand and to be able to predict these changes, as they are likely to influence the potential retardation of future radionuclide migration. This study modelled the mineralogical evolution and geochemical reactions of BVG rock in contact with ENFG. Importantly, the rock sample comprised a hydraulically-conductive dolomite-rich fracture, and though dolomite is only a minor phase in the rock overall, it is a major phase in direct contact with current groundwater. Simulations were conducted using PHREEQC, and predictions compared with data from experiments lasting up to fifteen years. The results showed that: (1) secondary phases such as talc, brucite and Mg-aluminosilicate precipitated, driven by dedolomitization; (2) solution pH initially dropped quickly as a result of brucite precipitation; (3) although zeolites were predicted stable secondary phases, they were absent in the experiments, possibly as a consequence of factors such as slow reaction kinetics, high leachate-to-rock ratios or elevated CO_2 concentrations. Overall, the modelling results of these long-term experiments indicate the important role of fluid-mineral reactions in controlling fluid chemistry and secondary phases, and so sufficient attention should be focused on the mineralogical composition of flowing features, as the minerals lining those can exert a critical influence on key geochemical reactions.

References

1. Adler M, Mäder U, Waber HN (1999) High-pH alteration of argillaceous rocks: an experimental study Schweiz Mineral Petrogr Mitt 79:445-454
2. Appelo C, Beekman H, Oosterbaan AJIP (1984) Hydrochemistry of springs from dolomite reefs in the southern Alps of northern Italy 150:125-138
3. Appelo C, Postma DJB, Roterdam (2005) Geochemistry, groundwater and pollution, CRC
4. Atkinson A, Everitt N, Guppy R (1988) Evolution of pH in a radwaste repository: Internal reactions between concrete constituents. UKAEA Harwell Lab.(UK). Materials Development Div,
5. Authority ND (2010a) Geological Disposal: Near-field evolution status report. NDA Report NDA/RWMD/033,
6. Authority ND (2010b) Geological Disposal: Steps Towards Implementation Nuclear Decommissioning Authority Report NDA/RWMD/013
7. Bateman K, Coombs P, Noy D, Pearce J, Wetton P, Haworth A, Linklater C (1999) Experimental simulation of the alkaline disturbed zone around a cementitious radioactive waste repository: numerical modelling and column experiments Geological Society, London, Special Publications 157:183-194
8. Berner U (1990) A thermodynamic description of the evolution of pore water chemistry and uranium speciation during the degradation of cement. Paul Scherrer Inst.(PSI),
9. Bérubé M-A, Choquette M, Locat J (1990) Effects of lime on common soil and rock forming minerals Applied Clay Science 5:145-163
10. Bethke C (1994) The Geochemist's Workbench, Version 2.0: A Users Guide to Rxn, Act2, Tact, React, and Gtplot. Craig M. Bethke,
11. Bethke C (1996) Geochemical reaction modeling: Concepts and applications. Oxford University Press on Demand,
12. Blanc P, Lassin A, Piantone P, Azaroual M, Jacquemet N, Fabbri A, Gaucher EC (2012) Thermoddem: A geochemical database focused on low temperature water/rock interactions and waste materials Applied Geochemistry 27:2107-2116

13. Braithwaite CJ, Heath RA Alkali–carbonate reactions and 'dedolomitization'in concrete: silica, the elephant in the corner. In, 2013. Geological Society of London,

14. Braney MC, Haworth A, Jefferies NL, Smith AC (1993) A study of the effects of an alkaline plume from a cementitious repository on geological materials Journal of Contaminant Hydrology 13:379-402 doi:https://doi.org/10.1016/0169-7722(93)90072-Z

15. Brun A, Engesgaard P (2002) Modelling of transport and biogeochemical processes in pollution plumes: literature review and model development Journal of Hydrology 256:211-227 doi:https://doi.org/10.1016/S0022-1694(01)00547-9

16. Bucher K, Stober I (2010) Fluids in the upper continental crust Geofluids 10:241-253

17. Bucher K, Weisenberger TB (2013) Fluid-induced mineral composition adjustments during exhumation: the case of Alpine stilbite Contributions to Mineralogy and Petrology 166:1489-1503

18. Chen X, Pao W, Thornton S, Small J (2016) Unsaturated hydro-mechanical–chemical constitutive coupled model based on mixture coupling theory: Hydration swelling and chemical osmosis International Journal of Engineering Science 104:97-109

19. Chen X, Thornton S (2018) Multi-Mineral Reactions Controlling Secondary Phase Evolution in a Hyper-Alkaline Plume Environmental Geotechnics

20. Chen X, Thornton SF, Pao WJIJoES (2018) Mathematical model of coupled dual chemical osmosis based on mixture-coupling theory 129:145-155

21. Chen X, Thornton SF, Small J (2015) Influence of hyper-alkaline pH leachate on mineral and porosity evolution in the chemically disturbed zone developed in the near-field host rock for a nuclear waste repository Transport in Porous Media 107:489-505

22. Cheng K Chemical consumption during alkaline flooding: A comparative evaluation. In: SPE Enhanced Oil Recovery Symposium, 1986. Society of Petroleum Engineers,

23. Choquette M, Berube M-A, Locat J (1991) Behavior of common rock-forming minerals in a strongly basic NaOH solution The Canadian Mineralogist 29:163-173

24. De Windt L, Marsal F, Tinseau E, Pellegrini DJP, Chemistry of the Earth PABC (2008) Reactive transport modeling of geochemical interactions at a concrete/argillite interface, Tournemire site (France) 33:S295-S305

25. Delany J, Lundeen S (1990) The LLNL thermochemical database Lawrence Livermore National Laboratory Report UCRL-21658 150

26. Derkowski A, Bristow TF, Wampler JM, Środoń J, Marynowski L, Elliott WC, Chamberlain CP (2013) Hydrothermal alteration of the Ediacaran Doushantuo Formation in the Yangtze Gorges area (South China) Geochimica et Cosmochimica Acta 107:279-298 doi:https://doi.org/10.1016/j.gca.2013.01.015

27. Eglinton M (1998) Resistance of concrete to destructive agencies Lea's chemistry of cement and concrete

28. Fernández R, Rodríguez M, Villa RVdl, Cuevas J (2010) Geochemical constraints on the stability of zeolites and C–S–H in the high pH reaction of bentonite Geochimica et Cosmochimica Acta 74:890-906 doi:https://doi.org/10.1016/j.gca.2009.10.042

29. Francis A, Cather R, Crossland IJNSRS, United Kingdon Nirex Limited, 57p (1997) Development of the Nirex Reference Vault Backfill; report on current status in 1994

30. Fridriksson T, Neuhoff P, Bird D, Arnórsson S (1999) Clays and zeolites record alteration history at Teigarhorn, eastern Iceland Geochemistry of the earth's surface Balkema, Rotterdam:377-380

31. Galí S, Ayora C, Alfonso P, Tauler E, Labrador M (2001) Kinetics of dolomite–portlandite reaction: Application to portland cement concrete Cement and Concrete Research 31:933-939 doi:https://doi.org/10.1016/S0008-8846(01)00499-9

32. Garcia E, Alfonso P, Tauler E (2020) Mineralogical Characterization of Dolomitic Aggregate Concrete: The Camarasa Dam (Catalonia, Spain) Minerals 10:117

33. Gaucher EC, Blanc P (2006) Cement/clay interactions – A review: Experiments, natural analogues, and modeling Waste Management 26:776-788 doi:https://doi.org/10.1016/j.wasman.2006.01.027

34. Glasser FP (2001) Mineralogical aspects of cement in radioactive waste disposal Mineralogical Magazine 65:621-633

35. Harris A, Hearne J, Nickerson A (2001a) The effect of reactive groundwaters on the behaviour of cementitious materials. AEA Technology Report AEAT/R/ENV/0467,

36. Harris A, Manning M, Thompson A (2001b) Testing of models of the dissolution of cements-leaching behaviour of Nirex Reference Vault Backfill. In: AEA Technology Report, AEAT/ERRA-0316. Nirex Ltd. Harwell, UK,

37. Hoch A, Baston G, Glasser F, Hunter F, Smith V (2012) Modelling evolution in the near field of a cementitious repository Mineralogical Magazine 76:3055-3069

38. Hodgkinson ES, Hughes CR (1999) The mineralogy and geochemistry of cement/rock reactions: high-resolution studies of experimental and analogue materials Geological Society, London, Special Publications 157:195-211

39. Kim Y-K et al. (2007) The Korean Final Repository for Low- and Intermediate-Level Radioactive Waste:1383-1387 doi:10.1115/ICEM2007-7130

40. Knauss KGJGeCA (1989) Muscovite dissolution kinetics as a function of pH and time at 70 C 53:1493-1501

41. Lichtner PC (1996) Continuum formulation of multicomponent-multiphase reactive transport Reviews in mineralogy 34:1-82

42. Lothenbach B et al. (2019) Cemdata18: A chemical thermodynamic database for hydrated Portland cements and alkali-activated materials Cement and Concrete Research 115:472-506

43. Mäder UK et al. (2006) Interaction of hyperalkaline fluid with fractured rock: Field and laboratory experiments of the HPF project (Grimsel Test Site, Switzerland) Journal of Geochemical Exploration 90:68-94 doi:https://doi.org/10.1016/j.gexplo.2005.09.006

44. Mayer KU, Frind EO, Blowes DW (2002) Multicomponent reactive transport modeling in variably saturated porous media using a generalized formulation for kinetically controlled reactions Water Resources Research 38:13-11-13-21

45. Min D, Mingshu T (1993) Mechanism of dedolomitization and expansion of dolomitic rocks Cement and Concrete Research 23:1397-1408

46. Moyce EB et al. (2014) Rock alteration in alkaline cement waters over 15 years and its relevance to the geological disposal of nuclear waste 50:91-105

47. Mullis J, Dubessy J, Poty B, O'Neil J (1994) Fluid regimes during late stages of a continental collision: Physical, chemical, and stable isotope measurements of fluid inclusions in fissure quartz from a geotraverse through the Central Alps, Switzerland Geochimica et cosmochimica Acta 58:2239-2267

48. Myers RJ, L'Hôpital E, Provis JL, Lothenbach B (2015) Effect of temperature and aluminium on calcium (alumino) silicate hydrate chemistry under equilibrium conditions Cement and Concrete Research 68:83-93

49. Parkhurst DL, Appelo C (1999) User's guide to PHREEQC (Version 2): A computer program for speciation, batch-reaction, one-dimensional transport, and inverse geochemical calculations

50. Pfingsten W, Paris B, Soler JM, Mäder UK (2006) Tracer and reactive transport modelling of the interaction between high-pH fluid and fractured rock: Field and laboratory experiments Journal of Geochemical Exploration 90:95-113

51. Plummer L, Wigley T, Parkhurst DJAjos (1978) The kinetics of calcite dissolution in CO 2-water systems at 5 degrees to 60 degrees C and 0.0 to 1.0 atm CO 2 278:179-216

52. Poole A, Sotiropoulos P (1980) Reactions between dolomitic aggregate and alkali pore fluids in concrete Quarterly Journal of Engineering Geology and Hydrogeology 13:281-287

53. Prommer H, Barry D, Zheng C (2003) MODFLOW/MT3DMS-based reactive multicomponent transport modeling Groundwater 41:247-257

54. Richardson IG (2014) Model structures for c-(a)-sh (i) Acta Crystallographica Section B: Structural Science, Crystal Engineering and Materials 70:903-923

55. Richardson IG, Brough AR, Brydson R, Groves GW, Dobson CM (1993) Location of aluminum in substituted calcium silicate hydrate (C-S-H) gels as determined by 29Si and 27Al NMR and EELS Journal of the American Ceramic Society 76:2285-2288

56. Rimstidt JD, Barnes HJGeCA (1980) The kinetics of silica-water reactions 44:1683-1699

57. Rochelle C, Milodowski A, Bateman K, Moyce E, Hudson-Edwards K (2016) A long-term experimental study of the reactivity of basement rock with highly alkaline cement waters: Reactions over the first 15 months Mineralogical Magazine 80:1089-1113

58. Rochelle C, Pearce J, Bateman K, Coombs P, Wetton P (1997) The Evaluation of Chemical Mass Transfer in the Disturbed Zone of a Deep Geological Disposal Facility for Radioactive Wastes. X, Interaction Between Synthetic Cement Porefluids

and BVG: observations from Experiments of 4, 9, and 15 Months Duration: British Geological Survey, Fluid Processes Series, Technical Report WE/97/016.

59. Savage D et al. (1992) Rate and mechanism of the reaction of silicates with cement pore fluids Applied Clay Science 7:33-45

60. Savage D, Rochelle CA (1993) Modelling reactions between cement pore fluids and rock: implications for porosity change Journal of Contaminant Hydrology 13:365-378 doi:https://doi.org/10.1016/0169-7722(93)90071-Y

61. Schwarzenbach EM, Lang SQ, Früh-Green GL, Lilley MD, Bernasconi SM, Méhay S (2013) Sources and cycling of carbon in continental, serpentinite-hosted alkaline springs in the Voltri Massif, Italy Lithos 177:226-244 doi:https://doi.org/10.1016/j.lithos.2013.07.009

62. Schwyn B, Wersin P, Berner U, Wieland E, Neall F (2003) Near-field chemistry of an ILW repository in Opalinus Clay Unpubl Nagra Internal Rep Nagra, Wettingen, Switzerland

63. Skogsberg M, Ingvarsson R (2006) Operational experience from SFR-Final repository for low-and intermediate level waste in Sweden.

64. Small J, Bryan N, Lloyd J, Milodowski A, Shaw S, Morris K (2016) Summary of the BIGRAD project and its implications for a geological disposal facility National Nuclear Laboratory, Report NNL (16) 13817

65. Soetaert K, Herman PM, Middelburg JJJGeCA (1996) A model of early diagenetic processes from the shelf to abyssal depths 60:1019-1040

66. Soler JM, Mäder UK (2007) Mineralogical alteration and associated permeability changes induced by a high-pH plume: Modeling of a granite core infiltration experiment Applied Geochemistry 22:17-29 doi:https://doi.org/10.1016/j.apgeochem.2006.07.015

67. Techer I, Bartier D, Boulvais P, Tinseau E, Suchorski K, Cabrera J, Dauzères A (2012) Tracing interactions between natural argillites and hyper-alkaline fluids from engineered cement paste and concrete: Chemical and isotopic monitoring of a 15-years old deep-disposal analogue Applied Geochemistry 27:1384-1402 doi:https://doi.org/10.1016/j.apgeochem.2011.08.013

68. Tinseau E, Bartier D, Hassouta L, Devol-Brown I, Stammose D (2006) Mineralogical characterization of the Tournemire argillite after in situ interaction with concretes Waste Management 26:789-800 doi:https://doi.org/10.1016/j.wasman.2006.01.024

69. Van der Lee J (1997) HYTEC, un modèle couplé hydro-géochimique de migration de polluants et de colloïdes. In: Technical Report LHM/RD/97/02. CIG, École des Mines de Paris Fontainbleau, France,

70. Van der Lee J (1998) Thermodynamic and mathematical concepts of CHESS

71. Weisenberger T, Bucher K (2010) Zeolites in fissures of granites and gneisses of the Central Alps Journal of Metamorphic Geology 28:825-847

72. Weisenberger T, Selbekk RS (2009) Multi-stage zeolite facies mineralization in the Hvalfjördur area, Iceland International Journal of Earth Sciences 98:985-999

73. Westall J (1986) „Zachary, J. L „Morel, FMM: MINEQL, a computer program for the calculation of the chemical equilibrium composition of aqueous systems. Tech. Note,

74. Wolery TJ (1992) EQ3/6, a software package for geochemical modeling of aqueous systems: package overview and installation guide (version 7.0)

75. Wolery TJ, Daveler SA (1992) EQ6, a computer program for reaction path modeling of aqueous geochemical systems: Theoretical manual, users guide, and related documentation (Version 7.0); Part 4. Lawrence Livermore National Lab., CA (United States),

76. Worley WG (1994) Dissolution kinetics and mechanisms in quartz-and grainite-water systems. Massachusetts Institute of Technology

77. Xie Q et al. (2013) Mechanism of palygorskite formation in the Red Clay Formation on the Chinese Loess Plateau, northwest China Geoderma 192:39-49 doi:https://doi.org/10.1016/j.geoderma.2012.07.021

Chapter 5: The influence of high pH leachate on a generic host rock for a nuclear waste repository: modelling of variable porosity and surface area

Abstract

Deep geological disposal is the preferred solution for long-term storage of radioactive waste in many countries. In a deep repository, cementitious materials are widely used in the structure and buffer/backfill of the repository for the stabilization of the hazardous materials. The cement acts as a physical barrier and also contributes chemically to waste containment by buffering the groundwater to a high pH, limiting the solubility of many radionuclides. This paper describes an experimental and modelling study which evaluates the geochemical interaction between young cement leachate (YCL, pH = 13) and a generic hard rock (in this case Hollington sandstone, representing a 'hard' host rock) during permeation with the leachate, as it drives mineralogical changes in the system. One-dimensional reactive transport was modelled using a mixing cell approach within the PHREEQC geochemical code to identify the essential parameters and understand and scale up the effect of variations in these parameters on the observed geochemical processes. This study also focused on the effects of variable porosity, reactive surface area and pore volume on improving the modelling of rock alteration in the system compared to conventional models that assume constant values for these properties. The numerical results showed that the interaction between the injected hyperalkaline leachate and the sandstone sample results in a series of mineralogical reactions. The main processes were the dissolution of quartz, kaolinite and k-feldspar which was coupled with the precipitation of Calcium silicate hydrate (CSH) gel and tobermorite-14A (C-S-H), prehnite (hydrated silicate), saponite-Mg (smectite clay) and mesolite (Na-Ca zeolite). The simulation showed that the

overall porosity of the system increased as primary minerals dissolve and no stable precipitation of the secondary C-S-H /C-A-S-H phases was predicted. The variable porosity scenario provides a better fitting to experimental data and more detailed trends of chemistry change within the column. The time and the number of moles of precipitated secondary phases were also improved which was related to greater exposure surface area of the minerals in the sandstone sample to the YCL.

List of Notations:

A_0	Initial Surface area of the mineral
A_i	Effective surface area of the mineral
A_r^t	Reactive surface area of the mineral at specific time
C_i	Total concentration of component i in water
D_L	Hydrodynamic dispersion coefficient
E_a	activation energy
$f_{H^+}, f_{H_2O}, f_{OH}, f_{CO_2}$	Inhibition factors
g	Gravity vector
$\dfrac{IAP}{K}$	Ion activity divided by equilibrium constant, equal to the saturation ratio (SR) of the reactant
$k_{H^+}, k_{H_2O}, k_{OH^-}, k_{CO_2}$	Solutes rate coefficients
l	Number of kinetic reactants
Lim_i	Limiting activity
m_t	Total mass of the rock sample
$m_{i,t}$	Mass of the reactant at given time
$m_{\frac{Diss}{prec}moles,t,i}$	Mass of dissolve/precipitated moles at given time
M	Moles of reactant
n	Order of reaction constant (Crystal grain size distribution)
p_l	Fluid pressure
P_{CO_2}	Partial pressure of carbon dioxide
q_l	Darcy flux for the liquid
R	gas constant
R_i	Reactant overall dissolution/precipitation rate
R_m	Overall dissolution/precipitation rate of kinetic reactant m
r_i	Reactant specific reaction rate
t	Time
v_{im}	Stoichiometric coefficient of component i in kinetic reactant m
V	Solution volume
V_m	Molar volume
V_{pore}	Pore fluid volume
V_{solid}	Solid volume of all minerals in the rock sample
V_T	Total solid and pore volume
$V_{\frac{Diss}{prec}mole,t}$	Volume of Dissolve/precipitated moles at given time
$[X]$	Ion activity of the element X
X_i	Mass fraction of each mineral in the rock sample
x	Distance
x_i	Empirical values
z_i	Empirical values
ϕ	Porosity
κ	Permeability tensor
μ_l	Liquid dynamic viscosity
ρ_l	Liquid density

5.1 Introduction

Radioactive waste includes abundant industrial residual materials that require a management plan for their safe disposal and containment, particularly due to their long-lived radioactivity and chemical toxicity. In many countries, the preferred method of radioactive waste disposal is immobilisation in copper or stainless-steel canisters and burial in an engineered deep geological disposal facility (Crossland, 2007). Cementitious materials are widely used in the structure and buffer/backfill of the repositories as part of a multi-barrier approach for the stabilization of the hazardous materials. The cement acts as a physical barrier and contributes chemically to waste containment by buffering the groundwater to a high pH, limiting the solubility of many radionuclides (Felipe-Sotelo et al., 2017).

The final assessment of any geological disposal relies on the ability of the host rock to retard the migration of contaminants to isolate them from the biosphere. Therefore, the safety assessment should predict the effect of the released radionuclides on the surrounding environment in the event of failure of the engineered barriers. Once a repository is closed, groundwater will interact with cementitious materials used to form the structure or in the waste form, and create a hyper-alkaline (up to pH 13.5) plume over time (Francis et al., 1997, Vasconcelos et al., 2018). This plume will migrate into the host rock, creating a chemically disturbed zone (CDZ). The chemical composition of the alkaline leachate emerging from the repository will continue to evolve over time as more ions are released from the cement minerals. The plume of young cement leachate (YCL) will also change as it migrates and reacts with the host rock minerals. Understanding the geochemical interactions that occur between the leachate and the host rock is critical, in order to define

the impact of the hyper-alkaline plume on the geological, mineralogical and physical behaviour of the host rock.

When high-pH leachate from a deep geological disposal facility migrates through a sandstone host rock, both mineral dissolution and precipitation processes will occur, changing the matrix porosity within the CDZ (Chen et al., 2015, Chen and Thornton, 2018). Dissolution of primary minerals (e.g. quartz, k-feldspar and aluminosilicate minerals) can increase the matrix porosity. In contrast, the precipitation of secondary clay minerals (e.g. saponite, illite and kaolinite) can reduce the porosity. The precipitated secondary minerals may have different sorption properties than the reacting primary minerals, which is important when considering the potential mobility of radionuclides. Several studies have examined the effects of an alkaline plume on clay minerals (Velde, 1965, Eberl and Hower, 1977, Mohnot et al., 1987, Chermak, 1993, Bauer and Berger, 1998). However, the kinetics of silicate mineral dissolution and precipitation kinetics of the secondary calcium silicate hydrate (C-S-H) and calcium aluminium silicate hydrate (C-A-S-H) phases in high-pH leachate, is less well known.

The British Geological Survey (BGS) conducted laboratory column experiments to investigate the mineralogical transformations and geochemical processes that may occur when a hyper-alkaline plume flows through sandstone (Small et al., 2016). The experiments provided a conceptual understanding of the processes involved, and information on essential parameters that control those processes. Although significant work has been done in the field of radionuclide fate and transport(Silva, 1991, Dozol and Hagemann, 1993, Savage, 1997, Monte et al., 2004, Putyrskaya and Klemt, 2007), describing how contaminants migrate through geological formations in which interactions

change physical and chemical properties of the host rock remains a challenge. The modelling of multiple geochemical kinetic reactions and the mineralogical evolution associated with hyper-alkaline leachate migration through host rock allows the role of mineral composition and geochemical properties on the chemical affinity and evolution of secondary C-S-H and C-A-S-H phases to be investigated.

This paper aims to model and evaluates the geochemical interaction between young cement leachate (YCL, pH = 13) and a generic hard rock (in this case Hollington sandstone, representing a 'hard' host rock) during permeation with the leachate, as it drives mineralogical changes in the system. The results of the column experiment undertaken by BGS (Small et al., 2016) are interpreted using the geochemical transport code PHREEQC (Parkhurst and Appelo, 2013) and the Lawrence Livermore National Laboratory (LLNL) database included therein.

The BGS experiment identified the key kinetic reactions and putative reactive pathways that controlled the primary mineral dissolution, mineral evolution, secondary mineral formation and column effluent evolution. The PHREEQC code can model and scale up multiple kinetic reactions to interpret effects due to variation in leachate chemistry from short duration of the laboratory experiments' to longer timescales. Additional modules were added to PHREEQC to calculate porosity changes resulting from the dissolution and precipitation reactions, and validated against the porosity changes observed in the column experiment. Fluid transport is usually modelled by a one-dimensional equation of the advection-dispersion process. The use of dynamic column experiment (transport process) allows the simulation of systems, in which the alkaline fluid flows through porous solid media under a steady-state flow regime. It also permits reactive transport to be studied for

either saturated or unsaturated soil. This study also focused on the effect of variable porosity, reactive surface area and pore volume on the alteration of the host rock, compared to fixed values of the same properties. The output from this modelling is then discussed for the near-field impacts anticipated at a deep geological repository.

5.2 Column experiment design

The model developed in this study was validated against the results of the BGS column experiment (Small et al., 2016), which was conducted as part of the Biogeochemical Gradients and Radionuclide Transport (BIGRAD, NE/H006464/1) project funded by the Natural Environment Research Council (NERC). The experiment consisted of a PEEK (Polyether ether ketone) column packed with crushed sandstone (see Figure 5.1; (Small et al., 2016). A solution representative of young cement leachate (pH 13.1 at 25°C) was pumped through the columns.
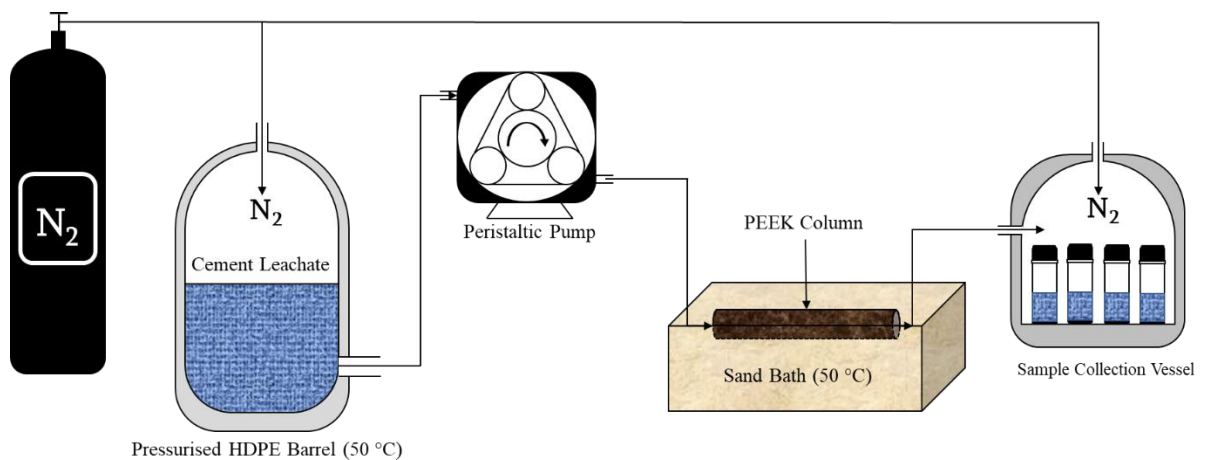
Figure 5.1: Schematic of the BGS column experiment.

5.2.1 Crushed sandstone

The crushed sandstone used in the packed columns was Hollington sandstone from the Triassic Bromsgrove formation in the UK Midlands (Small et al., 2016). The sandstone was initially disaggregated, sieved through a 500 µm nylon mesh, homogenised in a rotary blender and packed into the PEEK columns (7.5 mm diameter and 300 mm long). Table (5.1) shows the composition and proportion of minerals in the sandstone sample (Chen et al., 2015), determined by a combination of backscattered scanning electron microscopy, energy-dispersive X-ray microanalysis, microchemical mapping and petrographically image analysis.

After packing, the columns were first saturated by 37 pore volumes (PV) of demineralised water (produced by reverse osmosis followed by filtration and UV sterilisation). Next, 413 PV of the synthetic young cement leachate (YCL) was pumped though the column (composition reported in Table 5.2). The YCL was prepared with boiled, N_2-sparged, deionised water and was kept in 25-litre N_2 over-pressured container to avoid carbonation reactions and a reduction in the leachate pH.

Table 5.1: Mineralogical composition of Hollington Sandstone (Chen et al., 2015)

Mineral	Mineral proportion (Volume %)
Quartz	75.5
K-feldspar	16
Kaolinite	3.5
Illite/chlorite/smectite	3.7
Muscovite	0.7
Phlogopite	0.2
Apatite	0.2
TiO_2	0.3

Table 5.2: Chemical composition of the synthetic young cement leachate (YCL) used in the British Geological Survey column experiment (Small et al., 2016).

Composition	YCL (mg/L)
Al^{3+}	-
Ca^{2+}	23
K^+	3202
Mg^{2+}	0.07-
Na^+	2178
Si^{4+}	-
OH^-	3192*
Measured pH	13.1 at 25°C (12.4 at 50°C)

Notes: * Calculated by assuming charge balance with cations. Equivalent to pH 12.4 at 50°C.

5.2.2 Column operation and sampling

The column was placed in a 50°C sand bath and connected to a 25-litre reservoir containing synthetic YCL. The reservoirs were heated to the experimental temperature of 50°C, and their headspace pressurised with N_2 to prevent CO_2 from entering the system (one atmosphere over-pressure). A constant flux of YCL (0.6 mL/h) was passed through the column for 233 days using peristaltic pumps. Column effluents were collected under an N_2 atmosphere to minimise their exposure to atmospheric CO_2. Table (5.3) summarises the initial experimental parameters.

Table 5.3: Initial experimental parameters

Initial porosity	Initial wet weight (g)	Weight of rock (g)	Pore volume (mL)
42.7%	110.756	21.249	5.97

Column effluent samples were collected within an N_2-flushed chamber using individual plastic (PPE) bottles. All collected solutions were filtered using 0.2 µm syringe PTFE (Acrodisc™) filters and then sub-sampled to determine pH, cations, and anions. The pH of a sub-sample was determined immediately using a combination electrode, calibrated at pH

7, 10, 13 and accurate to $\pm$ 0.02 pH units. Sub-samples for cation analysis (4 mL) were diluted two-fold with 18 MΩ demineralised water and then acidified with concentrated HNO$_3$ (1% v/v) to preserve the sample. Cation analysis was undertaken using a combination of ICP-OES (Inductively Coupled Plasma - Optical Emission Spectrometry) and ICP-MS (Inductively Coupled Plasma - Mass Spectrometry). A second undiluted subsample was taken for the determination of anions by IC (Ion Chromatography). All fluid samples were stored at < 5°C until required for analysis.

5.2.3 Tracer test

Independent tracer tests on the unreacted sandstone were carried out on duplicate columns to estimate the initial porosity using 0.1 mol dm^{-3} NaClO$_4$ at pH 6.5 as the permeant solution (the specific activity of the HTO, C$_0$ was approximately 17 Bq cm^{-3}). The tritiated solution was injected continuously into the column, and when the specific activity at the outlet reached a steady-state, the injected fluid was swapped to the tracer-free solution, and the elution profile was also recorded. The HTO tracer tests were repeated at the end of the column experiment when the HTO was added to the YCL. The specific activity of solutions was determined by liquid scintillation analysis (2100 TR, Packard, Canberra, Australia), measuring the energy range between 1 and 18.6 keV and liquid scintillation cocktail Gold Star (Meridian, UK). No chemiluminescence was observed for the alkaline solutions; therefore, no neutralisation of the samples was required before measurements. The porosity of initial column samples was also estimated from the initial dry and wet weights of the column. The values from both methods were in agreement within +/- 2% of volume.

5.3 Modelling approach

PHREEQC (version 3.6.1) (Parkhurst and Appelo, 2013) was used to perform all the thermodynamic and kinetic simulations. The code can perform a wide range of complex geochemical calculations between aqueous, gas and mineral dissolution/precipitation, along with surface complexion and ion exchange. The LLNL thermochemical database was used to describe the high-pH cement leachate/host rock system (Delany and Lundeen, 1990). However, this database does not contain an adequate description of the dissolution/precipitation kinetics of C-S-H and C-A-S-H phases (e.g. specific kinetic rate, reactive surface areas, etc.). Therefore, a hybrid kinetic-equilibrium approach was implemented based on the mixing cell concept, which overcomes this shortcoming (Chen and Thornton, 2018, Van der Lee, 1998, Bethke, 1996). Note, despite the variety of PHREEQC built in geochemical reactions, it does not integrate the correlation between porosity and permeability evolution in porous media within its reactive transport code. Thus, the variation of permeability was not included in the modelling.

5.3.1 Transport process

Figure 5.2 explains the concept of 1-D column advective-dispersive transport simulation in PHREEQC. The column can first be divided into a series of cells which all have the same amount of pore volume. Then, the length of each cell and the time step (the time to move the pore volume from one cell to the next one, this time is also linked to each advection and diffusion reaction period) can be defined manually along with the type of boundary condition at the column inlet and outlet. With flux boundary conditions, the simulation starts with the advection process in which the direction of fluid flow is into the higher-numbered cell. Next, the moving fluid is mixed with the adjacent cells for dispersion

(which happen multiple times within each single advection step). Lastly, equilibrium and kinetic reactions are calculated. At the end of the simulation, all physical and chemical changes data (the number of moles for pure phases, kinetic reactants and solid-solution composition, and equilibrium-kinetic phases) are automatically updated and saved for each cell number.

In This study, the flow was modelled with inflow at one end and outflow at the other. It was modelled by subdividing the column into ten cells of equal length (30 mm each, Figure 5.2). The simulation was performed for a series of time steps (each time step was set at 26 hours). The mean flow was set at 0.6 ml/h (based on the experiment). For the first and last cell, a flux-type boundary condition was chosen. Within the simulation, the extended form of Darcy's law was used to govern the movement of the solution flux through the flow path of the 1D saturated column, as below (Nardi et al., 2014):

$$q_l = -\frac{\kappa}{\mu_l}\,(\nabla p_l - \rho_l g) \qquad (5.1)$$

where q_l is the Darcy flux (m^3 m^{-2} s^{-1}) for the liquid, κ is permeability tensor (m^2), μ_l is liquid dynamic viscosity (Pa s), p_l is fluid pressure (Pa), ρ_l is liquid density (kg m^{-3}) and g is gravity vector (m s^{-2}). The advection-reaction-dispersion for the chemicals can be described as:

$$\frac{\partial C_i}{\partial t} = \underbrace{-q_l\,\frac{\partial C_i}{\partial x}}_{Advection} + \underbrace{D_L\,\frac{\partial^2 C_i}{\partial x^2}}_{Dispersion} - \sum_{m=1}^{l} v_{im} R_m \qquad (5.2)$$

where C_i is the total concentration of component i in water (mol kgw^{-1}), t is time (s), x is the distance (m), D_L is hydrodynamic dispersion coefficient (m^2 s^{-1}), v_{im} is the

stoichiometric coefficient of component i in kinetic reactant m (dimensionless), and $\boldsymbol{R_m}$ is the overall dissolution/precipitation rate of kinetic reactant m (mol kgw^{-1} s^{-1}), l is the number of kinetic reactants. Equation (5.2) will be solved by an explicit finite difference algorithm for each time step using a split-operator scheme, where the chemical interaction term ($v_{im}R_m$) for each mineral is calculated separately after the advection step and after the dispersion step for all equilibrium and kinetic reactions.
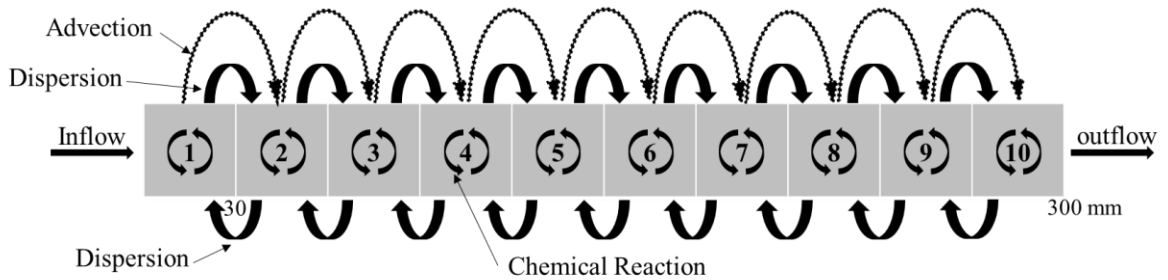
Figure 5.2: Transport modelling concept

5.3.2 Kinetic modelling of dissolution and precipitation rates

Dissolution of quartz, k-feldspar and kaolinite were modelled kinetically. The first two were included in the geochemical modelling because they were the dominant primary minerals in Hollington sandstone (>91% by volume). Kaolinite was included because it could potentially affect the evolution of the pore solution chemistry due to its high

dissolution rate (Carroll and Walther, 1990, Bauer and Berger, 1998). The remaining minor phases (illite, muscovite, etc.) in Hollington sandstone were excluded from the model.

The rate of each mineral dissolution/precipitation reaction was calculated using equation (5.3), which assumes the rate is proportional to the normalised surface area and degree of disequilibrium (Appelo and Postma, 2005):

$$R_i = r_i \left(\frac{A_i}{V}\right) \left(\frac{M_i}{M_{0i}}\right)^n \left(1 - \left(\frac{IAP}{K}\right)_i\right) \quad for\ each\ mineral\ i \qquad (5.3)$$

where R_i is the overall dissolution/precipitation rate (mol L^{-1} s^{-1}), r_i is the specific reaction rate (mol m^{-2} s^{-1}), A_i is the effective surface area of the mineral (m^2 g^{-1}), V is the pore volume (L), M_i is the moles of solid at a given time, M_{0i} is the initial moles of solid, and (IAP/K) is equal to the saturation ratio (SR) value of the mineral where IAP is the Ion Activity Product and K is the equilibrium constant. In the above equation, the molar concentration (m/m_0) has n power, which is a function of the initial crystal grain size distribution that affects the solid dissolution rate. Usually, a value of 2/3 is used for uniformly dissolved cubes or spheres of the monodisperse population (Appelo and Postma, 2005). The term (1-SR) ensures that the rate of dissolution is highest when the system is far from equilibrium but tends to zero as equilibrium is approached. It also allows the rate equation to be applied for both supersaturation and undersaturation states, while the rate approaches zero (Equilibrium) as IAP/K approaches one.

Along with the kinetic rates and reactive surface areas used for each mineral in the model, the unit of the effective surface area A_k in equation (5.3) is $(m^2 g^{-1})$. This correlates the surface area with the solid amount of minerals as the YCL–mineral reaction proceeds.

Therefore, the initial mass of each mineral was included in equation (5.3) and the value was updated in each iteration to account for the changes in mass; otherwise, the dissolution/precipitation rate will be per unit mass for each mineral. Moreover, during the geochemical reaction, the dissolution/precipitation process will continue to change the mass of each mineral and hence the volume of the pore fluid. Consequently, the effective surface area in (m^2) for each mineral i can be described as:

$$A_i = A_0 m_t X_i \qquad for\ each\ mineral\ i \qquad (5.4)$$

where m_t is the total mass of the rock sample, A_0 is the initial surface area and X_i is the mass fraction of each mineral in the rock sample (Beckingham et al., 2016).

The values of the specific dissolution rate, k, for silicate minerals undergoing weathering is highly dependent on temperature (Worley, 1994, Appelo and Postma, 2005). Therefore, published k values for k-feldspar dissolution at 281 K were corrected for temperature (see Table 5.4, Table 5.5). The value of k for quartz and kaolinite was taken from the experimental literature (Knauss and Wolery, 1988, Carroll and Walther, 1990). The kinetic information from the literature used for the minerals in Hollington sandstone is summarised in Table (5.6), along with the rates and reactive surface areas used for each mineral in the model.

Table 5.4: Temperature factors used to calculate silicate weathering rate k_i, at temperatures (T K) other than 8°C (281 K).

$$pk_{i,T} = -\log k_{i,T} = pk_{i,281} + \frac{E_a}{2.303R}\left[\frac{1}{T} - \frac{1}{281}\right]$$

	pk_H	pk_{H_2O}	pk_{OH}	pk_{CO_2}
$pk_{i,281}$ (K-feldspar)	11.7	14.5	13.1	13
$\dfrac{E_a}{2.303\,R}$	3500	2000	2500	2000

The equation below then calculates the specific dissolution rate:

$$k_{K-feldspar} = k_{H^+}\frac{[H^+]^{0.5}}{f_H} + k_{H_2O}\frac{1}{f_{H_2O}} + k_{OH^-}\frac{[OH^-]^{0.3}}{f_{OH}} + k_{CO_2}\frac{[P_{CO_2}]^{0.6}}{f_{CO_2}} \qquad (5.5)$$

where $k_{K-feldspar}$ is the specific reaction rate (mol m^{-2} s^{-1}), $k_{H^+}, k_{H_2O}, k_{OH^-}, k_{CO_2}$ are solute rate coefficients (mol m^{-2} s^{-1}), and $f_H, f_{H_2O}, f_{OH}, f_{CO_2}$ are inhibition factors. n and o are constant values, which for k-feldspar are equal to 0.5 and 0.3, respectively (Appelo and Postma, 2005).

$$f_H = \left[1 + \frac{[BC]}{Lim_{BC,H}}\right]^{x_{BC}} \left[1 + \frac{[Al^{3+}]}{Lim_{Al,H}}\right]^{x_{Al}} \qquad (5.6)$$

$$f_{H_2O} = \left[1 + \frac{[BC]}{Lim_{BC,H_2O}}\right]^{z_{BC}} \left[1 + \frac{[Al^{3+}]}{Lim_{Al,H_2O}}\right]^{z_{Al}} \qquad (5.7)$$

$$f_{OH} = f_{CO_2} = 1 \qquad (5.8)$$

where *Lim* is the limiting activity, [BC] indicates the sum of the base cations Na^+, K^+, Mg^+ and Ca^+ activities, x_i and z_i are empirical values as in Table (5.5).

Table 5.5: Values of empirical exponents and limiting activity in the equation of $\boldsymbol{f_H}$ and $\boldsymbol{f_{H_2O}}$ (Appelo and Postma, 2005).

x_{BC}	x_{Al}	z_{BC}	z_{Al}	lim_{Al}	lim_{BC}
0.15	0.4	0.15	0.14	4e^{-6}	5e^{-4}

Table 5.6: Kinetic modelling approach and parameters for the primary minerals in Hollington sandstone rock.

Mineral	Modelling Approach	Surface area (m^2/g)	Rate constant at (at 50°C) (mol m^{-2} s^{-1})
Quartz	Kinetic	0.02 (De Windt et al., 2008)	k = 1x10$^{-12.7}$ (Knauss and Wolery, 1988)
K-feldspar	Kinetic	0.02 (De Windt et al., 2008)	k = 7.26 x10^{-13} (Appelo and Postma, 2005)
Kaolinite	Kinetic	20 (Klajmon et al., 2017)	k = 1x10$^{-12.5}$ (Carroll and Walther, 1990)

5.3.3 Secondary phases

The overall reaction for the evolution of hyper-alkaline cement leachate is well known (Glasser, 2001, Harris et al., 2001a, Harris et al., 2001b, Gaucher and Blanc, 2006, Helinski et al., 2007). Generally, after hydration of the cement materials, high sodium and potassium alkali leachate will break through, followed by the dissolution of portlandite and progression of calcium that forms C-S-H-gels and high Ca/Si ratio minerals. Due to the composition of Hollington sandstone and the hyper-alkalinity of YCL, the major secondary minerals that are likely to form are C-S-H, C-A-S-H and zeolite minerals phases (Chen et al., 2015). The C-S-H phases were represented in this study by C-S-H -gel and tobermorite-14A, which is the most evolved C-S-H mineral that forms from C-S-H -gel (Bethke, 1996). In terms of aluminosilicate minerals, prehnite and saponite-Mg were selected as an analogue for the hydrated silicate and clay phases, respectively. Saponite is usually represented in thermodynamic models as an (Na, Mg, Ca, K)-bearing aluminosilicate and will act as a potential sink for Mg. Conversely, prehnite has been identified as a possible precipitated secondary phase from previous geochemical modelling of cement leachate-host rock interactions (Rose, 1991, Pfingsten et al., 2006, Gysi and Stefánsson, 2012) . At the same time, the high sodium-calcium ratio of the cementitious porewater favours the formation of aluminous zeolites, such as laumontite, analcime, mesolite and mordenite minerals (Walker, 1960, Savage et al., 1987, De Windt et al., 2008, Idiart et al., 2020). Therefore, those phases, together with phillipsite, were selected as potential Ca/Na/K-bearing zeolites which will remove Na and K from the pore fluid if they precipitate. The last mineral included in the simulation was hydrogarnet, a calcium aluminate phase that is usually formed with the C-S-H -gel and included in the modelling of cement alternation

reactions (Chaparro et al., 2017, Wilson et al., 2017, Wilson et al., 2018).This mineral is most likely to form in the presence of a high Ca/(Al+Si) ratio and at high temperature (Nakahira et al., 2008, Vasconcelos et al., 2018). Also, in case the dissolution of portlandite was high, hydrogarnet will be altered to Friedel's salt once reacted with *Ca(OH)₂*, which will result in an increase in pH (Wilson et al., 2017, Wilson et al., 2018). It is noteworthy that the precipitation and potential dissolution of the secondary minerals formed as a result of the primary mineral weathering was modelled using the equilibrium approach (Table 5.7).

Table 5.7: Secondary minerals included in the model using an equilibrium approach. Data from LLNL thermochemical database (Delany and Lundeen, 1990).

Mineral	Structural formula	Rate constant at (at 50°C) (mol m^{-2} s^{-1})
C-S-H		
C-S-H -gel	$Ca_5Si_6H_{21}O_{27.5}$	60.84
Tobermorite-14A	$Ca_5Si_6H_{21}O_{27.5}$	63.84
Zeolite		
Analcime	$NaAlSi_2O_6: H_2O$	6.13
Laumontite	$CaAl_2Si_4O_{12}: 4H_2O$	13.66
Mesolite	$Na_2Ca_2(Al_2Si_3O_{10})3: 8H2O$	13.61
Phillipsite	$K_{2.8}Na_{3.2}Ca_{0.8}Al_{7.6}Si_{24.4}O_{64}: 24H_2O$	6.65
Mordenite	$Ca_{.28}Na_{.36}Al_{.94}Si_{5.06}O_{12}: 3.4H_2O$	-5.19
Others		
Prehnite	$Ca_2Al_2Si_3O_{10}(OH)_2$	32.93
Saponite-Mg	$Mg_{3.165}Al_{.33}Si_{3.67}O_{10}(OH)_2$	26.25
Hydrogarnet	$Ca_3Al_2(OH)_{12}$	82.28

5.3.4 Variable porosity calculation

The overall system in Figure (5.3) shows a water-saturated structure with the effect of transport and kinetic dissolution/precipitation processes on the mineral surface area and pore volume.
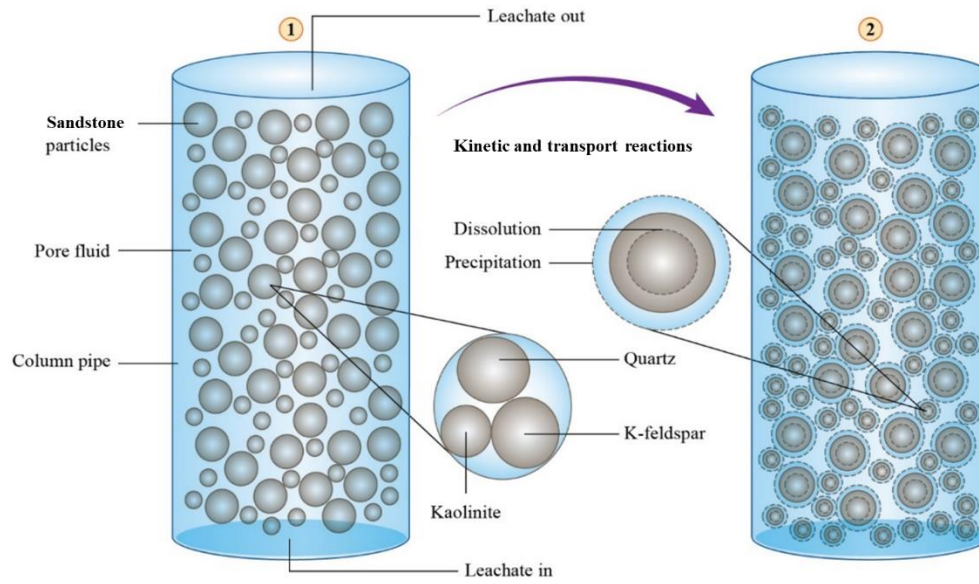
Figure 5.3: Porosity evolution concept

The whole system can be described by the equation of conservation of volume as:

$$V_{system}^{t=0} = V_{system}^{t} \qquad (5.9)$$

$$V_{Pore}^{t=0} + V_{Solid}^{t=0} = V_{Pore}^{t} + V_{Solid}^{t} \qquad (5.10)$$

Rearranging equation (5.10) leads to

$$V_{Pore}^{t} = V_{Pore}^{t=0} + V_{Solid}^{t=0} - V_{Solid}^{t} \qquad (5.11)$$

where V_{pore} and V_{solid} are the pore fluid and solid volume of all minerals in the rock sample. If both sides of equation (5.11) are divided by the total volume V_T, then

$$\phi_t = \phi_{t=0} + \frac{V_{Solid}^{t=0}}{V_T} - \frac{V_{Solid}^{t}}{V_T} \qquad (5.12)$$

$$\Delta\phi_t = \phi_{t=0} \pm \sum \left(\frac{V_{\frac{Diss}{prec}mole,t}}{V_T} \right) \qquad (5.13)$$

$$(Note: "+" for\ dissolving;\ "-"\ for\ precipitating)$$

$$\Rightarrow \Delta\phi_t = \phi_{t=0} \pm \sum \left(\frac{V_{mi} * M_{i,t}}{V_T} \right) \qquad (5.14)$$

$$(note:\ for\ each\ mineral\ i)$$

where ϕ is the porosity, V_m is molar volume and M is the number of moles. To link the evolved porosity with the mineral surface area (equation 5.4), a mathematical equation was developed as (Lichtner, 1988):

$$A_r^t = A_r^{t=0} \left(\frac{1 - \phi_t}{1 - \phi_{t=0}} \right)^{2/3} \qquad (5.15)$$

where $A_r^{t=0}$ is the reactive surface area of the mineral at the initial porosity. Along with the evolved surface area, the dissolution/precipitation process for each mineral will change its mass and hence the volume of the pore fluid.

$$V_{pore,total} = V_{Pore}^{t=0} \pm \sum V_{\frac{Diss}{prec}moles,t} \qquad (5.16)$$

$$(Note: "+" for\ dissolving;\ "-"\ for\ precipitating)$$

$$m_{i,t} = m_{i,t=0} \pm m_{\frac{Diss}{prec}moles,t,i} \qquad (5.17)$$

$$(Note: "-" for\ dissolving; "+" for\ precipitating, for\ each\ mineral\ i)$$

Ultimately, substituting Equation (5.15) into Equation (5.3), combined with the changes in mass and pore volume over time (Equations 5.16 and 5.17), leads to a new equation:

$$R_i = \frac{r_i}{V_t} \left(A_{r,i}^{t=0} \left(\frac{1 - \phi_t}{1 - \phi_{t=0}} \right)^{2/3} m_{i,t} \right) \left(\frac{M}{M_0} \right)_i^n \left(1 - \left(\frac{IAP}{K} \right)_i \right) \qquad (5.18)$$

$$(note: \; for \; each \; mineral \; i)$$

5.4 Results and discussion

The cement leachate composition at the outlet of the column was sampled regularly to assess changes in the fluid composition induced by precipitation of components in the leachate and/or dissolution of the primary phases in the sandstone. Figures (5.4–5.21) compare the experimental results and model simulations during the leachate transport through the column. The modelled pH and solute concentrations are compared against the experimental measurements. The concentration and saturation indices (= log (IAP/Ksp) or log (SR)) of all significant elements involved in the evolution of geochemical reactions are plotted against time and cell numbers. Two types of analysis were performed and compared: one is the traditional fixed porosity, pore volume and reactive surface area method; the other is the more complex model with variable porosity and reactive surface area developed in this study.

The modelled concentrations of Na and K are shown in Figure (5.4). The simulated profiles agree well with the experimental results, as the chemistry of the injecting fluid mainly controls their concentrations, rather than dissolution and precipitation of primary and secondary minerals. The modelling shows that analcime was close to equilibrium, but instead the concentration of Na decreased slightly as this ion was removed by the precipitation of mesolite (Na-Ca zeolite, Figure 5.5). The plots show that mesolite redissolved following precipitation at an early stage of the experiment, Meanwhile, the

initial high concentration of K ions reacts as a buffer for k-feldspar dissolution. This is also reflected in the saturation indices in Figure (5.6), which shows that k-feldspar has a lower tendency for dissolution in the beginning and starts to dissolve later compared to quartz and kaolinite. Some studies have also suggested that the solubility of k-feldspar can be decreased by high pH values (Brown et al., 2008).

Quartz, kaolinite and k-feldspar dissolve as a result of varying degrees of reaction with the YCL. In Figure (5.6), both quartz and kaolinite have a negative saturation index in both scenarios (fixed and variable porosity), which implies continuous dissolution throughout the experiment. This is related to the fact that the precipitation of secondary phases consumes ions in the cement leachate and those released from the dissolution of the primary minerals. Consequently, the precipitation of secondary minerals can help maintain conditions which are far from equilibrium, leading to faster dissolution rates. Conversely, k-feldspar is initially at equilibrium (For 500 h) before it starts to dissolve. Comparing the saturation indices, all three minerals in the variable porosity model show a steeper decrease in values, with k-feldspar beginning to dissolve earlier in this model.

The initial fast reaction with the YCL will begin with the reaction of fine mineral particles on the grain surfaces, resulting in the rapid release of Si and Al ions into the solution. This was correlated in the analysis, as shown in Figure 5.7 (Plot A and B). The trend and magnitude of Si and Al in plots A and B are reproduced well and are correlated with the experimental data, exhibiting similar changes in concentration behaviour. The values start with an initial rise in Si and Al concentrations until maximum values are reached, after which they were removed (accompanied by Ca consumption), and the concentrations decreased to a steady-state value. Despite a similar trend between the experimental and

226

modelling results, the decrease in Si concentration (Plot A) is smaller in the experimental results. This could be related to the fact that some secondary phases will precipitate on the surfaces of the primary minerals, reducing the reactive surface area and the dissolution process. This will restrict the precipitation of the secondary phases and the removal of Si from the solution. In general, the reduction in the concentration of Ca (Figure 5.7C), Si and Al were marked, mainly due to the formation of secondary C-S-H /C-A-S-H mineral phases with different Ca/Si ratios (Savage et al., 1992, Savage et al., 2002, Pfingsten et al., 2006, Savage et al., 2007, Savage et al., 2010, Savage, 2011) as shown by the saturation indices of C-S-H -gel, tobermorite-14A, prehnite, saponite-Mg and mesolite (Figures 5.8 to 5.12). This type of precipitation has also been observed in natural systems (Alexander et al., 1998, Pitty and Alexander, 2010). After some time, the precipitated secondary phases will dissolve again, creating a slight increase in the Ca concentration observed in the later stage of the experiment (Figure 5.7C).

The Si and Al curves in Figure (5.7) D and E show two different patterns of ion consumption. During the first 300 hours, the amount of Si and Al consumption is evenly balanced in all the cells, but with higher initial concentrations in the first five cells as a result of Si and Al release from the dissolution process. After reaching a peak (around 800 hours, plot A and B), the following time plots show the opposite behaviour as the precipitation of C-S-H and C-A-S-H led to lower values of concentrations in the first 5 cells. The figures also indicate that the consumption of both ions is greatest in the first 1300 hours, which also represents the period during which C-S-H /C-A-S-H precipitate before starting to dissolve again (Figures 5.8 to 5.11).

As the dissolution of the primary minerals (quartz, kaolinite and k-feldspar) did not release Ca, the concentration of this ion was controlled by the initial chemical composition of the background solution. During the breakthrough of the injected hyperalkaline solution, the high Ca concentration in the background solution will mostly be retarded due to the precipitation of secondary C-S-H /C-A-S-H phases once there were enough Si ions released from the dissolution of primary minerals. This will cause mineral precipitation toward the inlet of the column, which explain the higher values of Ca, Si and Al at the end of the column (Figure 5.7D, E and F). Moreover, the plot (7F) shows that the Ca concentration is removed within the seven cells and primarily in the first 26 hours. Later, from 1300 hours the Ca concentration starts to increase again as C-S-H /C-A-S-H phases start to dissolve until complete dissolution around 2300 hours (the same time when the saturation indices decrease to less than zero in Figures 5.8 to 5.11).

Figures 5.8 to 5.12 shows the evolution of the saturation indices for C-S-H-gel, tobermorite-14A, prehnite, saponite-Mg and mesolite at different times in the experiment. The positive SI values indicate that the cement pore fluid is super-saturated with respect to those phases and hence thermodynamic precipitation may occur. Conversely, dissolution will occur when the SI is negative (under saturation). The simulation predicted that only those five minerals could potentially precipitate during the experiment. It should be noted that the lack of zeolite formation in the experiments could also be related to the experiment temperature, as some studies have observed zeolites precipitation only above 60°C (Hodgkinson and Hughes, 1999, Fernandez et al., 2012). Moreover, the kinetics of zeolite precipitation may be very slow, relative to the residence time in the column (ie there is a kinetic limitation even though the fluid chemistry supports precipitation). The number of

dissolved/precipitated moles for those secondary phases is presented in Figures (5.13 to 5.17). It is noteworthy that in equation (5.3), if the mineral is precipitating, then the value of *(1-SR)* will be negative and hence the number of moles. This is reasonable as it indicates that the mineral is being removed from the solution. Consequently, the number of precipitated moles is represented by the lower side of the charts while the dissolved number of moles is in the upper side. In general, all five plots show that the zone of secondary mineral precipitation is displaced in the fixed porosity model. The number of precipitated moles is also higher in all five plots and especially for saponite-Mg, which shows a much higher degree of precipitation in the variable porosity model. Both findings agree well with the fact that in the variable porosity model, the ions will be released faster from the primary minerals because of the higher exposure between the minerals in the sandstone and the YCL. Hence, the precipitation cycle will start earlier as well.

The variable porosity model (Figure 5.18) also demonstrates a better fit in ion concentration because it led to more reactive surface area with the YCL. The time to the peak point and the decreasing slope is a more realistic representation of the system since more ions were released to the synthetic leachate, resulting in greater precipitation. Figure (5.19) shows that as the dissolution process takes place, the volume of quartz and kaolinite decreases, and the porosity increases. While k-feldspar was initially precipitating, the plot shows two lines, one for precipitation (negative moles) and one for dissolution (positive moles). Both curves start with a high value of dissolved/precipitated moles and decrease along the column. Simultaneously, the volume of k-feldspar increases slightly in the beginning, accompanied the decrease in the k-feldspar porosity (this is also reflected in the saturation index plot, which shows slight precipitation at the initial hours, Figure 5.6) until

dissolution starts and the volume decreases. On other hand, the number of moles released was highest from kaolinite despite its low weight percentage, which indicates its high reaction rate with the YCL.

Figure (5.20) shows that an overall increase in the porosity and pore volume results from the decreased mineral volume, especially with no stable precipitation of secondary C-S-H or C-A-S-H phases (redissolution, Figures 5.8 to 5.11). The analysis also demonstrates that the change in porosity decreases towards the column outlet (increased cell numbers), similar to the dissolution process, except for the first cell, which has a slightly lower porosity value than the second. This may result from the higher precipitation of C-S-H /C-A-S-H phases close to the column flow inlet, as noticed in the experiment (Small et al., 2016). The pH value is usually a good indicator of the chemical evolution in geochemical systems. However, Figure (5.21) shows that both experimental and simulated pH values are very similar and were not delayed significantly. This means that the studied system has not changed significantly in terms of mineral alternation.
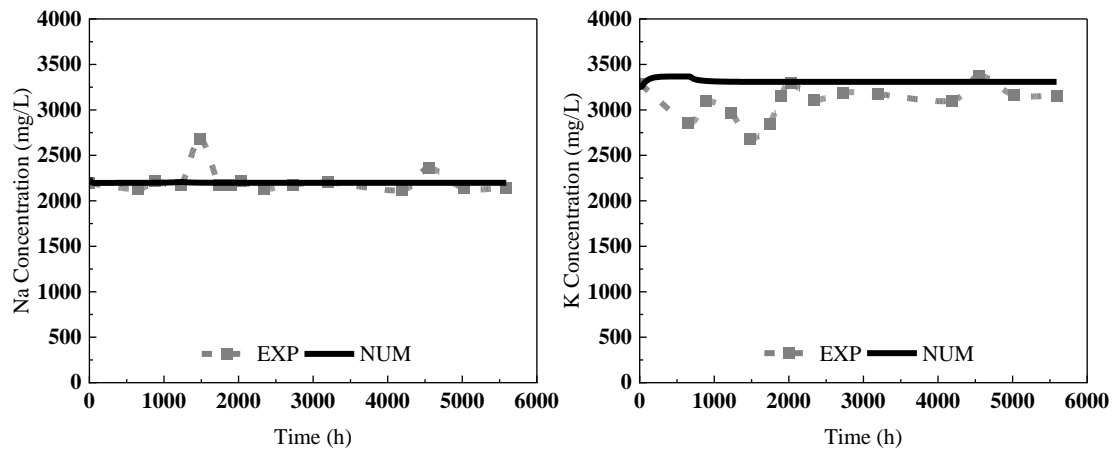
Figure 5.4: Potassium and sodium ion concentrations versus time (for variable porosity model).
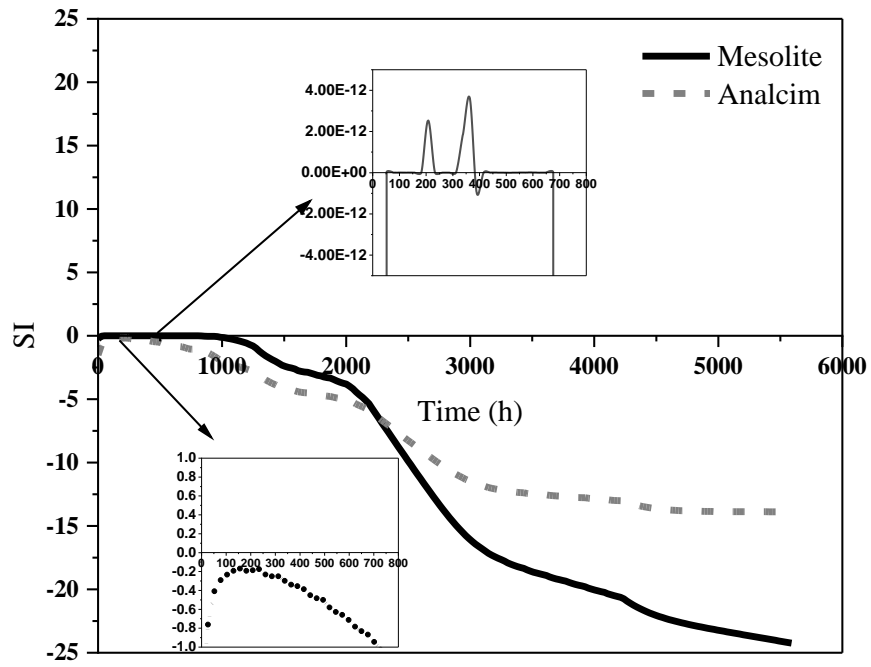
Figure 5.5: Saturation indices for analcime and mesolite versus time (for variable porosity model).
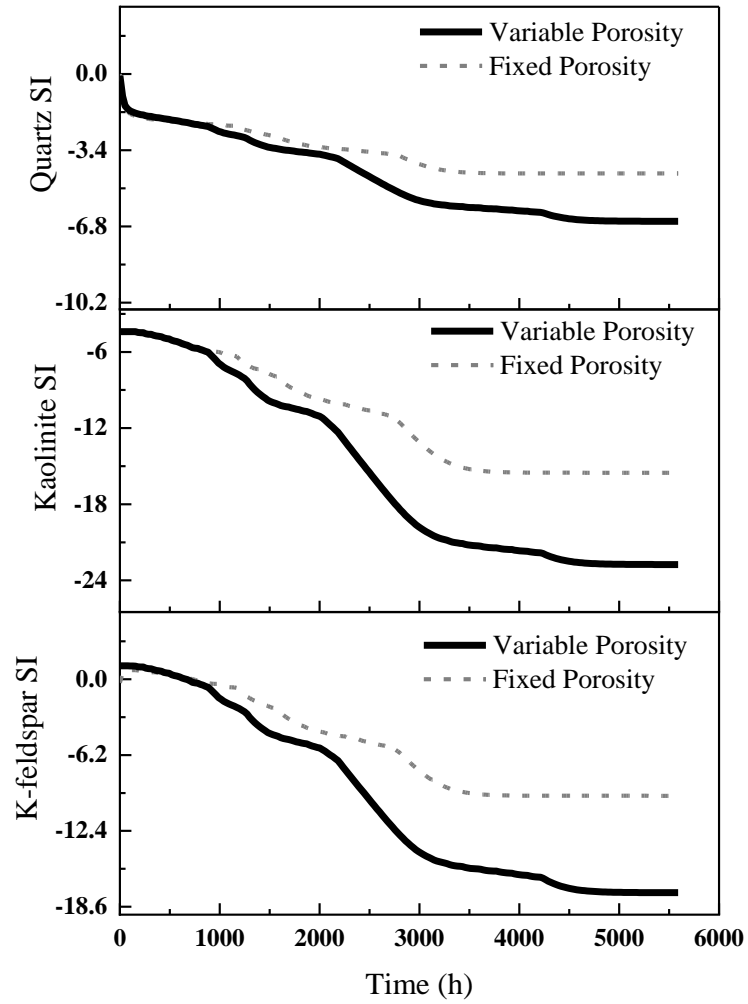
Figure 5.6: Saturation indices for primary minerals versus time for both fixed and variable porosity models.
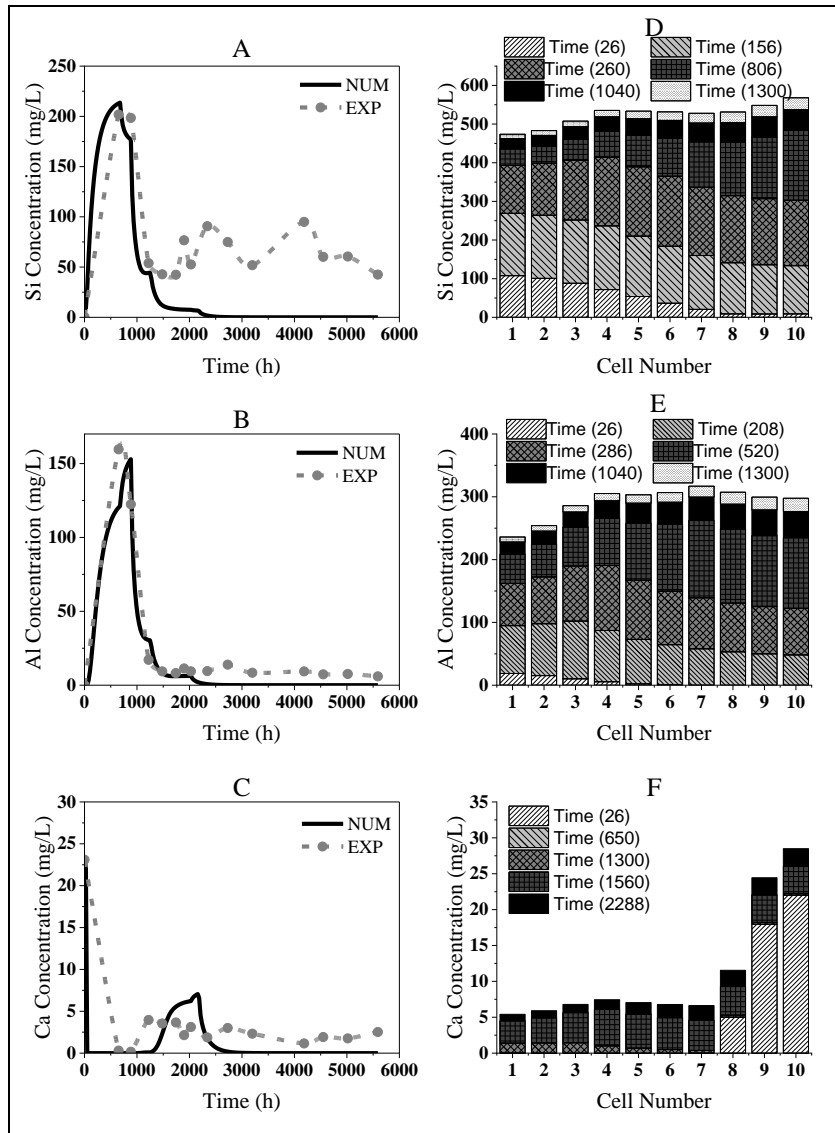
Figure 5.7: Silicon, aluminium and calcium ion concentrations versus time (h) and along the ten cells for variable porosity model.
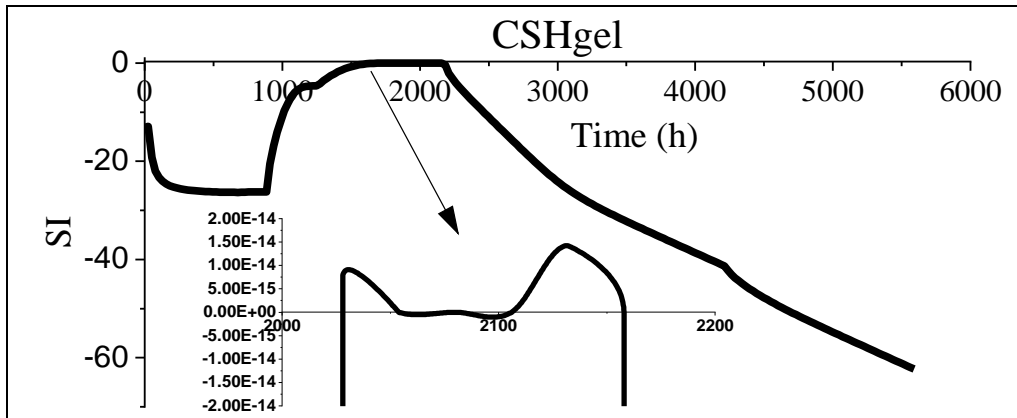
Figure 5.8: Saturation index for C-S-H-gel versus time for variable porosity models.
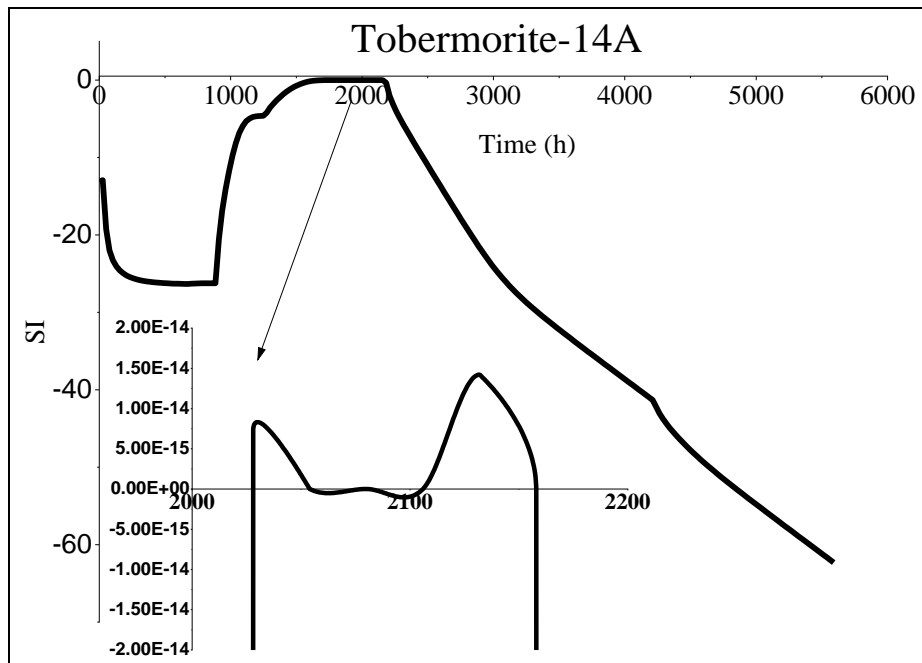
Figure 5.9: Saturation index for tobermorite-14A versus time for variable porosity models.

234
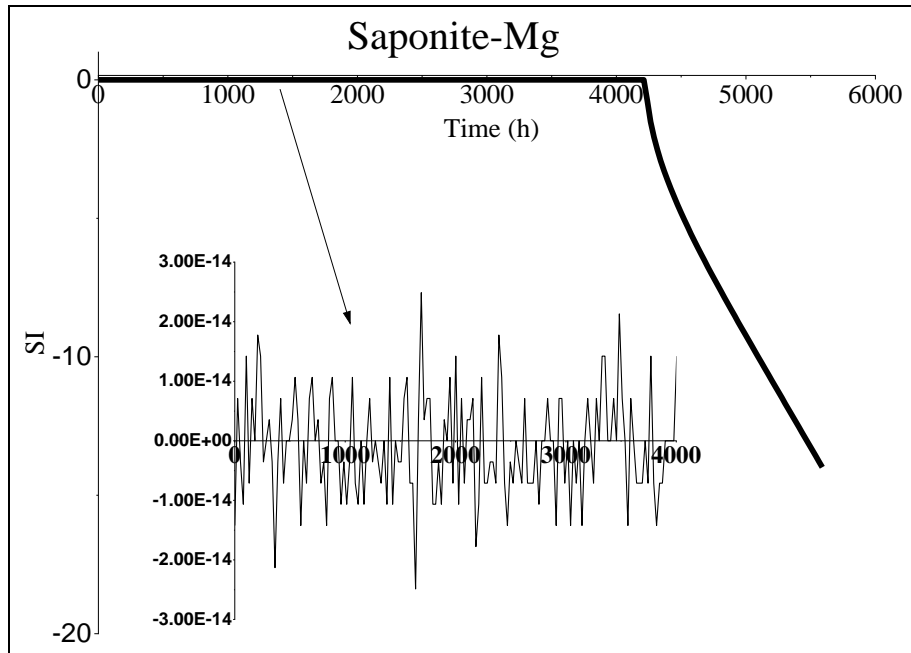
Figure 5.10: Saturation index for saponite-Mg versus time for variable porosity models.
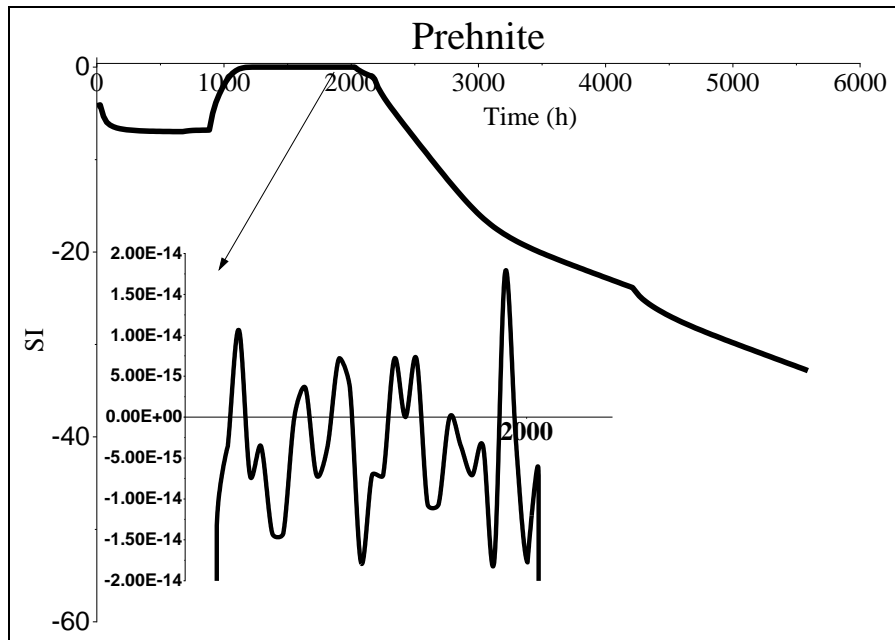
Figure 5.11: Saturation index for prehnite versus time for variable porosity models.
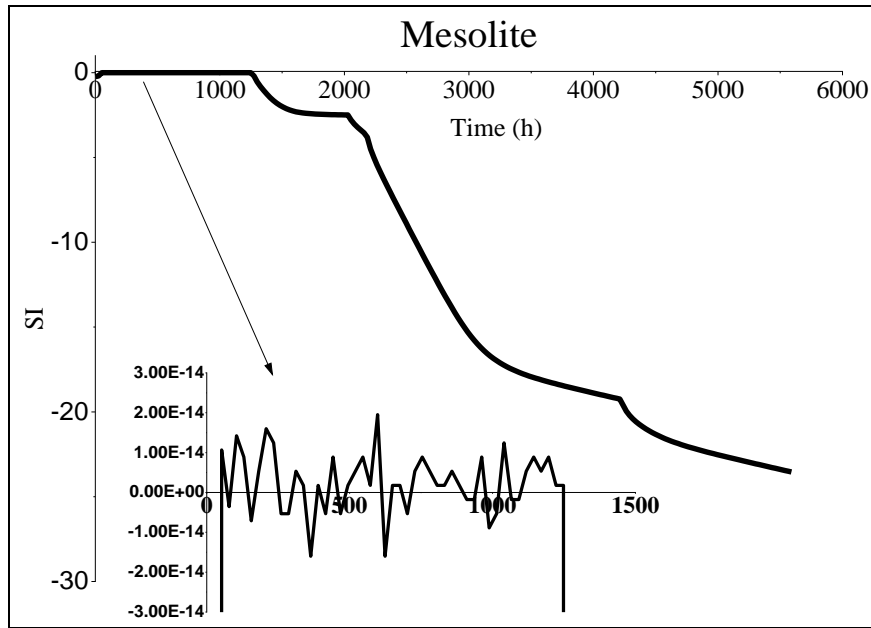
Figure 5.12: Saturation index for mesolite versus time for variable porosity models.
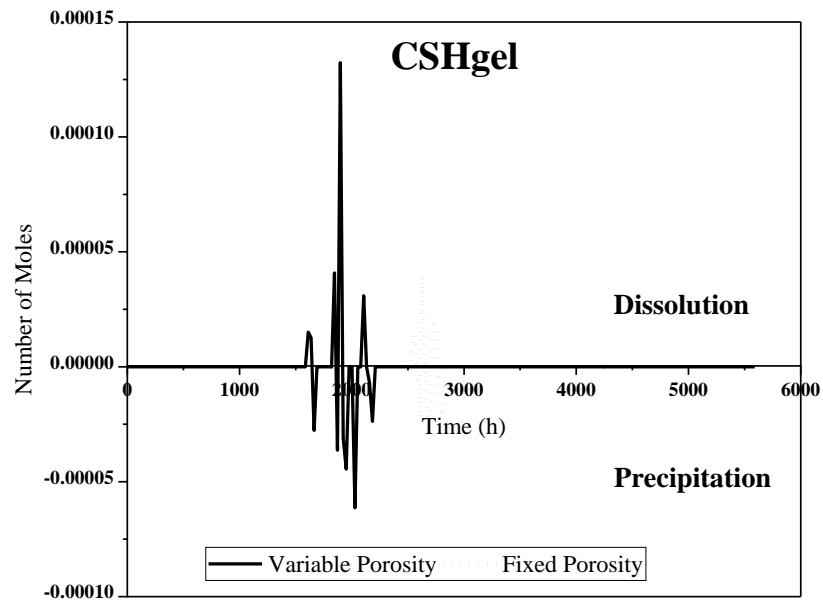
Figure 5.13: Number of precipitated/dissolved moles for C-S-H-gel versus time for variable porosity models.
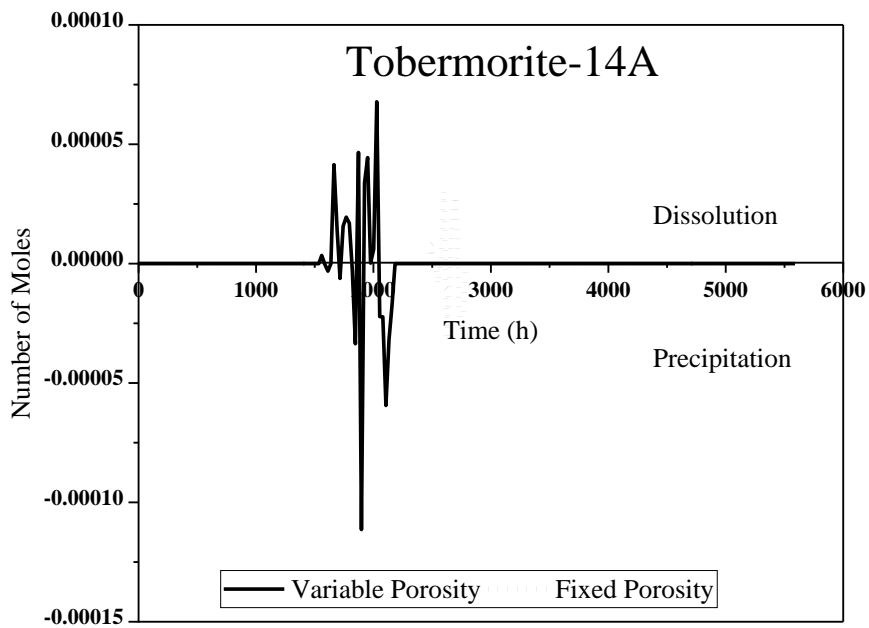
Figure 5.14: Number of precipitated/dissolved moles for tobermorite-14A versus time for variable porosity models.
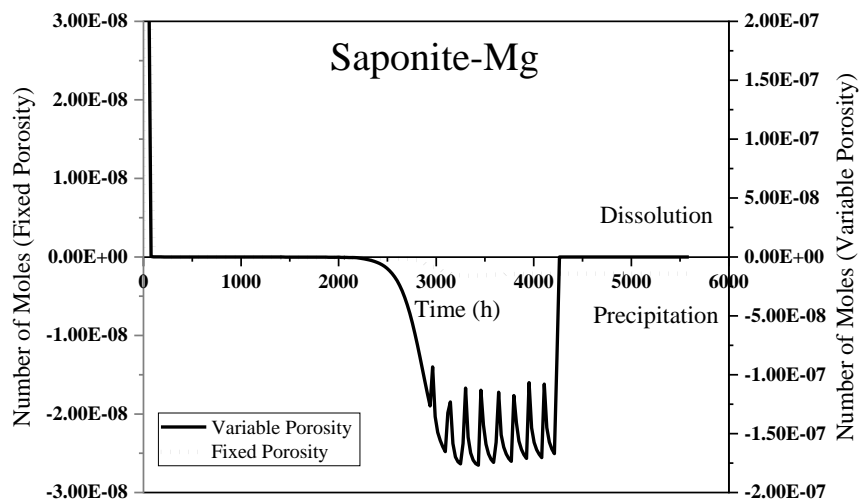
Figure 5.15: Number of precipitated/dissolved moles for saponite-Mg versus time for variable porosity models.
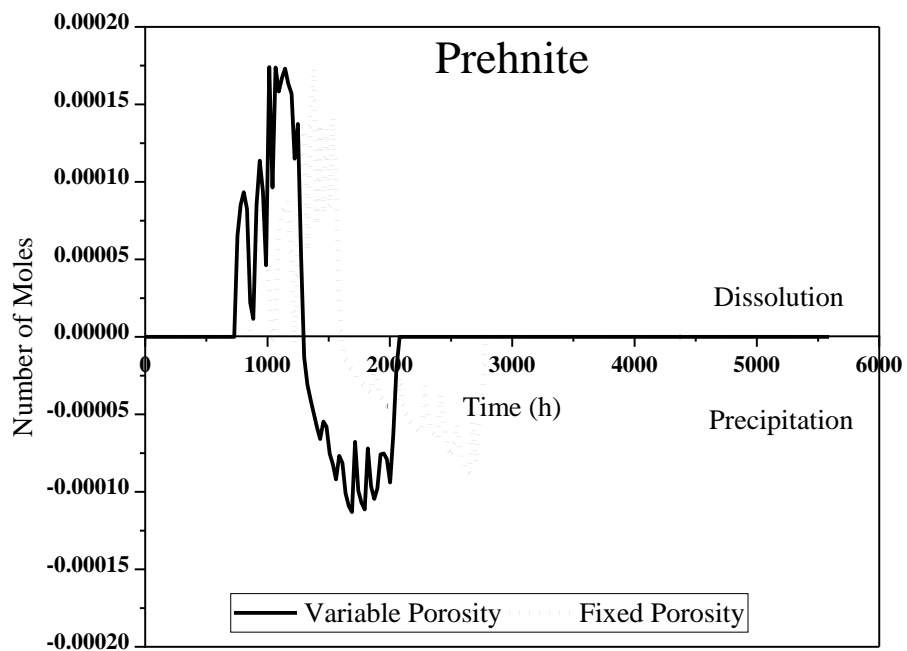
Figure 5.16: Number of precipitated/dissolved moles for prehnite versus time for variable porosity models.
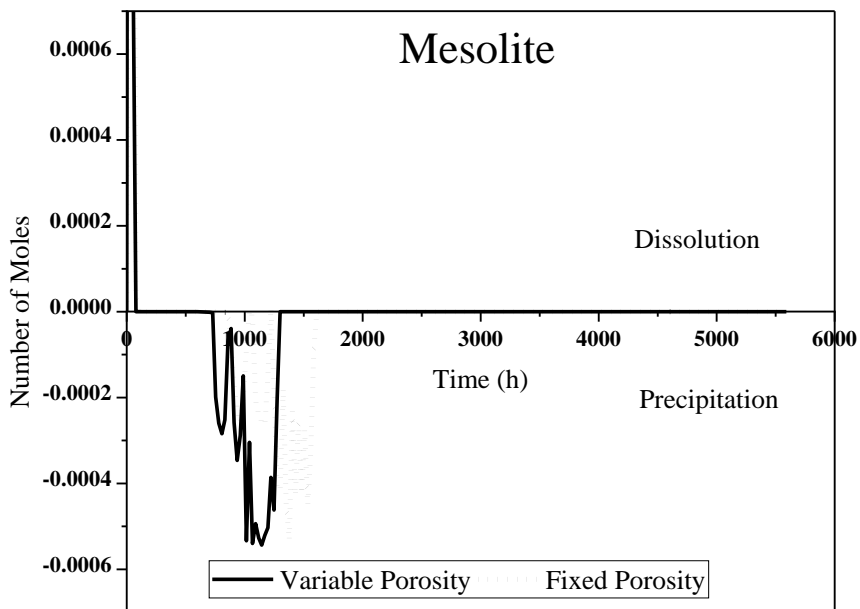
Figure 5.17: Number of precipitated/dissolved moles for mesolite versus time for variable porosity models.
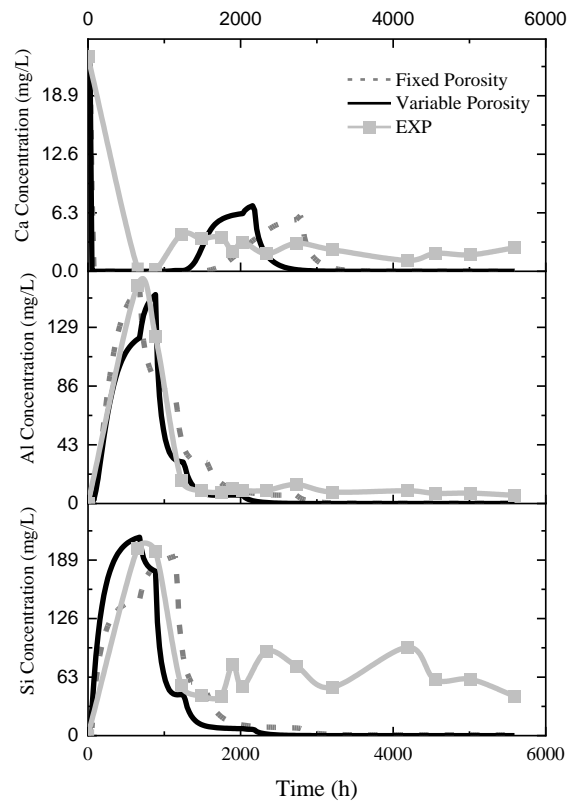
Figure 5.18: Silicon, aluminium and calcium ion concentrations versus time for both fixed and variable porosity models.
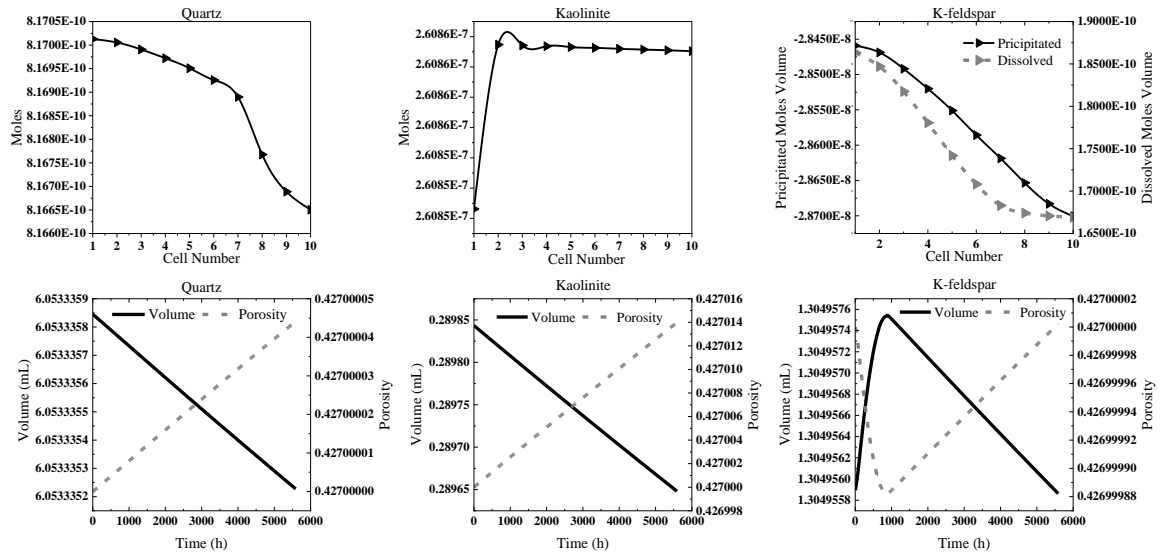
Figure 5.19: Number of dissolve moles in each cell and porosity with volume changes per time for quartz, kaolinite and k-feldspar (for variable porosity model).
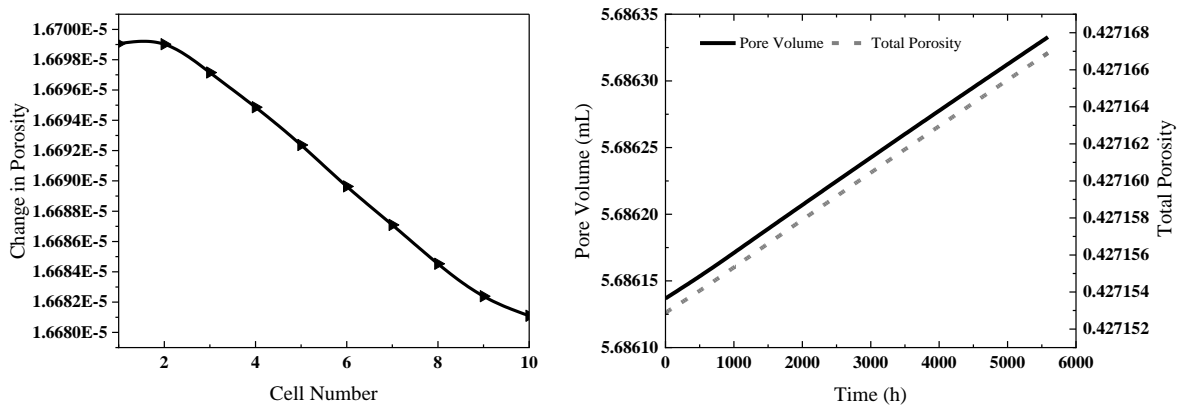
Figure 5.20: Changes in total porosity and pore volume of the system (for variable porosity model).
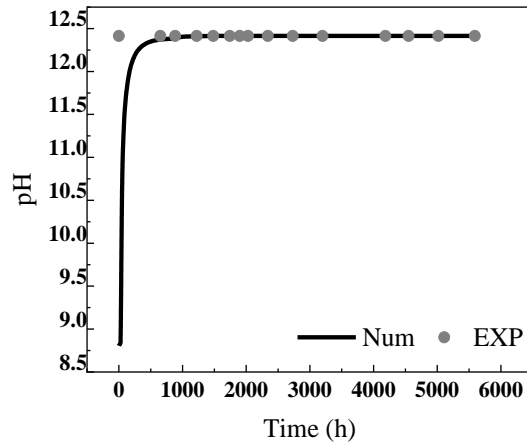
Figure 5.21: Variation in injected leachate pH at 50°C versus time (for variable porosity model).

5.5 Conclusion

The geochemical modelling code PHREEQC was used to evaluate two different porosity, 1D transport, models for a column experiment in which the host rock mineralogy and geochemistry changes when exposed to a YCL. The column experiment was undertaken to identify the dominant geochemical reactions and examine the effect of variable porosity, reactive surface area and pore volume on the geochemical alternation. The model captures the critical elements that describe the chemical evolution of the cement hyperalkaline leachate during the dissolution of primary minerals and the precipitation of secondary C-S-H /C-A-S-H phases during migration through the sandstone. The experimental results are reproduced well by the model simulations, supporting the geochemical interpretation of the reactions which control the leachate chemistry, mineral transformations and porosity evolution of the sandstone. The modelled concentration profiles showed that decreases in Ca, Al and Si concentrations were related to the formation of C-S-H /C-A-S-H and zeolite minerals as secondary phases (e.g. C-S-H-gels and mesolite). The overall porosity of the

system increased in the simulation as a result of primary mineral dissolution and specifically in the absence of stable precipitation of the secondary C-S-H /C-A-S-H phases. The variable porosity model showed a better fit in terms of the ion concentration and precipitation of secondary phases, due to better exposure between the YCL and the minerals in the host sandstone. The work in this paper demonstrates the importance of modelling experimental studies, which with suitable analogues can develop confidence in simulating hyperalkaline cement leachate transport in engineered barriers constructed for the containment of nuclear waste.

References

1. ALEXANDER, W., MAZUREK, M., WABER, H., ARLINGER, J., ERLANDSON, A., HALLBECK, L., PEDERSEN, K., BOEHLMANN, W., FRITZ, P. & GEYER, S. 1998. MAQARIN natural analogue study: phase III. Swedish Nuclear Fuel and Waste Management Co.

2. APPELO, C. & POSTMA, D. J. B., ROTERDAM 2005. Geochemistry, groundwater and pollution, CRC.

3. BAUER, A. & BERGER, G. 1998. Kaolinite and smectite dissolution rate in high molar KOH solutions at 35 and 80 C. *Applied Geochemistry,* 13**,** 905-916.

4. BECKINGHAM, L. E., MITNICK, E. H., STEEFEL, C. I., ZHANG, S., VOLTOLINI, M., SWIFT, A. M., YANG, L., COLE, D. R., SHEETS, J. M. & AJO-FRANKLIN, J. B. 2016. Evaluation of mineral reactive surface area estimates for prediction of reactivity of a multi-mineral sediment. *Geochimica et Cosmochimica Acta,* 188**,** 310-329.

5. BETHKE, C. 1996. *Geochemical reaction modeling: Concepts and applications*, Oxford University Press on Demand.

6. BROWN, G. E., TRAINOR, T. P. & CHAKA, A. M. 2008. Chapter 7 - Geochemistry of Mineral Surfaces and Factors Affecting Their Chemical Reactivity. *In:* NILSSON, A., PETTERSSON, L. G. M. & NØRSKOV, J. K. (eds.) *Chemical Bonding at Surfaces and Interfaces.* Amsterdam: Elsevier.

7. CARROLL, S. A. & WALTHER, J. V. 1990. Kaolinite dissolution at 25 degrees, 60 degrees, and 80 degrees C. *American Journal of Science,* 290**,** 797-810.

8. CHAPARRO, M. C., SAALTINK, M. W. & SOLER, J. M. 2017. Reactive transport modelling of cement-groundwater-rock interaction at the Grimsel Test Site. *Physics and Chemistry of the Earth, Parts A/B/C,* 99**,** 64-76.

9. CHEN, X. & THORNTON, S. 2018. Multi-Mineral Reactions Controlling Secondary Phase Evolution in a Hyper-Alkaline Plume. *Environmental Geotechnics.*

10. CHEN, X., THORNTON, S. F. & SMALL, J. 2015. Influence of hyper-alkaline pH leachate on mineral and porosity evolution in the chemically disturbed zone developed in the near-field host rock for a nuclear waste repository. *Transport in Porous Media,* 107**,** 489-505.

11. CHERMAK, J. 1993. Low temperature experimental investigation of the effect of high pH KOH solutions on the Opalinus shale, Switzerland. *Clays and Clay Minerals,* 41**,** 365-372.

12. CROSSLAND, I. G. J. C. C. R. 2007. Cracking of the Nirex Reference Vault Backfill: a review of its likely occurrence and significance. 250**,** 1.

13. DE WINDT, L., MARSAL, F., TINSEAU, E. & PELLEGRINI, D. 2008. Reactive transport modeling of geochemical interactions at a concrete/argillite interface, Tournemire site (France). *Physics and Chemistry of the Earth, Parts A/B/C,* 33**,** S295-S305.

14. DELANY, J. & LUNDEEN, S. 1990. The LLNL thermochemical database. *Lawrence Livermore National Laboratory Report UCRL-21658,* 150.

15. DOZOL, M. & HAGEMANN, R. 1993. Radionuclide migration in groundwaters: Review of the behaviour of actinides (Technical Report). *Pure and Applied Chemistry.*

16. EBERL, D. & HOWER, J. 1977. The hydrothermal transformation of sodium and potassium smectite into mixed-layer clay. *Clays and Clay Minerals,* 25**,** 215-227.

17. FELIPE-SOTELO, M., HINCHLIFF, J., FIELD, L., MILODOWSKI, A., PREEDY, O. & READ, D. 2017. Retardation of uranium and thorium by a cementitious backfill developed for radioactive waste disposal. *Chemosphere,* 179**,** 127-138.

18. FERNANDEZ, R., CUEVAS, J., RODRIGUEZ, M., VIGIL DE LA VILLA, R. & CUNADO, M. A. 2012. The stability of zeolites and CSH in the high pH reaction of bentonite.

19. FRANCIS, A., CATHER, R. & CROSSLAND, I. J. N. S. R. S., UNITED KINGDON NIREX LIMITED, 57P 1997. Development of the Nirex Reference Vault Backfill; report on current status in 1994.

20. GAUCHER, E. C. & BLANC, P. 2006. Cement/clay interactions – A review: Experiments, natural analogues, and modeling. *Waste Management,* 26**,** 776-788.

21. GLASSER, F. P. 2001. Mineralogical aspects of cement in radioactive waste disposal. *Mineralogical Magazine,* 65**,** 621-633.

22. GYSI, A. P. & STEFÁNSSON, A. 2012. Experiments and geochemical modeling of CO2 sequestration during hydrothermal basalt alteration. *Chemical Geology,* 306**,** 10-28.

23. HARRIS, A., HEARNE, J. & NICKERSON, A. 2001a. The effect of reactive groundwaters on the behaviour of cementitious materials. AEA Technology Report AEAT/R/ENV/0467.

24. HARRIS, A., MANNING, M. & THOMPSON, A. 2001b. Testing of models of the dissolution of cements-leaching behaviour of Nirex Reference Vault Backfill. *AEA Technology Report, AEAT/ERRA-0316.* Nirex Ltd. Harwell, UK.

25. HELINSKI, M., FAHEY, M. & FOURIE, A. 2007. Numerical modeling of cemented mine backfill deposition. *Journal of Geotechnical and Geoenvironmental engineering,* 133**,** 1308-1319.

26. HODGKINSON, E. S. & HUGHES, C. R. 1999. The mineralogy and geochemistry of cement/rock reactions: high-resolution studies of experimental and analogue materials. *Geological Society, London, Special Publications,* 157**,** 195-211.

27. IDIART, A., LAVIÑA, M., KOSAKOWSKI, G., COCHEPIN, B., MEEUSSEN, J. C., SAMPER, J., MON, A., MONTOYA, V., MUNIER, I. & POONOOSAMY, J. 2020. Reactive transport modelling of a low-pH concrete/clay interface. *Applied Geochemistry,* 115**,** 104562.

28. KLAJMON, M., HAVLOVÁ, V., ČERVINKA, R., MENDOZA, A., FRANCŮ, J., BERENBLYUM, R. & ARILD, Ø. 2017. REPP-CO2: Equilibrium Modelling of CO2-Rock-Brine Systems. *Energy Procedia,* 114**,** 3364-3373.

29. KNAUSS, K. G. & WOLERY, T. J. 1988. The dissolution kinetics of quartz as a function of pH and time at 70 C. *Geochimica et Cosmochimica Acta,* 52**,** 43-53.

30. LICHTNER, P. C. 1988. The quasi-stationary state approximation to coupled mass transport and fluid-rock interaction in a porous medium. *Geochimica et Cosmochimica Acta,* 52**,** 143-165.

31. MOHNOT, S., BAE, J. & FOLEY, W. 1987. A study of alkali/mineral reactions. *SPE Reservoir Engineering,* 653**,** 663.

32. MONTE, L., BRITTAIN, J. E., HAKANSON, L., SMITH, J. T. & VAN DER PERK, M. 2004. Review and assessment of models for predicting the migration of radionuclides from catchments. *J Environ Radioact,* 75**,** 83-103.

33. NAKAHIRA, A., NAGANUMA, H., KUBO, T. & YAMASAKI, Y. 2008. Synthesis of monolithic tobermorite from blast furnace slag and evaluation of its Pb removal ability. *Journal of the Ceramic Society of Japan,* 116**,** 500-504.

34. NARDI, A., IDIART, A., TRINCHERO, P., DE VRIES, L. M. & MOLINERO, J. 2014. Interface COMSOL-PHREEQC (iCP), an efficient numerical framework for the solution of coupled multiphysics and geochemistry. *Computers & Geosciences,* 69**,** 10-21.

35. PARKHURST, D. L. & APPELO, C. 2013. Description of input and examples for PHREEQC version 3: a computer program for speciation, batch-reaction, one-dimensional transport, and inverse geochemical calculations. US Geological Survey.

36. PFINGSTEN, W., PARIS, B., SOLER, J. M. & MÄDER, U. K. 2006. Tracer and reactive transport modelling of the interaction between high-pH fluid and fractured rock: Field and laboratory experiments. *Journal of Geochemical Exploration,* 90**,** 95-113.

37. PITTY, A. & ALEXANDER, W. 2010. A natural analogue study of cement buffered, hyperalkaline groundwaters and their interaction with a repository host rock IV: an examination of the Khushaym Matruk (central Jordan) and Maqarin (northern Jordan) sites. *NDA-RWMD Technical Report, NDA, Moors Row, UK.*

38. PUTYRSKAYA, V. & KLEMT, E. 2007. Modeling 137Cs migration processes in lake sediments. *J Environ Radioact,* 96**,** 54-62.

39. ROSE, N. 1991. Dissolution rates of prehnite, epidote, and albite. *Geochimica et Cosmochimica Acta,* 55**,** 3273-3286.

40. SAVAGE, D. 1997. Review of the potential effects of alkaline plume migration from a cementitious repository for radioactive waste. *Research & Development Technical Report P,* 60.

41. SAVAGE, D. 2011. A review of analogues of alkaline alteration with regard to long-term barrier performance. *Mineralogical Magazine,* 75**,** 2401-2418.

42. SAVAGE, D., BATEMAN, K., HILL, P., HUGHES, C., MILODOWSKI, A., PEARCE, J., RAE, E. & ROCHELLE, C. 1992. Rate and mechanism of the reaction of silicates with cement pore fluids. *Applied Clay Science,* 7**,** 33-45.

43. SAVAGE, D., BENBOW, S., WATSON, C., TAKASE, H., ONO, K., ODA, C. & HONDA, A. 2010. Natural systems evidence for the alteration of clay under alkaline conditions: an example from Searles Lake, California. *Applied Clay Science,* 47**,** 72-81.

44. SAVAGE, D., CAVE, M. R., MILODOWSKI, A. E. & GEORGE, I. 1987. Hydrothermal alteration of granite by meteoric fluid: an example from the Carnmenellis Granite, United Kingdom. *Contributions to Mineralogy and Petrology,* 96**,** 391-405.

45. SAVAGE, D., NOY, D. & MIHARA, M. 2002. Modelling the interaction of bentonite with hyperalkaline fluids. *Applied Geochemistry,* 17**,** 207-223.

46. SAVAGE, D., WALKER, C., ARTHUR, R., ROCHELLE, C., ODA, C. & TAKASE, H. 2007. Alteration of bentonite by hyperalkaline fluids: A review of the role of secondary minerals. *Physics and Chemistry of the Earth, Parts A/B/C,* 32**,** 287-297.

47. SILVA, R. J. J. M. O. P. L. A. 1991. Mechanisms for the retardation of uranium (VI) migration. 257.

48. SMALL, J., BRYAN, N., LLOYD, J., MILODOWSKI, A., SHAW, S. & MORRIS, K. 2016. Summary of the BIGRAD project and its implications for a geological disposal facility. *National Nuclear Laboratory, Report NNL (16),* 13817.

49. VAN DER LEE, J. 1998. Thermodynamic and mathematical concepts of CHESS.

50. VASCONCELOS, R. G. W., BEAUDOIN, N., HAMILTON, A., HYATT, N. C., PROVIS, J. L. & CORKHILL, C. L. 2018. Characterisation of a high pH cement backfill for the geological disposal of nuclear waste: The Nirex Reference Vault Backfill. *Applied Geochemistry,* 89**,** 180-189.

51. VELDE, B. 1965. Experimental determination of muscovite polymorph stabilities. *American Mineralogist: Journal of Earth and Planetary Materials,* 50**,** 436-449.

52. WALKER, G. P. 1960. Zeolite zones and dike distribution in relation to the structure of the basalts of eastern Iceland. *The Journal of Geology,* 68**,** 515-528.

53. WILSON, J., BENBOW, S. & METCALFE, R. 2017. Understanding the Long-term Evolution of Cement Backfills: Alteration of NRVB Due to Reaction with Groundwater Solutes. Report.

54. WILSON, J. C., BENBOW, S. & METCALFE, R. 2018. Reactive transport modelling of a cement backfill for radioactive waste disposal. *Cement and Concrete Research,* 111**,** 81-93.

55. WORLEY, W. G. 1994. *Dissolution kinetics and mechanisms in quartz-and grainite-water systems.* Massachusetts Institute of Technology.

Chapter 6: Analysis of uranium sorption in a laboratory column experiment using a reactive transport and surface complexation model

Abstract

The transport and retardation of radioactive elements in hyper alkaline conditions of radioactive waste repositories is a challenging field that is still poorly understood. In this study, the transport and attenuation of uranium in a column experiment was modelled by considering kinetic reactions, advection-dispersion and chemical/physical retardation processes. The modelling was first performed for three-alluvium samples from Yucca Mountain in circumneutral pH to moderately alkaline conditions. Sorption of uranyl (UO_2^{2+} (U_{VI})) was found to strongly depend on the surface complexation model assumed, with no significant removal of U_{VI} by precipitation or ion exchange process. The surface/edge site reaction of Al-hydroxyl group in kaolinite were shown to have a high affinity for uranyl adsorption, while the hydrous ferric oxide edge on hematite adsorbed most of the uranyl ions. The model was then used to interpret uranium transport in a laboratory column filled with Hollington sandstone under hyper alkaline (pH 13) conditions. The simulation results show that uranium adsorption on the Al-hydroxyl edge of kaolinite exceeds adsorption by the C-S-H phase. This result may reflect the lack of surface complexation parameters for C-S-H minerals. Hence, further studies are required in the field of surface complexation reactions for C-S-H phases.

List of Notations:

A_0 — Initial Surface area of the mineral

A — Effective surface area of the mineral

A_r^t — Reactive surface area of the mineral at specific time

C_i — Total concentration of component i in water

D_L — Hydrodynamic dispersion coefficient

$\dfrac{IAP}{K}$ — Ion activity divided by equilibrium constant, equal to the saturation ratio (SR) of the reactant

k_i — Reactant specific reaction rate

l — Number of kinetic reactants

M_i — Moles of reactant

m_t — Total mass of the rock sample

m_i — Moles of reactant at a given time

m_{0i} — Initial moles of reactant

n — Order of reaction constant (Crystal grain size distribution)

q_l — Darcy flux for the liquid

R_m — Overall dissolution/precipitation rate of kinetic reactant m

R_i — Reactant overall dissolution rate

t — Time

v_{im} — Stoichiometric coefficient of component i in kinetic reactant m

V — Solution volume

x — Distance

X_i — Mass fraction of each mineral in the rock sample

ϕ — Porosity

6.1 Introduction

Uranium is a radioactive and toxic element which, besides its natural occurrence, can be distributed to the environment through human activities such as oil and gas production, mining processes, and the nuclear industry (Campos et al., 2011, Chandrajith et al., 2010, Merkel and Hasche-Berger, 2006, Merkel and Hasche-Berger, 2008, Ricka et al., 2010). Those industrial processes can enrich the radionuclides activities of uranium and its decay products known as NORM (Naturally Occurring Radioactive material) (Protection, 2003). In an oxidising environment the most stable and soluble form of uranium is (Uranyl UO_2^{2+} (U_{VI})), which can react with sulphates, carbonates and nitrates to form complex phases with altered speciation and transport characteristics (Zielinski et al., 1997, Meinrath, 1998, Tutu et al., 2009, Ribera et al., 1996, Grenthe et al., 1992). In subsurface applications the aqueous concentration and mobility of U_{VI} ions without a complexing ligand are widely recognised to be controlled by sorption at mineral surfaces (Barnett et al., 2002, Prikryl et al., 2001, Turner et al., 1996a, Thomson et al., 1986, Payne and Waite, 1991). The interaction between dissolved radionuclides and minerals in the host rock (sorption at solid/solution interface) is critical when evaluating the immobilisation of radionuclides. Uranyl sorption on mineral surfaces can involve multiple processes (binding sites), such as absorption, adsorption, ion exchange and edge/surface complexation. These processes can significantly influence the transport of pollutants and radionuclides in soils and rocks. For example, adsorption refers to the adherence of ions to the solid surface, while absorption implies uptake of ions into the solid. Conversely, ion exchange involves the substitution of one ion for another over the solid surface (Appelo and Postma, 2005). In earlier studies, sorption models use the K_d (distribution coefficient) approach, which sums all interactions

between the solid/water interaction (Ticknor, 1994, Missana et al., 2008, Glynn, 2003, Davis et al., 2004, Curtis et al., 2004).

In recent years, a mechanistic approach has been developed based on several absorption/adsorption laboratory experiments conducted on site-specific clay materials to generate a surface complexation model (SCM) that can describe the migration behaviour, stability constants and stoichiometry of different metal/metalloid ions reactions. The SCM can describe and simulate sorption between aqueous uranyl and the surface of clay minerals (sorbent) by fitting the thermodynamic data from other referenced studies under different chemical conditions for various aqueous (uranium) species (Bradbury and Baeyens, 2005, Zachara and McKinley, 1993, Kim, 2001, Davis, Davis et al., 2002, Koretsky, 2000). Through the mass action equation, the surface complexes formed can be then integrated within the reactive transport models (Curtis et al., 2006, Papini et al., 1999).

In high heat generating waste disposal concepts, swelling clays (e.g. bentonite) will be widely used, in part, because of their capability to sorb heavy metals. These clays can sorb heavy metals due to their high osmotic swelling capacity and large specific surface area (Barnett et al., 2000, Barnett et al., 2002, McLing, 1998). Moreover, clay minerals can simultaneously maintain a fixed, usually negative charge within the particle structure which encourages ion exchange within the interlayer's spaces, while the variable charge is generated at the clay edges, which may be positive or negative depending on the pH value. Therefore, both cations and/or anions can potentially be sorbed to neutralise the structural charge. Three common surface complexation models are usually used to fit the experimental results; the double/diffuse layer model (DLM), the triple-layer model (TLM), and the constant capacitance model (CCM) (Waite et al., 1994, Turner et al., 1998,

Hiemstra et al., 1989, Fletcher and Sposito, 1989, Turner et al., 1996a). Due to the low hydraulic conductivity of clay soils, most investigations have been carried out in static systems using batch experiments with powdered material left in contact for periods of time with cement leachate (Claret et al., 2002, Ramírez et al., 2002, Fernández et al., 2009, Takahashi et al., 2007). Fewer studies have performed dynamic experiments using diffusion set-ups or advective experiments (Adler et al., 1999).

This work aims to establish a reactive transport model with a series of kinetic and equilibrium reactions and incorporate uranyl aqueous speciation and surface charge measurements that control uranium removal from the solution. The modelling results were obtained using PHREEQC geochemical code. The effect of variable mineralogy on uranium sorption was studied at room temperature and fixed pH value.

6.2 Experiment

In this study, a reactive transport model combined with a diffuse layer model (DLM) was used to analyse the adsorption of uranyl ions from aqueous solution in column experiments. The objective was to determine the key parameters that control the sorption of this radionuclide at the solid-solution interface in the host rock of a candidate geological repository. The model was first applied to three alluvium samples from Yucca Mountain that are rich in smectite clay and equilibrated with circumneutral to moderately alkaline solutions. Once the model was validated against the experimental results, it was then used to interpret the transport of uranium in a highly alkaline solution through Hollington Sandstone, a material mainly composed of silicate minerals with minor amounts of

kaolinite and hematite. Note, Hollington Sandstone has been used in this study as a mineral analogue for host rocks of UK's low/intermediate nuclear waste disposal.

6.2.1 Yucca Mountain alluvium

The Yucca Mountain project in Nevada has been proposed as a geological repository site for the disposal of radioactive wastes. A series of sorption studies (batch, column, and in situ field transport) have been conducted on the alluvium soil to demonstrate its capability to retard the transport of radionuclides in the subsurface.

Three flow-through column experiments were conducted in the early 2000's with continuous flow and fully saturated conditions using alluvium from the southern area of Yucca Mountain (Scism, 2005). The columns were filled with alluvium that had been wet sieved to retain the 2000-75 µm size-fraction. The experimental parameters for the three column tests are shown in Table (6.1). The key mineral phases in the alluvium were identified and quantified using X-ray Diffraction (XRD) following the procedure published by (Chipera and Bish, 2002). Table (6.2) shows the mineralogy of the alluvium in each of the three columns.

Table 6.1: initial parameters for the Yucca Mountain alluvium column experiments.

	Column 1	Column 2	Column 3
Column length	45 cm	46 cm	45 cm
Column diameter	2.5 cm	2.5 cm	2.5 cm
Particle size (µm)	75-2000	75-2000	75-2000
pH range	8.4-8.7	8.2-8.5	8.4-8.7
Dry sample weight (g)	374.61	356.59	390.72
Water inside column weight (g)	89.82	102.4	85.98
Average flow rate (ml/hr)	2.6	2.2	2.2
Porosity	0.41	0.44	0.39

Table 6.2: Yucca Mountain alluvium sample mineralogy using (XRD). Values in weight %.

Mineral	Column 1	Column 2	Column 3
Quartz	15.3	8.7	10.1
Plagioclase	23	26	28.4
K-feldspar	24.4	30.6	17.5
Clinoptilolite	7.6	11.6	12
Mica	1.3	1.8	1
Kaolinite	0.5	0.4	0.2
Cristobalite	5.8	8.1	5.9
Tridymite	4.1	1.6	4.3
Opal-CT	13.6	-	-
Hematite	0.4	0.5	0.6
Smectite	4.6	8	19.4
Total	100.6	97.4	99.4

The background solutions (groundwater) used in the experiment was taken from water wells drilled close to each alluvium sample wells. The water chemistry and ion concentration data for each column are shown in Table (6.3). A concentrated $UO_2(NO_3)_2$ solution was diluted in the groundwaters to produce a uranium tracer solution with a concentration of 1×10^{-6} M. The columns were initially allowed to equilibrate with groundwaters and then the uranium tracer solution was injected at an initial flow rate of 10 ml/hr, which decreased to 3 ml/hr as the experiment continued. The fluid sample at the column outlet was placed in a reciprocating shaker, followed by centrifugation to separate the solids. Simultaneously, control samples that contained only a tracer without alluvium were also shaken and centrifuged to estimate the amount of uranium sorbed to the tube walls. Aqueous uranium concentrations were determined by Liquid Scintillation Counting (LSC) (the concentration in the tracer solution was measured before and after the experiment). Further details of the experimental procedure and protocol are provided in (Scism, 2005).

Table 6.3: Chemistry of the site groundwater used as an influent solution to the column experiments for the Yucca Mountain alluvium experiments.

Ion concentration (mg/L)	Column 1	Column 2	Column 3
Alkalinity (As HCO_3^-)	189	100	212
Ca^{2+}	3.7	13	0.92
Mg^{2+}	0.31	2.5	0.03
Na^+	91.5	43	107.3
K^+	3.7	5.2	3.4
Cl^-	6.1	6.9	5.6
SO_4^{2-}	22	14	18.7
NO_3^-	2.21	1.4	1.2
pH	8.6	7.78	8.85

*All solutions have been charged balanced with chloride in PHREEQC

6.2.2 Hollington Sandstone

Hollington sandstone is part of the Lower Triassic Bromsgrove Sandstone Group. It is mainly composed of silicate minerals with minor quantities of clay and hematite. Its porous nature allows the study of rock-cement-leachate reactive transport reactions in strata with a similar mineralogical composition to that a proposed geological radioactive waste repository. Column experiments on crushed Hollington sandstone permeated with a synthetic young cement leachate at a temperature of 50°C (Small et al., 2016) are used to predict the transport of aqueous U_{VI} in Hollington sandstone. Tables (6.4) and (6.5) show the mineralogical composition of the sandstone sample used in the experiment and the chemical composition of the synthetic young cement leachate, respectively. Further details of the experimental set-up and procedures are provided in (Baqer et al., 2021).

Table 6.4: Mineralogical composition of Hollington Sandstone **(Chen et al., 2015b)**

Mineral	Mineral proportion (Volume %)
Quartz	75.5
K-feldspar	16
Kaolinite	3.5
Illite/chlorite/smectite	3.7
Muscovite	0.7
Phlogopite	0.2
Apatite	0.2
TiO$_2$	0.3

Table 6.5: Chemical composition of the synthetic young cement leachate (YCL) used in the Hollington sandstone column experiment (Small et al., 2016).

Composition	YCL (mg/L)
Al^{3+}	-
Ca^{2+}	23
K$^+$	3202
Mg^{2+}	0.07-
Na$^+$	2178
Si^{4+}	-
OH$^-$	3192*
Measured pH	13.1 at 25°C (12.4 at 50°C)

Notes: * Calculated by assuming charge balance with cations. Equivalent to pH 12.4 at 50°C.

6.3 Modelling approach

The geochemical speciation code PHREEQC (version 3.6.1) (Parkhurst and Appelo, 2013) was used to simulate the transport and sorption of uranium in the column experiments. The kinetics of dissolution and precipitation, equilibrium reaction and porosity evolution have been incorporated in the coding. A hybrid mixed kinetic-equilibrium approach was used to overcome the shortage and uncertainties of some kinetic reaction parameters (e.g. reactive surface area, specific dissolution/precipitation kinetics) (Chen and Thornton, 2018, Van der Lee, 1998, Bethke, 1996). The LLNL thermochemical database was used as a starting point to compile the details of different chemical reactions (aqueous reactions, mineral

dissolution/precipitation, surface complexation, ion exchange) (Delany and Lundeen, 1990). Uranium thermodynamic data were obtained from the "Second update on the chemical thermodynamics of uranium, neptunium, plutonium, americium and technetium" published by the OECD Nuclear Energy Agency (Grenthe et al., 2020). Surface complexation and ion exchange reaction were obtained from the literature and then added manually to the database.

6.3.1 Equilibrium/kinetic modelling of dissolution and precipitation

The sorption of a soluble radionuclide can be highly affected by dissolution/precipitation processes which occur at mineral surfaces. In some circumstances, the dissolution of some mineral phases can result in the nucleation of clay minerals or hydrous oxides as a coating on the mineral surfaces, which will increase the number and density of sorption sites (Ticknor, 1994). Also, precipitation process can sometimes involve radionuclides, removing them from the solution by formation of a secondary phase. The alluvium soil sample contains 11 minerals with different percentages in each column. To ensure consistency in the results and to highlight the sorption effect of each mineral, all the mineral phases were included in the modelling except for "Opal-CT" since it is only found in column 1. The higher percentage minerals (quartz, plagioclase, k-feldspar, clinoptilolite, cristobalite, and smectite) were modelled kinetically while the rest were included in the equilibrium reaction. Equation (6.1) below was used to calculate the rate of mineral dissolution/precipitation reactions (Appelo and Postma, 2005):

$$R_i = k_i \left(\frac{A_i}{V}\right)\left(\frac{M_i}{M_{i0}}\right)^n \left(1 - \left(\frac{IAP}{K}\right)_i\right) \quad for\ each\ mineral\ i \qquad (6.1)$$

where R is the overall dissolution/precipitation rate (mol L^{-1} s^{-1}), k is the specific dissolution/precipitation rate (mol m^{-2} s^{-1}), A is the effective surface area of the mineral (m^2 g^{-1}), V is the pore volume (L), M is the moles of solid at a given time, M_0 is the initial moles of solid, and (IAP/K) is equal to the saturation ratio (SR) value of the mineral where IAP is the Ion Activity Product and K is the equilibrium constant. In the above equation, the molar concentration (M/M_0) has n power, which is a function of the initial crystal grain size distribution that affects the solid dissolution rate. Usually, a value of 2/3 is used for uniformly dissolving cubes or spheres in the monodisperse population (Appelo and Postma, 2005). Table (6.6) shows the specific kinetic rates and the reactive surface areas for the kinetically modelled minerals. To investigate the effect of precipitation on uranium removal from solution, four uranium mineral phases were added in the equilibrium reactions (In PHREEQC) during the simulation of the Yucca Mountain and Hollington sandstone experiments (CaUO₄, Uranophane, Becquerelite, Rutherfordine). These phases were chosen based on the common stable uranium minerals found in the literature (ATKINS et al., 1988, Wronkiewicz et al., 1992, Gorman-Lewis et al., 2008, Felipe-Sotelo et al., 2017). Also, Tobermorite-14A, CSH-gel, $CaUO_4$, and $Na_2U_2O_7$ were included in the modelling of the Hollington sandstone experiment as a possible precipitating phase in a high alkaline environment.

Table 6.6: Kinetic parameters for the primary minerals in the Yucca Mountain alluvium and Hollington rock sample.

Mineral	Modelling approach	Surface area (m^2/g)	Rate constant (Mol m^{-2} s^{-1})
Yucca Mountain (25ºC)			
Quartz	Kinetic	0.02 (De Windt et al., 2008)	$k = 1\times10^{-13.6}$ (Knauss and Wolery, 1988)
K-feldspar	Kinetic	0.02 (De Windt et al., 2008)	$k = 2\times10^{-14}$ (Appelo and Postma, 2005)
Plagioclase	Kinetic	0.02 (Watson et al., 2009)	$k = 1\times10^{-15.6}$ (Watson et al., 2009)
Clinoptilolite	Kinetic	0.02 (Watson et al., 2009)	$k = 1\times10^{-29.9}$ (Watson et al., 2009)
Cristobalite	Kinetic	0.02 (Watson et al., 2009)	$k = 1\times10^{-12.3}$ (Fernández et al., 2010)
Smectite	Kinetic	51 (Golubev et al., 2006)	$k = 1\times10^{-18.1}$ (Golubev et al., 2006)
Hollington Sandstone (50ºC)			
Quartz	Kinetic	0.02 (De Windt et al., 2008)	$k = 1\times10^{-12.7}$ (Knauss and Wolery, 1988)
K-feldspar	Kinetic	0.02 (De Windt et al., 2008)	$k = 6\times10^{-13}$ (Appelo and Postma, 2005)
Kaolinite	Kinetic	20 (Klajmon et al., 2017)	$k = 1\times10^{-12.5}$ (Carroll and Walther, 1990)

6.3.2 Dynamic porosity and reactive surface area

During the mineral dissolution/precipitation cycle, the system being studied can undergo several physical and chemical changes that affect radionuclide transport and sorption. In the model a dynamic porosity was used to emulate changes in the porosity that result from dissolution/precipitation reactions. Equation (6.2) shows the correlation between mineral mass and surface area during flow of the tracer solution in the column.

$$A_i = A_0 m_t X_i \qquad for\ each\ mineral\ i \qquad (6.2)$$

where m_t is the total mass of the rock sample, A_0 is the initial surface area ($m^2 g^{-1}$), and X_i is the mass fraction of each mineral in the rock sample (Beckingham et al., 2016). The

surface area is then coupled with the evolved porosity through equation (6.3) (Lichtner, 1988):

$$A_r^t = A_r^{t=0} \left(\frac{1 - \phi_t}{1 - \phi_{t=0}} \right)^{2/3} \quad (6.3)$$

where $A_r^{t=0}$ is the reactive surface area of the mineral at the initial porosity ($\phi_{t=0}$), and the mineral kinetic rate can be calculated using equation (6.4). The changed porosity can then again be calculated from the volume of the dissolved/precipitated moles of mineral. Further details concerning the mathematical derivation of the dynamic porosity model are provided in (Baqer et al., 2021).

$$R_i = \frac{k_i}{V} \left(A_{r,i}^{t=0} \left(\frac{1 - \phi_t}{1 - \phi_{t=0}} \right)^{2/3} m_{i,t} \right) \left(\frac{M}{M_0} \right)_i^n \left(1 - \left(\frac{IAP}{K} \right)_i \right) \quad (6.4)$$

$$(note:\ for\ each\ mineral\ i)$$

6.3.3 Transport process

The transport of the uranium tracer solution through the column was modelled using the one-dimensional (1D) mixed cells concept with flux type boundary conditions and a mass entering the column per unit time. This is applicable to a laboratory column with a diameter much smaller than the column length (Table 6.1) because of the near-zero concentration gradient at the column end (Appelo and Postma, 2005). The column was divided into ten equal length cells along the flow path, with additional cells at each end for inflow and outflow. The simulation was performed for a series of time steps in which each step is equal to the time taken for the pore solution in one cell to move into the next cell. The

simulation was performed for 700 hours, and the advection-dispersion process through the column was modelled using the equation of advection-reaction-dispersion described below (Equation 6.5) (Nardi et al., 2014):

$$\frac{\partial C_i}{\partial t} = \underbrace{-q_l \frac{\partial C_i}{\partial x}}_{Advection} + \underbrace{D_L \frac{\partial^2 C_i}{\partial x^2}}_{Dispersion} - \sum_{m=1}^{l} v_{im} R_m \qquad (6.5)$$

where C_i is the total concentration of component i in water (mol kgw^{-1}), q_l is the Darcy flux (m^3 m^{-2} s^{-1}) for the liquid, t is time (s), x is the distance (m), D_L is hydrodynamic dispersion coefficient (m^2 s^{-1}), v_{im} is the stoichiometric coefficient of component i in kinetic reactant m (dimensionless), R_m is the overall dissolution/precipitation rate of kinetic reactant m (mol kgw^{-1} s^{-1}), and l is the number of kinetic reactants. For each time step, advection was modelled first, followed by dispersion, then finally the chemical reactions were modelled, so the solution composition in each cell could be updated. The reader is referred to (Baqer et al., 2021) for more details concerning the transport model.

In the Yucca Mountain experiment, different flow rates for the pulse solution were used for each column. Based on the time step in each column, the velocity will vary, and therefore each column will have a different dispersivity value. Table (6.7) shows the modelling input parameters for the transport process simulation in the three columns.

Table 6.7: Input parameters for modelling transport process in the three Yucca Mountain alluvium columns.

	Column 1	Column 2	Column 3
Step time (hour)	95	60	40
Dispersivity (*m*)	0.04	0.03	0.06
Diffusion coefficient (*m²/s*)	0.3 x 10^{-9}	0.3 x 10^{-9}	0.3 x 10^{-9}

6.3.4 Uranium speciation

The aqueous speciation of the uranyl (UO_2^{2+}) ion is strongly influenced by pH, as it determines the stability of different ion complexes and the distribution of the surface sites, which will consequently shape the sorption mechanism (Chisholm-Brause et al., 1994). For example, where CO_2 is present, neutral uranyl-carbonate species start to form at pH values >6.5, and negatively charged uranyl-carbonate species dominate in alkaline conditions (Nair et al., 2014). Formation of negatively charged complexes will affect adsorption to partially ionised surface/edges sites (Guimarães et al., 2016, Ticknor, 1994). Table (6.8) lists equilibrium constants for uranium aqueous speciation reactions at 25 °C and pCO$_2$ = 10$^{-3.5}$ atm (Grenthe et al., 2020).

Table 6.8: Equilibrium constant for uranyl complexes added to PHREEQC database.

Reaction	Log k
$UO_2^{+2} + H_2O \rightarrow UO_2(OH)^+ + H^+$	-5.25
$UO_2^{+2} + 2H_2O \rightarrow UO_2(OH)_2 + 2H^+$	-12.15
$UO_2^{+2} + 3H_2O \rightarrow UO_2(OH)_3^- + 3H^+$	-20.25
$UO_2^{+2} + 4H_2O \rightarrow UO_2(OH)_4^{-2} + 4H^+$	-32.4
$UO_2^{+2} + CO_3^{-2} \rightarrow UO_2CO_3$	9.94
$UO_2^{+2} + 2CO_3^{-2} \rightarrow UO_2(CO_3)_2^{-2}$	16.61
$UO_2^{+2} + 3CO_3^{-2} \rightarrow UO_2(CO_3)_3^{-4}$	21.84
$2UO_2^{+2} + CO_3^{-2} + 3H_2O \rightarrow (UO_2)_2CO_3(OH)_3^- + 3H^+$	-0.86
$UO_2^{+2} + 2Ca^{+2} + 3CO_3^{-2} \rightarrow Ca_2UO_2(CO_3)_3$	30.70
$UO_2^{+2} + Mg^{+2} + 3CO_3^{-2} \rightarrow MgUO_2(CO_3)_3^{-2}$	26.1

6.3.5 Sorption

The focus of this study is modelling uranium sorption onto minerals containing Fe (e.g., hydrous ferric oxide) and clays (Barnett et al., 2002, Cheng et al., 2007, Ho and Miller, 1986, Ames et al., 1983, Echevarria et al., 2001, Missana et al., 2004). Smectite contains

several types of sorption site with high affinity for aqueous uranium complexes (Barnett et al., 2000, Davis et al., 2004), and kaolinite contains aluminol surface/edges that also have high affinity for uranium species (Borovec, 1981, Kohler et al., 1992). Furthermore, the presence of iron ions in hematite can further enhance uranium sorption, hence it has also been included in the surface complexation model (Davis et al., 2004, Dong and Wan, 2014). Most published literature model sorption with cation exchange and surface complexation mechanisms (Turner et al., 1996a, Missana et al., 2008, Bachmaf and Merkel, 2011, Korichi and Bensmaili, 2009, Nair et al., 2014). The advance in this study is that it models both ion exchange and surface complexation as multi-site complexation phenomena at the clay-water interface (Figure 6.1).
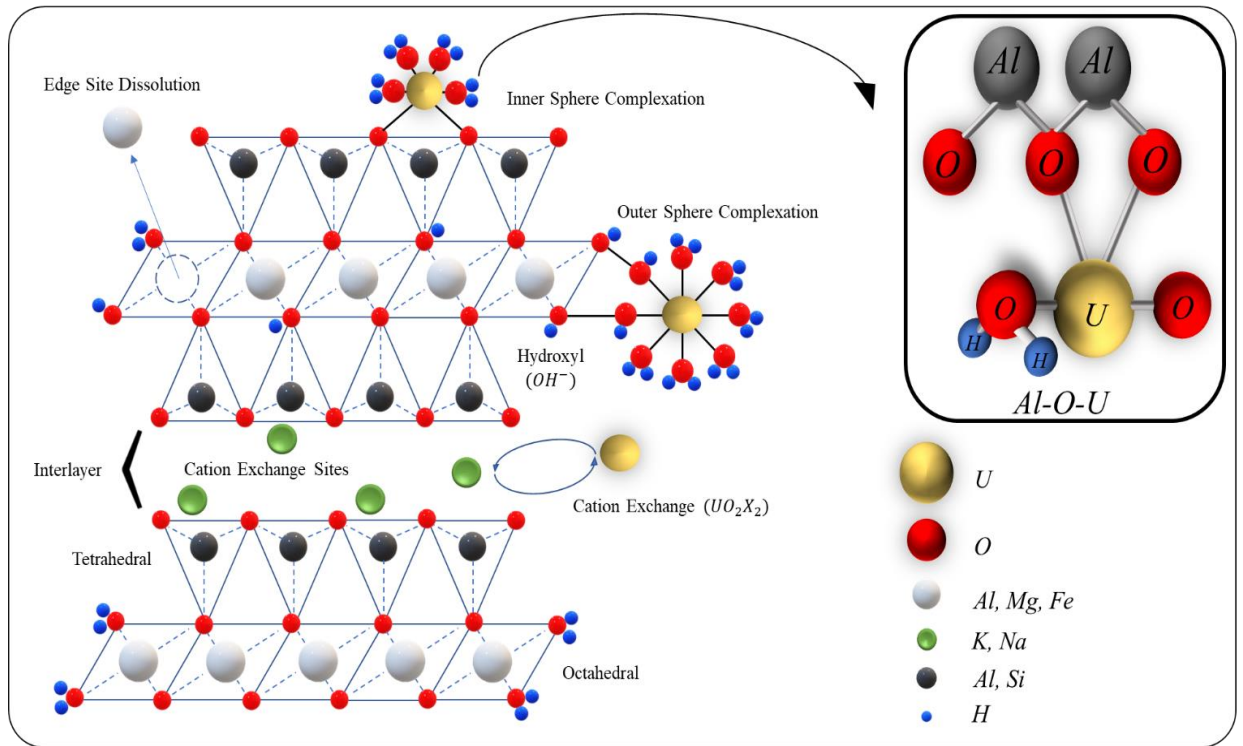
Figure 6.1: Multi-site complexation model of uranium on smectite clay.

1.2.1.1. Ion Exchange

Uranyl sorption at smectite interlayer cation exchange sites is included in the model. It assumed that these sites are initially occupied by either Ca^{2+} or Na$^+$ cations (Na$^+$ is readily displaced by UO_2^{2+}, whereas Ca^{2+} has a similar affinity to interlayer cation exchange sites to uranyl (Tsunashima et al., 1981, McKinley et al., 1995, Hiemstra et al., 1989)). The stoichiometry and equilibrium constants assumed for these cation exchange reactions are shown in Table (6.9). The site density (X$^-$) is assumed to equal the cation exchange capacity (CEC), which for smectite equals 810 meq/kg (Appelo and Postma, 2005).

Table 6.9: Equilibrium constants used for the cation exchange reactions

Exchange Species	Log k	Reference
$UO_2^{2+} + 2NaX = UO_2X_2 + 2Na^+$	0.45	(Marques Fernandes et al., 2012)
$UO_2^{2+} + CaX_2 = UO_2X_2 + Ca^{2+}$	0.049	(Guimarães et al., 2016)

1.2.1.2. Surface complexation

A surface complexation model (SCM) (Guimarães et al., 2016, Dong and Wan, 2014, Dangelmayr et al., 2017, Korichi and Bensmaili, 2009, Nair et al., 2014) is used for uranium sorption onto various surface and edge sites on clay minerals to overcome the limitation of reactive solute transport using the average K$_d$ value (laboratory calculated) approach (which depends on, and is limited to, a specific water composition) (Glynn, 2003, Reardon, 1981, Zhu, 2003, Bethke and Brady, 2000, Davis et al., 1978, Kent et al., 1988). The model assumes that the mineral surface includes a group of functional hydroxyl surfaces denoted as ($\equiv SOH$), and that the sorption of uranium is highly dependent on the

behaviour of these functional groups at surface and edge sites on clay minerals. Such sites are amphoteric, so protonation and deprotonation equilibrium reactions of these sites are included in the model (Missana et al., 2008)

$$\equiv SOH_2^+ \iff \equiv SOH + H^+ \qquad K_1 \qquad (6.6)$$

$$\equiv SOH \iff \equiv SO^- + H^+ \qquad K_2 \qquad (6.7)$$
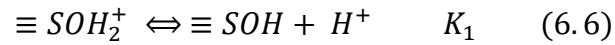
where K_1 and K_2 are the equilibrium constants (Table 6.10).

In this study a double/diffuse layer SCM model was used, and the moles of each aqueous species are computed based on a constant thickness for the diffuse layer. Before applying the DLM for the adsorption of uranyl ions onto clay surfaces, several variables must be defined: (1) the chemical reaction at the clay-water interface, (2) the surface complexation equilibrium constant (*Log k*), and (3) surface site density and amount of available binding sites.

Usually, for smectite, the binding of uranyl aqueous complexes takes place on the aluminol and silanol edges, and on the aluminol edge site for kaolinite (Bachmaf and Merkel, 2011, McKinley et al., 1995, Turner et al., 1996b, Zachara and McKinley, 1993). The amount of edge/surfaces associated with surface complexation is usually 10-20% of the sorption sites (Anderson and Sposito, 1991, Pabalan and Turner, 1996, McKinley et al., 1995, Hiemstra et al., 1989). Table (6.10) shows the surface edge site reactions on aluminol/silanol hydroxyl groups included in the PHREEQC modelling to best fit the experimental uranyl sorption results. (Dzombach and Morel, 1990) recommend using 10% of the total specific surface area measured by the N_2-BET method to account for the area of the crystallite surface edge sites, or site density value of 2.3 sites/nm^2 for all minerals. Therefore, the total

number of moles of binding site surfaces was calculated from the weight percentage and surface area of each mineral in the bulk sample of alluvium in the column. Note that the surface complexation reaction of carbonate complexes has been ignored in this study since they have high solubility.

Table 6.10: Surface complexation reactions applied in the model

Edge site reaction	Log k
Smectite	
$\equiv AlOH + H^+ \Leftrightarrow \equiv Al - OH_2^+$	12.3[a]
$\equiv AlOH \Leftrightarrow \equiv AlO^- + H^+$	-13.6[a]
$\equiv AlOH + UO_2^{+2} \Leftrightarrow \equiv AlO - UO_2^+ + H^+$	7.7[b]
$\equiv SiOH + H^+ \Leftrightarrow \equiv Si - OH_2^+$	-0.95[a]
$\equiv SiOH \Leftrightarrow \equiv SiO^- + H^+$	-6.95[a]
$\equiv SiOH + UO_2^{+2} \Leftrightarrow \equiv SiO - UO_2^+ + H^+$	0.75[b]
Kaolinite	
$\equiv AlOH + H^+ \Leftrightarrow \equiv Al - OH_2^+$	13.33[c]
$\equiv AlOH \Leftrightarrow \equiv AlO^- + H^+$	-4.72[c]
$\equiv AlOH + UO_2^{+2} + H_2O \Leftrightarrow \equiv AlO - UO_2OH + 2H^+$	6[c]
Hematite	
$\equiv FeOH + H^+ \Leftrightarrow \equiv Fe - OH_2^+$	-5.1[d]
$\equiv FeOH \Leftrightarrow \equiv FeO^- + H^+$	-10.7[d]
$\equiv FeOH + UO_2^{+2} \Leftrightarrow \equiv FeO - UO_2^+ + H^+$	14.11[e]

(a) (Mckinley et al., 1993)
(b) (Guimarães et al., 2016)
(c) **(Bachmaf and Merkel, 2010b)**
(d) (Davis et al., 1978)
(e) (Sherman et al., 2008)

6.4 Results and discussion

6.4.1 Yucca Mountain alluvium

The final composition of the effluent solution was calculated after a series of geochemical reactions combined with fluid flow and uranium sorption. The results were obtained by implementing multiple binding-site ion complexation containing fixed and edge aluminol/silonal sites. Table (6.11) shows the predicted composition of the site

groundwater after equilibration with mineral phases in Yucca Mountain alluvium and atmospheric carbon dioxide.

Table 6.11: Background solution Predicted composition of the site groundwater after equilibration with mineral phases in Yucca Mountain alluvium and atmospheric carbon dioxide

Elements	Molality (Column 1) mol/kg	Molality (Column 2) mol/kg	Molality (Column 3) mol/kg
HCO_3^-	3.099×10^{-3}	1.640×10^{-3}	3.477×10^{-3}
Ca^{2+}	9.235×10^{-5}	3.244×10^{-4}	2.296×10^{-5}
Mg^{2+}	1.276×10^{-5}	1.029×10^{-4}	1.235×10^{-6}
Na^+	3.981×10^{-3}	1.871×10^{-3}	4.669×10^{-3}
K^+	9.466×10^{-5}	1.330×10^{-4}	8.699×10^{-5}
Cl^-	5.090×10^{-4}	1.947×10^{-4}	7.197×10^{-4}
SO_4^{2-}	2.291×10^{-4}	1.458×10^{-4}	1.948×10^{-4}
NO_3^-	1.578×10^{-4}	9.997×10^{-5}	8.570×10^{-5}
Ionic strength (mol/kgw)	4.626×10^{-4}	3.044×10^{-3}	5.112×10^{-3}

In all cases the initial uranium breakthrough curves almost occur at the same time as the HTO-tracer (Figure 6.2). However, uranium transport was significantly retarded by the columns. As the pulse solution was injected into the column, uranium started to break through the alluvium sample and react with the mineral phases. The modelling results describe the adsorption of uranyl well: the uranium concentration starts to increase in the existing fluid until it reaches a maximum concentration of 0.0078 mg/L, 0.023 mg/L, and 0.08 mg/L for columns 1, 2 and 3, respectively (Figure 6.3). However, the highest value of the uranium concentration was still much lower than the pulse solution concentration (0.24 mg/L), implying that uranium retardation happens simultaneously with the fluid flow.

The simulated saturation indices of uranium phases ($CaUO_4$, uranophane, becquerelite, rutherfordine, Figure 6.4) indicate that they are undersaturated and the precipitation of solid uranium phases is unlikely to occur in the experiment. Therefore, precipitation can be excluded as a possible uranium removal mechanism in this experiment. This is usually the

case since the nucleation kinetics of solid phases is considered to be very slow to affect uranium removal significantly (Dangelmayr et al., 2017). Consequently, the decrease in uranium concentration is due to the sorption of uranyl ions by ion exchange and surface complexation reactions only.

Figure (6.5) shows the number of moles of uranium adsorbed by cation exchange processes. As the experiment proceeds, the pulse solution is exposed more to the smectite mineral; thus, more uranyl is exchanged on the smectite binding sites. However, the amount of adsorbed uranyl is minimal throughout the experiment, which agrees well with other studies that highlight the dominance of ion exchange in the region of low pH only (McKinley et al., 1995, Zachara and McKinley, 1993, Davis and Kent, 2018). Therefore, uranium binding to a fixed site by ion exchange process is most likely not the dominant sorption mechanism in this model as well.

Figure (6.6) illustrates the results of the four surface edges sites ($AlOH_{Smectite}$, $SiOH$, $AlOH_{Koalinite}$, $FeOH$), which confirm the modelling approach for uranium sorption of binding to a variable charge site by surface complexation. As expected, uranyl ions form an inner surface complex on smectite, kaolinite and hydrous ferric oxide. When assessing the adsorption results of each surface site, column 3 shows the highest adsorption value in all four sites, followed by column 2 and finally column 1. This agrees well with the highest smectite and hematite weight percent in column 3 and the lowest weight percentage in column 1. Moreover, from Table (6.11), column 3 has the highest ionic strength while column 1 has the lowest, which agrees with the results of other literature that shows a more elevated surface complexation potential with higher ionic strength (Chisholm-Brause et al.,

2001, Hennig et al., 2002, Sylwester et al., 2000, Bauer et al., 2001, Korichi and Bensmaili, 2009, Schindler et al., 2015, Turner and Sassman, 1996).

The result reveals that the aluminol sites ($\equiv AlO - UO_2^+$) are more reactive than silonal sites ($\equiv SiO - UO_2^+$) for smectite. The number of adsorbed moles on the aluminol edge is much higher (6 orders of magnitude), which agrees well with higher uranyl affinity toward aluminol edges. This may be justified by the lower tendency of the ($\equiv SiO - UO_2^+$) group to donate its oxygen and form inner-sphere surface species (Morris et al., 1994, Kowal-Fouchard et al., 2004). Even with the high weight percent of smectite clay in the alluvium samples, it has the lowest sorption capacity for uranium. The aluminol surface edge sites in kaolinite have shown a higher affinity for uranyl adsorption, which is also reported in other studies (Borovec, 1981, Kohler et al., 1992, Payne et al., 2004) for a pH range between 5-9. This can be related to the higher number of the exposed surface sites at the Al-octahedral sheet (Kaolinite has a 1:1 clay structure), which results in greater uptake of uranyl ions.

In all three columns and among the four surface complexes, the $\equiv FeOH$ site has the highest number of adsorbed uranyl moles. The same behaviour has also been reported in other studies (Dzombak and Morel, 1991, Waite et al., 1994, Sherman et al., 2008, Hsi and Langmuir, 1985), in which for the region of neutral and alkaline pH, a very small mass weight percentage ($\approx 1\%$) of iron hydroxides (goethite, hematite, ferrihydrite) is a major sink for uranium. More importantly, (Liger et al., 1999) found that in the presence of hematite, uranium reduction through sorption can occur within hours at neutral pH; the reaction kinetics between the adsorbed uranium and ferrous iron is enhanced by hematite according to a first-order pseudo kinetic law.

The distribution of uranium species in PHREEQC also shows the presence and dominance of $Ca_2UO_2(CO_3)^3$, $CaUO_2(CO_3)_3^{-2}$ complexes. This is consistent with the view of several authors that neutral and negatively charged uranium-carbonate ions are unlikely to bond with the negatively ferric-hydroxide surfaces (Morrison et al., 1995, Geipel et al., 1998, Ho and Miller, 1986). Moreover, (Fox et al., 2006, Dong and Brooks, 2008, Stewart et al., 2010, Nair and Merkel, 2011a, Nair and Merkel, 2011b) found that the availability of Ca and Mg ions in the solution can also shift the aqueous speciation of uranium toward more stable (neutral) or negatively charged Ca-Mg-ternary complexes. The simulation results also indicate a general dissolution of smectite, clinoptilolite, and cristobalite in all three columns (Figure 6.7), which will result in an increase in the pore volume of each column and hence the porosity (Figure 6.8).

6.4.2 Hollington Sandstone

In this experiment, uranium in a high alkaline pH solution will migrate through the sandstone sample and alter the solution composition due to the dissolution of primary silicate minerals in the rock. Later, the solution will be equilibrated by the precipitation of calcium silicate hydrate (C-S-H) phases or C-(Al)-(K)-S-H phases whenever Al and K ions are present in the solution. The experiment has been conducted in a CO_2 free environment which is the usual case in a cementitious geological repository due to the interaction with cement-Ca and precipitation of calcite ($CaCO_3$) (Disposal, 2010, Vines and Lever, 2013, Auroy et al., 2013). Therefore, in an oxidising environment, U_{VI} ions would be expected to be in the form of uranyl hydroxide complexes with limited solubility compared with the carbonate species (Tits et al., 2011, Bourdon et al., 2003).

The model simulations show that there is no significant precipitation of C-S-H or uranium composed phases (Figure 6.9). Tobermorite-14A, CSH-gel, and $CaUO_4$ are all in multiple cycles of precipitation and dissolution that cancel out the effect of both processes. Meanwhile, $Na_2U_2O_7$ is almost close to equilibrium but never reached. Therefore, no significant retardation is expected by the edge surfaces of the C-S-H phases or precipitation of uranium. This result is also represented in Figure (6.10), which shows that in the case of no sorption, the uranium concentration at the column end reaches its initial injected concentration (0.24 mg/L) and achieves a steady-state value. Conversely, in the full sorption model uranium breakthrough occurs simultaneously as in the previous case but with significant retardation of uranium.

In this study, the aim was also to investigate the progression of uranium sorption on the surfaces of the C-S-H phases in an alkaline environment. In fact (Langmuir, 1997) concluded that hyper alkalinity conditions can encourage the sorption of uranyl (UO_2^{2+}) cations due to the availability of neutral and negatively charged surfaces. Furthermore, the C-S-H phases have a high surface area and high retention capacity for radionuclide migration, especially for uranyl (VI) cations due to poor crystallisation (Johnson, 2004, Gougar et al., 1996, Ma et al., 2019). Meanwhile (Tits et al., 2011) found that C-S-H phases can absorb uranyl cations by forming inner sphere surfaces (surface complexation) with the silonal edges.

As there was no significant precipitation of secondary C-S-H phases, an assumption was made to treat the smectite clay in the Hollington sandstone as a secondary C-S-H mineral. This assumption has also been made due to the lack of surface complexation parameters for C-S-H minerals. The modelled results for this assumption are shown in Figure (6.11).

Again, the results show that aluminol surface complexation on kaolinite dominates uranyl adsorption. So, even in high alkaline conditions, it still overcomes the adsorption of both aluminol and silonal edges on the C-S-H phase. However, it is worth mentioning that (Harfouche et al., 2006, Evans, 2008, Pointeau et al., 2004) have experimentally found that uranyl (UO_2^{2+}) can substitute for Ca^{2+} in the interlayer of C-S-H phases. Unfortunately, this reaction could not be modelled in this study due to a lack of the relevant surface complexation and ion exchange parameters.

In the study of (Korichi and Bensmaili, 2009), the authors also found that increasing the uranium concentration in the pulse solution will decrease the adsorption percentage, and in the case of low initial concentration, uranyl ions will have high mobility at the beginning before adsorption occurs. This behaviour was perfectly captured in the modelling results of this study, where a small peak in uranium concentration occurs at the beginning of the experiment before it drops down once the adsorption reaction dominates (Figure 6.10 and 6.11).

The applied uranium transport and sorption methods in this study provide insight into the key parameters that have the most significant impact on minimising uranyl mobility in a geological repository. It also indicates the required data needed to construct a consistent and reliable model for the reactive transport and sorption process of radionuclide migration in the geochemical application. Finally, the result of this study shows that the prediction of uranium migration is highly site-specific as it depends on the mineralogy and the geochemistry of the geosphere.
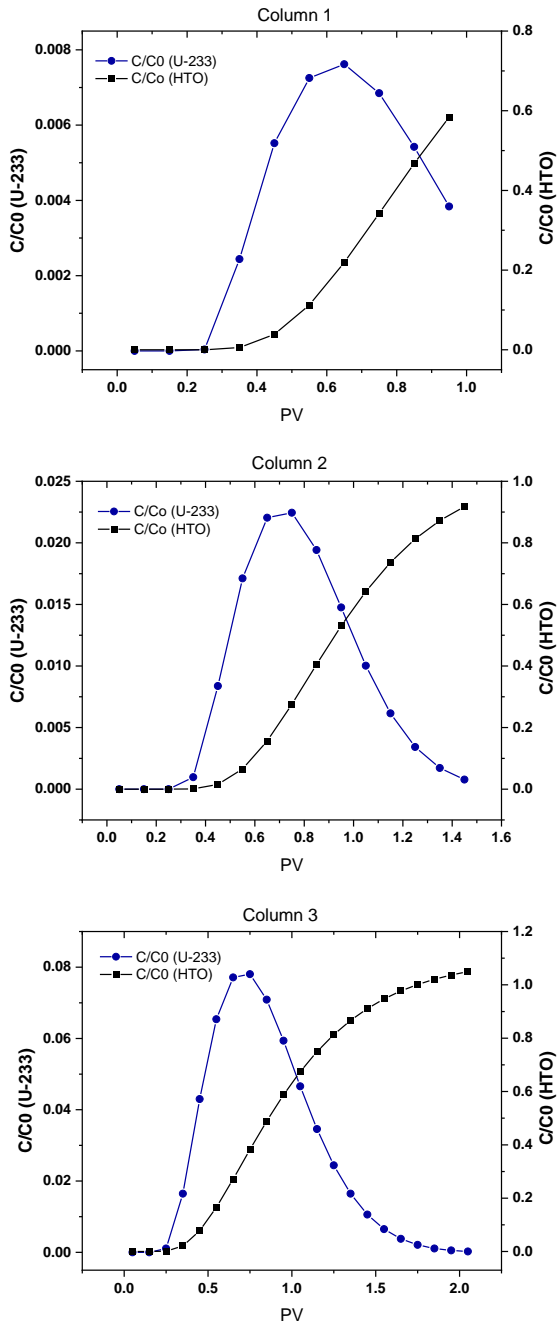
Figure 6.2: Uranium and HTO-tracer breakthrough curves for Yucca Mountain alluvium columns 1, 2 and 3.
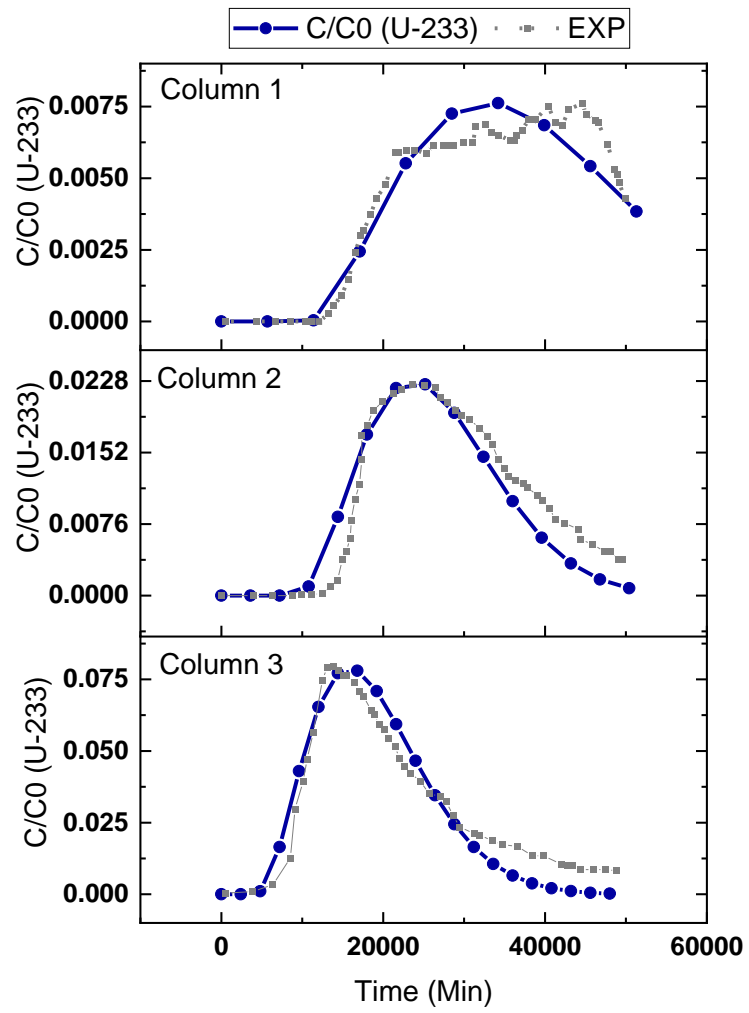
Figure 6.3: Experimental and modelling results for uranium breakthrough curves in Yucca Mountain alluvium columns 1, 2 and 3.
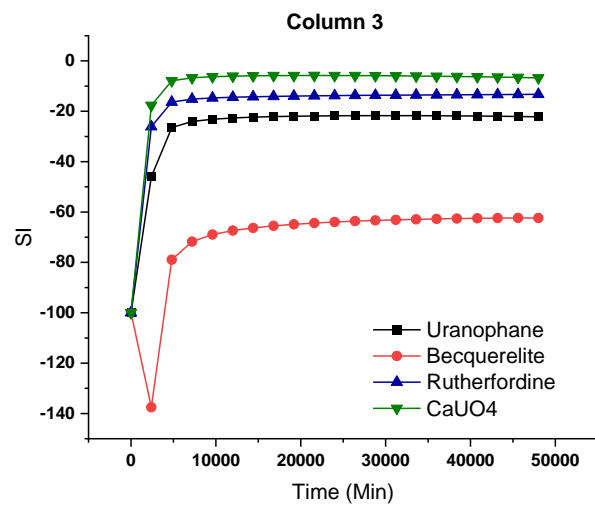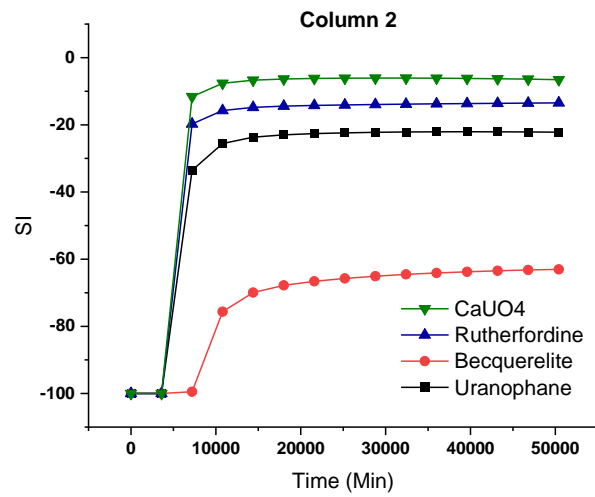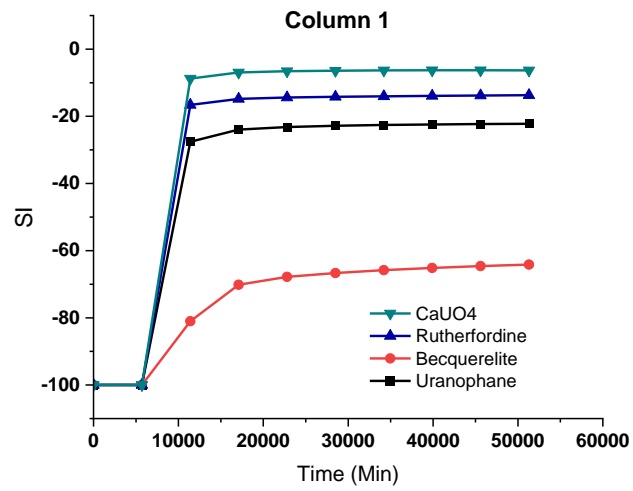
Figure 6.4: Saturation indices for uranium secondary phases in Yucca Mountain alluvium columns 1, 2 and 3.
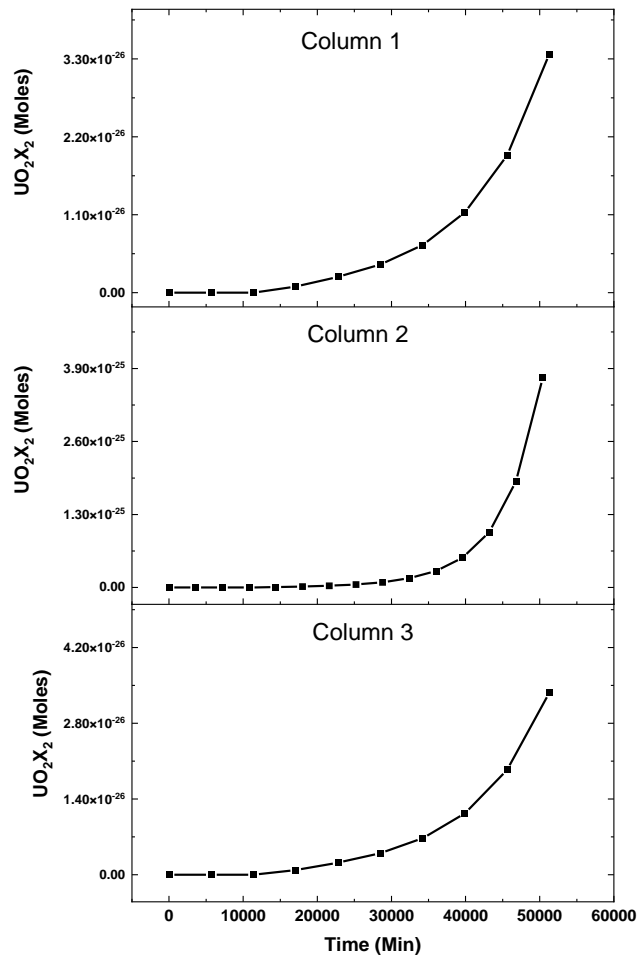
Figure 6.5: Number of adsorbed moles by cation exchange in Yucca Mountain alluvium columns 1, 2 and 3.
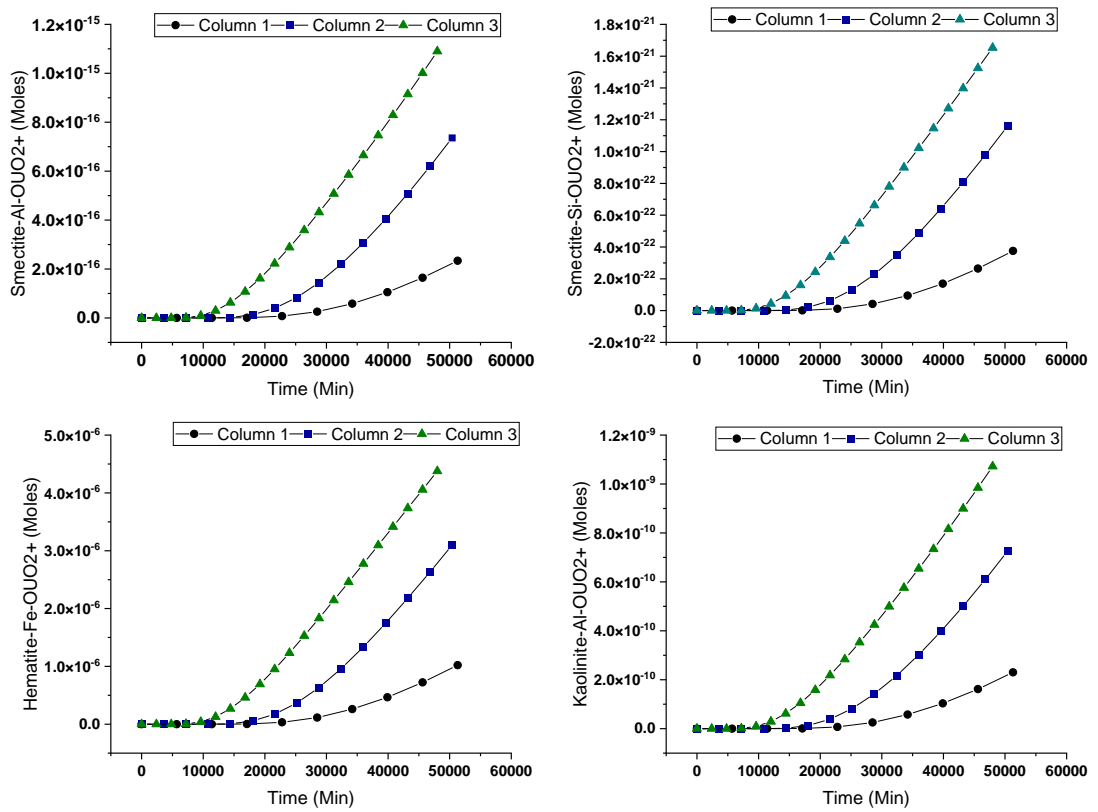
Figure 6.6: Number of adsorbed moles for surface complexation model in Yucca Mountain alluvium columns 1, 2 and 3.
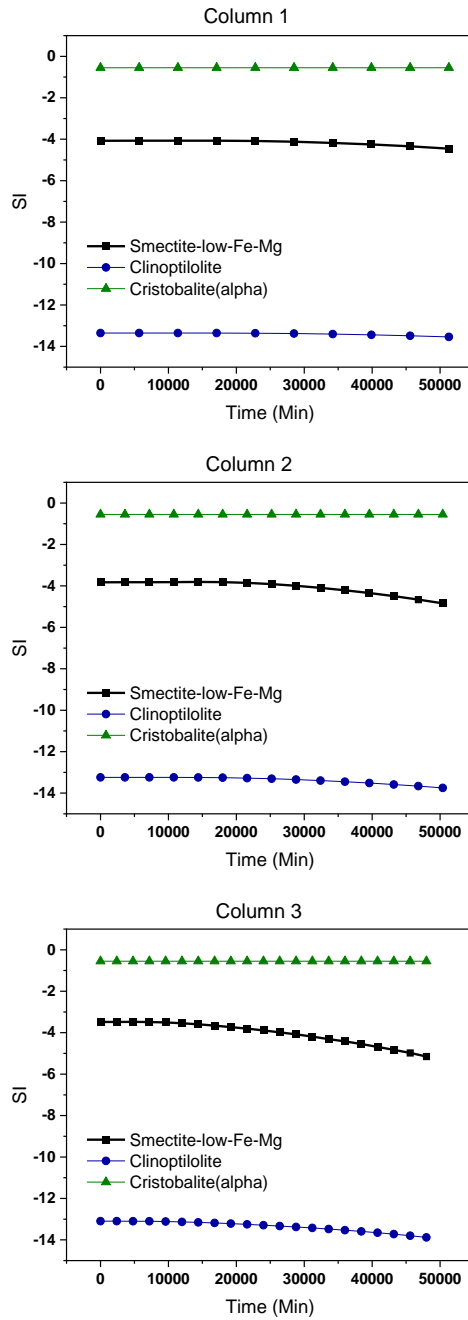
Figure 6.7: Saturation indices for smectite, clinoptilolite, and cristobalite in Yucca Mountain alluvium columns 1, 2 and 3.
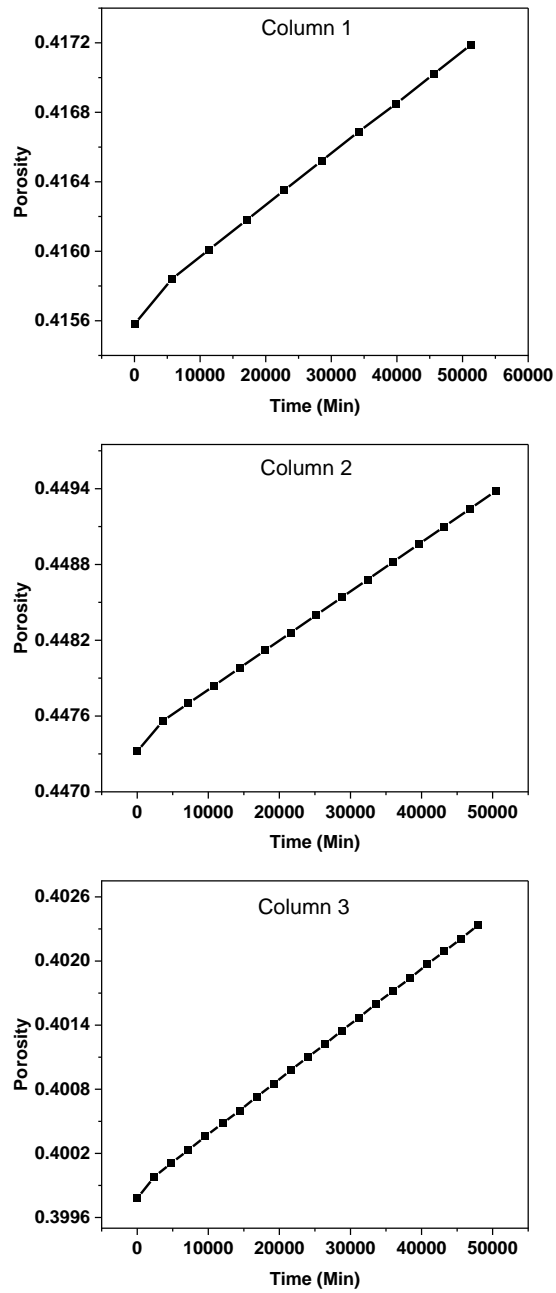
Figure 6.8: Predicted porosity evolution in the Yucca Mountain alluvium column experiments.
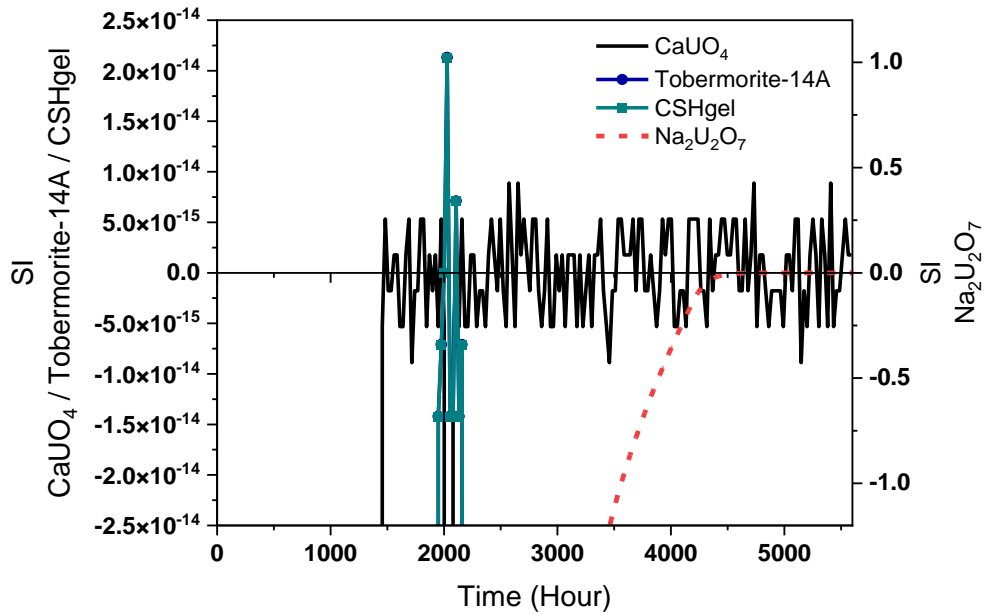
Figure 6.9: Modelled saturation indices for Tobermorite-14A, CSH-gel, CaUO$_4$, and Na$_2$U$_2$O$_7$ in the Hollington sandstone experiment.
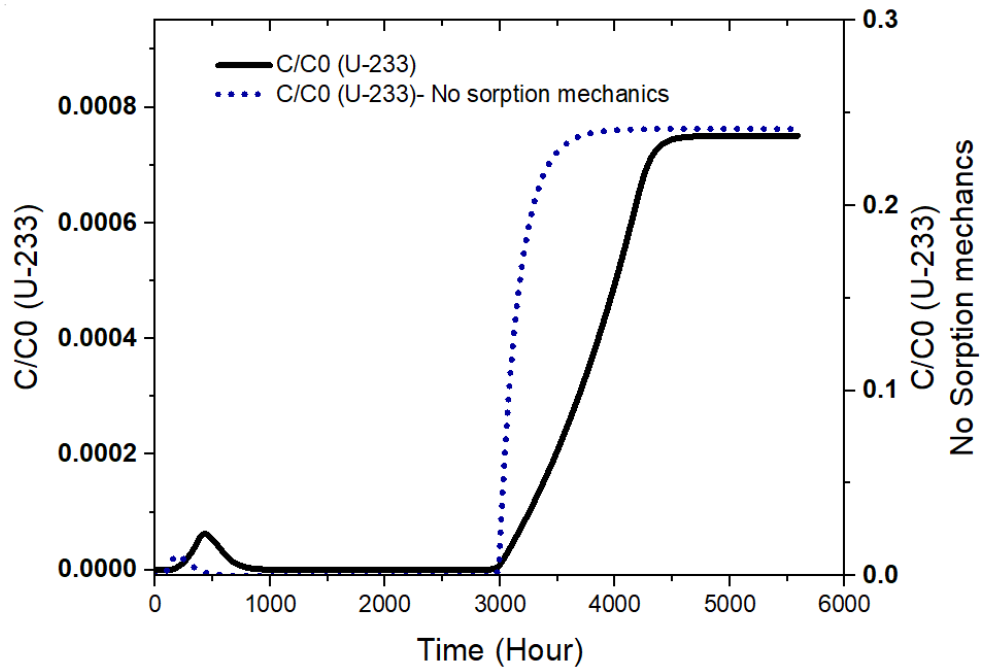
Figure 6.10: Simulated uranium breakthrough curves in the Hollington sandstone experiment. The solid line represents the model with sorption kinetics and the dotted line represents the model without sorption kinetics.
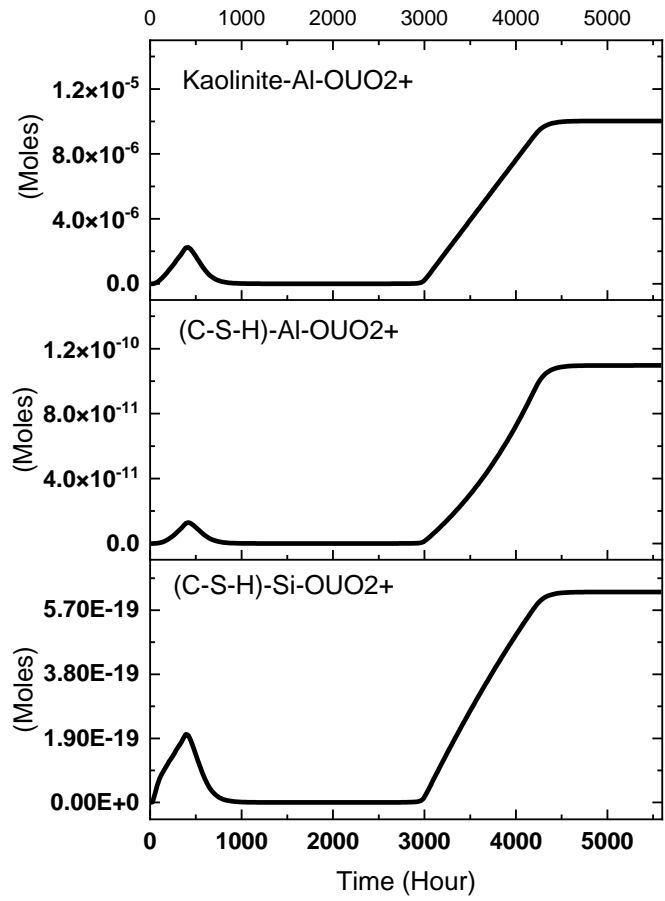
Figure 6.11:Number of adsorbed moles on kaolinite and C-S-H phase by surface complexation model in Hollington sandstone experiment.

6.5 Conclusion

Modelling uranium retardation is still a challenging task with all the variables included in the process, such as characterisation of the sorbent material (mineral type and composition, density of sorption sites, surface area), solid-solution ratio, solution composition, carbon dioxide presence, and pH value. Usually, in the region of low pH and ionic strength, uranium is retarded by forming an outer sphere complex with the fixed charge surface (ion exchange process). In contrast, at neutral pH and high ionic strength, the formation of inner-sphere complexation due to amorphic surface/edge sites occurs (surface complexation) controls the sorption process. Precipitation of uranium phases is most likely to be neglected in modelling experimental uranium sorption since the nucleation kinetics of solid phases is considered very slow to affect uranium reduction significantly. In this study, reactive transport with a double-layer surface complexation model has been implemented to model uranium sorption in a column experiment with a dynamic transport process. The model was first applied to an alluvium soil sample from Yucca Mountain in a neutral pH environment. The result shows that the aluminol surface edge sites in kaolinite have a higher affinity for uranyl adsorption than both aluminol and silonal edges in smectite clay.

Meanwhile, hydrous ferric oxide edge ($\equiv FeOH$) on hematite adsorbed most of the uranyl ions. Subsequently, the model was applied to Hollington sandstone in a high pH environment. The modelling simulation shows that there is no significant precipitation of C-S-H or uranium composed phases. Tobermorite-14A, CSH-gel, and $CaUO_4$ are all in multiple cycles of precipitation and dissolution that cancel out the effect of both processes. Meanwhile, $Na_2U_2O_7$ is almost close to equilibrium but never reached. Like Yucca

Mountain, the aluminol surface edge sites in kaolinite overcome the adsorption of both aluminol and silonal edges on the C-S-H phase. It is worth mentioning that the surface complexation reaction on C-S-H phases was not modelled adequately due to the lack of modelling parameters and further studies are needed in this field.

References

1. ADLER, M., MÄDER, U. & WABER, H. N. 1999. High-pH alteration of argillaceous rocks: an experimental study. *Schweiz. Mineral. Petrogr. Mitt,* 79**,** 445-454.
2. AMES, L. L., MCGARRAH, J. E. & WALKER, B. A. 1983. Sorption of uranium and radium by biotite, muscovite, and phlogopite. *Clays and Clay Minerals,* 31**,** 343-351.
3. ANDERSON, S. J. & SPOSITO, G. 1991. Cesium-adsorption method for measuring accessible structural surface charge. *Soil Science Society of America Journal,* 55**,** 1569-1576.
4. APPELO, C. & POSTMA, D. J. B., ROTERDAM 2005. Geochemistry, groundwater and pollution, CRC.
5. ATKINS, M., BECKLEY, A. N. & GLASSER, F. P. 1988. Influence of Cement on the Near Field Environment and its Specific Interactions with Uranium and Iodine. *Radiochimica Acta,* 44-45**,** 255-262.
6. AUROY, M., POYET, S., LE BESCOP, P. & TORRENTI, J. Impact of carbonation on the durability of cementitious materials: water transport properties characterization. EPJ Web of Conferences, 2013. EDP Sciences, 01008.
7. BACHMAF, S. & MERKEL, B. J. 2010. Sorption of uranium(VI) at the clay mineral–water interface. *Environmental Earth Sciences,* 63**,** 925-934.
8. BACHMAF, S. & MERKEL, B. J. 2011. Sorption of uranium (VI) at the clay mineral–water interface. *Environmental Earth Sciences,* 63**,** 925-934.
9. BAQER, Y., BATEMAN, K., TAN, V., STEWART, D. I., CHEN, X. & THORNTON, S. F. 2021. The Influence of Hyper-Alkaline Leachate on a Generic

Host Rock Composition for a Nuclear Waste Repository: Experimental Assessment and Modelling of Novel Variable Porosity and Surface Area. *Transport in Porous Media,* 140**,** 559-580.

10. BARNETT, M., JARDINE, P., BROOKS, S. & SELIM, H. 2000. Adsorption and transport of uranium (VI) in subsurface media. *Soil Science Society of America Journal,* 64**,** 908-917.

11. BARNETT, M. O., JARDINE, P. M. & BROOKS, S. C. 2002. U (VI) adsorption to heterogeneous subsurface media: application of a surface complexation model. *Environmental science & technology,* 36**,** 937-942.

12. BAUER, A., SCHÄFER, T., DOHRMANN, R., HOFFMANN, H. & KIM, J. 2001. Smectite stability in acid salt solutions and the fate of Eu, Th and U in solution. *Clay Minerals,* 36**,** 93-103.

13. BECKINGHAM, L. E., MITNICK, E. H., STEEFEL, C. I., ZHANG, S., VOLTOLINI, M., SWIFT, A. M., YANG, L., COLE, D. R., SHEETS, J. M. & AJO-FRANKLIN, J. B. 2016. Evaluation of mineral reactive surface area estimates for prediction of reactivity of a multi-mineral sediment. *Geochimica et Cosmochimica Acta,* 188**,** 310-329.

14. BETHKE, C. 1996. *Geochemical reaction modeling: Concepts and applications*, Oxford University Press on Demand.

15. BETHKE, C. M. & BRADY, P. V. 2000. How the Kd approach undermines ground water cleanup. *Groundwater,* 38**,** 435-443.

16. BOROVEC, Z. 1981. The adsorption of uranyl species by fine clay. *Chemical Geology,* 32**,** 45-58.

17. BOURDON, B., TURNER, S., HENDERSON, G. M. & LUNDSTROM, C. C. 2003. Introduction to U-series geochemistry. *Reviews in mineralogy and geochemistry,* 52**,** 1-21.

18. BRADBURY, M. H. & BAEYENS, B. 2005. Modelling the sorption of Mn (II), Co (II), Ni (II), Zn (II), Cd (II), Eu (III), Am (III), Sn (IV), Th (IV), Np (V) and U (VI) on montmorillonite: Linear free energy relationships and estimates of surface binding constants for some selected heavy metals and actinides. *Geochimica et Cosmochimica Acta,* 69**,** 875-892.

19. CAMPOS, M. B., DE AZEVEDO, H., NASCIMENTO, M. R. L., ROQUE, C. V. & RODGHER, S. 2011. Environmental assessment of water from a uranium mine (Caldas, Minas Gerais State, Brazil) in a decommissioning operation. *Environmental Earth Sciences,* 62**,** 857-863.

20. CARROLL, S. A. & WALTHER, J. V. 1990. Kaolinite dissolution at 25 degrees, 60 degrees, and 80 degrees C. *American Journal of Science,* 290**,** 797-810.

21. CHANDRAJITH, R., SENEVIRATNA, S., WICKRAMAARACHCHI, K., ATTANAYAKE, T., ATURALIYA, T. & DISSANAYAKE, C. 2010. Natural radionuclides and trace elements in rice field soils in relation to fertilizer application: study of a chronic kidney disease area in Sri Lanka. *Environmental Earth Sciences,* 60**,** 193-201.

22. CHEN, X. & THORNTON, S. 2018. Multi-Mineral Reactions Controlling Secondary Phase Evolution in a Hyper-Alkaline Plume. *Environmental Geotechnics*.

23. CHEN, X., THORNTON, S. F. & SMALL, J. 2015. Influence of hyper-alkaline pH leachate on mineral and porosity evolution in the chemically disturbed zone developed in the near-field host rock for a nuclear waste repository. *Transport in Porous Media,* 107**,** 489-505.

24. CHENG, T., BARNETT, M. O., RODEN, E. E. & ZHUANG, J. 2007. Reactive transport of uranium (VI) and phosphate in a goethite-coated sand column: an experimental study. *Chemosphere,* 68**,** 1218-1223.

25. CHIPERA, S. J. & BISH, D. L. 2002. FULLPAT: a full-pattern quantitative analysis program for X-ray powder diffraction using measured and calculated patterns. *Journal of Applied Crystallography,* 35**,** 744-749.

26. CHISHOLM-BRAUSE, C., CONRADSON, S. D., BUSCHER, C., ELLER, P. G. & MORRIS, D. E. 1994. Speciation of uranyl sorbed at multiple binding sites on montmorillonite. *Geochimica et Cosmochimica Acta,* 58**,** 3625-3631.

27. CHISHOLM-BRAUSE, C. J., BERG, J. M., MATZNER, R. A. & MORRIS, D. E. 2001. Uranium (VI) sorption complexes on montmorillonite as a function of solution chemistry. *Journal of Colloid and Interface Science,* 233**,** 38-49.

28. CLARET, F., BAUER, A., SCHÄFER, T., GRIFFAULT, L. & LANSON, B. 2002. Experimental investigation of the interaction of clays with high-pH solutions: A case

study from the Callovo-Oxfordian formation, Meuse-Haute Marne underground laboratory (France). *Clays and Clay Minerals,* 50**,** 633-646.

29. CURTIS, G. P., DAVIS, J. A. & NAFTZ, D. L. 2006. Simulation of reactive transport of uranium (VI) in groundwater with variable chemical conditions. *Water Resources Research,* 42.

30. CURTIS, G. P., FOX, P., KOHLER, M. & DAVIS, J. A. 2004. Comparison of in situ uranium KD values with a laboratory determined surface complexation model. *Applied Geochemistry,* 19**,** 1643-1653.

31. DANGELMAYR, M. A., REIMUS, P. W., WASSERMAN, N. L., PUNSAL, J. J., JOHNSON, R. H., CLAY, J. T. & STONE, J. J. 2017. Laboratory column experiments and transport modeling to evaluate retardation of uranium in an aquifer downgradient of a uranium in-situ recovery site. *Applied geochemistry,* 80**,** 1-13.

32. DAVIS, J. Surface Complexation Modeling of Uranium (VI) Adsorption on Natural Mineral Assemblage NUREG/CR-6708, US Nuclear Regulatory Commission, Rockville, MD (2001). JA DAVIS, TE PAYNE, and TD WAITE, Simulating Adsorption by a Weathered Schist with Surface Complexation Models. *Geochemistry of Soil Radionuclides," Special Pub,* 59**,** 61-86.

33. DAVIS, J. A., JAMES, R. O. & LECKIE, J. O. 1978. Surface ionization and complexation at the oxide/water interface: I. Computation of electrical double layer properties in simple electrolytes. *Journal of colloid and interface science,* 63**,** 480-499.

34. DAVIS, J. A. & KENT, D. B. 2018. Surface complexation modeling in aqueous geochemistry. *Mineral-water interface geochemistry***,** 177-260.

35. DAVIS, J. A., MEECE, D. E., KOHLER, M. & CURTIS, G. P. 2004. Approaches to surface complexation modeling of Uranium(VI) adsorption on aquifer sediments. *Geochim Cosmochim Acta,* 68.

36. DAVIS, J. A., PAYNE, T. E. & WAITE, T. D. 2002. Simulating the pH and pCO2 dependence of uranium (VI) adsorption by a weathered schist with surface complexation models. *Geochemistry of soil radionuclides,* 59**,** 61-86.

37. DE WINDT, L., MARSAL, F., TINSEAU, E. & PELLEGRINI, D. 2008. Reactive transport modeling of geochemical interactions at a concrete/argillite interface,

Tournemire site (France). *Physics and Chemistry of the Earth, Parts A/B/C,* 33**,** S295-S305.

38. DELANY, J. & LUNDEEN, S. 1990. The LLNL thermochemical database. *Lawrence Livermore National Laboratory Report UCRL-21658,* 150.

39. DISPOSAL, G. 2010. Radionuclide behaviour status report, NDA (Radioactive Waste Management Directorate) Report no. NDA/RWMD/034, Didcot, Oxon, OX11 0RH, UK.

40. DONG, W. & BROOKS, S. C. 2008. Formation of aqueous MgUO2 (CO3) 32− complex and uranium anion exchange mechanism onto an exchange resin. *Environmental science & technology,* 42**,** 1979-1983.

41. DONG, W. & WAN, J. 2014. Additive surface complexation modeling of uranium (VI) adsorption onto quartz-sand dominated sediments. *Environmental science & technology,* 48**,** 6569-6577.

42. DZOMBACH, D. & MOREL, F. 1990. Surface complexing modeling. Hydrous ferric oxide. Wiley-Interscience, New York, USA.

43. DZOMBAK, D. A. & MOREL, F. M. 1991. *Surface complexation modeling: hydrous ferric oxide*, John Wiley & Sons.

44. ECHEVARRIA, G., SHEPPARD, M. I. & MOREL, J. 2001. Effect of pH on the sorption of uranium in soils. *Journal of Environmental Radioactivity,* 53**,** 257-264.

45. EVANS, N. D. 2008. Binding mechanisms of radionuclides to cement. *Cement and concrete research,* 38**,** 543-553.

46. FELIPE-SOTELO, M., HINCHLIFF, J., FIELD, L., MILODOWSKI, A., PREEDY, O. & READ, D. 2017. Retardation of uranium and thorium by a cementitious backfill developed for radioactive waste disposal. *Chemosphere,* 179**,** 127-138.

47. FERNÁNDEZ, R., CUEVAS, J. & MÄDER, U. K. 2010. Modeling experimental results of diffusion of alkaline solutions through a compacted bentonite barrier. *Cement and Concrete Research,* 40**,** 1255-1264.

48. FERNÁNDEZ, R., MÄDER, U. K., RODRÍGUEZ, M., VIGIL DE LA VILLA, R. & CUEVAS, J. 2009. Alteration of compacted bentonite by diffusion of highly alkaline solutions. *European Journal of Mineralogy,* 21**,** 725-735.

49. FLETCHER, P. & SPOSITO, G. 1989. The chemical modelling of clay/electrolyte interactions for montmorillonite. *Clay Minerals,* 24**,** 375-391.

50. FOX, P. M., DAVIS, J. A. & ZACHARA, J. M. 2006. The effect of calcium on aqueous uranium (VI) speciation and adsorption to ferrihydrite and quartz. *Geochimica et Cosmochimica Acta,* 70**,** 1379-1387.

51. GEIPEL, G., BERNHARD, G., BRENDLER, V. & NITSCHE, H. 1998. Complex Formation between UO2+ 2 and CO2-3: Studied by Laser-Induced Photoacoustic Spectroscopy (LIPAS). *Radiochimica acta,* 82**,** 59-62.

52. GLYNN, P. D. 2003. Modeling Np and Pu transport with a surface complexation model and spatially variant sorption capacities: implications for reactive transport modeling and performance assessments of nuclear waste disposal sites. *Computers & Geosciences,* 29**,** 331-349.

53. GOLUBEV, S. V., BAUER, A. & POKROVSKY, O. S. 2006. Effect of pH and organic ligands on the kinetics of smectite dissolution at 25 C. *Geochimica et Cosmochimica Acta,* 70**,** 4436-4451.

54. GORMAN-LEWIS, D., BURNS, P. C. & FEIN, J. B. 2008. Review of uranyl mineral solubility measurements. *The Journal of Chemical Thermodynamics,* 40**,** 335-352.

55. GOUGAR, M., SCHEETZ, B. & ROY, D. 1996. Ettringite and C☐ S☐ H Portland cement phases for waste ion immobilization: A review. *Waste management,* 16**,** 295-303.

56. GRENTHE, I., FUGER, J., KONINGS, R. J., LEMIRE, R. J., MULLER, A. B., NGUYEN-TRUNG, C. & WANNER, H. 1992. *Chemical thermodynamics of uranium*, North-Holland Amsterdam.

57. GRENTHE, I., GAONA, X., RAO, L., PLYASUNOV, A., RUNDE, W., GRAMBOW, B., KONINGS, R., SMITH, A., MOORE, E. & RAGOUSSI, M.-E. 2020. Second update on the chemical thermodynamics of uranium, neptunium, plutonium, americium and technetium. Chemical thermodynamics volume 14. Organisation for Economic Co-Operation and Development.

58. GUIMARÃES, V., RODRÍGUEZ-CASTELLÓN, E., ALGARRA, M., ROCHA, F. & BOBOS, I. 2016. Influence of pH, layer charge location and crystal thickness

distribution on U(VI) sorption onto heterogeneous dioctahedral smectite. *Journal of Hazardous Materials,* 317**,** 246-258.

59. HARFOUCHE, M., WIELAND, E., DÄHN, R., FUJITA, T., TITS, J., KUNZ, D. & TSUKAMOTO, M. 2006. EXAFS study of U (VI) uptake by calcium silicate hydrates. *Journal of colloid and interface science,* 303**,** 195-204.

60. HENNIG, C., REICH, T., DÄHN, R. & SCHEIDEGGER, A. 2002. Structure of uranium sorption complexes at montmorillonite edge sites. *Radiochimica Acta,* 90**,** 653-657.

61. HIEMSTRA, T., VAN RIEMSDIJK, W. & BOLT, G. 1989. Multisite proton adsorption modeling at the solid/solution interface of (hydr) oxides: A new approach: I. Model description and evaluation of intrinsic reaction constants. *Journal of colloid and interface science,* 133**,** 91-104.

62. HO, C. & MILLER, N. 1986. Adsorption of uranyl species from bicarbonate solution onto hematite particles. *Journal of Colloid and Interface Science,* 110**,** 165-171.

63. HSI, C.-K. D. & LANGMUIR, D. 1985. Adsorption of uranyl onto ferric oxyhydroxides: Application of the surface complexation site-binding model. *Geochimica et Cosmochimica Acta,* 49**,** 1931-1941.

64. JOHNSON, C. A. 2004. Cement stabilization of heavy-metal-containing wastes. *Geological Society, London, Special Publications,* 236**,** 595-606.

65. KENT, D. B., TRIPATHI, V. S., BALL, N. B., LECKIE, J. & SIEGEL, M. 1988. Surface-complexation modeling of radionuclide adsorption in subsurface environments. Stanford Univ.

66. KIM, S. 2001. Sorption mechanism of U (VI) on a reference montmorillonite: binding to the internal and external surfaces. *Journal of Radioanalytical and Nuclear Chemistry,* 250**,** 55-62.

67. KLAJMON, M., HAVLOVÁ, V., ČERVINKA, R., MENDOZA, A., FRANCŮ, J., BERENBLYUM, R. & ARILD, Ø. 2017. REPP-CO2: Equilibrium Modelling of CO2-Rock-Brine Systems. *Energy Procedia,* 114**,** 3364-3373.

68. KNAUSS, K. G. & WOLERY, T. J. 1988. The dissolution kinetics of quartz as a function of pH and time at 70 C. *Geochimica et Cosmochimica Acta,* 52**,** 43-53.

69. KOHLER, M., WIELAND, E. & LECKIE, J. Metal-ligand-surface interaction during sorption of uranyl and neptunyl on oxides and silicates. International symposium on water-rock interaction, 1992. 51-54.

70. KORETSKY, C. 2000. The significance of surface complexation reactions in hydrologic systems: a geochemist's perspective. *Journal of Hydrology,* 230**,** 127-171.

71. KORICHI, S. & BENSMAILI, A. 2009. Sorption of uranium (VI) on homoionic sodium smectite experimental study and surface complexation modeling. *Journal of hazardous materials,* 169**,** 780-793.

72. KOWAL-FOUCHARD, A., DROT, R., SIMONI, E. & EHRHARDT, J. 2004. Use of spectroscopic techniques for uranium (VI)/montmorillonite interaction modeling. *Environmental science & technology,* 38**,** 1399-1407.

73. LANGMUIR, D. 1997. Aqueous environmental. *Geochemistry Prentice Hall: Upper Saddle River, NJ,* 600.

74. LICHTNER, P. C. 1988. The quasi-stationary state approximation to coupled mass transport and fluid-rock interaction in a porous medium. *Geochimica et Cosmochimica Acta,* 52**,** 143-165.

75. LIGER, E., CHARLET, L. & VAN CAPPELLEN, P. 1999. Surface catalysis of uranium (VI) reduction by iron (II). *Geochimica et Cosmochimica Acta,* 63**,** 2939-2955.

76. MA, B., CHARLET, L., FERNANDEZ-MARTINEZ, A., KANG, M. & MADÉ, B. 2019. A review of the retention mechanisms of redox-sensitive radionuclides in multi-barrier systems. *Applied geochemistry,* 100**,** 414-431.

77. MARQUES FERNANDES, M., BAEYENS, B., DÄHN, R., SCHEINOST, A. C. & BRADBURY, M. H. 2012. U(VI) sorption on montmorillonite in the absence and presence of carbonate: A macroscopic and microscopic study. *Geochimica et Cosmochimica Acta,* 93**,** 262-277.

78. MCKINLEY, J., ZACHARA, J. & SMITH, S. An experimental and modeling investigation of UO 2 2+ interaction with smectite clays. 205th ACS national meeting, 1993.

79. MCKINLEY, J. P., ZACHARA, J. M., SMITH, S. C. & TURNER, G. D. 1995. The influence of uranyl hydrolysis and multiple site-binding reactions on adsorption of U (VI) to montmorillonite.

80. MCLING, T. 1998. Uranium sorption onto natural sands as a function of sediment characteristics and solution pH. *Adsorption of metals by geomedia: Variables, mechanisms, and model applications*, 181.

81. MEINRATH, G. 1998. Speciation of uranium. *Uranium mining and hydrogeology II. Proceedings.*

82. MERKEL, B. J. & HASCHE-BERGER, A. 2006. Uranium in the Environment. *Mining Impacts and*.

83. MERKEL, B. J. & HASCHE-BERGER, A. 2008. *Uranium, mining and hydrogeology*, Springer Science & Business Media.

84. MISSANA, T., ALONSO, U., GARCIA-GUTIERREZ, M., ALBARRAN, N. & LOPEZ, T. 2008. Experimental study and modeling of uranium (VI) sorption onto a Spanish smectite. *MRS Online Proceedings Library (OPL),* 1124.

85. MISSANA, T., GARC1A-GUTIÉRREZ, M. & ALONSO, U. 2004. Kinetics and irreversibility of cesium and uranium sorption onto bentonite colloids in a deep granitic environment. *Applied Clay Science,* 26, 137-150.

86. MORRIS, D. E., CHISHOLM-BRAUSE, C. J., BARR, M. E., CONRADSON, S. D. & ELLER, P. G. 1994. Optical spectroscopic studies of the sorption of UO2+ 2 species on a reference smectite. *Geochimica et Cosmochimica Acta,* 58, 3613-3623.

87. MORRISON, S. J., SPANGLER, R. R. & TRIPATHI, V. S. 1995. Adsorption of uranium (VI) on amorphous ferric oxyhydroxide at high concentrations of dissolved carbon (IV) and sulfur (VI). *Journal of Contaminant Hydrology,* 17, 333-346.

88. NAIR, S., KARIMZADEH, L. & MERKEL, B. J. 2014. Surface complexation modeling of Uranium (VI) sorption on quartz in the presence and absence of alkaline earth metals. *Environmental earth sciences,* 71, 1737-1745.

89. NAIR, S. & MERKEL, B. J. 2011a. Effect of Mg-Ca-Sr on the sorption behavior of uranium (VI) on silica. *The New Uranium Mining Boom.* Springer.

90. NAIR, S. & MERKEL, B. J. 2011b. Impact of alkaline earth metals on aqueous speciation of uranium (VI) and sorption on quartz. *Aquatic Geochemistry,* 17**,** 209-219.

91. NARDI, A., IDIART, A., TRINCHERO, P., DE VRIES, L. M. & MOLINERO, J. 2014. Interface COMSOL-PHREEQC (iCP), an efficient numerical framework for the solution of coupled multiphysics and geochemistry. *Computers & Geosciences,* 69**,** 10-21.

92. PABALAN, R. T. & TURNER, D. R. 1996. Uranium(6+) sorption on montmorillonite: experimental and surface complexation modeling study. *Aquat Geochem,* 2.

93. PAPINI, M. P., KAHIE, Y. D., TROIA, B. & MAJONE, M. 1999. Adsorption of lead at variable pH onto a natural porous medium: Modeling of batch and column experiments. *Environmental science & technology,* 33**,** 4457-4464.

94. PARKHURST, D. L. & APPELO, C. 2013. Description of input and examples for PHREEQC version 3: a computer program for speciation, batch-reaction, one-dimensional transport, and inverse geochemical calculations. US Geological Survey.

95. PAYNE, T., DAVIS, J., LUMPKIN, G., CHISARI, R. & WAITE, T. 2004. Surface complexation model of uranyl sorption on Georgia kaolinite. *Applied Clay Science,* 26**,** 151-162.

96. PAYNE, T. & WAITE, T. 1991. Surface complexation modelling of uranium sorption data obtained by isotope exchange techniques. *Radiochimica Acta,* 52**,** 487-494.

97. POINTEAU, I., LANDESMAN, C., GIFFAUT, E. & REILLER, P. 2004. Reproducibility of the uptake of U (VI) onto degraded cement pastes and calcium silicate hydrate phases. *Radiochimica Acta,* 92**,** 645-650.

98. PRIKRYL, J. D., JAIN, A., TURNER, D. R. & PABALAN, R. T. 2001. UraniumVI sorption behavior on silicate mineral mixtures. *Journal of contaminant hydrology,* 47**,** 241-253.

99. PROTECTION, R. 2003. the Management of Radioactive Waste in the Oil and Gas Industry. *Safety Reports Series,* 34.

100.   RAMíREZ, S., CUEVAS, J., VIGIL, R. & LEGUEY, S. 2002. Hydrothermal alteration of "La Serrata" bentonite (Almeria, Spain) by alkaline solutions. *Applied Clay Science,* 21**,** 257-269.

101.   REARDON, E. 1981. Kd's—Can they be used to describe reversible ion sorption reactions in contaminant migration? *Groundwater,* 19**,** 279-286.

102.   RIBERA, D., LABROT, F., TISNERAT, G. & NARBONNE, J.-F. 1996. Uranium in the environment: occurrence, transfer, and biological effects. *Reviews of environmental contamination and toxicology.* Springer.

103.   RICKA, A., KUCHOVSKY, T., SRACEK, O. & ZEMAN, J. 2010. Determination of potential mine water discharge zones in crystalline rocks at Rozna, Czech Republic. *Environmental Earth Sciences,* 60**,** 1201-1213.

104.   SCHINDLER, M., LEGRAND, C. A. & HOCHELLA JR, M. F. 2015. Alteration, adsorption and nucleation processes on clay–water interfaces: mechanisms for the retention of uranium by altered clay surfaces on the nanometer scale. *Geochimica et Cosmochimica Acta,* 153**,** 15-36.

105.   SCISM, C. D. 2005. The Sorption/Desorption Behavior of Uranium in Transport Studies Using Yucca Mountain Alluvium. Los Alamos National Lab.(LANL), Los Alamos, NM (United States).

106.   SHERMAN, D. M., PEACOCK, C. L. & HUBBARD, C. G. 2008. Surface complexation of U (VI) on goethite (α-FeOOH). *Geochimica et Cosmochimica Acta,* 72**,** 298-310.

107.   SMALL, J., BRYAN, N., LLOYD, J., MILODOWSKI, A., SHAW, S. & MORRIS, K. 2016. Summary of the BIGRAD project and its implications for a geological disposal facility. *National Nuclear Laboratory, Report NNL (16),* 13817.

108.   STEWART, B. D., MAYES, M. A. & FENDORF, S. 2010. Impact of uranyl−calcium− carbonato complexes on uranium (VI) adsorption to synthetic and natural sediments. *Environmental science & technology,* 44**,** 928-934.

109.   SYLWESTER, E., HUDSON, E. & ALLEN, P. 2000. The structure of uranium (VI) sorption complexes on silica, alumina, and montmorillonite. *Geochimica et Cosmochimica Acta,* 64**,** 2431-2438.

110.	TAKAHASHI, T., OHKUBO, T., SUZUKI, K. & IKEDA, Y. 2007. High resolution solid-state NMR studies on dissolution and alteration of Na-montmorillonite under highly alkaline conditions. *Microporous and Mesoporous Materials,* 106**,** 284-297.

111.	THOMSON, B. M., LONGMIRE, P. A. & BROOKINS, D. G. 1986. Geochemical constraints on underground disposal of uranium mill tailings. *Applied geochemistry,* 1**,** 335-343.

112.	TICKNOR, K. 1994. Uranium sorption on geological materials. *Radiochimica Acta,* 64**,** 229-236.

113.	TITS, J., GEIPEL, G., MACÉ, N., EILZER, M. & WIELAND, E. 2011. Determination of uranium (VI) sorbed species in calcium silicate hydrate phases: A laser-induced luminescence spectroscopy and batch sorption study. *Journal of colloid and interface science,* 359**,** 248-256.

114.	TSUNASHIMA, A., BRINDLEY, G. & BASTOVANOV, M. 1981. Adsorption of uranium from solutions by montmorillonite; compositions and properties of uranyl montmorillonites. *Clays and Clay Minerals,* 29**,** 10-16.

115.	TURNER, D. R., PABALAN, R. T. & BERTETTI, F. P. 1998. Neptunium (V) sorption on montmorillonite: An experimental and surface complexation modeling study. *Clays and Clay Minerals,* 46**,** 256-269.

116.	TURNER, D. R. & SASSMAN, S. A. 1996. Approaches to sorption modeling for high-level waste performance assessment. *Journal of Contaminant Hydrology,* 21**,** 311-332.

117.	TURNER, G., ZACHARA, J., MCKINLEY, J. & SMITH, S. 1996a. Surface-charge properties and UO22+ adsorption of a subsurface smectite. *Geochimica et Cosmochimica Acta,* 60**,** 3399-3414.

118.	TURNER, G. D., ZACHARA, J. M., MCKINLEY, J. P. & SMITH, S. C. 1996b. Surface-charge properties and UO22+ adsorption of a subsurface smectite. *Geochim Cosmochim Acta,* 60.

119.	TUTU, H., CUKROWSKA, E. M., MCCARTHY, T. S., HART, R. & CHIMUKA, L. 2009. Radioactive disequilibrium and geochemical modelling as

evidence of uranium leaching from gold tailings dumps in the Witwatersrand Basin. *International Journal of Environmental and Analytical Chemistry,* 89**,** 687-703.

120.   VAN DER LEE, J. 1998. Thermodynamic and mathematical concepts of CHESS.

121.   VINES, S. & LEVER, D. An integrated approach to geological disposal of UK wastes containing carbon-14. International Conference on Radioactive Waste Management and Environmental Remediation, 2013. American Society of Mechanical Engineers, V001T01A060.

122.   WAITE, T., DAVIS, J., PAYNE, T., WAYCHUNAS, G. & XU, N. 1994. Uranium (VI) adsorption to ferrihydrite: Application of a surface complexation model. *Geochimica et Cosmochimica Acta,* 58**,** 5465-5478.

123.   WATSON, C., HANE, K., SAVAGE, D., BENBOW, S., CUEVAS, J. & FERNANDEZ, R. 2009. Reaction and diffusion of cementitious water in bentonite: results of 'blind'modelling. *Applied Clay Science,* 45**,** 54-69.

124.   WRONKIEWICZ, D. J., BATES, J. K., GERDING, T. J., VELECKIS, E. & TANI, B. S. 1992. Uranium release and secondary phase formation during unsaturated testing of UO2 at 90 C. *Journal of Nuclear Materials,* 190**,** 107-127.

125.   ZACHARA, J. M. & MCKINLEY, J. P. 1993. Influence of hydrolysis on the sorption of metal cations by smectites: Importance of edge coordination reactions. *Aquatic Sciences,* 55**,** 250-261.

126.   ZHU, C. 2003. A case against Kd-based transport models: natural attenuation at a mill tailings site. *Computers & geosciences,* 29**,** 351-359.

127.   ZIELINSKI, R., ASHER-BOLINDER, S., MEIER, A., JOHNSON, C. & SZABO, B. 1997. Natural or fertilizer-derived uranium in irrigation drainage: a case study in southeastern Colorado, USA. *Applied Geochemistry,* 12**,** 9-21.

Chapter 7: Overall Conclusion, Summary, and Future Work

This thesis details the development of hyper-alkaline leachate reactive transport modelling coupled with (1) multiple minerals kinetical dissolution/precipitation; (2) dynamic porosity (3) sorption, with the application focused on radioactive waste disposal.

Chapter 3 showed that in a reaction between a crystalline basement rock and alkaline groundwater, the mineralogical and geochemical transformation of the system is driven primarily by the fluid chemistry that controls the dissolution/precipitation of the primary minerals, thereby controlling long-term chemical equilibria and mineralogical composition of the host rock impacted by the hyper-alkaline leachate. Moreover, dolomite was shown to be a major controlling phase in the geochemical evolution of BVG rock minerals' interactions with YCL. The dissolution of dolomite provides a continuous source of calcium, carbonate and magnesium ions. Consequently, Ca^{2+} and CO_3^{2-} precipitate in the form of calcite ($CaCO_3$), while Mg^{2+} binds with OH^- to form brucite, $Mg(OH)_2$, which results in the pH dropping. Furthermore, sometimes the precipitation of secondary phases consumes ions in the cement leachate, helping to maintain conditions that are far from equilibrium, which leads to faster dissolution rates. Overall, the modelling results are in line with experimental results, which further support the MKE approach to interpreting the evolution of multiple mineral phases.

Chapter 4 showed that the initial high concentration of calcium ions in the ICL appeared to be the main driving force initiating the dissolution of calcium-rich minerals (e.g. the dedolomitization process) even under low pH conditions, which played a significant role in the precipitation of secondary talc, brucite and Mg-aluminosilicate. Meanwhile, most of

the magnesium released during dedolomitization drove brucite and Mg-silicate (talc and saponite-Mg) precipitation, which lowered the pH even more and created a sink for Mg ions. The initial large drop in silicon and calcium concentrations supported the formation of CSH phases but after the large drop in pH. Most of the initially precipitated CSH phases redissolved and a substitution between aluminium and silicon ions took place to produce more stable CASH phases. Later, those secondary CASH phases were able to bind with the magnesium and create Mg-aluminosilicate.

The modelling results obtained from the geochemical analysis showed potential for precipitation of mesolite, stilbite and scolecite, which all are part of the zeolite family. Although those minerals did not precipitate in the experiment, this does not necessarily indicate that the situation would be the same in the actual geosphere. A plausible explanation for this is the rapid removal of silicon and aluminium by CSH and CASH phases, which could suppress the formation of zeolites as they may have slower precipitation kinetic. Additionally, zeolite formation is preferred in the pore spaces in which leachate flux is minimal, and in these experiments the leachate to rock ratio was very high. Moreover, the composition and nature of rock type can influence the amount of CO_2 released into the hyper-alkaline leachate, which can also buffer the formation of zeolites, highlighting again the important role of dolomite in the evolution of the geochemical system.

Typically, the chemical interaction between a hyper-alkaline leachate and the host rock results in a series of mineralogical reactions, including cycles of mineral dissolution and precipitation (calcium silicate hydrate gel, CSH phases, CASH phases, hydrated silicate

and Na-Ca zeolites), which changed the porosity of the studied matrix (pore water is consumed to form hydration products).

The newly evolved porosity can then lead to the evolution of permeability and reactive surface area of the reactive minerals, which results in a reactive transport process for the radionuclide in the porous media. The field of reactive transport modelling aims to study the hydro-chemical coupling between chemical reactions and fluid transport and define the future state of the studied system over time. Numerical simulation of these hydro-chemical reactions is of great importance to assess the environmental impact, durability, reliability and safety of nuclear waste disposal systems in underground geological repositories. Couplers are interested in reactive transport modelling to predict the behaviour of the aqueous components because of the related complex hydro-geochemical reactions, such as the dissolution/precipitation processes of minerals in the surrounding geosphere.

In Chapter 5, a reactive transport model for host rock alternation and radionuclide migration in porous media was constructed using variable porosity, reactive surface area and pore volume. The modelling investigated cement leachate flow in saturated and homogenous porous media with mass transport, and chemical reaction and alternation processes (mineral dissolution/precipitation, changes in porosity, reactive surface area of minerals, pore volume). The geochemical evolution of the system was driven by cement leachate advection and solute diffusion, which both featured aqueous speciation and mineral dissolution/precipitation under kinetic or thermodynamic equilibrium reactions. Full coupling between changes in mineral volume and porosity evolution is therefore linked to the chemical reactions of mineral dissolution and precipitation.

Initially, the results showed that a high Ca concentration in the background solution would be slowed mainly due to the precipitation of secondary CSH/CASH phases once there were enough Si ions released from the dissolution of primary silicate minerals, which would also help maintain conditions that are far from equilibrium, leading to faster dissolution rates. The drop in Si concentration was also found to be smaller in the experimental results. This could be related to the fact that some secondary phases precipitate on the surfaces of the primary minerals, reducing the reactive surface area and slowing the dissolution process and, consequently, restricting the precipitation of the secondary phases and the removal of Si from the solution. The lack of zeolite formation in the experiments could also be related to the experimental temperature, as some studies have observed zeolite precipitation only above 60°C. Moreover, the kinetics of zeolite precipitation may be very slow, relative to the residence time in the column (i.e. there is a kinetic limitation even though the fluid chemistry supports precipitation).

The use of the reactive transport model agreed well with the fact that in the variable porosity model, ions are released faster from the primary minerals because of the higher exposure between the minerals in the sandstone and the YCL, resulting in an earlier start of the precipitation cycle. The variable porosity model also demonstrated a better fit in ion concentration because it led to more reactive surface area with the YCL. The time to the peak point and the decreasing slope were more realistic representations of the system because more ions were released to the synthetic leachate, resulting in a higher degree of precipitation. The model further demonstrated that the dissolution of primary minerals in the host rock is the initial driving mechanism for the chemical evolution of the system, whereas the subsequent precipitation of several secondary phases controls the long-term

chemical equilibria and mineralogical composition of the host rock impacted by the alkaline leachate.

By using a reactive transport model linked with the sorption process, a better modelling outcome and detailed results could be obtained. A dynamic porosity can emulate changes in fluid flow through the column. At the same time, a reactive surface area can cover the number of edge surfaces available for ion exchange and surface complexation in clay. The key point in the reactive transport process is to link the mineral volumes and surface areas with porosity evolution and advection-diffusion transport. In reactive transport models, uranium is usually removed through sorption onto mineral surfaces and precipitation as uranium complexes.

In chapter 6, The effect of variable mineralogy on uranium sorption was studied at room temperature and fixed pH value. As the pulse solution was injected into the column, uranium started to break through the alluvium sample and react with the mineral phases. However, the highest value of the uranium concentration was still much lower than the pulse solution concentration, implying that uranium retardation happens simultaneously with the fluid flow. The simulated saturation indices of uranium phases indicate that they are undersaturated and the precipitation of solid uranium phases is unlikely to occur in the experiment.

Ion exchange includes the reaction of uranyl with the binding sites of the clay mineral. This mechanism dominates in the region of low pH and ionic strength by forming an outer sphere complexation with the fixed charge surface. However, at neutral pH and high ionic strength the formation of inner-sphere complexation due to amorphic surface/edge sites

occurs (surface complexation) and controls the sorption process. Furthermore, in soil-water reactions, the ion exchanger will usually adjust its composition to achieve chemical equilibrium with the groundwater composition. Therefore, it will act as a buffer against any infiltration of pollutants into the system.

In the study, as expected, uranyl ions form an inner surface complex on smectite, kaolinite and hydrous ferric oxide, which confirm the modelling approach for uranium sorption by binding to a variable charge site by surface complexation. The result reveals that the aluminol sites ($\equiv AlO - UO_2^+$) are more reactive than silonal sites ($\equiv SiO - UO_2^+$) for smectite. The number of adsorbed moles on the aluminol edge is much higher (6 orders of magnitude), which agrees well with higher uranyl affinity toward aluminol edges. Moreover, the aluminol surface edge sites in kaolinite have also shown a high affinity for uranyl adsorption, which can be related to the higher number of the exposed surface sites at the Al-octahedral sheet.

The $\equiv FeOH$ site has the highest number of adsorbed uranyl moles. The same behaviour has also been reported in other studies, in which for the region of neutral and alkaline pH, a very small mass weight percentage ($\approx 1\%$) of iron hydroxides (goethite, hematite, ferrihydrite) is a major sink for uranium. The model simulations also show that there is no significant precipitation of CSH or uranium composed phases. Tobermorite-14A, CSH-gel, and $CaUO_4$ are all in multiple cycles of precipitation and dissolution that cancel out the effect of both processes. Meanwhile, $Na_2U_2O_7$ is almost close to equilibrium but never reached. Therefore, no significant retardation is expected by the edge surfaces of the CSH phases or precipitation of uranium.

The aim in this study was also to investigate the progression of uranium sorption on the surfaces of the CSH phases in an alkaline environment. Again, the results show that aluminol surface complexation on kaolinite dominates uranyl adsorption. So, even in high alkaline conditions, it still overcomes the adsorption of both aluminol and silonal edges on the CSH phase. However, it is worth mentioning that it was experimentally found that uranyl (UO_2^{2+}) can substitute for Ca^{2+} in the interlayer of the CSH phases. Unfortunately, this reaction could not be modelled in this study due to a lack of the relevant surface complexation and ion exchange parameters. The applied uranium transport and sorption methods in this study has provide insight into the key parameters that have the most significant impact on minimising uranyl mobility in a geological repository. It also implies the required data needed to construct a consistent and reliable model for the reactive transport and sorption process of radionuclide migration in the geochemical application.

Overall, the findings from the numerical modelling and theoretical analysis provided an in-depth understanding of the long-term interactions between host rock and alkaline leachate, and the usefulness of iterating between modelling and experimental results to achieve a better understanding of the system under study. Modelling multi-mineral evolution in the CDZ surrounding a nuclear waste geological disposal facility, characterised by both equilibrium and kinetic reactions, remains a challenging field. Furthermore, the modelling results of these long-term experiments signify the important role of fluid-mineral reactions in controlling fluid chemistry and secondary phases, suggesting that sufficient attention should be focused on the mineralogical composition of flowing features, as the minerals lining those can exert a critical influence on key geochemical reactions. This phenomenon highlights the importance of the modelling procedure for this kind of complex long-term

geochemical reaction, as it allows a better understanding of the potential chemical and physical reactions that occur in the geosphere. It can also allow the extension of the timescale from relatively short-duration lab tests to the long timescales of performance assessments. Additionally, it can reveal the type of dissolved or precipitated secondary minerals that can contribute effectively to the retardation of radionuclide migration.

The performed study showed that the sorption of uranyl on smectite is highest in a pH environment where uranyl-hydroxyl ions are dominant. Conversely, at pH > 8, uranyl-carbonate ions reduce sorption on the negatively charged sites of smectite. In general, sorption of positively charged ions is associated with a high pH, whereas sorption of negatively charged ions is favourable at a low pH. Thus, in terms of radionuclide retardation in cementitious geological repositories, mineral precipitation and porosity evolution will be the dominant factors in stopping radionuclide migration during the initial and intermediate stages of evolved cement leachate. Meanwhile, the sorption mechanism will take control in the last stage (old cement leachate). Finally, the result of this study shows that the prediction of uranium migration is highly site-specific as it depends on the mineralogy and the geochemistry of the geosphere.

7.1 Summary

- Mineralogical and geochemical transformation of the system is driven primarily by the fluid chemistry that controls the dissolution/precipitation of the primary minerals.

- The subsequent precipitation of several secondary phases controls the long-term chemical equilibria and mineralogical composition of the host rock impacted by the alkaline leachate.

- The precipitation of secondary phases consumes ions in the cement leachate, helping maintain conditions far from equilibrium.

- The initial high concentration of calcium ions in the ICL appeared to be the main driving force initiating the dissolution of calcium-rich minerals.

- The magnesium released during dedolomitization drove brucite and Mg-silicate (talc and saponite-Mg) precipitation, which lowered the pH and created a sink for Mg ions.

- Most of the initially precipitated CSH phases redissolved, and a substitution between aluminium and silicon ions took place to produce more stable CASH phases.

- The rapid removal of silicon and aluminium by CSH and CASH phases could suppress the formation of zeolites as they may have slower precipitation kinetics.

- CO_2 released into the hyper-alkaline leachate can buffer the formation of zeolites.

- Some secondary phases precipitate on the surfaces of the primary minerals, reducing the reactive surface area and slowing the dissolution process and, consequently, restricting the precipitation of the secondary phases.

- In the variable porosity model, ions are released faster from the primary minerals because of the higher exposure between the minerals in the sandstone and the YCL, resulting in an earlier start of the precipitation cycle.

- The simulated saturation indices of uranium phases indicate that the precipitation of solid uranium phases is unlikely to occur in the experiment.

- Uranyl ions form an inner surface complex on smectite, kaolinite and hydrous ferric oxide.

- The aluminol sites ($\equiv AlO - UO_2^+$) are more reactive than silonal sites ($\equiv SiO - UO_2^+$) for smectite (The number of adsorbed moles on the aluminol edge is higher by 6 orders of magnitude).

- The aluminol surface edge sites in kaolinite have shown a high affinity for uranyl adsorption, which can be related to the higher number of exposed surface sites at the Al-octahedral sheet.

- The $\equiv FeOH$ site has the highest number of adsorbed uranyl moles.

- No significant retardation is expected by the edge surfaces of the CSH phases or precipitation of uranium in the experiment.

- In terms of radionuclide retardation in cementitious geological repositories, mineral precipitation and porosity evolution will be the dominant factors in stopping radionuclide migration during the initial and intermediate stages of evolved cement leachate. Meanwhile, the sorption mechanism will take control in the last stage (old cement leachate).

- The result of this study shows that the prediction of uranium migration is highly site-specific as it depends on the mineralogy and the geochemistry of the geosphere.

7.2 Limitation of this Research

Whether an experiment can be modelled correctly by numerical methods depends on (1) the experimental data obtained, (2) the modelling tools and methods, (3) the theoretical analysis, and (4) the relationship between the experiment and modelling (some parameters might be important for modelling, however, is not necessary for the experiment). One of the challenges of modelling this kind of experiment was the unknown parameters caused by the different scientific focus for the experiment. For example, the experimental study was focused on mineral evolution, instead of dissolution/precipitation kinetics, with no interest in dissolution parameters such as surface area. However, such information is essential for modelling dissolution kinetics. At least 3 parameters (e.g. empirical constant, initial surface area and moles of solids at a given time) may be needed to simulate the dissolution kinetics of one mineral; hence at least 18 uncertain parameters must be considered to model the reaction kinetics of 6 minerals, a significant uncertainty. Such a challenge shows the importance of applying "mixed kinetics and equilibrium methods" to interpret the evolution of multiple mineral phases, which should be based on proper assumptions in order to achieve a reasonably accurate prediction.

Furthermore, one of the major uncertainties in modelling evolving porous media arises from the uncertainty in identifying the value of the reactive surface area, which has a first-order effect on the timing and the level of dissolution/precipitation reactions. Commonly, the rate of dissolution in the experiment is 1-3 orders of magnitude higher than in the natural system. This can be explained by the difference in reactive and total surface area

between natural and experimental systems (White and Peterson, 1990, White and Brantley, 2003, Velbel, 1993).

Another area which requires improvement is the development of strategies for coupling fluid flow and reactive transport. Global implicit, sequential-iterative or sequential non-iterative schemes are often used to solve most reactive transport problems (Steefel et al., 2015). Irrespective of the numerical algorithm used, permeabilities and reactivities are updated with a time lag. Although this is not often done for porosity and diffusion coefficients, it does suggest that there is the possibility of errors in small mass balance at each time step. In addition, the simulation of an evolving porous media may be complicated when attempting to update the relevant parameters of the media as the evolution proceeds because of the interactions between flow and transport. In many published models, both multi-component and groundwater flow problems are solved sequentially. This does not apply, however, to evolving porous media because the evolution of porosity affects the flow equation through the storage term and modifies the permeability. Decoupling flow and reactive transport should help avoid numerically induced minor mass balance errors. Interestingly, there have been recent attempts to recouple both multiphase flow and reactive transport through the variation of porosity (Seigneur et al., 2018).

Processes occurring at the pore and macroscopic scales cannot be adequately described by porosity evolution alone. Unfortunately, the rigorous mathematical frameworks required for such an integrated approach are not yet available. Instead of these formulations, the geometrical organisation of the pore scale may be adequate. For instance, fluid-skeleton interactions could be described based on the surface area as pathways with high tortuosity. This is known to have lower transport properties caused by increased surface area.

Likewise, advection-reaction-dispersion-equation is the most commonly applied in terms of the mathematical formulation of the reactive transport system. However, its correlation with spreading and mixing leads to some limitations in the transport process, such as tailing and scale dependence of porosity which makes it inadequate for reactive transport applications (Carrera et al., 2022, Xu and Pruess, 2001). Therefore, an alternative formulation is needed such that the limitation of the transport equation can be overcome.

Finally, In PHREEQC, the 1D advection-dispersion transport is calculated by an explicit finite difference algorithm. Sometimes, when the grid is coarse, the algorithm will compute numerical dispersion, which can be large or small in magnitude depending on the modelled reactions. Likewise, for the sorption reaction, the software has some uncertainties in defining the composition of the sorbed species, the number of sites, and the surface area. Therefore, most models of surface complexation applications depend on experimental data for specific materials from the studied site. PHREEQC also has a limited capability to integrate a system with complex kinetic reactions due to its explicit time simulation method (MacQuarrie and Mayer, 2005). Moreover, despite the variety of PHREEQC built-in geochemical reactions, it does not integrate the correlation between porosity and permeability evolution in porous media within its reactive transport code. Thus, the variation of permeability was not included in the modelling.

7.3 Contribution to Science

This work contributed to the reactive transport model by applying the MKE approach in interpreting multi-mineral reactions coupled with the geochemical evolution of the porous media via PHREEQC software. During experimental permeation with hyper-alkaline leachate originating from the cementitious barrier of a geological disposal facility. PHREEQC permits access to its geochemical library, which allows the interpretation of new secondary phases such as CSH, CASH, and cement hydrates minerals which have complex chemical compositions. Likewise, surface complexation and cation exchange reaction and parameters are performed under specific conditions.

This study used a mixing cell to identify the essential parameters and understand and scale up the effect of variations in the key parameters while modelling geochemical processes. A significant modification was the simulation of the chemical reactions based on a user-defined rate expression. At the same time, physical changes were integrated by manually calculating the changes in the mineral volume. Hence, a coupling between chemical-physical reactions is initiated with the possibility of simulating time-dependent geochemical reactions that depend on solute temperature, pH and saturation ratios of minerals. Consequently, studying the effect of variable porosity, reactive surface area and pore volume on improving the modelling of rock alteration compared to previous attempts that assume constant values for these properties.

7.4 Current Challenges and Future Work

One of the major areas that must be addressed is developing a comprehensive modelling algorithm for capturing complete clogging and collapse of the solid matrix. Though it is easy to implement most published empirical correlations in codes with macroscopic scale descriptions, it is challenging to simulate extreme scenarios of evolving media. Most geochemical solvers currently do not address the disappearance of the water phase, which is triggered by the complete clogging of the medium. In relative transport modelling, this problem is captured by setting a threshold porosity value that defines no migration of flow and solute. Efforts have been made to verify the best way of implementing relationships among permeability, porosity and tortuosity, but it is quite challenging to observe different reactive transport modelling obtaining similar results under clogging conditions (Xie et al., 2015). Conversely, in some simulations a high porosity increase, which is not practical, is occasionally observed. This is a mechanically driven issue that is not considered by many reactive transport modelling efforts today.

Another challenging issue is modelling unsaturated flow relationships. Modelling unsaturated transport and reactive processes using Richard's equation or two-phase models requires building correlations that will capture the transport and hydraulic properties of the medium. Models proposed by (Brooks and Corey, 1964, Van Genuchten, 1980) describe the characteristics of water retention and the relative permeabilities of fluid phases, but require the use of many model parameters. (Della Vecchia et al., 2015) proposed a model that correlates water retention with the distribution of pore size for clays. In the same vein, (Suazo et al., 2016) investigated how water retention curves evolve during the cement hydration process. Few attempts, however, have been made to predict the evolution of these

parameters as the porous media undergo chemical fluctuations. Furthermore, there is no direct correlation between porosity and unsaturated parameters, so these parameters are often assumed to be constant.

In addition, building an integrated model for an evolving medium is challenging. Reactive surface area, effective porosity and tortuosity are key variables in evolving porous media. Surface area and tortuosity are often connected to diffusion, where reactivity and empirical correlations are subsequently applied in updating their values as the porous media evolve. Although inherently correlated, the relationships between different evolving model parameters are often independent of each other (Koponen et al., 1997). Though it is difficult to establish generic correlations between these observations, common trends can be observed (Knackstedt and Zhang, 1994, Koponen et al., 1997). Koponen et al. (1997) observed that an incremental increase in porosity tends to increase diffusivity, but causes a decrease in surface area. (Saripalli et al., 2002) also observed that there is a possible correlation between tortuosity and surface area.

Most efforts to determine effective transport properties have been focused on establishing correlations based on tortuosity, porosity and/or surface area. Although diffusivity and permeability describe various transport processes, they both depend on tortuosity and the size of the pore throat in the same manner. In some instances, when reproducing experimental results at alteration depths, systematic errors may surface. Failing to reproduce at degradation depths as breakthrough curves are being produced is an indication of developing a more integrated framework for the parameters evolving with the media.

Finally, the use of imaging techniques has allowed for a deeper understanding of the pore network structure and how its properties evolve. In combination with high-resolution reactive transport modelling at the pore scale, these techniques will further have the capability to assess, in greater accuracy, how the pore structure evolves (Molins et al., 2012, Steefel et al., 2013, Molins et al., 2014). In a study conducted by (Molins et al., 2017), the researchers were able to replicate the dissolution process in a fractured multi-mineral formation by capturing the heterogeneity distribution of the minerals in the rock. Another investigation reproduced worm-holing processes at the pore-scale through direct simulation (Molins, 2015). Furthermore, with pore-scale modelling, the opportunity to assess how dissolution and precipitation processes affect the structure of the pores has been provided by a number of studies (Molins, 2015, Noiriel, 2015, Pereira Nunes et al., 2016, Bultreys et al., 2016). To characterise media at smaller scales and consequently improve the performance of pore-scale models, it is critical to further improve the resolution of imaging techniques. Nevertheless, it appears unrealistic to expect that the large time- and spatial-scale limitations of pore-scale simulations will be able to be addressed anytime in the near future.

References

1. BROOKS, R. H. & COREY, A. T. 1964. Hydraulic properties of porous media and their relation to drainage design. *Transactions of the ASAE,* 7**,** 26-0028.

2. BULTREYS, T., BOONE, M. A., BOONE, M. N., DE SCHRYVER, T., MASSCHAELE, B., VAN HOOREBEKE, L. & CNUDDE, V. 2016. Fast laboratory-based micro-computed tomography for pore-scale research: Illustrative experiments and perspectives on the future. *Advances in water resources,* 95**,** 341-351.

3. CARRERA, J., SAALTINK, M. W., SOLER-SAGARRA, J., WANG, J. & VALHONDO, C. 2022. Reactive transport: a review of basic concepts with emphasis on biochemical processes. *Energies,* 15**,** 925.

4. DELLA VECCHIA, G., DIEUDONNÉ, A. C., JOMMI, C. & CHARLIER, R. 2015. Accounting for evolving pore size distribution in water retention models for compacted clays. *International Journal for Numerical and Analytical Methods in Geomechanics,* 39**,** 702-723.

5. KNACKSTEDT, M. & ZHANG, X. 1994. Direct evaluation of length scales and structural parameters associated with flow in porous media. *Physical Review E,* 50**,** 2134.

6. KOPONEN, A., KATAJA, M. & TIMONEN, J. 1997. Permeability and effective porosity of porous media. *Physical Review E,* 56**,** 3319.

7. MACQUARRIE, K. T. & MAYER, K. U. 2005. Reactive transport modeling in fractured rock: A state-of-the-science review. *Earth-Science Reviews,* 72**,** 189-227.

8. MOLINS, S. 2015. Reactive interfaces in direct numerical simulation of pore-scale processes. *Reviews in Mineralogy and Geochemistry,* 80**,** 461-481.

9. MOLINS, S., TREBOTICH, D., MILLER, G. H. & STEEFEL, C. I. 2017. Mineralogical and transport controls on the evolution of porous media texture using direct numerical simulation. *Water Resources Research,* 53**,** 3645-3661.

10. MOLINS, S., TREBOTICH, D., STEEFEL, C. I. & SHEN, C. 2012. An investigation of the effect of pore scale flow on average geochemical reaction rates using direct numerical simulation. *Water Resources Research,* 48.

11. MOLINS, S., TREBOTICH, D., YANG, L., AJO-FRANKLIN, J. B., LIGOCKI, T. J., SHEN, C. & STEEFEL, C. I. 2014. Pore-scale controls on calcite dissolution rates from flow-through laboratory and numerical experiments. *Environmental science & technology,* 48**,** 7453-7460.

12. NOIRIEL, C. 2015. Resolving time-dependent evolution of pore-scale structure, permeability and reactivity using X-ray microtomography. *Reviews in Mineralogy and Geochemistry,* 80**,** 247-285.

13. PEREIRA NUNES, J., BIJELJIC, B. & BLUNT, M. 2016. Pore-space structure and average dissolution rates: A simulation study. *Water Resources Research,* 52**,** 7198-7212.

14. SARIPALLI, K. P., SERNE, R. J., MEYER, P. D. & MCGRAIL, B. P. 2002. Prediction of diffusion coefficients in porous media using tortuosity factors based on interfacial areas. *Groundwater,* 40**,** 346-352.

15. SEIGNEUR, N., LAGNEAU, V., CORVISIER, J. & DAUZÈRES, A. 2018. Recoupling flow and chemistry in variably saturated reactive transport modelling-An algorithm to accurately couple the feedback of chemistry on water consumption, variable porosity and flow. *Advances in Water Resources,* 122**,** 355-366.

16. STEEFEL, C., APPELO, C., ARORA, B., JACQUES, D., KALBACHER, T., KOLDITZ, O., LAGNEAU, V., LICHTNER, P., MAYER, K. U. & MEEUSSEN, J. 2015. Reactive transport codes for subsurface environmental simulation. *Computational Geosciences,* 19**,** 445-478.

17. STEEFEL, C. I., MOLINS, S. & TREBOTICH, D. 2013. Pore scale processes associated with subsurface CO2 injection and sequestration. *Reviews in Mineralogy and Geochemistry,* 77**,** 259-303.

18. SUAZO, G., FOURIE, A. & DOHERTY, J. 2016. Experimental study of the evolution of the soil water retention curve for granular material undergoing cement hydration. *Journal of Geotechnical and Geoenvironmental Engineering,* 142**,** 04016022.

19. VAN GENUCHTEN, M. T. 1980. A closed-form equation for predicting the hydraulic conductivity of unsaturated soils. *Soil science society of America journal,* 44**,** 892-898.

20. VELBEL, M. A. 1993. Constancy of silicate-mineral weathering-rate ratios between natural and experimental weathering: implications for hydrologic control of differences in absolute rates. *Chemical Geology,* 105**,** 89-99.

21. WHITE, A. F. & BRANTLEY, S. L. 2003. The effect of time on the weathering of silicate minerals: why do weathering rates differ in the laboratory and field? *Chemical Geology,* 202**,** 479-506.

22. WHITE, A. F. & PETERSON, M. L. 1990. Role of reactive-surface-area characterization in geochemical kinetic models. ACS Publications.

23. XIE, M., MAYER, K. U., CLARET, F., ALT-EPPING, P., JACQUES, D., STEEFEL, C., CHIABERGE, C. & SIMUNEK, J. 2015. Implementation and evaluation of permeability-porosity and tortuosity-porosity relationships linked to mineral dissolution-precipitation. *Computational Geosciences,* 19**,** 655-671.

24. XU, T. & PRUESS, K. 2001. Modeling multiphase non-isothermal fluid flow and reactive geochemical transport in variably saturated fractured rocks: 1. Methodology. *American Journal of Science,* 301**,** 16-33.

List of Abbreviations

1D	one-dimension
BVG	Borrowdale Volcanic Group
BGS	British Geological Survey
BIGRAD	Biogeochemical Gradients and Radionuclide Transport
C-(A)-(K)-S-H	Calcium Aluminium-Potassium Silicate Hydrate
CASH	Calcium Aluminium Silicon Hydrate
CPB	Cement Paste Backfills
CCM	Constant Capacitance Model
CDZ	Chemical Disturbed Zone
CEC	Cation Exchange Capacity
CFL	Courant Friedrichs Lewy
CPU	Central Processing Unit
CSH	Calcium Silicate Hydrate
CT	Computed Tomography
D2Q5	2-dimensional domain with 5 separate velocities
DG	Discontinuous Galerkin
DLM	Double/diffuse Layer Model
ENFG	Evolved Near-Field Groundwater
GDF	Geological Disposal Facility
HC	Fluid transport effect on chemical reactions
HM	Fluid pressure effect on mechanical deformation
IAP	Ion Activity Product
IC	Ion Chromatography
ICL	Intermediate Cement Leachate
ICP-MS	Inductively Coupled Plasma - Mass Spectrometry
ICP-OES	Inductively Coupled Plasma - Optical Emission Spectrometry
IIPG	Incomplete Interior Penalty Galerkin
ILW	Intermediate Level nuclear Waste
Kd	Distribution Coefficient
LLNL	Lawrence Livermore National Laboratory

LSC	Liquid Scintillation Counting
LSM	Level Set Method
LU	Lower-Upper
MKE	Mixed Kinetic-Equilibrium
NERC	Natural Environment Research Council
NIPG	Non-symmetric Interior Penalty Galerkin method
NORM	Naturally Occurring Radioactive Material
NRVB	Nirex Reference Vault Backfill
NS	Navier-Stokes
NSARP	Nirex Safety Assessment research programme
NUFT	Nonisothermal Unsaturated-saturated Flow and Transport
OBB-DG	Oden Babuska Baumann- Discontinuous Galerkin
OCL	Old Cement Leachate
PARSIM	Parallel Simulator
PEEK	Polyether Ether Ketone
PNM	Pore Network Modelling
PPE	Polyphenylene Ether
PTFE	Polytetrafluoroethylene
PV	Pore Volumes
REV	Representative Elementary Volume
REX	Redox Experiment
SCM	Surface Complexation Model
SI	Saturation Index
SIPG	Symmetric Interior Penalty Galerkin formulation
SPH	Smoothed Particle Hydrodynamics
SR	Saturation Ratio
TC	Temperature effect on chemical reactions
THMC	Thermal, Hydrological, Mechanical and Chemical
TLM	Triple Layer Model
TM	Temperature effect on mechanical deformation
TOT	Tetrahedral-Octahedral-Tetrahedral

USGS	U.S. Geological Survey
XRD	X-ray Diffraction
YCL	Young Cement Leachate
YNFP	Young Near-Field Porewater

Appendix: PHREEQC Input Files

1. A Geochemical Modelling of Multi-minerals Evolution for a 15 Months Experiment

```
SOLUTION 1
    temp      70
    pH        11.67
    pe        12 O2(g) -0.68
    redox     pe
    units     mg/l
    density   1
    C(4)      166
    Ca        51.8
    K         3230
    Mg        0.089
    Na        1890
    Cl        63.7
    S(6)      1
    N(5)      1
    Br        0.5
    F         19
    Si        9.2
    Sr        0.018
    Mn        0.01
    Ba        0.01
    Fe        0.1
    Al        12.2
    -water    1 # kg


Save solution 1
Use solution 1

EQUILIBRIUM_PHASES 1
O2(g) -0.68 10
Calcite 0 0
Talc 0 0    #Mg3Si4O10(OH)2
quartz 1.02 1
Dolomite 0 0.025   #CaMg(CO3)2
k-feldspar 0 0
Tobermorite-11A 0 0
brucite 0 0


#for 35g of rock sample we have the following:
#12% Orthoclase = 4.2g
#41% Quartz = 14.35g
#29% Dolomite = 10.15g
#13% Muscovite = 4.55g
#2% hematite = 0.7g
#3% Calcite = 1.05g
```

```
#those value will be converted to initial number of moles for each
elements.

#-------------------------------------------------------

KINETICS 1

Quartz
 -tol    1e-8
 -M0     0.239                      # moles of Quartz
 -M      0.239
 -parms 0.02    0.15     #(A0 = 0.02 m2/g and V = 0.15 L)
#-------------------------
Dolomite;
 -tol    1e-8
 -M0     0.055                      # moles of Dolomite
 -M      0.055
 -parms 0.02    0.15     #(A0 = 0.02 m2/g and V = 0.15 L)
#-------------------------
Calcite
 -tol    1e-8
 -M0     0.010                      # moles of Calcite
 -M      0.010
 -parms  0.02      0.15   #(A=0.02 m2/g, V=0.15 L)
#-------------------------
K-feldspar
 -tol    1e-8
 -M0     0.015                       # moles of K-feldspar
 -M      0.015
 -parms  0.02  0.15        #(A=0.02 m2/g, V=0.15 L)
#-------------------------

-steps   30 60 90 120 150 180 210 240 270 300 330 360 390 420 450 day #
15 months

INCREMENTAL_REACTIONS false

#---------------------------------------------------------

RATES

Quartz
 # d qu / dt = (A0 / V) * ((m / m0)^0.67) * k * (1 - SR_qr)
 #  k = 10^-12.2 mol/m2/s (70 C)
 #  A0, initial surface of quartz (m2/g)
 #  V, solution volume (L)
 #PARM(1) = A
 #PARM(2) = V
-start
  10 rate = PARM(1) / PARM(2) * ((M/M0)^0.67) * (10^-12.2) * (1 -
SR("Quartz")) * 14.35
  20 moles= rate * time
  30 save moles
-end
#---------------------------
Dolomite  #http://www.hydrochemistry.eu/a&p/ from this book
-start
```

```
 10 rate = -1.2e-11 * 10000 * 1e-3 * log(SR("Dolomite")) * 10.15 *
(PARM(1)/PARM(2)) * ((M/M0)^2)
 20 moles = rate * time
 30 save moles
-end
#---------------------------
Calcite
#PARM(1) = A
#PARM(2) = V
#rf unit is mmole/cm2/s, mmole must be converted to mole and area
should converted to cm2
-start
 10  si_cc = SI("Calcite")
 20  k1 = 10^(0.198 - 444.0 / TK )
 30  k2 = 10^(2.84 - 2177.0 / TK)
 40  if TC <= 25 then k3 = 10^(-5.86 - 317.0 / TK )
 50  if TC > 25 then k3  = 10^(-1.1 - 1737.0 / TK )
 60  rf = k1*ACT("H+")+k2*ACT("H2CO3")+k3*ACT("H2O")
 70  rate = PARM(1)/PARM(2) * (10000) * ((M/M0)^0.67) * 1e-3 * rf * (1
- 10^(2/3*si_cc))* 1.05   #1e-3 to convert to mole
 80  moles = rate * time
 90 SAVE moles
-end
#---------------------------
K-feldspar
 -start
                    # specific rates from Table 8.7 in mol/m2/s
                    # parm(1) = A in m2/g, parm(2) = V in L
 1 A0 = parm(1)
 2 V = parm(2)
                    # find activities of inhibiting ions...

 3 a_Al = act("Al+3")
 4 BC = act("Na+") + act("K+") + act("Mg+2") + act("Ca+2")

                    # temp corrected with the Arrhenius eqn, Table 8.8
                    # the difference in temperature, TK gives solution
temp in Kelvin...

 10 dif_T = 1/TK - 1/281

 # rate by H+...
 20 pk_H = 11.7 + 3500 * dif_T
 22 rate_H = 10^-pk_H * (act("H+")^0.5) / (((1 + a_Al / 4e-6)^0.4) *
((1 + BC / 5e-4)^0.15))

 # rate by hydrolysis...
 30 pk_w = 14.5 + 2000 * dif_T
 32 rate_w = 10^-pk_w / (((1 + a_Al / 4e-6)^0.14) * ((1 + BC / 5e-
4)^0.15))

 # rate by OH-...
 40 pk_OH = 13.1 + 2500 * dif_T
 42 rate_OH = (10^-pk_OH) * (act("OH-")^0.3)

 # rate by CO2...
 50 pk_CO2 = 13.0 + 2000 * dif_T
```

```
52 rate_CO2 = (10^-pk_CO2) * ((SR("CO2(g)"))^0.6)

 # Sum the rate contributions...
 60 rate_t = rate_H + rate_w + rate_OH + rate_CO2


 70 rate = rate_t * A0 / V * ((m/m0)^0.67) * (1 - SR("K-feldspar")) *
4.2

 80 moles = rate * time

 90 save moles

 -end
#----------------------------------------------------------------------
------

SELECTED_OUTPUT

  #  -totals                Ca  Mg Na K S(-2) Sr Al C(4) Cl(-1) S(6) Fe
N(5) Br  F
  #  -equilibrium_phases   Dolomite Hematite Calcite Portlandite Talc
Goethite Tobermorite-9A Mesolite

USER_PUNCH
# ^ User defined output; useful to convert directly to mmol/kgw for
example
      -headings Time Ca Na K Si CO3 Cl SI("Dolomite") SI("Quartz")
SI("Calcite") SI("Talc") SI("Hillebrandite") SI("Saponite-Ca") SI("K-
feldspar")  SI("Tobermorite-11A")  Mg  SI("Brucite") pH
#SI("Ca2K2Si2O4")# Ca(mM) Mg(mM) Na(mM) K(mM) SO4(mM) Fe(mM) Doc(mM)
AlX3_fraction base_cations_fraction Jurbanite_diff(mM)
#     -start
010 PUNCH   TOTAL_TIME/(60*60*24*30)
020 PUNCH   tot("Ca")*40*1000           # mol used for concentrations
of species
030 PUNCH   tot("Na")*23*1000              # tot used for total
element concentrations
040 PUNCH tot("K")*39*1000
050 PUNCH tot("Si")*28.09*1000
060 PUNCH tot("C(4)")*60*1000
070 PUNCH tot("Cl")*24*1000
080 PUNCH SI("Dolomite")
090 PUNCH SI("Quartz")
100 PUNCH SI("Calcite")
110 PUNCH SI("Talc")
120 PUNCH SI("Hillebrandite")
130 PUNCH SI("Saponite-Ca")
140 PUNCH SI("K-feldspar")
150 PUNCH SI("Tobermorite-11A")
160 PUNCH tot("Mg")*24*1000
170 PUNCH SI("Brucite")
180 PUNCH  -LA("H+")
190 PUNCH EQUI("Talc")
200 PUNCH EQUI("Calcite")
210 PUNCH EQUI("Portlandite")
220 PUNCH EQUI("Quartz")
```

```
230 PUNCH EQUI("Brucite")
240 PUNCH SI("CSHtob2")
250 PUNCH SI("apophyllite")
260 PUNCH log(SR("Dolomite"))
270 PUNCH tot("Al")

      -end

End
```

2. Modelling of multi-mineral kinetical evolution in hyper-alkaline leachate for 15 years experiment

```
SOLUTION 1
    temp      70
    pH        10.84
    pe        12 O2(g) -0.68
    redox     pe
    units     mg/l
    density   1
    Al        4.17
    B         0.335
    Ba        0.017
    Br        23.2
    C(4)      20
    Ca        1930
    Cl(-1)    15100
    F         0.03
    Fe        0.12
    K         185
    Li        0.153
    Mg        0.117
    Mn        0.01
    N(5)      20
    Na        9160
    S(6)      1090
    Si        2.07
    Sr        166
    -water    1 # kg

Save solution 1

use solution 1

#-------------------------------------------------

PHASES
CSHtob2 ;(CaO)0.83333(SiO2)(H2O)1.3333 + 0.50003H2O = 0.83333Ca++ +
SiO2 + H2O + 1.66666OH- ; log_K      -8.0014      ; -
analytical_expression   100.35344189250   0     -5814.81586527851 -
35.9075880599      0

#-------------------------------------------------

REACTION 1 #Evaporation of 34% of fluid, remove 34% (18.87 mole) of 1
Kg (1 L, 55.51 mole) of water
 H2O -1.0
 12 moles in 30 steps    #(21.6% of evaporation)

#-------------------------------------------------

EQUILIBRIUM_PHASES 1
O2(g) -0.68 10
```

```
Quartz 0 0
Calcite -1 0.2        #CaCO3
Dolomite 0 0         #CaMg(CO3)2
k-feldspar 1 0.0006     #KAlSi3O8
hematite 0 0
Muscovite -2 0
brucite -0.5 0


#------------------------------------------------

#for 35g of rock sample we have the following:
#12% Orthoclase = 4.2g
#41% Quartz = 14.35g
#29% Dolomite = 10.15g
#13% Mica (Muscovite) = 4.55g
#2% hematite = 0.7g
#3% Calcite = 1.05g



#Those value will be converted to initial number of moles for each
elements by dividing with molar mass.

#---------------------------------------------------

KINETICS 1

Quartz
 -tol   1e-8
 -M0    0.239                      # moles of Quartz
 -M     0.239
 -parms 0.02 0.14     #(A0 = 0.02 m2/g and V = 0.14 L)
#------------------------
Dolomite
 -tol   1e-8
 -M0    0.055                      # moles of Dolomite
 -M     0.055
 -parms 0.02 0.14      #(A0 = 0.02 m2/g and V = 0.14 L)
#------------------------
Calcite
 -tol    1e-8
 -M0     0.010                     # moles of Calcite
 -M      0.010
 -parms  0.02 0.14    #(A=0.02 m2/g, V=0.14 L)
#------------------------
K-feldspar
 -tol    1e-8
 -M0     0.0151                      # moles of K-feldspar
 -M      0.0151
 -parms  0.02 0.14        #(A=0.02 m2/g, V=0.14 L)
#------------------------
Muscovite
 -tol    1e-8
 -M0     0.011                      # moles of Muscovite
 -M      0.011
 -parms  1.1  0.14        #(A=1.1 m2/g, V=0.14 L)
#------------------------
```

```
-steps    180 360 540 720 900 1080 1260 1440 1620 1800 1980 2160 2340
2520 2700 2880 3060 3240 3420 3600 3780 3960 4140 4320 4500 4680 4860
5040 5220 5400 day #18 month=15 years

INCREMENTAL_REACTIONS false

#--------------------------------------------------------

RATES

Quartz
 # d qu / dt = (A0 / V) * ((m / m0)^0.67) * k * (1 - SR_qr)
 #  k = 10^-12.2 mol/m2/s (70 C)
 #  A0, initial surface of quartz (m2/g)
 #  V, solution volume (L)
 #PARM(1) = A
 #PARM(2) = V
-start
  10 rate = (PARM(1)/PARM(2)) * ((M/M0)^0.67) * (10^-12.2) * (1 -
SR("Quartz")) * 14.35
  20 moles= rate * time
  30 save moles
  40 PUT(rate,1)
-end
#--------------------------
Dolomite  #http://www.hydrochemistry.eu/a&p/ from this book
-start
 10 rate = (PARM(1)/PARM(2)) * ((M/M0)^0.67) * (-1.2e-12) * 10000 *
(1e-3) * log(SR("Dolomite")) * 10.15
 20 moles = rate * time
 30 save moles
 40 PUT(rate,2)
-end
#--------------------------
Calcite
#PARM(1) = A
#PARM(2) = V
#rf unit is mmole/cm2/s, mmole must be converted to mole and area
should converted to cm2
-start
 10  si_cc = SI("Calcite")
 20  k1 = 10^(0.198 - 444.0 / TK )
 30  k2 = 10^(2.84 - 2177.0 / TK)
 40  if TC <= 25 then k3 = 10^(-5.86 - 317.0 / TK )
 50  if TC > 25 then k3  = 10^(-1.1 - 1737.0 / TK )
 60  rf = k1*ACT("H+")+k2*ACT("H2CO3")+k3*ACT("H2O")
 70  rate = (PARM(1)/PARM(2)) * (10000) * ((M/M0)^0.67) * (1e-3) * rf *
(1 - (10^(2/3*si_cc)))* 1.05   #1e-3 to convert to mole
 80  moles = rate * time
 90  SAVE moles
-end
#----------------------------
K-feldspar
 -start
                 # specific rates from Table 8.7 in mol/m2/s
                 # parm(1) = A in m2/g, parm(2) = V in L
```

327

```
#1 A0 = parm(1)
#2 V = parm(2)
                    # find activities of inhibiting ions...

 3 a_Al = act("Al+3")
 4 BC = act("Na+") + act("K+") + act("Mg+2") + act("Ca+2")

                    # temp corrected with the Arrhenius eqn, Table 8.8
                    # the difference in temperature, TK gives solution
temp in Kelvin...

 10 dif_T = 1/TK - 1/281

 # rate by H+...
 20 pk_H = 11.7 + 3500 * dif_T
 22 rate_H = (10^-pk_H) * (act("H+")^0.5) / (((1 + a_Al / 4e-6)^0.4) *
((1 + BC / 5e-4)^0.15))

 # rate by hydrolysis...
 30 pk_w = 14.5 + 2000 * dif_T
 32 rate_w = (10^-pk_w) / (((1 + a_Al / 4e-6)^0.14) * ((1 + BC / 5e-
4)^0.15))

 # rate by OH-...
 40 pk_OH = 13.1 + 2500 * dif_T
 42 rate_OH = (10^-pk_OH) * (act("OH-")^0.3)

 # rate by CO2...
 50 pk_CO2 = 13.0 + 2000 * dif_T
 52 rate_CO2 = (10^-pk_CO2) * ((SR("CO2(g)"))^0.6)

 # Sum the rate contributions...
 60 rate_t = rate_H + rate_w + rate_OH + rate_CO2


 70 rate = rate_t * (PARM(1)/PARM(2)) * ((m/m0)^0.67) * (1 - SR("K-
feldspar")) * 4.2

 80 moles = rate * time

 90 save moles

100 PUT(rate,3)

 -end
#----------------------------------------------------------------------
------
Muscovite
#PARM(1) = A
#PARM(2) = V
#r_specific unit is mole/cm2/s, area should converted to cm2

-start
 10  r_specific = (10^-18.1) * ((ACT("H+"))^0.22)
 20  rate = PARM(1)/PARM(2) * (10000) * (M/M0)^0.67  * r_specific *
4.55   #10000 to convert area to cm2
 30  moles = rate * time
```

```
  40 SAVE moles
-end
#----------------------------------------------------------------------
------

SELECTED_OUTPUT

 USER_PUNCH
# ^ User defined output; useful to convert directly to mmol/kgw
      -headings Time Ca Na K Si CO3 Cl(-1) Mg Al F SI("Calcite")
SI("Talc") SI("Saponite-Mg") SI("Saponite-Ca") SI("Saponite-K")
SI("Saponite-Na") SI("Brucite") SI("Celestite") SI("Nontronite-K")
SI("Nontronite-Ca") SI("Nontronite-Na") SI("Nontronite-Mg")
SI("Smectite-low-Fe-Mg") SI("Strontianite") SI("Tobermorite-9A")
SI("Tobermorite-11A") SI("Tobermorite-14A") SI("Dolomite") SI("Quartz")
SI("K-feldspar") SI("Albite") SI("Analcime") SI("Andradite")
SI("Anhydrite") SI("Bassanite") SI("Beidellite-Ca") SI("Boehmite")
SI("Chrysotile") SI("Clinochlore-14A") SI("Clinochlore-7A")
SI("Celadonite") SI("CSHgel") SI("Chalcedony") SI("Clinoptilolite")
SI("Clinoptilolite-Ca") SI("Clinozoisite") SI("Diaspore")
SI("Dicalcium_silicate") SI("Diopside") SI("Enstatite") SI("Epidote")
SI("Epidote-ord") SI("Ferrite-Ca") SI("Ferrite-Dicalcium") SI("Ferrite-
Mg") SI("Forsterite") SI("Foshagite") SI("Goethite") SI("Gibbsite")
SI("Grossular") SI("Gypsum") SI("Gyrolite") SI("Hillebrandite")
SI("Heulandite") SI("Jadeite") SI("Laumontite") SI("Lawsonite")
SI("Maximum_Microcline") SI("Mesolite") SI("Larnite") SI("Merwinite")
SI("Monohydrocalcite") SI("Monticellite") SI("Montmor-Ca") SI("Montmor-
K") SI("Montmor-Mg") SI("Montmor-Na") SI("Mordenite") SI("Natrolite")
SI("Pargasite") SI("Paragonite") SI("Petalite") SI("Phlogopite")
SI("Portlandite") SI("Prehnite") SI("Pseudowollastonite")
SI("Rankinite") SI("Sanidine_high") SI("Scolecite") SI("Stilbite")
SI("Tremolite") SI("Wollastonite") SI("Zoisite") SI("Muscovite")
SI("Illite") Rate_Quartz Rate_Dolomite Rate_Kfeldspar KIN("Talc")
KIN_Delta("Talc") SI("Aragonite")
-start

010 PUNCH TOTAL_TIME/(60*60*24*30)
020 PUNCH tot("Ca")*40*1000
030 PUNCH tot("Na")*23*1000                    # tot used for total element
concentrations
040 PUNCH tot("K")*39.1*1000
050 PUNCH tot("Si")*28.09*1000
060 PUNCH tot("C(4)")*60*1000
070 PUNCH tot("Cl(-1)")*35.45*1000
080 PUNCH tot("Mg")*24.3*1000
090 PUNCH tot("Al")*27*1000
100 PUNCH tot("F")*19*1000
110 PUNCH SI("Calcite")
120 PUNCH SI("Talc")
130 PUNCH SI("Saponite-Mg")
140 PUNCH SI("Saponite-Ca")
150 PUNCH SI("Saponite-K")
160 PUNCH SI("Saponite-Na")
170 PUNCH SI("Brucite")
180 PUNCH SI("Celestite")
190 PUNCH SI("Nontronite-K")
200 PUNCH SI("Nontronite-Ca")
```

```
210 PUNCH SI("Nontronite-Na")
220 PUNCH SI("Nontronite-Mg")
230 PUNCH SI("Smectite-low-Fe-Mg")
240 PUNCH SI("Strontianite")
250 PUNCH SI("Tobermorite-9A")
260 PUNCH SI("Tobermorite-11A")
270 PUNCH SI("Tobermorite-14A")
280 PUNCH SI("Dolomite")
290 PUNCH SI("Quartz")
300 PUNCH SI("K-feldspar")
310 PUNCH SI("Albite")
320 PUNCH SI("Analcime")
330 PUNCH SI("Andradite")
340 PUNCH SI("Anhydrite")
350 PUNCH SI("Bassanite")
360 PUNCH SI("Beidellite-Ca")
370 PUNCH SI("Boehmite")
380 PUNCH SI("Chrysotile")
390 PUNCH SI("Clinochlore-14A")
400 PUNCH SI("Clinochlore-7A")
410 PUNCH SI("Celadonite")
420 PUNCH SI("CSHgel")
430 PUNCH SI("Chalcedony")
440 PUNCH SI("Clinoptilolite")
450 PUNCH SI("Clinoptilolite-Ca")
460 PUNCH SI("Clinozoisite")
470 PUNCH SI("Diaspore")
480 PUNCH SI("Dicalcium_silicate")
490 PUNCH SI("Diopside")
500 PUNCH SI("Enstatite")
510 PUNCH SI("Epidote")
520 PUNCH SI("Epidote-ord")
530 PUNCH SI("Ferrite-Ca")
540 PUNCH SI("Ferrite-Dicalcium")
550 PUNCH SI("Ferrite-Mg")
560 PUNCH SI("Forsterite")
570 PUNCH SI("Foshagite")
580 PUNCH SI("Goethite")
590 PUNCH SI("Gibbsite")
600 PUNCH SI("Grossular")
610 PUNCH SI("Gypsum")
620 PUNCH SI("Gyrolite")
630 PUNCH SI("Hillebrandite")
640 PUNCH SI("Heulandite")
650 PUNCH SI("Jadeite")
660 PUNCH SI("Laumontite")
670 PUNCH SI("Lawsonite")
680 PUNCH SI("Maximum_Microcline")
690 PUNCH SI("Mesolite")
700 PUNCH SI("Larnite")
710 PUNCH SI("Merwinite")
720 PUNCH SI("Monohydrocalcite")
730 PUNCH SI("Monticellite")
740 PUNCH SI("Montmor-Ca")
750 PUNCH SI("Montmor-K")
760 PUNCH SI("Montmor-Mg")
770 PUNCH SI("Montmor-Na")
```

```
780 PUNCH SI("Mordenite")
790 PUNCH SI("Natrolite")
800 PUNCH SI("Pargasite")
810 PUNCH SI("Paragonite")
820 PUNCH SI("Petalite")
830 PUNCH SI("Phlogopite")
840 PUNCH SI("Portlandite")
850 PUNCH SI("Prehnite")
860 PUNCH SI("Pseudowollastonite")
870 PUNCH SI("Rankinite")
880 PUNCH SI("Sanidine_high")
890 PUNCH SI("Scolecite")
900 PUNCH SI("Stilbite")
910 PUNCH SI("Tremolite")
920 PUNCH SI("Wollastonite")
930 PUNCH SI("Zoisite")
940 PUNCH SI("Muscovite")
950 PUNCH SI("Illite")
960 PUNCH GET(1)
970 PUNCH GET(2)
980 PUNCH GET(3)
990 PUNCH KIN("Brucite")
1000 PUNCH mol("Talc")
1100 PUNCH SI("Aragonite")


        -end

End
```

3. The influence of high pH leachate on a generic host rock for a nuclear waste repository: modelling of variable porosity and surface area

3.1. Fixed Porosity

```
SOLUTION 0
    temp       50
    pH         12.415 #originally 13.1 at 25C
    pe         4
    redox      pe
    units      mg/l
    density    1
    K          3636
    Na         2185
    -water     1 # kg

save solution 0

end


SOLUTION 1-10
    temp       50
    pH         7.83
    pe         4
    redox      pe
    units      mg/l
    density    1
    Al         0.02
    Br(-1)     4340
    Ca         23.1
    Cl(-1)     4300
    K          3202
    Mg         0.07
    Na         2178
    Si         0.36
    -water     1 # kg

EQUILIBRIUM_PHASES 1-10

O2(g) -0.68 10

quartz 0 0.009              #SiO2
K-feldspar 0.75 0       #AlKO8Si3
Kaolinite -4.5 0.007        #Al2Si2O5(OH)4
CSHgel 0 0
Tobermorite-14A 0 0
saponite-Mg 0 0
analcime 0 0
hydrogarnet 0 0
prehnite 0 0
Laumontite 0 0
mesolite 0 0
```

```
Phillipsite 0 0
Mordenite 0 0


#------------------------------------------------------------------
#The weight composition of the sandstone sample is 75.5% Quartz, 16% K-
feldspar, 3.7% Illite and 3.5% Kaolinite for a total of 21.249 g
#Quartz mass = 16.04 g
#K-feldspar mass = 3.4 g
#kaolinite mass = 0.743 g
#Illite mass = 0.786 g

#Quartz Molar Weight = 60.08
#K-feldspar Molar Weight = 278.33
#Kaolinite Molar Weight = 258.16
#Illite Molar Weight = 389.34
#------------------------------------------------------------------

KINETICS 1-10

K-feldspar
  -tol 1e-8
  -m0 0.012
  -parms 0.02 0.005968                              # A0 in m2/g, V in L
(= Pore volume)


#---------------------

Quartz
 -tol 1e-8
 -m0 0.267
 -parms 0.02  0.005968                              # A0 in m2/g, V in L

#-----------------------

Kaolinite
 -tol 1e-8
 -m0 0.003
 -parms 20  0.005968

#---------------------


-steps 0 648 893 1224 1488 1733 1899 2039 2329 2737 3199 3774 4177 4560
5017 5429 5593 hour

INCREMENTAL_REACTIONS false

#------------------------------------------------------------------

RATES

Quartz

#k = 10^-12.7 @ 50C
 -start
```

```
 10 A0 = parm(1)
 20 V = parm(2)

 30 Mass_Q = (m0) * 60.08

 40 rate = A0/V * ((m/m0)^0.67) * (10^-12.7) * (1 - SR("Quartz")) *
Mass_Q
 50 moles = rate * time

 60 PUT(moles,1)
 70 Diss_Mass = GET(1) * 60.08

 80 save moles

 -end



#-------------------------------------------------

K-feldspar
 -start

 1 A0 = parm(1)
 2 V = parm(2)

        # find activities of inhibiting ions...

 3 a_Al = act("Al+3")
 4 BC = act("Na+") + act("K+") + act("Mg+2") + act("Ca+2")

        # temp corrected with the Arrhenius eqn, Table 8.8
        # the difference in temperature, TK gives solution temp in
Kelvin...

 10 dif_T = 1/TK - 1/281

                  # rate by H+...
 20 pk_H = 11.7 + 3500 * dif_T
 22 rate_H = 10^-pk_H * act("H+")^0.5 / ((1 + a_Al / 4e-6)^0.4 * (1 +
BC / 5e-4)^0.15)

                  # rate by hydrolysis...
 30 pk_w = 14.5 + 2000 * dif_T
 32 rate_w = 10^-pk_w / ((1 + a_Al / 4e-6)^0.14 * (1 + BC / 5e-4)^0.15)

                  # rate by OH-...
 40 pk_OH = 13.1 + 2500 * dif_T
 42 rate_OH = 10^-pk_OH * act("OH-")^0.3

                  # rate by CO2...
 50 pk_CO2 = 13.0 + 2000 * dif_T
 52 rate_CO2 = 10^-pk_CO2 * (10^SI("CO2(g)"))^0.6

                  # Sum the rate contributions...
 60 rate_t = rate_H + rate_w + rate_OH + rate_CO2
```

```
                          # normalize to mol/kgw, correct for m/m0 and the
approach to equi...

 70 Mass_Kf = (m0) * 278.33

 80 rate = (rate_t) * (A0 / V) * ((m/m0)^0.67) * (1 - SR("K-feldspar"))
* Mass_Kf
 90 moles = rate * time

 100 PUT(moles,2)
 110 Diss_Mass = GET(2) * 278.33

 120 save moles

-end
#----------------------------------------------------------------------
---

Kaolinite

  -start

 10 k = 10^-12.5
 11 PUT (k,100)
 20 A0 = parm(1)
 30 V = parm(2)

 40 Mass_K = (m0) * 258.16

 50 rate = A0/V * ((m/m0)^0.67) * (k) * (1 - SR("kaolinite")) * Mass_K
 60 moles = rate * time

 70 PUT(moles,3)
 80 Diss_Mass = GET(3) * 258.16

 90 save moles

-end


#----------------------------------------------------------------------
---

use solution 0


 TRANSPORT

        -cells             10
        -length            0.03
        -shifts            215
        -time_step         26 hour
        -flow_direction    forward
        -boundary_condition  flux flux
        -dispersivity      0.09
        -correct_disp      true
        -diffusion_coef    0.3e-9
```

```
        -punch_cells            1-10
        -punch_frequency        1
        -print_cells            10




SELECTED_OUTPUT

USER_PUNCH


-heading  Time K Na Ca Al Si Br Mg SI("Quartz") SI("k-feldspar")
SI("Saponite-K") SI("Prehnite") SI("Talc") SI("Kalsilite")
SI("natrolite") SI("CSHgel") SI("Gibbsite") SI("MESOLITE")
SI("Saponite-Ca") SI("Saponite-Mg") SI("Saponite-Na") SI("Tobermorite-
11A") SI("Tobermorite-14A") SI("kaolinite") SI("Illite") SI("Calcite")
SI("Dolomite") saponite-Mg CSHgel Tobermorite-14A analcime hydrogarnet
Friedelsalt prehnite Laumontite mesolite Jennite Phillipsite Mordenite
saponite-Ca quartz kaolinite k-feldspar


-start

 10  PUNCH   TOTAL_TIME/(60*60)
 20  PUNCH   TOT("K")*39*1000
 30  PUNCH   TOT("Na")*23*1000
 40  PUNCH   TOT("Ca")*40*1000
 50  PUNCH   TOT("Al")*27*1000
 60  PUNCH   TOT("Si")*28.1*1000
 70  PUNCH   TOT("Br")*79.9*1000
 80  PUNCH   TOT("Mg")*24*1000
 90  PUNCH   SI("Quartz")
100  PUNCH   SI("k-feldspar")
110  PUNCH   SI("Saponite-K")
120  PUNCH   SI("Prehnite")
130  PUNCH   SI("Talc")
140  PUNCH   SI("Kalsilite")
150  PUNCH   SI("natrolite")
160  PUNCH   SI("CSHgel")
170  PUNCH   SI("Gibbsite")
180  PUNCH   SI("MESOLITE")
190  PUNCH   SI("Saponite-Ca")
200  PUNCH   SI("Saponite-Mg")
210  PUNCH   SI("Saponite-Na")
220  PUNCH   SI("Tobermorite-11A")
230  PUNCH   SI("Tobermorite-14A")
240  PUNCH   SI("kaolinite")
250  PUNCH   SI("Illite")
260  PUNCH   SI("Calcite")
270  PUNCH   SI("Dolomite")
280  PUNCH   EQUI_DELTA("saponite-Mg")
290  PUNCH   EQUI_DELTA("CSHgel")
300  PUNCH   EQUI_DELTA("Tobermorite-14A")
310  PUNCH   EQUI_DELTA("analcime")
320  PUNCH   EQUI_DELTA("hydrogarnet")
330  PUNCH   EQUI_DELTA("Friedelsalt")
```

```
340 PUNCH   EQUI_DELTA("prehnite")
350 PUNCH   EQUI_DELTA("Laumontite")
360 PUNCH   EQUI_DELTA("mesolite")
370 PUNCH   EQUI_DELTA("Jennite")
380 PUNCH   EQUI_DELTA("Phillipsite")
390 PUNCH   EQUI_DELTA("Mordenite")
400 PUNCH   EQUI_DELTA("saponite-Ca")
410 PUNCH   KIN_DELTA("quartz")
420 PUNCH   KIN_DELTA("kaolinite")
430 PUNCH   KIN_DELTA("k-feldspar")

End
```

3.2.Variable Porosity

```
SOLUTION 0
    temp       50
    pH         12.415 #originally 13.1 at 25C
    pe         4
    redox      pe
    units      mg/l
    density    1
    K          3290
    Na         2185
    -water     1 # kg


save solution 0

end

SOLUTION 1-10
    temp       50
    pH         7.83
    pe         4
    redox      pe
    units      mg/l
    density    1
    Al         0.02
    Br(-1)     4340
    Ca         23.1
    Cl(-1)     4300
    K          3202
    Mg         0.07
    Na         2178
    Si         0.36
    -water     1 # kg



EQUILIBRIUM_PHASES 1-10
O2(g) -0.68 10

quartz 0 0            #SiO2
K-feldspar 1.1 0.005    #AlKO8Si3
Kaolinite -4.4 0.005       #Al2Si2O5(OH)4
CSHgel 0 0
Tobermorite-14A 0 0
saponite-Mg 0 0
analcime 0 0
hydrogarnet 0 0
prehnite 0 0
Laumontite 0 0
mesolite 0 0
Phillipsite 0 0
Mordenite 0 0
```

```
#-------------------------------------------------------------------

KINETICS 1-10

Quartz

 -tol 1e-8
 -m0 0.267
 -parms 0.02 0.005968

Kaolinite

 -tol 1e-8
 -m0 0.0030
 -parms 20 0.005968

K-feldspar
 -tol    1e-8
 -M0     0.012
 -parms  0.02 0.005968




#-cvode                    true




-steps 0 26 52 78 104 130 156 182 208 234 260 286 312 338 364 390 416
442 468 494 520 546 572 598 624 650 676 702 728 754 780 806 832 858 884
910 936 962 988 1014 1066 1092 1118 1144 1170 1196 1222 1248 1274 1300
1326 1353 1378 1404 1430 1456 1482 1508 1534 1560 1586 1612 1638 1664
1690 1716 1742 1768 1794 1820 1846 1872 1898 1924 1950 1976 2002 2028
2054 2080 2106 2132 2158 2184 2210 2236 2262 2288 2314 2340 2366 2392
2418 2444 2470 2496 2522 2548 2574 2600 2626 2652 2678 2704 2730 2756
2782 2808 2834 2860 2886 2912 2938 2964 2990 3016 3042 3068 3094 3120
3146 3172 3198 3224 3250 3276 3302 3328 3354 3380 3406 3432 3458 3484
3510 3536 3562 3585 3614 3640 3666 3692 3718 3744 3770 3796 3822 3848
3874 3900 3926 3952 3978 4004 4030 4056 4082 4108 4134 4160 4186 4212
4238 4264 4290 4316 4342 4368 4394 4420 4446 4472 4498 4524 4550 4676
4602 4628 4654 4680 4706 4732 4758 4784 4810 4836 4862 4888 4914 4940
4966 4992 5018 5044 5070 5096 5122 5148 5174 5200 5226 5252 5278 5304
5330 5356 5382 5408 5434 5460 5486 5512 5538 5564 5590 hour


INCREMENTAL_REACTIONS false

#----------------------------------------------------------------------
---

RATES

Quartz

-start
```

```
1 kq = 10^-12.7

2 PUT(kq,87)


#Initial values for Quartz and K-feldspar


3 PV = 5.968     # Pore Volume...mL from expe (excel file)

4 Por1 = 0.427

5 TV = PV/Por1     #mL....the volume is for cylindrical shape pipe


#The weight composition of the sandstone sample is 75.5% Quartz, 16% K-
feldspar and 3.5% Kaolinite for a total of 21.249 g

6 QMass1 = 0.755 * 21.249   #Quartz initial mass...g

7 Qden = 2650   #Quartz Density...g/L

8 QV1 = QMass1 / Qden     #Quartz initial Volume...L

9 QPor1 = GET_POR(1)

10 QMW = 60.08     #Quartz molar weight...g/Mol

11 Qmol1 = QMass1 / QMW     #Quartz initial moles...mole

12 A0_Q = parm(1) * (((1-GET(1000)) / (1-0.427))^2/3)  #Quartz initial
surface area m2/g

13 Qmass = (Qmass1 + GET(8))

#Total reactive surface area = A0_Q * Quartz initial mass    m2


14 rate_Q = (A0_Q/(parm(2)+ GET(1002))) *  Qmass *  ((m/m0)^0.67) *
(kq) * (1 - SR("Quartz"))

15 moles = rate_Q * time
#mole

16 PUT(Qmol1,1)
17 PUT(moles,2)


#calculate new porosity:


18  Dmol_Q = GET(2)              #Quartz Dissolve moles...moles

19  DmolMass_Q = -1 * (Dmol_Q * QMW)     #Quartz Dissolve moles
mass...g

20  QMV = QMW / Qden              #Quartz molar volume...L/mole
```

```
21  DmolVol_Q = -1 * (Dmol_Q * QMV)        #Quartz Dissolve moles
volume....L

22  QPor2 = -1 * (DmolVol_Q / (TV/1000))    #Quartz extra porosity

23  Q_New_Porosity = QPor1 + QPor2


24 PUT(DmolVol_Q,3)
25 PUT(QPor1,4)
26 PUT(QPor2,5)
27 PUT(Q_New_Porosity,6)
28 PUT(A0_Q,7)
29 PUT(DmolMass_Q,8)
30 PUT(Qmass,9)

31 save moles

-end

#---------------------

Kaolinite

-start

1 PV = 5.968    # Pore Volume...mL from expe (excel file)

2 Por1 = 0.427

3 TV = PV/Por1     #mL....the volume is for cylindrical shape pipe


10 kk = 10^-12.5 #@T=50, PH=12.6

11 PUT(kk,89)

#The weight composition of the sandstone sample is 75.5% Quartz, 16% K-
feldspar and 3.5% Kaolinite for a total of 21.249 g

20 KMass1 = 0.035 * 21.249   #Kaolinite initial mass...g

30 Kden = 2650   #kaolinite Density...g/L

40 KV1 = KMass1 / Kden    #kaolinite initial Volume...L

50 KPor1 = GET_POR(1)

60 KMW = 258.16      #Kaolinite molar weight...g/Mol

70 Kmol1 = KMass1 / KMW     #Kaolinite initial moles...mole

80 A0_K = parm(1) * (((1-GET(1000)) / (1-0.427))^2/3)  #Kaolinite
initial surface area m2/g

90 Kmass = (Kmass1 + GET(80))
```

```
#Total reactive surface area = A0_K * Kaolinite initial mass    m2

100 rate_K = (A0_K/(parm(2)+ GET(1002))) * Kmass *  ((m/m0)^0.67) *
(kk) * (1 - SR("Kaolinite"))

110 moles = rate_K * time
#mole

120 PUT(Kmol1,10)
130 PUT(moles,20)

#calculate new porosity:


140  Dmol_K = GET(20)            #kaolinite Dissolve moles...moles

150  DmolMass_K = -1 *(Dmol_K * KMW)     #kaolinite Dissolve moles
mass...g

160  KMV = KMW / Kden            #kaolinite molar volume...L/mole

170  DmolVol_K = -1 *(Dmol_K * KMV)     #Kaolinite Dissolve moles
volume....L

180  KPor2 = -1 * (DmolVol_K / (TV/1000))   #Kaolinite extra porosity

190  K_New_Porosity = KPor1 + KPor2



200 PUT(DmolVol_K,30)
210 PUT(KPor1,40)
220 PUT(KPor2,50)
230 PUT(K_New_Porosity,60)
240 PUT(A0_K,70)
250 PUT(DmolMass_K,80)
260 PUT(Kmass,90)



270 SAVE moles

-end

#---------------------------

K-feldspar


 -start

1 PV = 5.968    # Pore Volume...mL from expe (excel file)

2 Por1 = 0.427

3 TV = PV/Por1     #mL....the volume is for cylindrical shape pipe
```

342

```
     # find activities of inhibiting ions...

 4 a_Al = act("Al+3")
 5 BC = act("Na+") + act("K+") + act("Mg+2") + act("Ca+2")

     # temp corrected with the Arrhenius eqn, Table 8.8
     # the difference in temperature, TK gives solution temp in
Kelvin...

 10 dif_T = 1/TK - 1/281

                 # rate by H+...
 20 pk_H = 11.7 + 3500 * dif_T
 22 rate_H = 10^-pk_H * act("H+")^0.5 / ((1 + a_Al / 4e-6)^0.4 * (1 +
BC / 5e-4)^0.15)

                 # rate by hydrolysis...
 30 pk_w = 14.5 + 2000 * dif_T
 32 rate_w = 10^-pk_w / ((1 + a_Al / 4e-6)^0.14 * (1 + BC / 5e-4)^0.15)

                 # rate by OH-...
 40 pk_OH = 13.1 + 2500 * dif_T
 42 rate_OH = 10^-pk_OH * act("OH-")^0.3

                 # rate by CO2...
 50 pk_CO2 = 13.0 + 2000 * dif_T
 52 rate_CO2 = 10^-pk_CO2 * (10^SI("CO2(g)"))^0.6

                 # Sum the rate contributions...
60 kkf = rate_H + rate_w + rate_OH + rate_CO2

61 PUT(kkf,88)


#The weight composition of the sandstone sample is 75.5% Quartz, 16% K-
feldspar and 3.5% Kaolinite for a total of 21.249 g

70  KfMass1 = 0.16 * 21.249   #Kfeldspar initial mass...g

80  Kfden = 2560   #Kfeldspar Density...g/L

90  KfV1 = KfMass1 / Kfden    #Kfeldspar initial Volume...L

100 KfPor1 = GET_POR(1)

110 KfMW = 278.33      #Kfeldspar molar weight...g/Mol

120 Kfmol1 = KfMass1 / KfMW    #Kfeldspar initial moles...mole

130 A0_Kf = parm(1) * (((1-GET(1000)) / (1-0.427))^2/3)   #Kfeldspar
initial surface area m2/g

140 Kfmass = (Kfmass1 + GET(800))

#Total reactive surface area = A0_Kf * Kfeldspar initial mass   m2
```

343

```
150 rate_Kf = (kkf) * (A0_Kf/(parm(2)+ GET(1002))) * Kfmass *
((m/m0)^0.67) * (1 - SR("K-feldspar"))

160 moles = rate_Kf * time

170 PUT(Kfmol1,100)
180 PUT(moles,200)

#calculate new porosity:


190  Dmol_Kf = GET(200)              #Kfeldspar Dissolve moles...moles

200  DmolMass_Kf = -1 *(Dmol_Kf * KfMW)     #Kfeldspar Dissolve moles
mass...g

210  KfMV = KfMW / Kfden              #Kfeldspar molar volume...L/mole

220  DmolVol_Kf = -1 *(Dmol_Kf * KfMV)      #Kfeldspar Dissolve moles
volume....L

230  KfPor2 = -1 *(DmolVol_Kf / (TV/1000))   #Kfeldspar extra
porosity....the (-) here is just to correct the (-) from the dissolve
mole volume equation.

240  Kf_New_Porosity = KfPor1 + KfPor2



250 PUT(DmolVol_Kf,300)
260 PUT(KfPor1,400)
270 PUT(KfPor2,500)
280 PUT(Kf_New_Porosity,600)
290 PUT(A0_Kf,700)
300 PUT(DmolMass_Kf,800)
310 PUT(Kfmass,900)

#--------------------------------

320 New_Total_V = -1 * (GET(3) + GET(30) + GET(300))

330 PUT(New_Total_V,1002)

340 Porosity_2 = GET(5) + GET(50) + GET(500)

350 PUT(Porosity_2,1001)

360 New_Porosity = GET_POR(1) + GET(1001)

370 PUT(New_Porosity,1000)

380 CHANGE_POR(New_Porosity,1)

390 save moles

 -end
```

```
#----------------------------------

use solution 0

 TRANSPORT

        -cells              10
        -shifts             215
        -time_step          26 hour
        -flow_direction     forward
        -boundary_conditions flux flux
        -lengths            10*0.03
        -dispersivity       10*0.09
        -correct_disp       true
        -diffusion_coef     0.3e-9
        -initial_time       0
        -punch_cells        1-10
        -punch_frequency    1
        -porosities         0.427




#------------------------------------------


SELECTED_OUTPUT


USER_PUNCH



-heading  Time SI("Quartz") SI("K-feldspar") SI("Kaolinite") Q_Mole1
Q_Moles Q_Dissolve_moles_volume Q_Por1 Q_Por2 Q_New_Poros Q_A0
Q_Dissolve_mole_mass Q_mass K_mol1 K_Moles K_Dissolve_moles_volume
K_Por1 K_Por2 K_New_Poros K_A0 K_Dissolve_mole_mass K_mass Kf_mol1
Kf_Moles Kf_Dissolve_moles_volume Kf_Por1 Kf_Por2 Kf_New_Poros Kf_A0
Kf_Dissolve_mole_mass Kf_mass Si Cl Ca Na K SI("CSHgel")
SI("Tobermorite-11A") SI("Tobermorite-14A") Tob11_Moles KIN_DELTA_Tob11
KIN_Tob11 Q_Moles KIN_DELTA_Q KIN_Q K_Moles KIN_DELTA_K KIN_K Kf_Moles
KIN_DELTA_Kf KIN_Kf Tob11_Mass1 Tob_11_Moles Tob11_Prec_Mole_V
Tob11_Prec_Mole_Mass A0-Tob11 Tob11_mass Tob11_Por2 Total_Por2
New_Porosity Tob14_Mass1 Tob14_Mole Tobe14_Pre_Mole_V
Tob14_Prec_Mole_Mass A0_Tob14 Tob14_mass Tob14_Por2 CSH_Mass1 CSH_Moles
CSH_Pre_Mole_V CSH_Pre_Mole_Mass A0_CSH CSH_Mass CSH_Por2 SI(Talc)
SI(Saponite-Ca) SI(Saponite-Mg) SI(Brucite) S_Mass1 S_Moles
S_Pre_Mole_V S_Pre_Mole_Mass A0_S S_Mass S_Por2 New_T_V B_Mass1 B_Moles
B_Pre_Mole_V B_Pre_Mole_Mass A0_B B_Mass B_Por2 T_Mass1 T_Moles
T_Pre_Mole_V T_Pre_Mole_Mass A0_T T_Mass T_Por2 E_Mass1 E_Moles
E_Pre_Mole_V E_Pre_Mole_Mass A0_E E_Mass E_Por2 P_Mass1 P_Moles
P_Pre_Mole_V P_Pre_Mole_Mass A0_P P_Mass P_Por2 I_Mass1 I_Moles
I_Pre_Mole_V I_Pre_Mole_Mass A0_I I_Mass I_Por2 Calcite Dolomite
Hydrotalcite Hydrotalcite-OH Ettringite Thaumasite Gypsum Brucite
Analcime Laumontite Clinoptilolite-Ca Mesolite Mordenite Phillipsite
illite Sepiolite Chalcedony saponite-Na Saponite-Ca Saponite-K K-
Feldspar Mg Al Q_spec.rate Kf_spec.rate Ka_spec.rate Natrolite Jennite
```

Thaumasite hydrogarnet katoite Friedelsalt prehnite saponite-Mg CSHgel
Tobermorite-14A analcime hydrogarnet Friedelsalt prehnite Laumontite
mesolite Jennite Phillipsite Mordenite saponite-Ca quartz kaolinite k-
feldspar

-start

```
 10  PUNCH  TOTAL_TIME/(3600)
 20  PUNCH  SI("Quartz")
 30  PUNCH  SI("K-feldspar")
 40  PUNCH  SI("Kaolinite")
 50  PUNCH  GET(1)
 60  PUNCH  GET(2)
 70  PUNCH  GET(3)
 80  PUNCH  GET(4)
 90  PUNCH  GET(5)
100  PUNCH  GET(6)
110  PUNCH  GET(7)
120  PUNCH  GET(8)
130  PUNCH  GET(9)
140  PUNCH  GET(10)
150  PUNCH  GET(20)
160  PUNCH  GET(30)
170  PUNCH  GET(40)
180  PUNCH  GET(50)
190  PUNCH  GET(60)
200  PUNCH  GET(70)
210  PUNCH  GET(80)
220  PUNCH  GET(90)
230  PUNCH  GET(100)
240  PUNCH  GET(200)
250  PUNCH  GET(300)
260  PUNCH  GET(400)
270  PUNCH  GET(500)
280  PUNCH  GET(600)
290  PUNCH  GET(700)
300  PUNCH  GET(800)
310  PUNCH  GET(900)
320  PUNCH  TOT("Si")*28.08*1000
330  PUNCH  TOT("Cl(-1)")*35.45*1000
340  PUNCH  TOT("Ca")*40.07*1000
350  PUNCH  TOT("Na")*23*1000
360  PUNCH  TOT("K")*39.1*1000
370  PUNCH  SI("CSHgel")
380  PUNCH  SI("Tobermorite-11A")
390  PUNCH  SI("Tobermorite-14A")
400  PUNCH  GET(20000)
410  PUNCH  KIN_DELTA("Tobermorite-11A")
420  PUNCH  KIN("Tobermorite-11A")
430  PUNCH  GET(2)
440  PUNCH  KIN_DELTA("Quartz")
450  PUNCH  KIN("Quartz")
460  PUNCH  GET(20)
470  PUNCH  KIN_DELTA("Kaolinite")
480  PUNCH  KIN("Kaolinite")
490  PUNCH  GET(200)
```

```
 500 PUNCH   KIN_DELTA("K-feldspar")
 510 PUNCH   KIN("K-feldspar")
 520 PUNCH   GET(10000)
 530 PUNCH   GET(20000)
 540 PUNCH   GET(30000)
 550 PUNCH   GET(40000)
 560 PUNCH   GET(50000)
 570 PUNCH   GET(60000)
 580 PUNCH   GET(70000)
 590 PUNCH   GET(1001)
 600 PUNCH   GET(1000)
 610 PUNCH   GET(100000)
 620 PUNCH   GET(200000)
 630 PUNCH   GET(300000)
 640 PUNCH   GET(400000)
 650 PUNCH   GET(500000)
 660 PUNCH   GET(600000)
 670 PUNCH   GET(700000)
 680 PUNCH   GET(1000000)
 690 PUNCH   GET(2000000)
 700 PUNCH   GET(3000000)
 710 PUNCH   GET(4000000)
 720 PUNCH   GET(5000000)
 730 PUNCH   GET(6000000)
 740 PUNCH   GET(7000000)
 750 PUNCH   SI("Talc")
 760 PUNCH   SI("Saponite-Ca")
 770 PUNCH   SI("Saponite-Mg")
 780 PUNCH   SI("Brucite")
 790 PUNCH   GET(10000000)
 800 PUNCH   GET(20000000)
 810 PUNCH   GET(30000000)
 820 PUNCH   GET(40000000)
 830 PUNCH   GET(50000000)
 840 PUNCH   GET(60000000)
 850 PUNCH   GET(70000000)
 860 PUNCH   GET(1002)
 870 PUNCH   GET(100000000)
 880 PUNCH   GET(200000000)
 890 PUNCH   GET(300000000)
 900 PUNCH   GET(400000000)
 910 PUNCH   GET(500000000)
 920 PUNCH   GET(600000000)
 930 PUNCH   GET(700000000)
 940 PUNCH   GET(1000000000)
 950 PUNCH   GET(2000000000)
 960 PUNCH   GET(3000000000)
 970 PUNCH   GET(4000000000)
 980 PUNCH   GET(5000000000)
 990 PUNCH   GET(6000000000)
1000 PUNCH   GET(7000000000)
1010 PUNCH   GET(10000000000)
1020 PUNCH   GET(20000000000)
1030 PUNCH   GET(30000000000)
1040 PUNCH   GET(40000000000)
1050 PUNCH   GET(50000000000)
1060 PUNCH   GET(60000000000)
```

```
1070 PUNCH   GET(70000000000)
1080 PUNCH   GET(100000000000)
1090 PUNCH   GET(200000000000)
1100 PUNCH   GET(300000000000)
1110 PUNCH   GET(400000000000)
1120 PUNCH   GET(500000000000)
1130 PUNCH   GET(600000000000)
1140 PUNCH   GET(700000000000)
1150 PUNCH   GET(1000000000000)
1160 PUNCH   GET(2000000000000)
1170 PUNCH   GET(3000000000000)
1180 PUNCH   GET(4000000000000)
1190 PUNCH   GET(5000000000000)
1200 PUNCH   GET(6000000000000)
1210 PUNCH   GET(7000000000000)
1220 PUNCH   SI("Calcite")
1230 PUNCH   SI("Dolomite")
1240 PUNCH   SI("Hydrotalcite")
1250 PUNCH   SI("Hydrotalcite-OH")
1260 PUNCH   SI("Ettringite")
1270 PUNCH   SI("Thaumasite")
1280 PUNCH   SI("Gypsum")
1290 PUNCH   SI("Brucite")
1300 PUNCH   SI("Analcime")
1310 PUNCH   SI("Laumontite")
1320 PUNCH   SI("Clinoptilolite-Ca")
1330 PUNCH   SI("Mesolite")
1340 PUNCH   SI("Mordenite")
1350 PUNCH   SI("Phillipsite")
1360 PUNCH   SI("illite")
1370 PUNCH   SI("Sepiolite")
1380 PUNCH   SI("Chalcedony")
1390 PUNCH   SI("saponite-Na")
1400 PUNCH   SI("Saponite-Ca")
1410 PUNCH   SI("Saponite-K")
1420 PUNCH   SI("K-Feldspar")
1430 PUNCH   TOT("Mg")*24.305*1000
1440 PUNCH   TOT("Al")*26.981*1000
1450 PUNCH   GET(87)
1460 PUNCH   GET(88)
1470 PUNCH   GET(89)
1480 PUNCH   SI("Natrolite")
1490 PUNCH   SI("Jennite")
1500 PUNCH   SI("Thaumasite")
1510 PUNCH   SI("hydrogarnet")
1520 PUNCH   SI("katoite")
1530 PUNCH   SI("Friedelsalt")
1540 PUNCH   SI("prehnite")
1550 PUNCH   EQUI_DELTA("saponite-Mg")
1560 PUNCH   EQUI_DELTA("CSHgel")
1570 PUNCH   EQUI_DELTA("Tobermorite-14A")
1580 PUNCH   EQUI_DELTA("analcime")
1590 PUNCH   EQUI_DELTA("hydrogarnet")
1600 PUNCH   EQUI_DELTA("Friedelsalt")
1610 PUNCH   EQUI_DELTA("prehnite")
1620 PUNCH   EQUI_DELTA("Laumontite")
1630 PUNCH   EQUI_DELTA("mesolite")
```

```
1640 PUNCH  EQUI_DELTA("Jennite")
1650 PUNCH  EQUI_DELTA("Phillipsite")
1660 PUNCH  EQUI_DELTA("Mordenite")
1670 PUNCH  EQUI_DELTA("saponite-Ca")
1680 PUNCH  KIN_DELTA("quartz")
1690 PUNCH  KIN_DELTA("kaolinite")
1700 PUNCH  KIN_DELTA("k-feldspar")




END

#-------------------------------------------------------------------
```

4. Analysis of uranium sorption in a laboratory column experiment using a reactive transport and surface complexation model

4.1. Yucca Mountain

4.1.1. Column 1

```
#Yucca Mountain_uranium desorption_19IM1A (Column 1)

#------------------------------------------------------------------------
---

SOLUTION_MASTER_SPECIES
# element    species    alk gfw_formula element_gfw
  Hto        Hto        0.0   20          20

SOLUTION_SPECIES
  Hto = Hto;         log_k 0; -gamma 1e6 0;     -dw 1e-13

#------------------------------------------------------------------------
---

SOLUTION 0
    temp      25
    pH        8.6
    pe        4
    redox     pe
    units     mg/l
    density   1
    C(4)      189
    Ca        3.7
    Cl(-1)    6.1 charge
    Hto       1e-09
    K         3.7
    Mg        0.31
    N(5)      2.334
    Na        91.5
    S(6)      22
    U(6)      0.24
    -water    1 # kg

save solution 0

end

SOLUTION 1-10
    temp      25
    pH        8.6
    pe        4
    redox     pe
    units     mg/l
    density   1
    C(4)      189
```

```
    Ca          3.7
    Cl(-1)      6.1 charge
    K           3.7
    Mg          0.31
    N(5)        2.21
    Na          91.5
    S(6)        22
    -water      1 # kg


EQUILIBRIUM_PHASES 1-10
CO2(g) -3.5 10

Quartz 0 0                      #SiO2
Plagioclase 0 0                  #NaAlSi3O8 - CaAl2Si2O8
k-feldspar 0 0                   #KAlSi3O8
Clinoptilolite 0 0.135          #(Na,K,Ca) 2-3Al 3(Al,Si) 2Si 13O 36•12H 2O
Cristobalite(alpha) 0 0          #SiO2
Smectite-high-Fe-Mg 0 0         ##CaNaKFeMgAlSi3

kaolinite 0 0                    #Al2Si2O5(OH)4
Tridymite 0 0                    #SiO2
Hematite 0 0                     #Fe2O3
Muscovite 0 0                    #Mica--KAl2(AlSi3O10)(F,OH)2


#opal-CT-----SiO2



CaUO4 0 0
Uranophane 0 0          #Ca(UO2)2(SiO3)2(OH)2
Becquerelite 0 0        #Ca(UO2)6O4(OH)6:8H2O
Rutherfordine 0 0       #UO2CO3

#---------------------------------------------------

EXCHANGE_SPECIES


UO2+2 + 2NaX = UO2X2 + 2Na+
log_k   0.45

UO2+2 + CaX2 = UO2X2 + Ca+2
log_k   0.049


EXCHANGE 1-10
        -equilibrate 1-10
        X               0.014


#CEC for smectite is 810 meq/kg.....for 17.23 g smectite, then CEC
equals to 14 meq

#------------------------------------------------

SURFACE_MASTER_SPECIES
```

```
             Surf_al       Surf_alOH          #Smectite aluminol surface edge
             Surf_si       Surf_siOH          #Smectite silonal surface edge
             Surf_kal      Surf_kalOH         #Kaolinite aluminol surface edge
             Surf_fe       Surf_feOH          #Hematite aluminol surface edge



    SURFACE_SPECIES

             Surf_alOH = Surf_alOH
                     log_k   0.0

             Surf_alOH + H+ = Surf_alOH2+
                     log_k   12.3

              Surf_alOH = Surf_alO- + H+
                     log_k   -13.6

              Surf_alOH + UO2+2  = Surf_alOUO2+ + H+
                     log_k   7.7

    #----------------------------------------------------------------------
    -------------------------

             Surf_siOH = Surf_siOH
                     log_k   0.0

             Surf_siOH + H+ = Surf_siOH2+
                     log_k   -0.95

              Surf_siOH = Surf_siO- + H+
                     log_k   -6.95

              Surf_siOH + UO2+2  = Surf_siOUO2+ + H+
                     log_k   0.75

    #----------------------------------------------------------------------
    -----------

             Surf_kalOH = Surf_kalOH
                     log_k   0.0

             Surf_kalOH + H+ = Surf_kalOH2+
                     log_k   13.33

              Surf_kalOH = Surf_kalO- + H+
                     log_k   -4.72

              Surf_kalOH + UO2+2 + H2O  = Surf_kalOUO2OH + 2H+
                     log_k   6

    #----------------------------------------------------------------------
    -----

             Surf_feOH = Surf_feOH
                     log_k   0.0

             Surf_feOH + H+ = Surf_feOH2+
```

```
             log_k   -5.1

        Surf_feOH = Surf_feO- + H+
             log_k   -10.7

        Surf_feOH + UO2+2  = Surf_feOUO2+ + H+
             log_k   14.11


#----------------------------------------------------------------------
-----


SURFACE 1
        -equil solution 1-10
        -sites_units        density
        -donnan 1e-10

        Surf_alOH        2.3 51 17.23 Dw 1e-13   #number of sites
density(per nm2)-surrace area (m2/g)-mass (g)
        Surf_siOH        2.3 51 17.23 Dw 1e-13   #number of sites
density(per nm2)-surrace area (m2/g)-mass (g)
        Surf_kalOH       2.3 20 1.87  Dw 1e-13   #number of sites
density(per nm2)-surrace area (m2/g)-mass (g)
        Surf_feOH        2.3 10 1.5   Dw 1e-13   #number of sites
density(per nm2)-surrace area (m2/g)-mass (g)


#----------------------------------------------------------------------
--------
#for 374.61g of rock sample we have the following:
#24.4% Orthoclase = 91.40 g = 0.328 mol         #278.33
#15.3% Quartz = 57.31 g = 0.954 mol             #60.08
#23% Plagioclase = 86.16 g = 0.318 mol          #270.77
#7.6% Clinoptilolite = 28.47 g = 0.0103 mol     #2,742.13
#5.8% Cristobalite(alpha) = 21.727 g = 0.3616 mol #60.08
#4.6% Smectite-low-Fe-Mg = 17.23 g = 0.044 mol   #389.34
#0.5% kaolinite = 1.87 g
#0.4% Hematite = 1.5 g
#----------------------------------------------------------------------
--------

KINETICS 1-10

Quartz
 -tol   1e-8
 -m0    0.954
 -parms 0.02 0.03
#------------------------
K-feldspar
 -tol   1e-8
 -m0    0.328
 -parms 0.02 0.03
#------------------------
Plagioclase
 -tol   1e-8
 -m0    0.318
 -parms 0.002 0.03
```

```
#--------------------------
Smectite-low-Fe-Mg
 -tol   1e-8
 -m0    0.044
 -parms 51 0.03
#--------------------------
Clinoptilolite
 -tol    1e-8
 -m0     0.0103
 -parms  0.002 0.03
#--------------------------
Cristobalite(alpha)
 -tol   1e-8
 -m0    0.3616
 -parms 0.002 0.03
#-----------------------------------

-steps 0 21 42 63 84 105 126 147 168 189 210 231 252 273 294 315 336
357 378 399 420 441 462 483 504 525 546 567 588 609 630 651 672 693 714
735 756 777 795 hour  #+time step/2

-cvode                    false

INCREMENTAL_REACTIONS false

#------------------------------------------------------------------------
--------

RATES


Quartz

-start

1 kq = 10^-13.6

2 If (SI("Quartz")>= 0) then goto 31


3 PV = 0.08982   # Pore Volume...mL from expe

4 Por1 = 0.41

5 TV = PV/Por1     #mL....the volume is for cylindrical shape pipe

6 QMass1 = 57.31   #Quartz initial mass...g

7 Qden = 2650   #Quartz Density...g/L

8 QV1 = QMass1 / Qden    #Quartz initial Volume...L

9 QPor1 = GET_POR(1)

10 QMW = 60.08     #Quartz molar weight...g/Mol

11 Qmol1 = QMass1 / QMW    #Quartz initial moles...mole
```

```
12 A0_Q = parm(1) * (((1-GET(1000)) / (1-0.41))^2/3)  #Quartz initial
surface area m2/g

13 Qmass = (Qmass1 + GET(8))

14 rate_Q = (A0_Q/(parm(2)+ GET(1002))) *  Qmass *  ((m/m0)^0.67) *
(kq) * (1 - SR("Quartz"))

15 moles = rate_Q * time
#mole

16 PUT(Qmol1,1)
17 PUT(moles,2)


#calculate new porosity:


18  Dmol_Q = GET(2)            #Quartz Dissolve moles...moles

19  DmolMass_Q = -1 * (Dmol_Q * QMW)      #Quartz Dissolve moles
mass...g

20  QMV = QMW / Qden            #Quartz molar volume...L/mole

21  DmolVol_Q = -1 * (Dmol_Q * QMV)       #Quartz Dissolve moles
volume....L

22  QPor2 = -1 * (DmolVol_Q / (TV/1000))   #Quartz extra porosity

23  Q_New_Porosity = QPor1 + QPor2


24 PUT(DmolVol_Q,3)
25 PUT(QPor1,4)
26 PUT(QPor2,5)
27 PUT(Q_New_Porosity,6)
28 PUT(A0_Q,7)
29 PUT(DmolMass_Q,8)
30 PUT(Qmass,9)

31 save moles

-end
#--------------------------
Cristobalite(alpha)

-start

1 kCr = 10^-12.31

2 If (SI("Cristobalite(alpha)")>= 0) then goto 31

3 PV = 0.08982    # Pore Volume...mL from expe

4 Por1 = 0.41
```

```
5 TV = PV/Por1      #mL....the volume is for cylindrical shape pipe

6 CrMass1 = 21.727      #Cristobalite initial mass...g

7 Crden = 2330   #Cristobalite Density...g/L

8 CrV1 = CrMass1 / Crden    #Cristobalite initial Volume...L

9 CrPor1 = GET_POR(1)

10 CrMW = 60.08      #Cristobalite molar weight...g/Mol

11 Crmol1 = CrMass1 / CrMW     #Cristobalite initial moles...mole

12 A0_Cr = parm(1) * (((1-GET(1000)) / (1-0.41))^2/3)  #Cristobalite
initial surface area m2/g

13 Crmass = (Crmass1 + GET(80))

14 rate_Cr = (A0_Cr/(parm(2)+ GET(1002))) *  Crmass *  ((m/m0)^0.67) *
(kCr) * (1 - SR("Cristobalite(alpha)"))

15 moles = rate_Cr * time
#mole

16 PUT(Crmol1,10)
17 PUT(moles,20)


#calculate new porosity:


18  Dmol_Cr = GET(20)          #Cristobalite Dissolve moles...moles

19  DmolMass_Cr = -1 * (Dmol_Cr * CrMW)     #Cristobalite Dissolve
moles mass...g

20  CrMV = CrMW / Crden           #Cristobalite molar
volume...L/mole

21  DmolVol_Cr = -1 * (Dmol_Cr * CrMV)     #Cristobalite Dissolve
moles volume....L

22  CrPor2 = -1 * (DmolVol_Cr / (TV/1000))   #Cristobalite extra
porosity

23  Cr_New_Porosity = CrPor1 + CrPor2


24 PUT(DmolVol_Cr,30)
25 PUT(CrPor1,40)
26 PUT(CrPor2,50)
27 PUT(Cr_New_Porosity,60)
28 PUT(A0_Cr,70)
29 PUT(DmolMass_Cr,80)
30 PUT(Crmass,90)
```

```
31 save moles

-end
#--------------------------------------------------
K-feldspar

 -start

1 PV = 0.08982    # Pore Volume...mL from expe

2 Por1 = 0.41

3 TV = PV/Por1     #mL....the volume is for cylindrical shape pipe


        # find activities of inhibiting ions...

 4 a_Al = act("Al+3")
 5 BC = act("Na+") + act("K+") + act("Mg+2") + act("Ca+2")

        # temp corrected with the Arrhenius eqn, Table 8.8
        # the difference in temperature, TK gives solution temp in
Kelvin...

 10 dif_T = 1/TK - 1/281

                  # rate by H+...
 20 pk_H = 11.7 + 3500 * dif_T
 22 rate_H = 10^-pk_H * act("H+")^0.5 / ((1 + a_Al / 4e-6)^0.4 * (1 +
BC / 5e-4)^0.15)

                  # rate by hydrolysis...
 30 pk_w = 14.5 + 2000 * dif_T
 32 rate_w = 10^-pk_w / ((1 + a_Al / 4e-6)^0.14 * (1 + BC / 5e-4)^0.15)

                  # rate by OH-...
 40 pk_OH = 13.1 + 2500 * dif_T
 42 rate_OH = 10^-pk_OH * act("OH-")^0.3

                  # rate by CO2...
 50 pk_CO2 = 13.0 + 2000 * dif_T
 52 rate_CO2 = 10^-pk_CO2 * (10^SI("CO2(g)"))^0.6

                  # Sum the rate contributions...
60 kkf = rate_H + rate_w + rate_OH + rate_CO2

61 PUT(kkf,88)

62 If (SI("K-feldspar")>= 0) then goto 320


70  KfMass1 = 91.40   #Kfeldspar initial mass...g

80  Kfden = 2560   #Kfeldspar Density...g/L

90  KfV1 = KfMass1 / Kfden    #Kfeldspar initial Volume...L
```

```
100 KfPor1 = GET_POR(1)

110 KfMW = 278.33       #Kfeldspar molar weight...g/Mol

120 Kfmol1 = KfMass1 / KfMW      #Kfeldspar initial moles...mole

130 A0_Kf = parm(1) * (((1-GET(1000)) / (1-0.41))^2/3)   #Kfeldspar
initial surface area m2/g

140 Kfmass = (Kfmass1 + GET(800))

150 rate_Kf = (kkf) * (A0_Kf/(parm(2)+ GET(1002))) * Kfmass *
((m/m0)^0.67) * (1 - SR("K-feldspar"))

160 moles = rate_Kf * time

170 PUT(Kfmol1,100)
180 PUT(moles,200)

#calculate new porosity:


190  Dmol_Kf = GET(200)            #Kfeldspar Dissolve moles...moles

200  DmolMass_Kf = -1 *(Dmol_Kf * KfMW)      #Kfeldspar Dissolve moles
mass...g

210  KfMV = KfMW / Kfden              #Kfeldspar molar volume...L/mole

220  DmolVol_Kf = -1 *(Dmol_Kf * KfMV)       #Kfeldspar Dissolve moles
volume....L

230  KfPor2 = -1 *(DmolVol_Kf / (TV/1000))   #Kfeldspar extra
porosity....the (-) here is just to correct the (-) from the dissolve
mole volume equation.

240  Kf_New_Porosity = KfPor1 + KfPor2



250 PUT(DmolVol_Kf,300)
260 PUT(KfPor1,400)
270 PUT(KfPor2,500)
280 PUT(Kf_New_Porosity,600)
290 PUT(A0_Kf,700)
300 PUT(DmolMass_Kf,800)
310 PUT(Kfmass,900)

320 save moles

-end
#----------------------------------------------------------
Clinoptilolite

-start
```

```
1 kCl = 10^-29.899

2 If (SI("Clinoptilolite")>= 0) then goto 31


3 PV = 0.08982    # Pore Volume...mL from expe

4 Por1 = 0.41

5 TV = PV/Por1    #mL....the volume is for cylindrical shape pipe

6 ClMass1 = 28.47   #Clinoptilolite  initial mass...g

7 Clden = 2150   #Clinoptilolite  Density...g/L

8 ClV1 = ClMass1 / Clden    #Clinoptilolite  initial Volume...L

9 ClPor1 = GET_POR(1)

10 ClMW = 2742.13     #Clinoptilolite  molar weight...g/Mol

11 Clmol1 = ClMass1 / ClMW     #Clinoptilolite  initial moles...mole

12 A0_Cl = parm(1) * (((1-GET(1000)) / (1-0.41))^2/3)  #Clinoptilolite
initial surface area m2/g

13 Clmass = (Clmass1 + GET(80000))

14 rate_Cl = (A0_Cl/(parm(2)+ GET(1002))) *  Clmass *  ((m/m0)^0.67) *
(kCl) *  (1 - SR("Clinoptilolite"))

15 moles = rate_Cl * time
#mole

16 PUT(Clmol1,10000)
17 PUT(moles,20000)


#calculate new porosity:


18  Dmol_Cl = GET(20000)            #Clinoptilolite  Dissolve
moles...moles

19  DmolMass_Cl = -1 * (Dmol_Cl * ClMW)     #Clinoptilolite  Dissolve
moles mass...g

20  ClMV = ClMW / Clden             #Clinoptilolite  molar
volume...L/mole

21  DmolVol_Cl = -1 * (Dmol_Cl * ClMV)      #Clinoptilolite  Dissolve
moles volume....L

22  ClPor2 = -1 * (DmolVol_Cl / (TV/1000))   #Clinoptilolite  extra
porosity

23  Cl_New_Porosity = ClPor1 + ClPor2
```

```
24 PUT(DmolVol_Cl,30000)
25 PUT(ClPor1,40000)
26 PUT(ClPor2,50000)
27 PUT(Cl_New_Porosity,60000)
28 PUT(A0_Cl,70000)
29 PUT(DmolMass_Cl,80000)
30 PUT(Clmass,90000)

31 save moles

-end
#------------------------------------------------------------------------
--------
Plagioclase

-start

1 kP = 10^-15.6

2 If (SI("Plagioclase")>= 0) then goto 31

3 PV = 0.08982    # Pore Volume...mL from expe

4 Por1 = 0.41

5 TV = PV/Por1     #mL....the volume is for cylindrical shape pipe

6 PMass1 = 86.16   #Plagioclase  initial mass...g

7 Pden = 2680   #Plagioclase  Density...g/L

8 PV1 = PMass1 / Pden    #Plagioclase  initial Volume...L

9 PPor1 = GET_POR(1)

10 PMW = 270.77    #Plagioclase  molar weight...g/Mol

11 Pmol1 = PMass1 / PMW     #Plagioclase  initial moles...mole

12 A0_P = parm(1) * (((1-GET(1000)) / (1-0.41))^2/3)  #Plagioclase
initial surface area m2/g

13 Pmass = (Pmass1 + GET(800000))

14 rate_P = (A0_P/(parm(2)+ GET(1002))) *  Pmass *  ((m/m0)^0.67) *
(kP) * (1 - SR("Plagioclase"))

15 moles = rate_P * time
#mole

16 PUT(Pmol1,100000)
17 PUT(moles,200000)


#calculate new porosity:
```

360

```
18  Dmol_P = GET(200000)            #Plagioclase  Dissolve
moles...moles

19  DmolMass_P = -1 * (Dmol_P * PMW)     #Plagioclase  Dissolve moles
mass...g

20  PMV = PMW / Pden             #Plagioclase  molar volume...L/mole

21  DmolVol_P = -1 * (Dmol_P * PMV)      #Plagioclase  Dissolve moles
volume....L

22  PPor2 = -1 * (DmolVol_P / (TV/1000))   #Plagioclase  extra porosity

23  P_New_Porosity = PPor1 + PPor2


24 PUT(DmolVol_P,300000)
25 PUT(PPor1,400000)
26 PUT(PPor2,500000)
27 PUT(P_New_Porosity,600000)
28 PUT(A0_P,700000)
29 PUT(DmolMass_P,800000)
30 PUT(Pmass,900000)

31 save moles

 -end

#-------------------------------------------------------------------
Smectite-low-Fe-Mg

-start

1 kSm = 10^-18.08

2 If (SI("Smectite-low-Fe-Mg")>= 0) then goto 40


3 PV = 0.08982    # Pore Volume...mL from expe

4 Por1 = 0.41

5 TV = PV/Por1     #mL....the volume is for cylindrical shape pipe

6 SmMass1 = 17.23   #Smectite initial mass...g

7 Smden = 2680   #Smectite Density...g/L

8 SmV1 = SmMass1 / Smden    #Smectite initial Volume...L

9 SmPor1 = GET_POR(1)

10 SmMW = 389.34     #Smectite molar weight...g/Mol

11 Smmol1 = SmMass1 / SmMW     #Smectite initial moles...mole
```

```
12 A0_Sm = parm(1) * (((1-GET(1000)) / (1-0.41))^2/3)   #Smectite
initial surface area m2/g

13 Smmass = (Smmass1 + GET(8000000))

14 rate_Sm = (A0_Sm/(parm(2)+ GET(1002))) *  Smmass *  ((m/m0)^0.67) *
(kSm) * (1 - SR("Smectite-low-Fe-Mg"))

15 moles = rate_Sm * time
#mole

16 PUT(Smmol1,1000000)
17 PUT(moles,2000000)


#calculate new porosity:


18  Dmol_Sm = GET(2000000)              #Smectite Dissolve moles...moles

19  DmolMass_Sm = -1 * (Dmol_Sm * SmMW)      #Smectite Dissolve moles
mass...g

20  SmMV = SmMW / Smden               #Smectite molar volume...L/mole

21  DmolVol_Sm = -1 * (Dmol_Sm * SmMV)       #Smectite Dissolve moles
volume....L

22  SmPor2 = -1 * (DmolVol_Sm / (TV/1000))    #Smectite extra porosity

23  Sm_New_Porosity = SmPor1 + SmPor2


24 PUT(DmolVol_Sm,3000000)
25 PUT(SmPor1,4000000)
26 PUT(SmPor2,5000000)
27 PUT(Sm_New_Porosity,6000000)
28 PUT(A0_Sm,7000000)
29 PUT(DmolMass_Sm,8000000)
30 PUT(Smmass,9000000)


#----------------------------

31 New_Total_V = -1 * (GET(3) + GET(30) + GET(300)+ GET(30000)+
GET(300000)+ GET(3000000))

32 PUT(New_Total_V,1002)

33 Porosity_2 = GET(5) + GET(50) + GET(500) + GET(50000) + GET(500000)
+ GET(5000000)

34 PUT(Porosity_2,1001)

35 New_Porosity = GET_POR(1) + GET(1001)
```

```
36 PUT(New_Porosity,1000)

37 CHANGE_POR(New_Porosity,1)

40 save moles

 -end
#----------------------------------------------------------------------

use solution 0


 TRANSPORT

        -cells               10
        -shifts              9
        -time_step           95 hour
        -flow_direction      forward
        -boundary_conditions flux flux
        -lengths             10*0.045
        -dispersivity        10*0.04
        -correct_disp        true
        -diffusion_coef      0.3e-9
        -initial_time        0
        -punch_cells         10
        -punch_frequency     1
        -multi_D             true
        -porosities          0.41




SELECTED_OUTPUT

 USER_PUNCH

     -headings Time Ca Na K Si CO3 Cl(-1) Mg Al U NO3 Hto UO2(CO3)2-
2_sorption UO2(OH)2_sorption Q1 Q2 Q3 Q4 Q5 Q6 Q7 Q8 Q9 Cr1 Cr2 Cr3 Cr4
Cr5 Cr6 Cr7 Cr8 Cr9 Kf1 Kf2 Kf3 Kf4 Kf5 Kf6 Kf7 Kf8 Kf9 Cl1 Cl2 Cl3 Cl4
Cl5 Cl6 Cl7 Cl8 Cl9 P1 P2 P3 P4 P5 P6 P7 P8 P9 S1 S2 S3 S4 S5 S6 S7 S8
S9 Porosity_T Porosity_2 Volume_2 calcite CaUO4 CSHgel haiweeite
kaolinite laumontite muscovite saponite-Ca sepiolite thaumasite
tobermorite-14A UO2(CO3)3-4 UO2(CO3)2-2 UO2(OH)3- UO2(OH)2 UO2CO3 UO2X2
Surf_alOUO2+ Surf_alO(UO2)3(OH)5 Surf_siOUO2+ Surf_siO(UO2)3(OH)5
Surf_kalOUO2OH Surf_feOUO2+ Uranophane Becquerelite Rutherfordine
Quartz K-feldspar Smectite-low-Fe-Mg Clinoptilolite Cristobalite(alpha)
Plagioclase
-start

010 PUNCH TOTAL_TIME/(60)
020 PUNCH tot("Ca")*40*1000
030 PUNCH tot("Na")*23*1000
040 PUNCH tot("K")*39.1*1000
050 PUNCH tot("Si")*28.09*1000
060 PUNCH tot("C(4)")*60*1000
070 PUNCH tot("Cl(-1)")*35.45*1000
080 PUNCH tot("Mg")*24.3*1000
```

```
090 PUNCH tot("Al")*27*1000
100 PUNCH tot("U(6)")*270*1000
110 PUNCH tot("N(5)")*62*1000
120 PUNCH tot("Hto")*22.03*1000
130 PUNCH KIN("UO2(CO3)2-2_sorption")*1000*238/3570
140 PUNCH KIN("UO2(OH)2_sorption")*1000*238/3570
150 PUNCH  GET(1)
160 PUNCH  GET(2)
170 PUNCH  GET(3)
180 PUNCH  GET(4)
190 PUNCH  GET(5)
200 PUNCH  GET(6)
210 PUNCH  GET(7)
220 PUNCH  GET(8)
230 PUNCH  GET(9)
240 PUNCH  GET(10)
250 PUNCH  GET(20)
260 PUNCH  GET(30)
270 PUNCH  GET(40)
280 PUNCH  GET(50)
290 PUNCH  GET(60)
300 PUNCH  GET(70)
310 PUNCH  GET(80)
320 PUNCH  GET(90)
330 PUNCH  GET(100)
340 PUNCH  GET(200)
350 PUNCH  GET(300)
360 PUNCH  GET(400)
370 PUNCH  GET(500)
380 PUNCH  GET(600)
390 PUNCH  GET(700)
400 PUNCH  GET(800)
410 PUNCH  GET(900)
420 PUNCH  GET(10000)
430 PUNCH  GET(20000)
450 PUNCH  GET(30000)
460 PUNCH  GET(40000)
470 PUNCH  GET(50000)
480 PUNCH  GET(60000)
490 PUNCH  GET(70000)
500 PUNCH  GET(80000)
510 PUNCH  GET(90000)
530 PUNCH  GET(100000)
540 PUNCH  GET(200000)
550 PUNCH  GET(300000)
560 PUNCH  GET(400000)
570 PUNCH  GET(500000)
580 PUNCH  GET(600000)
590 PUNCH  GET(700000)
600 PUNCH  GET(800000)
610 PUNCH  GET(900000)
630 PUNCH  GET(1000000)
640 PUNCH  GET(2000000)
650 PUNCH  GET(3000000)
660 PUNCH  GET(4000000)
670 PUNCH  GET(5000000)
680 PUNCH  GET(6000000)
```

```
 690 PUNCH   GET(7000000)
 700 PUNCH   GET(8000000)
 710 PUNCH   GET(9000000)
 720 PUNCH   GET(1000)
 730 PUNCH   GET(1001)
 740 PUNCH   GET(1002)
 750 PUNCH   SI("Calcite")
 760 PUNCH   SI("CaUO4")
 770 PUNCH   SI("CSHgel")
 780 PUNCH   SI("Haiweeite")
 790 PUNCH   SI("Kaolinite")
 800 PUNCH   SI("Laumontite")
 810 PUNCH   SI("Muscovite")
 820 PUNCH   SI("Saponite-Ca")
 830 PUNCH   SI("Sepiolite")
 840 PUNCH   SI("Thaumasite")
 850 PUNCH   SI("Tobermorite-14A")
 860 PUNCH   MOL("UO2(CO3)3-4")
 870 PUNCH   MOL("UO2(CO3)2-2")
 880 PUNCH   MOL("UO2(OH)3-")
 890 PUNCH   MOL("UO2(OH)2")
 900 PUNCH   MOL("UO2CO3")
 910 PUNCH   MOL("UO2X2")
 920 PUNCH   MOL("Surf_alOUO2+")
 930 PUNCH   MOL("Surf_alO(UO2)3(OH)5")
 940 PUNCH   MOL("Surf_siOUO2+")
 950 PUNCH   MOL("Surf_siO(UO2)3(OH)5")
 960 PUNCH   MOL("Surf_kalOUO2OH")
 970 PUNCH   MOL("Surf_feOUO2+")
 980 PUNCH   SI("Uranophane")
 990 PUNCH   SI("Becquerelite")
1000 PUNCH   SI("Rutherfordine")
1010 PUNCH   SI("Quartz")
1020 PUNCH   SI("K-feldspar")
1030 PUNCH   SI("Smectite-low-Fe-Mg")
1040 PUNCH   SI("Clinoptilolite")
1050 PUNCH   SI("Cristobalite(alpha)")
1060 PUNCH   SI("Plagioclase")


End
```

4.1.2. Column 2

```
#Yucca Mountain_uranium desorption_10SA (Column 2)

#-----------------------------------------------------------------------
---

SOLUTION_MASTER_SPECIES
# element    species    alk gfw_formula element_gfw
  Hto        Hto        0.0   20           20

SOLUTION_SPECIES
  Hto = Hto;        log_k 0; -gamma 1e6 0;      -dw 1e-13


#-----------------------------------------------------------------------
---


SOLUTION 0
    temp      25
    pH        7.78
    pe        4
    redox     pe
    units     mg/l
    density   1
    C(4)      100
    Ca        13
    Cl(-1)    6.9
    Hto       1e-10
    K         5.2
    Mg        2.5
    N(5)      1.524
    Na        43
    S(6)      14
    U(5)      0.24
    -water    1 # kg

save solution 0

end

SOLUTION 1-10
    temp      25
    pH        7.78
    pe        4
    redox     pe
    units     mg/l
    density   1
    C(4)      100
    Ca        13
    Cl(-1)    6.9
    K         5.2
    Mg        2.5
    N(5)      1.4
    Na        43
    S(6)      14
```

```
      -water    1 # kg


EQUILIBRIUM_PHASES 1-10
CO2(g) -3.5 10

Quartz 0 0                      #SiO2
Plagioclase 0 0                  #NaAlSi3O8 - CaAl2Si2O8
k-feldspar 0 0                   #KAlSi3O8
Clinoptilolite 0 0.22          #(Na,K,Ca) 2-3Al 3(Al,Si) 2Si 13O 36•12H 2O
Cristobalite(alpha) 0 0        #SiO2
Smectite-high-Fe-Mg 0 0        ##CaNaKFeMgAlSi3

kaolinite 0 0                    #Al2Si2O5(OH)4
Tridymite 0 0                    #SiO2
Hematite 0 0                     #Fe2O3
Muscovite 0 0                    #Mica--KAl2(AlSi3O10)(F,OH)2


#opal-CT-----SiO2



CaUO4 0 0
Uranophane 0 0          #Ca(UO2)2(SiO3)2(OH)2
Becquerelite 0 0        #Ca(UO2)6O4(OH)6:8H2O
Rutherfordine 0 0       #UO2CO3


#--------------------------------------------------------------------
-------
EXCHANGE_SPECIES


UO2+2 + 2NaX = UO2X2 + 2Na+
log_k   0.45

UO2+2 + CaX2 = UO2X2 + Ca+2
log_k   0.049


EXCHANGE 1-10
        -equilibrate 1-10
        X                0.023


#CEC for smectite is 810 meq/kg.....for 28.5 g smectite, then CEC
equals to 23 meq

#-----------------------------------------------

SURFACE_MASTER_SPECIES

        Surf_al    Surf_alOH        #Smectite aluminol surface edge
        Surf_si    Surf_siOH        #Smectite silonal surface edge
        Surf_kal   Surf_kalOH       #Kaolinite aluminol surface edge
        Surf_fe    Surf_feOH        #Hematite aluminol surface edge


SURFACE_SPECIES
```

```
      Surf_alOH = Surf_alOH
            log_k   0.0

      Surf_alOH + H+ = Surf_alOH2+
            log_k   12.3

       Surf_alOH = Surf_alO- + H+
            log_k   -13.6

       Surf_alOH + UO2+2  = Surf_alOUO2+ + H+
            log_k   7.7

#----------------------------------------------------------------------
------------------------

      Surf_siOH = Surf_siOH
            log_k   0.0

      Surf_siOH + H+ = Surf_siOH2+
            log_k   -0.95

       Surf_siOH = Surf_siO- + H+
            log_k   -6.95

       Surf_siOH + UO2+2  = Surf_siOUO2+ + H+
            log_k   0.75

#----------------------------------------------------------------------
-----------

      Surf_kalOH = Surf_kalOH
            log_k   0.0

      Surf_kalOH + H+ = Surf_kalOH2+
            log_k   13.33

       Surf_kalOH = Surf_kalO- + H+
            log_k   -4.72

       Surf_kalOH + UO2+2 + H2O  = Surf_kalOUO2OH + 2H+
            log_k   6

#----------------------------------------------------------------------
-----
      Surf_feOH = Surf_feOH
            log_k   0.0

      Surf_feOH + H+ = Surf_feOH2+
            log_k   -5.1

      Surf_feOH = Surf_feO- + H+
            log_k   -10.7

       Surf_feOH + UO2+2  = Surf_feOUO2+ + H+
            log_k   14.11
```

```
#----------------------------------------------------------------------
-----


SURFACE 1
        -equil solution 1-10
        -sites_units          density
        -donnan 1e-10

        Surf_alOH         2.3 51 28.5 Dw 1e-13    #number of sites
density(per nm2)-surrace area (m2/g)-mass (g)
        Surf_siOH         2.3 51 28.5 Dw 1e-13    #number of sites
density(per nm2)-surrace area (m2/g)-mass (g)
        Surf_kalOH        2.3 20 1.42 Dw 1e-13    #number of sites
density(per nm2)-surrace area (m2/g)-mass (g)
        Surf_feOH         2.3 10 1.78 Dw 1e-13    #number of sites
density(per nm2)-surrace area (m2/g)-mass (g)


#------------------------------------------------------------------------
--------
#for 356.6g of rock sample we have the following:
#30.6% Orthoclase = 109.12 g = 0.392 mol      #278.33
#8.7% Quartz = 31.02 g = 0.51 mol             #60.08
#26% Plagioclase = 92.7 g = 0.342 mol           #270.77
#11.6% Clinoptilolite = 41.36 g = 0.015 mol   #2,742.13
#8.1% Cristobalite(alpha) = 28.88 g = 0.48 mol #60.08
#8% Smectite-low-Fe-Mg = 28.5 g = 0.073 mol  #389.34
#0.4% kaolinite = 1.42 g
#0.5% Hematite = 1.78 g
#------------------------------------------------------------------------
--------

KINETICS 1-10

Quartz
 -tol   1e-8
 -m0    0.51
 -parms 0.02 0.03
#-------------------------
K-feldspar
 -tol   1e-8
 -m0     0.392
 -parms  0.02 0.03
#-------------------------
Plagioclase
 -tol   1e-8
 -m0     0.342
 -parms  0.002 0.03
#-------------------------
Smectite-low-Fe-Mg
 -tol   1e-8
 -m0    0.073
 -parms 51 0.03
#-------------------------
Clinoptilolite
 -tol   1e-8
```

```
 -m0      0.015
 -parms  0.002 0.03
#-------------------------
Cristobalite(alpha)
 -tol   1e-8
 -m0     0.48
 -parms 0.002 0.03
#-----------------------------------

-steps 0 21 42 63 84 105 126 147 168 189 210 231 252 273 294 315 336
357 378 399 420 441 462 483 504 525 546 567 588 609 630 651 672 693 714
735 756 777 795 hour  #+time step/2

-cvode                    false

INCREMENTAL_REACTIONS false

#----------------------------------------------------------------------
--------

RATES

Quartz

-start

1 kq = 10^-13.6

2 If (SI("Quartz")>= 0) then goto 31


3 PV = 0.1024     # Pore Volume...mL from expe

4 Por1 = 0.44

5 TV = PV/Por1      #mL....the volume is for cylindrical shape pipe

6 QMass1 = 31.02   #Quartz initial mass...g

7 Qden = 2650    #Quartz Density...g/L

8 QV1 = QMass1 / Qden     #Quartz initial Volume...L

9 QPor1 = GET_POR(1)

10 QMW = 60.08       #Quartz molar weight...g/Mol

11 Qmol1 = QMass1 / QMW     #Quartz initial moles...mole

12 A0_Q = parm(1) * (((1-GET(1000)) / (1-0.44))^2/3)  #Quartz initial
surface area m2/g

13 Qmass = (Qmass1 + GET(8))

14 rate_Q = (A0_Q/(parm(2)+ GET(1002))) *  Qmass *  ((m/m0)^0.67) *
(kq) * (1 - SR("Quartz"))
```

```
15 moles = rate_Q * time
#mole

16 PUT(Qmol1,1)
17 PUT(moles,2)


#calculate new porosity:


18  Dmol_Q = GET(2)              #Quartz Dissolve moles...moles

19  DmolMass_Q = -1 * (Dmol_Q * QMW)      #Quartz Dissolve moles
mass...g

20  QMV = QMW / Qden              #Quartz molar volume...L/mole

21  DmolVol_Q = -1 * (Dmol_Q * QMV)      #Quartz Dissolve moles
volume....L

22  QPor2 = -1 * (DmolVol_Q / (TV/1000))   #Quartz extra porosity

23  Q_New_Porosity = QPor1 + QPor2


24 PUT(DmolVol_Q,3)
25 PUT(QPor1,4)
26 PUT(QPor2,5)
27 PUT(Q_New_Porosity,6)
28 PUT(A0_Q,7)
29 PUT(DmolMass_Q,8)
30 PUT(Qmass,9)

31 save moles

-end
#----------------------------
Cristobalite(alpha)

-start

1 kCr = 10^-12.31

2 If (SI("Cristobalite(alpha)")>= 0) then goto 31

3 PV = 0.1024    # Pore Volume...mL from expe

4 Por1 = 0.44

5 TV = PV/Por1     #mL....the volume is for cylindrical shape pipe

6 CrMass1 = 28.88     #Cristobalite initial mass...g

7 Crden = 2330   #Cristobalite Density...g/L

8 CrV1 = CrMass1 / Crden    #Cristobalite initial Volume...L
```

```
9 CrPor1 = GET_POR(1)

10 CrMW = 60.08      #Cristobalite molar weight...g/Mol

11 Crmol1 = CrMass1 / CrMW     #Cristobalite initial moles...mole

12 A0_Cr = parm(1) * (((1-GET(1000)) / (1-0.44))^2/3)  #Cristobalite
initial surface area m2/g

13 Crmass = (Crmass1 + GET(80))

14 rate_Cr = (A0_Cr/(parm(2)+ GET(1002))) *  Crmass *  ((m/m0)^0.67) *
(kCr) * (1 - SR("Cristobalite(alpha)"))

15 moles = rate_Cr * time
#mole

16 PUT(Crmol1,10)
17 PUT(moles,20)


#calculate new porosity:


18  Dmol_Cr = GET(20)           #Cristobalite Dissolve moles...moles

19  DmolMass_Cr = -1 * (Dmol_Cr * CrMW)     #Cristobalite Dissolve
moles mass...g

20  CrMV = CrMW / Crden            #Cristobalite molar
volume...L/mole

21  DmolVol_Cr = -1 * (Dmol_Cr * CrMV)      #Cristobalite Dissolve
moles volume....L

22  CrPor2 = -1 * (DmolVol_Cr / (TV/1000))   #Cristobalite extra
porosity

23  Cr_New_Porosity = CrPor1 + CrPor2


24 PUT(DmolVol_Cr,30)
25 PUT(CrPor1,40)
26 PUT(CrPor2,50)
27 PUT(Cr_New_Porosity,60)
28 PUT(A0_Cr,70)
29 PUT(DmolMass_Cr,80)
30 PUT(Crmass,90)

31 save moles

-end
#------------------------------------------------
K-feldspar

 -start
```

```
1 PV = 0.1024    # Pore Volume...mL from expe

2 Por1 = 0.44

3 TV = PV/Por1    #mL....the volume is for cylindrical shape pipe


        # find activities of inhibiting ions...

 4 a_Al = act("Al+3")
 5 BC = act("Na+") + act("K+") + act("Mg+2") + act("Ca+2")

        # temp corrected with the Arrhenius eqn, Table 8.8
        # the difference in temperature, TK gives solution temp in
Kelvin...

 10 dif_T = 1/TK - 1/281

                    # rate by H+...
 20 pk_H = 11.7 + 3500 * dif_T
 22 rate_H = 10^-pk_H * act("H+")^0.5 / ((1 + a_Al / 4e-6)^0.4 * (1 +
BC / 5e-4)^0.15)


                    # rate by hydrolysis...
 30 pk_w = 14.5 + 2000 * dif_T
 32 rate_w = 10^-pk_w / ((1 + a_Al / 4e-6)^0.14 * (1 + BC / 5e-4)^0.15)


                    # rate by OH-...
 40 pk_OH = 13.1 + 2500 * dif_T
 42 rate_OH = 10^-pk_OH * act("OH-")^0.3


                    # rate by CO2...
 50 pk_CO2 = 13.0 + 2000 * dif_T
 52 rate_CO2 = 10^-pk_CO2 * (10^SI("CO2(g)"))^0.6


                    # Sum the rate contributions...
60 kkf = rate_H + rate_w + rate_OH + rate_CO2

61 If (SI("K-feldspar")>= 0) then goto 320


70  KfMass1 = 109.12   #Kfeldspar initial mass...g

80  Kfden = 2560   #Kfeldspar Density...g/L

90  KfV1 = KfMass1 / Kfden    #Kfeldspar initial Volume...L

100 KfPor1 = GET_POR(1)

110 KfMW = 278.33      #Kfeldspar molar weight...g/Mol

120 Kfmol1 = KfMass1 / KfMW      #Kfeldspar initial moles...mole

130 A0_Kf = parm(1) * (((1-GET(1000)) / (1-0.44))^2/3)   #Kfeldspar
initial surface area m2/g

140 Kfmass = (Kfmass1 + GET(800))
```

```
150 rate_Kf = (kkf) * (A0_Kf/(parm(2)+ GET(1002))) * Kfmass *
((m/m0)^0.67) * (1 - SR("K-feldspar"))

160 moles = rate_Kf * time

170 PUT(Kfmol1,100)
180 PUT(moles,200)

#calculate new porosity:


190  Dmol_Kf = GET(200)            #Kfeldspar Dissolve moles...moles

200  DmolMass_Kf = -1 *(Dmol_Kf * KfMW)     #Kfeldspar Dissolve moles
mass...g

210  KfMV = KfMW / Kfden              #Kfeldspar molar volume...L/mole

220  DmolVol_Kf = -1 *(Dmol_Kf * KfMV)     #Kfeldspar Dissolve moles
volume....L

230  KfPor2 = -1 *(DmolVol_Kf / (TV/1000))   #Kfeldspar extra
porosity....the (-) here is just to correct the (-) from the dissolve
mole volume equation.

240  Kf_New_Porosity = KfPor1 + KfPor2



250 PUT(DmolVol_Kf,300)
260 PUT(KfPor1,400)
270 PUT(KfPor2,500)
280 PUT(Kf_New_Porosity,600)
290 PUT(A0_Kf,700)
300 PUT(DmolMass_Kf,800)
310 PUT(Kfmass,900)

320 save moles

-end
#------------------------------------------------------------
Clinoptilolite

-start

1 kCl = 10^-29.899

2 If (SI("Clinoptilolite")>= 0) then goto 31


3 PV = 0.1024    # Pore Volume...mL from expe

4 Por1 = 0.44

5 TV = PV/Por1     #mL....the volume is for cylindrical shape pipe
```

```
6 ClMass1 = 41.36   #Clinoptilolite  initial mass...g

7 Clden = 2150   #Clinoptilolite  Density...g/L

8 ClV1 = ClMass1 / Clden    #Clinoptilolite  initial Volume...L

9 ClPor1 = GET_POR(1)

10 ClMW = 2742.13    #Clinoptilolite  molar weight...g/Mol

11 Clmol1 = ClMass1 / ClMW    #Clinoptilolite  initial moles...mole

12 A0_Cl = parm(1) * (((1-GET(1000)) / (1-0.44))^2/3)  #Clinoptilolite
initial surface area m2/g

13 Clmass = (Clmass1 + GET(80000))

14 rate_Cl = (A0_Cl/(parm(2)+ GET(1002))) * Clmass *  ((m/m0)^0.67) *
(kCl) * (1 - SR("Clinoptilolite"))

15 moles = rate_Cl * time
#mole

16 PUT(Clmol1,10000)
17 PUT(moles,20000)


#calculate new porosity:


18  Dmol_Cl = GET(20000)          #Clinoptilolite  Dissolve
moles...moles

19  DmolMass_Cl = -1 * (Dmol_Cl * ClMW)     #Clinoptilolite  Dissolve
moles mass...g

20  ClMV = ClMW / Clden           #Clinoptilolite  molar
volume...L/mole

21  DmolVol_Cl = -1 * (Dmol_Cl * ClMV)      #Clinoptilolite  Dissolve
moles volume....L

22  ClPor2 = -1 * (DmolVol_Cl / (TV/1000))   #Clinoptilolite  extra
porosity

23  Cl_New_Porosity = ClPor1 + ClPor2


24 PUT(DmolVol_Cl,30000)
25 PUT(ClPor1,40000)
26 PUT(ClPor2,50000)
27 PUT(Cl_New_Porosity,60000)
28 PUT(A0_Cl,70000)
29 PUT(DmolMass_Cl,80000)
30 PUT(Clmass,90000)

31 save moles
```

375

```
-end
#--------------------------------------------------------------------
--------
Plagioclase

-start

1 kP = 10^-15.6

#2 If (SI("Plagioclase")>= 0) then goto 31

3 PV = 0.1024     # Pore Volume...mL from expe

4 Por1 = 0.44

5 TV = PV/Por1     #mL....the volume is for cylindrical shape pipe

6 PMass1 = 92.7   #Plagioclase  initial mass...g

7 Pden = 2680   #Plagioclase  Density...g/L

8 PV1 = PMass1 / Pden    #Plagioclase  initial Volume...L

9 PPor1 = GET_POR(1)

10 PMW = 270.77    #Plagioclase  molar weight...g/Mol

11 Pmol1 = PMass1 / PMW     #Plagioclase  initial moles...mole

12 A0_P = parm(1) * (((1-GET(1000)) / (1-0.44))^2/3)  #Plagioclase
initial surface area m2/g

13 Pmass = (Pmass1 + GET(800000))

14 rate_P = (A0_P/(parm(2)+ GET(1002))) *  Pmass *  ((m/m0)^0.67) *
(kP) * (1 - SR("Plagioclase"))

15 moles = rate_P * time
#mole

16 PUT(Pmol1,100000)
17 PUT(moles,200000)


#calculate new porosity:


18  Dmol_P = GET(200000)          #Plagioclase  Dissolve
moles...moles

19  DmolMass_P = -1 * (Dmol_P * PMW)     #Plagioclase  Dissolve moles
mass...g

20  PMV = PMW / Pden             #Plagioclase  molar volume...L/mole
```

```
21  DmolVol_P = -1 * (Dmol_P * PMV)        #Plagioclase  Dissolve moles
volume....L

22  PPor2 = -1 * (DmolVol_P / (TV/1000))    #Plagioclase  extra porosity

23  P_New_Porosity = PPor1 + PPor2


24 PUT(DmolVol_P,300000)
25 PUT(PPor1,400000)
26 PUT(PPor2,500000)
27 PUT(P_New_Porosity,600000)
28 PUT(A0_P,700000)
29 PUT(DmolMass_P,800000)
30 PUT(Pmass,900000)

31 save moles

 -end

#-------------------------------------------------------------------
Smectite-low-Fe-Mg

-start

1 kSm = 10^-18.08

2 If (SI("Smectite-low-Fe-Mg")>= 0) then goto 40


3 PV = 0.1024     # Pore Volume...mL from expe

4 Por1 = 0.44

5 TV = PV/Por1     #mL....the volume is for cylindrical shape pipe

6 SmMass1 = 28.5   #Smectite initial mass...g

7 Smden = 2680   #Smectite Density...g/L

8 SmV1 = SmMass1 / Smden    #Smectite initial Volume...L

9 SmPor1 = GET_POR(1)

10 SmMW = 389.34     #Smectite molar weight...g/Mol

11 Smmol1 = SmMass1 / SmMW     #Smectite initial moles...mole

12 A0_Sm = parm(1) * (((1-GET(1000)) / (1-0.44))^2/3)  #Smectite
initial surface area m2/g

13 Smmass = (Smmass1 + GET(8000000))

14 rate_Sm = (A0_Sm/(parm(2)+ GET(1002))) *  Smmass *  ((m/m0)^0.67) *
(kSm) * (1 - SR("Smectite-low-Fe-Mg"))
```

```
15 moles = rate_Sm * time
#mole

16 PUT(Smmol1,1000000)
17 PUT(moles,2000000)


#calculate new porosity:


18  Dmol_Sm = GET(2000000)              #Smectite Dissolve moles...moles

19  DmolMass_Sm = -1 * (Dmol_Sm * SmMW)      #Smectite Dissolve moles
mass...g

20  SmMV = SmMW / Smden              #Smectite molar volume...L/mole

21  DmolVol_Sm = -1 * (Dmol_Sm * SmMV)      #Smectite Dissolve moles
volume....L

22  SmPor2 = -1 * (DmolVol_Sm / (TV/1000))   #Smectite extra porosity

23  Sm_New_Porosity = SmPor1 + SmPor2


24 PUT(DmolVol_Sm,3000000)
25 PUT(SmPor1,4000000)
26 PUT(SmPor2,5000000)
27 PUT(Sm_New_Porosity,6000000)
28 PUT(A0_Sm,7000000)
29 PUT(DmolMass_Sm,8000000)
30 PUT(Smmass,9000000)


#---------------------------

31 New_Total_V = -1 * (GET(3) + GET(30) + GET(300)+ GET(30000)+
GET(300000)+ GET(3000000))

32 PUT(New_Total_V,1002)

33 Porosity_2 = GET(5) + GET(50) + GET(500) + GET(50000) + GET(500000)
+ GET(5000000)

34 PUT(Porosity_2,1001)

35 New_Porosity = GET_POR(1) + GET(1001)

36 PUT(New_Porosity,1000)

37 CHANGE_POR(New_Porosity,1)

40 save moles

 -end
#----------------------------------------------------------------------
```

378

```
use solution 0

 TRANSPORT

        -cells               10
        -shifts              14
        -time_step           60 hour
        -flow_direction      forward
        -boundary_conditions flux flux
        -lengths             10*0.046
        -dispersivity        10*0.03
        -correct_disp        true
        -diffusion_coef      0.3e-9
        -initial_time        0
        -punch_cells         10
        -punch_frequency     1
        -multi_D             true
        -porosities          0.44




 SELECTED_OUTPUT

 USER_PUNCH

        -headings Time Ca Na K Si CO3 Cl(-1) Mg Al U NO3 Hto UO2(CO3)2-
2_sorption UO2(OH)2_sorption Q1 Q2 Q3 Q4 Q5 Q6 Q7 Q8 Q9 Cr1 Cr2 Cr3 Cr4
Cr5 Cr6 Cr7 Cr8 Cr9 Kf1 Kf2 Kf3 Kf4 Kf5 Kf6 Kf7 Kf8 Kf9 Cl1 Cl2 Cl3 Cl4
Cl5 Cl6 Cl7 Cl8 Cl9 P1 P2 P3 P4 P5 P6 P7 P8 P9 S1 S2 S3 S4 S5 S6 S7 S8
S9 Porosity_T Porosity_2 Volume_2 calcite CaUO4 CSHgel haiweeite
kaolinite laumontite muscovite saponite-Ca sepiolite thaumasite
tobermorite-14A UO2(CO3)3-4 UO2(CO3)2-2 UO2(OH)3- UO2(OH)2 UO2CO3 UO2X2
Surf_alOUO2+ Surf_alO(UO2)3(OH)5 Surf_siOUO2+ Surf_siO(UO2)3(OH)5
Surf_kalOUO2OH Surf_feOUO2+ Uranophane Becquerelite Rutherfordine
Quartz K-feldspar Smectite-low-Fe-Mg Clinoptilolite Cristobalite(alpha)
Plagioclase
-start

010 PUNCH TOTAL_TIME/(60)
020 PUNCH tot("Ca")*40*1000
030 PUNCH tot("Na")*23*1000
040 PUNCH tot("K")*39.1*1000
050 PUNCH tot("Si")*28.09*1000
060 PUNCH tot("C(4)")*60*1000
070 PUNCH tot("Cl(-1)")*35.45*1000
080 PUNCH tot("Mg")*24.3*1000
090 PUNCH tot("Al")*27*1000
100 PUNCH tot("U(6)")*270*1000
110 PUNCH tot("N(5)")*62*1000
120 PUNCH tot("Hto")*22.03*1000
130 PUNCH KIN("UO2(CO3)2-2_sorption")*1000*238/3570
140 PUNCH KIN("UO2(OH)2_sorption")*1000*238/3570
 150 PUNCH  GET(1)
 160 PUNCH  GET(2)
 170 PUNCH  GET(3)
 180 PUNCH  GET(4)
```

```
190 PUNCH   GET(5)
200 PUNCH   GET(6)
210 PUNCH   GET(7)
220 PUNCH   GET(8)
230 PUNCH   GET(9)
240 PUNCH   GET(10)
250 PUNCH   GET(20)
260 PUNCH   GET(30)
270 PUNCH   GET(40)
280 PUNCH   GET(50)
290 PUNCH   GET(60)
300 PUNCH   GET(70)
310 PUNCH   GET(80)
320 PUNCH   GET(90)
330 PUNCH   GET(100)
340 PUNCH   GET(200)
350 PUNCH   GET(300)
360 PUNCH   GET(400)
370 PUNCH   GET(500)
380 PUNCH   GET(600)
390 PUNCH   GET(700)
400 PUNCH   GET(800)
410 PUNCH   GET(900)
420 PUNCH   GET(10000)
430 PUNCH   GET(20000)
450 PUNCH   GET(30000)
460 PUNCH   GET(40000)
470 PUNCH   GET(50000)
480 PUNCH   GET(60000)
490 PUNCH   GET(70000)
500 PUNCH   GET(80000)
510 PUNCH   GET(90000)
530 PUNCH   GET(100000)
540 PUNCH   GET(200000)
550 PUNCH   GET(300000)
560 PUNCH   GET(400000)
570 PUNCH   GET(500000)
580 PUNCH   GET(600000)
590 PUNCH   GET(700000)
600 PUNCH   GET(800000)
610 PUNCH   GET(900000)
630 PUNCH   GET(1000000)
640 PUNCH   GET(2000000)
650 PUNCH   GET(3000000)
660 PUNCH   GET(4000000)
670 PUNCH   GET(5000000)
680 PUNCH   GET(6000000)
690 PUNCH   GET(7000000)
700 PUNCH   GET(8000000)
710 PUNCH   GET(9000000)
720 PUNCH   GET(1000)
730 PUNCH   GET(1001)
740 PUNCH   GET(1002)
750 PUNCH   SI("Calcite")
760 PUNCH   SI("CaUO4")
770 PUNCH   SI("CSHgel")
780 PUNCH   SI("Haiweeite")
```

```
 790 PUNCH   SI("Kaolinite")
 800 PUNCH   SI("Laumontite")
 810 PUNCH   SI("Muscovite")
 820 PUNCH   SI("Saponite-Ca")
 830 PUNCH   SI("Sepiolite")
 840 PUNCH   SI("Thaumasite")
 850 PUNCH   SI("Tobermorite-14A")
 860 PUNCH   MOL("UO2(CO3)3-4")
 870 PUNCH   MOL("UO2(CO3)2-2")
 880 PUNCH   MOL("UO2(OH)3-")
 890 PUNCH   MOL("UO2(OH)2")
 900 PUNCH   MOL("UO2CO3")
 910 PUNCH   MOL("UO2X2")
 920 PUNCH   MOL("Surf_alOUO2+")
 930 PUNCH   MOL("Surf_alO(UO2)3(OH)5")
 940 PUNCH   MOL("Surf_siOUO2+")
 950 PUNCH   MOL("Surf_siO(UO2)3(OH)5")
 960 PUNCH   MOL("Surf_kalOUO2OH")
 970 PUNCH   MOL("Surf_feOUO2+")
 980 PUNCH   SI("Uranophane")
 990 PUNCH   SI("Becquerelite")
1000 PUNCH   SI("Rutherfordine")
1010 PUNCH   SI("Quartz")
1020 PUNCH   SI("K-feldspar")
1030 PUNCH   SI("Smectite-low-Fe-Mg")
1040 PUNCH   SI("Clinoptilolite")
1050 PUNCH   SI("Cristobalite(alpha)")
1060 PUNCH   SI("Plagioclase")


End
```

4.1.3. Column 3

```
#Yucca Mountain_uranium desorption_22SA (Column 3)

#-----------------------------------------------------------------------
---

SOLUTION_MASTER_SPECIES
# element    species    alk gfw_formula element_gfw
  Hto        Hto        0.0   20           20

SOLUTION_SPECIES
  Hto = Hto;         log_k 0; -gamma 1e6 0;      -dw 1e-13

#-----------------------------------------------------------------------
---


SOLUTION 0
    temp       25
    pH         8.85
    pe         4
    redox      pe
    units      mg/l
    density    1
    C(4)       212
    Ca         0.92
    Cl(-1)     5.6 charge
    Hto        1e-09
    K          3.4
    Mg         0.03
    N(5)       1.324
    Na         107.3
    S(6)       18.7
    U(6)       0.24
    -water     1 # kg

save solution 0

end

SOLUTION 1-10
     temp       25
    pH         8.85
    pe         4
    redox      pe
    units      mg/l
    density    1
    C(4)       212
    Ca         0.92
    Cl(-1)     5.6 charge
    K          3.4
    Mg         0.03
    N(5)       1.2
    Na         107.3
    S(6)       18.7
```

```
      -water    1 # kg


EQUILIBRIUM_PHASES 1-10
CO2(g) -3.5 10

Quartz 0 0                    #SiO2
Plagioclase 0 0                 #NaAlSi3O8 - CaAl2Si2O8
k-feldspar 0 0                  #KAlSi3O8
Clinoptilolite 0 0.535        #(Na,K,Ca) 2-3Al 3(Al,Si) 2Si 13O 36•12H
2O
Cristobalite(alpha) 0 0       #SiO2
Smectite-high-Fe-Mg 0 0       ##CaNaKFeMgAlSi3

kaolinite 0 0                   #Al2Si2O5(OH)4
Tridymite 0 0                   #SiO2
Hematite 0 0                    #Fe2O3
Muscovite 0 0                   #Mica--KAl2(AlSi3O10)(F,OH)2

#opal-CT-----SiO2


CaUO4 0 0
Uranophane 0 0          #Ca(UO2)2(SiO3)2(OH)2
Becquerelite 0 0        #Ca(UO2)6O4(OH)6:8H2O
Rutherfordine 0 0       #UO2CO3

EXCHANGE_SPECIES


UO2+2 + 2NaX = UO2X2 + 2Na+
log_k   0.45

UO2+2 + CaX2 = UO2X2 + Ca+2
log_k   0.049


EXCHANGE 1-10
       -equilibrate 1-10
       X                0.0614


#CEC for smectite is 810 meq/kg.....for 75.79 g smectite, then CEC
equals to 61.38 meq

#-------------------------------------------------

SURFACE_MASTER_SPECIES

       Surf_al    Surf_alOH          #Smectite aluminol surface edge
       Surf_si    Surf_siOH          #Smectite silonal surface edge
       Surf_kal   Surf_kalOH         #Kaolinite aluminol surface edge
       Surf_fe    Surf_feOH          #Hematite aluminol surface edge


SURFACE_SPECIES
```

383

```
        Surf_alOH = Surf_alOH
                log_k   0.0

        Surf_alOH + H+ = Surf_alOH2+
                log_k   12.3

         Surf_alOH = Surf_alO- + H+
                log_k   -13.6

         Surf_alOH + UO2+2  = Surf_alOUO2+ + H+
                log_k   7.7

#-------------------------------------------------------------------
-------------------------

        Surf_siOH = Surf_siOH
                log_k   0.0

        Surf_siOH + H+ = Surf_siOH2+
                log_k   -0.95

         Surf_siOH = Surf_siO- + H+
                log_k   -6.95

         Surf_siOH + UO2+2  = Surf_siOUO2+ + H+
                log_k   0.75

#-------------------------------------------------------------------
-----------

        Surf_kalOH = Surf_kalOH
                log_k   0.0

        Surf_kalOH + H+ = Surf_kalOH2+
                log_k   13.33

         Surf_kalOH = Surf_kalO- + H+
                log_k   -4.72

         Surf_kalOH + UO2+2 + H2O  = Surf_kalOUO2OH + 2H+
                log_k   6

#-------------------------------------------------------------------
-----
        Surf_feOH = Surf_feOH
                log_k   0.0

        Surf_feOH + H+ = Surf_feOH2+
                log_k   -5.1

         Surf_feOH = Surf_feO- + H+
                log_k   -10.7

         Surf_feOH + UO2+2  = Surf_feOUO2+ + H+
                log_k   14.11
```

```
#-----------------------------------------------------------------------
-----


SURFACE 1
        -equil solution 1-10
        -sites_units         density
        -donnan 1e-10

        Surf_alOH         2.3 51 75.79 Dw 1e-13    #number of sites
density(per nm2)-surrace area (m2/g)-mass (g)
        Surf_siOH         2.3 51 75.79 Dw 1e-13    #number of sites
density(per nm2)-surrace area (m2/g)-mass (g)
        Surf_kalOH        2.3 20 0.781 Dw 1e-13    #number of sites
density(per nm2)-surrace area (m2/g)-mass (g)
        Surf_feOH         2.3 10 2.34  Dw 1e-13    #number of sites
density(per nm2)-surrace area (m2/g)-mass (g)


#--------------------------------------------------------------------------
--------
#for 390.72 g of rock sample we have the following:
#17.5% Orthoclase = 68.37 g = 0.245 mol      #278.33
#10.1% Quartz = 39.46 g = 0.656 mol            #60.08
#28.4% Plagioclase = 110.96 g = 0.409 mol           #270.77
#12% Clinoptilolite = 46.88 g = 0.017 mol    #2,742.13
#5.9% Cristobalite(alpha) = 23.05 g = 0.3836 mol #60.08
#19.4% Smectite-low-Fe-Mg = 75.79 g = 0.194 mol  #389.34
#0.2% kaolinite = 0.781 g
#0.6% Hematite = 2.34 g
#--------------------------------------------------------------------------
--------

KINETICS 1-10

Quartz
 -tol   1e-8
 -m0    0.656
 -parms 0.02 0.03
#------------------------
K-feldspar
 -tol   1e-8
 -m0     0.245
 -parms  0.02 0.03
#------------------------
Plagioclase
 -tol   1e-8
 -m0     0.409
 -parms  0.002 0.03
#------------------------
Smectite-low-Fe-Mg
 -tol   1e-8
 -m0     0.194
 -parms 51 0.03
#------------------------
Clinoptilolite
 -tol    1e-8
```

```
 -m0      0.017
 -parms  0.002 0.03
#--------------------------
Cristobalite(alpha)
 -tol   1e-8
 -m0    0.3836
 -parms 0.002 0.03
#----------------------------------


-steps 0 21 42 63 84 105 126 147 168 189 210 231 252 273 294 315 336
357 378 399 420 441 462 483 504 525 546 567 588 609 630 651 672 693 714
735 756 777 795 hour  #+time step/2

-cvode                 false

INCREMENTAL_REACTIONS false

#-----------------------------------------------------------------------
--------

RATES


Quartz

-start

1 kq = 10^-13.6

2 If (SI("Quartz")>= 0) then goto 31


3 PV = 0.08598    # Pore Volume...mL from expe

4 Por1 = 0.39

5 TV = PV/Por1     #mL....the volume is for cylindrical shape pipe

6 QMass1 = 39.46   #Quartz initial mass...g

7 Qden = 2650   #Quartz Density...g/L

8 QV1 = QMass1 / Qden    #Quartz initial Volume...L

9 QPor1 = GET_POR(1)

10 QMW = 60.08      #Quartz molar weight...g/Mol

11 Qmol1 = QMass1 / QMW     #Quartz initial moles...mole

12 A0_Q = parm(1) * (((1-GET(1000)) / (1-0.39))^2/3)  #Quartz initial
surface area m2/g

13 Qmass = (Qmass1 + GET(8))
```

```
14 rate_Q = (A0_Q/(parm(2)+ GET(1002))) *  Qmass *  ((m/m0)^0.67) *
(kq) * (1 - SR("Quartz"))

15 moles = rate_Q * time
#mole

16 PUT(Qmol1,1)
17 PUT(moles,2)


#calculate new porosity:


18  Dmol_Q = GET(2)              #Quartz Dissolve moles...moles

19  DmolMass_Q = -1 * (Dmol_Q * QMW)     #Quartz Dissolve moles
mass...g

20  QMV = QMW / Qden              #Quartz molar volume...L/mole

21  DmolVol_Q = -1 * (Dmol_Q * QMV)      #Quartz Dissolve moles
volume....L

22  QPor2 = -1 * (DmolVol_Q / (TV/1000))   #Quartz extra porosity

23  Q_New_Porosity = QPor1 + QPor2


24 PUT(DmolVol_Q,3)
25 PUT(QPor1,4)
26 PUT(QPor2,5)
27 PUT(Q_New_Porosity,6)
28 PUT(A0_Q,7)
29 PUT(DmolMass_Q,8)
30 PUT(Qmass,9)

31 save moles

-end
#--------------------------
Cristobalite(alpha)

-start

1 kCr = 10^-12.31

2 If (SI("Cristobalite(alpha)")>= 0) then goto 31

3 PV = 0.08598     # Pore Volume...mL from expe

4 Por1 = 0.39

5 TV = PV/Por1     #mL....the volume is for cylindrical shape pipe

6 CrMass1 = 23.05     #Cristobalite initial mass...g

7 Crden = 2330   #Cristobalite Density...g/L
```

```
8 CrV1 = CrMass1 / Crden     #Cristobalite initial Volume...L

9 CrPor1 = GET_POR(1)

10 CrMW = 60.08       #Cristobalite molar weight...g/Mol

11 Crmol1 = CrMass1 / CrMW     #Cristobalite initial moles...mole

12 A0_Cr = parm(1) * (((1-GET(1000)) / (1-0.39))^2/3)   #Cristobalite
initial surface area m2/g

13 Crmass = (Crmass1 + GET(80))

14 rate_Cr = (A0_Cr/(parm(2)+ GET(1002))) *  Crmass *  ((m/m0)^0.67) *
(kCr) * (1 - SR("Cristobalite(alpha)"))

15 moles = rate_Cr * time
#mole

16 PUT(Crmol1,10)
17 PUT(moles,20)


#calculate new porosity:


18  Dmol_Cr = GET(20)              #Cristobalite Dissolve moles...moles

19  DmolMass_Cr = -1 * (Dmol_Cr * CrMW)     #Cristobalite Dissolve
moles mass...g

20  CrMV = CrMW / Crden             #Cristobalite molar
volume...L/mole

21  DmolVol_Cr = -1 * (Dmol_Cr * CrMV)      #Cristobalite Dissolve
moles volume....L

22  CrPor2 = -1 * (DmolVol_Cr / (TV/1000))   #Cristobalite extra
porosity

23  Cr_New_Porosity = CrPor1 + CrPor2


24 PUT(DmolVol_Cr,30)
25 PUT(CrPor1,40)
26 PUT(CrPor2,50)
27 PUT(Cr_New_Porosity,60)
28 PUT(A0_Cr,70)
29 PUT(DmolMass_Cr,80)
30 PUT(Crmass,90)

31 save moles

-end
#---------------------------------------------------
K-feldspar
```

```
 -start

1 PV = 0.08598     # Pore Volume...mL from expe

2 Por1 = 0.39

3 TV = PV/Por1     #mL....the volume is for cylindrical shape pipe


       # find activities of inhibiting ions...

 4 a_Al = act("Al+3")
 5 BC = act("Na+") + act("K+") + act("Mg+2") + act("Ca+2")

       # temp corrected with the Arrhenius eqn, Table 8.8
       # the difference in temperature, TK gives solution temp in
Kelvin...

 10 dif_T = 1/TK - 1/281

                    # rate by H+...
 20 pk_H = 11.7 + 3500 * dif_T
 22 rate_H = 10^-pk_H * act("H+")^0.5 / ((1 + a_Al / 4e-6)^0.4 * (1 +
BC / 5e-4)^0.15)

                    # rate by hydrolysis...
 30 pk_w = 14.5 + 2000 * dif_T
 32 rate_w = 10^-pk_w / ((1 + a_Al / 4e-6)^0.14 * (1 + BC / 5e-4)^0.15)

                    # rate by OH-...
 40 pk_OH = 13.1 + 2500 * dif_T
 42 rate_OH = 10^-pk_OH * act("OH-")^0.3

                    # rate by CO2...
 50 pk_CO2 = 13.0 + 2000 * dif_T
 52 rate_CO2 = 10^-pk_CO2 * (10^SI("CO2(g)"))^0.6

                    # Sum the rate contributions...
60 kkf = rate_H + rate_w + rate_OH + rate_CO2

61 If (SI("K-feldspar")>= 0) then goto 320


70  KfMass1 = 68.37   #Kfeldspar initial mass...g

80  Kfden = 2560   #Kfeldspar Density...g/L

90  KfV1 = KfMass1 / Kfden    #Kfeldspar initial Volume...L

100 KfPor1 = GET_POR(1)

110 KfMW = 278.33      #Kfeldspar molar weight...g/Mol

120 Kfmol1 = KfMass1 / KfMW     #Kfeldspar initial moles...mole
```

```
130 A0_Kf = parm(1) * (((1-GET(1000)) / (1-0.39))^2/3)    #Kfeldspar
initial surface area m2/g

140 Kfmass = (Kfmass1 + GET(800))

150 rate_Kf = (kkf) * (A0_Kf/(parm(2)+ GET(1002))) * Kfmass *
((m/m0)^0.67) * (1 - SR("K-feldspar"))

160 moles = rate_Kf * time

170 PUT(Kfmol1,100)
180 PUT(moles,200)

#calculate new porosity:


190  Dmol_Kf = GET(200)            #Kfeldspar Dissolve moles...moles

200  DmolMass_Kf = -1 *(Dmol_Kf * KfMW)      #Kfeldspar Dissolve moles
mass...g

210  KfMV = KfMW / Kfden           #Kfeldspar molar volume...L/mole

220  DmolVol_Kf = -1 *(Dmol_Kf * KfMV)       #Kfeldspar Dissolve moles
volume....L

230  KfPor2 = -1 *(DmolVol_Kf / (TV/1000))   #Kfeldspar extra
porosity....the (-) here is just to correct the (-) from the dissolve
mole volume equation.

240  Kf_New_Porosity = KfPor1 + KfPor2



250 PUT(DmolVol_Kf,300)
260 PUT(KfPor1,400)
270 PUT(KfPor2,500)
280 PUT(Kf_New_Porosity,600)
290 PUT(A0_Kf,700)
300 PUT(DmolMass_Kf,800)
310 PUT(Kfmass,900)

320 save moles

-end
#------------------------------------------------------------
Clinoptilolite

-start

1 kCl = 10^-29.899

2 If (SI("Clinoptilolite")>= 0) then goto 31


3 PV = 0.08598     # Pore Volume...mL from expe
```

```
4 Por1 = 0.39

5 TV = PV/Por1     #mL....the volume is for cylindrical shape pipe

6 ClMass1 = 46.88   #Clinoptilolite  initial mass...g

7 Clden = 2150   #Clinoptilolite  Density...g/L

8 ClV1 = ClMass1 / Clden    #Clinoptilolite  initial Volume...L

9 ClPor1 = GET_POR(1)

10 ClMW = 2742.13     #Clinoptilolite  molar weight...g/Mol

11 Clmol1 = ClMass1 / ClMW     #Clinoptilolite  initial moles...mole

12 A0_Cl = parm(1) * (((1-GET(1000)) / (1-0.39))^2/3)  #Clinoptilolite
initial surface area m2/g

13 Clmass = (Clmass1 + GET(80000))

14 rate_Cl = (A0_Cl/(parm(2)+ GET(1002))) *  Clmass *  ((m/m0)^0.67) *
(kCl) * (1 - SR("Clinoptilolite"))

15 moles = rate_Cl * time
#mole

16 PUT(Clmol1,10000)
17 PUT(moles,20000)


#calculate new porosity:


18  Dmol_Cl = GET(20000)            #Clinoptilolite  Dissolve
moles...moles

19  DmolMass_Cl = -1 * (Dmol_Cl * ClMW)     #Clinoptilolite  Dissolve
moles mass...g

20  ClMV = ClMW / Clden             #Clinoptilolite  molar
volume...L/mole

21  DmolVol_Cl = -1 * (Dmol_Cl * ClMV)      #Clinoptilolite  Dissolve
moles volume....L

22  ClPor2 = -1 * (DmolVol_Cl / (TV/1000))   #Clinoptilolite  extra
porosity

23  Cl_New_Porosity = ClPor1 + ClPor2


24 PUT(DmolVol_Cl,30000)
25 PUT(ClPor1,40000)
26 PUT(ClPor2,50000)
27 PUT(Cl_New_Porosity,60000)
28 PUT(A0_Cl,70000)
```

```
29 PUT(DmolMass_Cl,80000)
30 PUT(Clmass,90000)

31 save moles

-end
#------------------------------------------------------------------------
--------
Plagioclase

-start

1 kP = 10^-15.6

2 If (SI("Plagioclase")>= 0) then goto 31

3 PV = 0.08598      # Pore Volume...mL from expe

4 Por1 = 0.39

5 TV = PV/Por1      #mL....the volume is for cylindrical shape pipe

6 PMass1 = 110.96   #Plagioclase  initial mass...g

7 Pden = 2680   #Plagioclase  Density...g/L

8 PV1 = PMass1 / Pden     #Plagioclase  initial Volume...L

9 PPor1 = GET_POR(1)

10 PMW = 270.77    #Plagioclase  molar weight...g/Mol

11 Pmol1 = PMass1 / PMW     #Plagioclase  initial moles...mole

12 A0_P = parm(1) * (((1-GET(1000)) / (1-0.39))^2/3)  #Plagioclase
initial surface area m2/g

13 Pmass = (Pmass1 + GET(800000))

14 rate_P = (A0_P/(parm(2)+ GET(1002))) *  Pmass *  ((m/m0)^0.67) *
(kP) * (1 - SR("Plagioclase"))

15 moles = rate_P * time
#mole

16 PUT(Pmol1,100000)
17 PUT(moles,200000)


#calculate new porosity:


18  Dmol_P = GET(200000)            #Plagioclase  Dissolve
moles...mole

19  DmolMass_P = -1 * (Dmol_P * PMW)     #Plagioclase  Dissolve moles
mass...g
```

392

```
20  PMV = PMW / Pden              #Plagioclase  molar volume...L/mole

21  DmolVol_P = -1 * (Dmol_P * PMV)     #Plagioclase  Dissolve moles
volume....L

22  PPor2 = -1 * (DmolVol_P / (TV/1000))   #Plagioclase  extra porosity

23  P_New_Porosity = PPor1 + PPor2


24 PUT(DmolVol_P,300000)
25 PUT(PPor1,400000)
26 PUT(PPor2,500000)
27 PUT(P_New_Porosity,600000)
28 PUT(A0_P,700000)
29 PUT(DmolMass_P,800000)
30 PUT(Pmass,900000)

31 save moles

 -end

#-------------------------------------------------------------------
Smectite-low-Fe-Mg

-start

1 kSm = 10^-18.08

2 If (SI("Smectite-low-Fe-Mg")>= 0) then goto 40


3 PV = 0.08598     # Pore Volume...mL from expe

4 Por1 = 0.39

5 TV = PV/Por1     #mL....the volume is for cylindrical shape pipe

6 SmMass1 = 75.79   #Smectite initial mass...g

7 Smden = 2680   #Smectite Density...g/L

8 SmV1 = SmMass1 / Smden     #Smectite initial Volume...L

9 SmPor1 = GET_POR(1)

10 SmMW = 389.34     #Smectite molar weight...g/Mol

11 Smmol1 = SmMass1 / SmMW     #Smectite initial moles...mole

12 A0_Sm = parm(1) * (((1-GET(1000)) / (1-0.39))^2/3)  #Smectite
initial surface area m2/g

13 Smmass = (Smmass1 + GET(8000000))
```

```
14 rate_Sm = (A0_Sm/(parm(2)+ GET(1002))) *  Smmass *  ((m/m0)^0.67) *
(kSm) * (1 - SR("Smectite-low-Fe-Mg"))

15 moles = rate_Sm * time
#mole

16 PUT(Smmol1,1000000)
17 PUT(moles,2000000)


#calculate new porosity:


18  Dmol_Sm = GET(2000000)              #Smectite Dissolve moles...moles

19  DmolMass_Sm = -1 * (Dmol_Sm * SmMW)     #Smectite Dissolve moles
mass...g

20  SmMV = SmMW / Smden              #Smectite molar volume...L/mole

21  DmolVol_Sm = -1 * (Dmol_Sm * SmMV)      #Smectite Dissolve moles
volume....L

22  SmPor2 = -1 * (DmolVol_Sm / (TV/1000))   #Smectite extra porosity

23  Sm_New_Porosity = SmPor1 + SmPor2


24 PUT(DmolVol_Sm,3000000)
25 PUT(SmPor1,4000000)
26 PUT(SmPor2,5000000)
27 PUT(Sm_New_Porosity,6000000)
28 PUT(A0_Sm,7000000)
29 PUT(DmolMass_Sm,8000000)
30 PUT(Smmass,9000000)


#----------------------------

31 New_Total_V = -1 * (GET(3) + GET(30) + GET(300)+ GET(30000)+
GET(300000)+ GET(3000000))

32 PUT(New_Total_V,1002)

33 Porosity_2 = GET(5) + GET(50) + GET(500) + GET(50000) + GET(500000)
+ GET(5000000)

34 PUT(Porosity_2,1001)

35 New_Porosity = GET_POR(1) + GET(1001)

36 PUT(New_Porosity,1000)

37 CHANGE_POR(New_Porosity,1)

40 save moles
```

```
 -end
#----------------------------------------------------------------

use solution 0

 TRANSPORT

        -cells              10
        -shifts             20
        -time_step          40 hour
        -flow_direction     forward
        -boundary_conditions flux flux
        -lengths            10*0.045
        -dispersivity       10*0.06
        -correct_disp       true
        -diffusion_coef     0.3e-9
        -initial_time       0
        -punch_cells        10
        -punch_frequency    1
        -multi_D            true
        -porosities         0.39




SELECTED_OUTPUT

 USER_PUNCH

        -headings Time Ca Na K Si CO3 Cl(-1) Mg Al U NO3 Hto UO2(CO3)2-
2_sorption UO2(OH)2_sorption Q1 Q2 Q3 Q4 Q5 Q6 Q7 Q8 Q9 Cr1 Cr2 Cr3 Cr4
Cr5 Cr6 Cr7 Cr8 Cr9 Kf1 Kf2 Kf3 Kf4 Kf5 Kf6 Kf7 Kf8 Kf9 Cl1 Cl2 Cl3 Cl4
Cl5 Cl6 Cl7 Cl8 Cl9 P1 P2 P3 P4 P5 P6 P7 P8 P9 S1 S2 S3 S4 S5 S6 S7 S8
S9 Porosity_T Porosity_2 Volume_2 calcite CaUO4 CSHgel haiweeite
kaolinite laumontite muscovite saponite-Ca sepiolite thaumasite
tobermorite-14A UO2(CO3)3-4 UO2(CO3)2-2 UO2(OH)3- UO2(OH)2 UO2CO3 UO2X2
Surf_alOUO2+ Surf_alO(UO2)3(OH)5 Surf_siOUO2+ Surf_siO(UO2)3(OH)5
Surf_kalOUO2OH Surf_feOUO2+ Uranophane Becquerelite Rutherfordine
Quartz K-feldspar Smectite-low-Fe-Mg Clinoptilolite Cristobalite(alpha)
Plagioclase
-start

010 PUNCH TOTAL_TIME/(60)
020 PUNCH tot("Ca")*40*1000
030 PUNCH tot("Na")*23*1000
040 PUNCH tot("K")*39.1*1000
050 PUNCH tot("Si")*28.09*1000
060 PUNCH tot("C(4)")*60*1000
070 PUNCH tot("Cl(-1)")*35.45*1000
080 PUNCH tot("Mg")*24.3*1000
090 PUNCH tot("Al")*27*1000
100 PUNCH tot("U(6)")*270*1000
110 PUNCH tot("N(5)")*62*1000
120 PUNCH tot("Hto")*22.03*1000
130 PUNCH KIN("UO2(CO3)2-2_sorption")*1000*238/3570
140 PUNCH KIN("UO2(OH)2_sorption")*1000*238/3570
 150 PUNCH  GET(1)
```

```
160 PUNCH   GET(2)
170 PUNCH   GET(3)
180 PUNCH   GET(4)
190 PUNCH   GET(5)
200 PUNCH   GET(6)
210 PUNCH   GET(7)
220 PUNCH   GET(8)
230 PUNCH   GET(9)
240 PUNCH   GET(10)
250 PUNCH   GET(20)
260 PUNCH   GET(30)
270 PUNCH   GET(40)
280 PUNCH   GET(50)
290 PUNCH   GET(60)
300 PUNCH   GET(70)
310 PUNCH   GET(80)
320 PUNCH   GET(90)
330 PUNCH   GET(100)
340 PUNCH   GET(200)
350 PUNCH   GET(300)
360 PUNCH   GET(400)
370 PUNCH   GET(500)
380 PUNCH   GET(600)
390 PUNCH   GET(700)
400 PUNCH   GET(800)
410 PUNCH   GET(900)
420 PUNCH   GET(10000)
430 PUNCH   GET(20000)
450 PUNCH   GET(30000)
460 PUNCH   GET(40000)
470 PUNCH   GET(50000)
480 PUNCH   GET(60000)
490 PUNCH   GET(70000)
500 PUNCH   GET(80000)
510 PUNCH   GET(90000)
530 PUNCH   GET(100000)
540 PUNCH   GET(200000)
550 PUNCH   GET(300000)
560 PUNCH   GET(400000)
570 PUNCH   GET(500000)
580 PUNCH   GET(600000)
590 PUNCH   GET(700000)
600 PUNCH   GET(800000)
610 PUNCH   GET(900000)
630 PUNCH   GET(1000000)
640 PUNCH   GET(2000000)
650 PUNCH   GET(3000000)
660 PUNCH   GET(4000000)
670 PUNCH   GET(5000000)
680 PUNCH   GET(6000000)
690 PUNCH   GET(7000000)
700 PUNCH   GET(8000000)
710 PUNCH   GET(9000000)
720 PUNCH   GET(1000)
730 PUNCH   GET(1001)
740 PUNCH   GET(1002)
750 PUNCH   SI("Calcite")
```

```
 760 PUNCH  SI("CaUO4")
 770 PUNCH  SI("CSHgel")
 780 PUNCH  SI("Haiweeite")
 790 PUNCH  SI("Kaolinite")
 800 PUNCH  SI("Laumontite")
 810 PUNCH  SI("Muscovite")
 820 PUNCH  SI("Saponite-Ca")
 830 PUNCH  SI("Sepiolite")
 840 PUNCH  SI("Thaumasite")
 850 PUNCH  SI("Tobermorite-14A")
 860 PUNCH  MOL("UO2(CO3)3-4")
 870 PUNCH  MOL("UO2(CO3)2-2")
 880 PUNCH  MOL("UO2(OH)3-")
 890 PUNCH  MOL("UO2(OH)2")
 900 PUNCH  MOL("UO2CO3")
 910 PUNCH  MOL("UO2X2")
 920 PUNCH  MOL("Surf_alOUO2+")
 930 PUNCH  MOL("Surf_alO(UO2)3(OH)5")
 940 PUNCH  MOL("Surf_siOUO2+")
 950 PUNCH  MOL("Surf_siO(UO2)3(OH)5")
 960 PUNCH  MOL("Surf_kalOUO2OH")
 970 PUNCH  MOL("Surf_feOUO2+")
 980 PUNCH  SI("Uranophane")
 990 PUNCH  SI("Becquerelite")
1000 PUNCH  SI("Rutherfordine")
1010 PUNCH  SI("Quartz")
1020 PUNCH  SI("K-feldspar")
1030 PUNCH  SI("Smectite-low-Fe-Mg")
1040 PUNCH  SI("Clinoptilolite")
1050 PUNCH  SI("Cristobalite(alpha)")
1060 PUNCH  SI("Plagioclase")
```

End

4.2.Hollington Sandstone

```
#Sandstone_uranium Transport_YCL


SOLUTION 0
    temp       50
    pH         12.415 #originally 13.1 at 25C
    pe         4
    redox      pe
    units      mg/l
    density    1
    K          3290
    Na         2185
    N(5)       0.124
    U          0.24
    -water     1 # kg
save solution 0

end

SOLUTION 1-10
    temp       50
    pH         7.83
    pe         4
    redox      pe
    units      mg/l
    density    1
    Al         0.02
    Br(-1)     4340
    Ca         23.1
    Cl(-1)     4300
    K          3202
    Mg         0.07
    Na         2178
    Si         0.36
    -water     1 # kg


EQUILIBRIUM_PHASES 1-10


quartz 0 0              #SiO2
K-feldspar 1.1 0.005    #AlKO8Si3
Kaolinite -4.4 0.005        #Al2Si2O5(OH)4

CSHgel 0 0
Tobermorite-14A 0 0
saponite-Mg 0 0
analcime 0 0
hydrogarnet 0 0
prehnite 0 0
Laumontite 0 0
mesolite 0 0
Mordenite 0 0
```

```
CaUO4 0 0
Na2U2O7 0 0
Uranophane 0 0          #Ca(UO2)2(SiO3)2(OH)2
Becquerelite 0 0        #Ca(UO2)6O4(OH)6:8H2O


#----------------------------------------------------------------------
#The weight composition of the sandstone sample is 75.5% Quartz, 16% K-
feldspar, 3.7% Smectite and 3.5% Kaolinite for a total of 21.249 g
#Quartz mass = 16.04 g
#K-feldspar mass = 3.4 g
#kaolinite mass = 0.743 g
#Smectite mass = 0.786 g

#Quartz Molar Weight = 60.08
#K-feldspar Molar Weight = 278.33
#Kaolinite Molar Weight = 258.16
#Smectite Molar Weight = 389.34


#----------------------------------------------------------------------
SURFACE_MASTER_SPECIES

        Surf_al    Surf_alOH       #Smectite aluminol surface edge
        Surf_si    Surf_siOH       #Smectite silonal surface edge
        Surf_kal   Surf_kalOH      #Kaolinite aluminol surface edge


SURFACE_SPECIES

        Surf_alOH = Surf_alOH
              log_k   0.0

        Surf_alOH + H+ = Surf_alOH2+
              log_k   12.3

         Surf_alOH = Surf_alO- + H+
              log_k   -13.6

         Surf_alOH + UO2+2  = Surf_alOUO2+ + H+
              log_k   7.7

#--------------------------------------------------------------------------
-------------------------

        Surf_siOH = Surf_siOH
              log_k   0.0

        Surf_siOH + H+ = Surf_siOH2+
              log_k   -0.95

        Surf_siOH = Surf_siO- + H+
              log_k   -6.95

        Surf_siOH + UO2+2  = Surf_siOUO2+ + H+
              log_k   0.75


#----------------------------------------------------------------------------
-----------
```

399

```
        Surf_kalOH = Surf_kalOH
              log_k   0.0

        Surf_kalOH + H+ = Surf_kalOH2+
              log_k   13.33

         Surf_kalOH = Surf_kalO- + H+
              log_k   -4.72

        Surf_kalOH + UO2+2 + H2O  = Surf_kalOUO2OH + 2H+
              log_k   6


#---------------------------------------------------------------------
-----
SURFACE 1-10
        -equil solution 1-10
        -sites_units          density
        -donnan 1e-10

        Surf_alOH         2.3 51 0.786 Dw 1e-13    #number of sites
density(per nm2)-surrace area (m2/g)-mass (g)
        Surf_siOH         2.3 51 0.786 Dw 1e-13    #number of sites
density(per nm2)-surrace area (m2/g)-mass (g)
        Surf_kalOH        2.3 20 0.743 Dw 1e-13    #number of sites
density(per nm2)-surrace area (m2/g)-mass (g)




#---------------------------------------------------------------------
--------
#for 374.61g of rock sample we have the following:
#24.4% Orthoclase = 91.40 g = 0.328 mol         #278.33
#15.3% Quartz = 57.31 g = 0.954 mol             #60.08
#23% Plagioclase = 86.16 g = 0.318 mol          #270.77
#7.6% Clinoptilolite = 28.47 g = 0.0103 mol     #2,742.13
#5.8% Cristobalite(alpha) = 21.727 g = 0.3616 mol #60.08
#4.6% Smectite-low-Fe-Mg = 17.23 g = 0.044 mol   #389.34
#0.5% kaolinite = 1.87 g
#0.4% Hematite = 1.5 g
#---------------------------------------------------------------------
--------

KINETICS 1-10

Quartz

 -tol 1e-8
 -m0 0.267
 -parms 0.02 0.005968

Kaolinite

 -tol 1e-8
 -m0 0.0030
 -parms 20 0.005968
```

```
K-feldspar
 -tol    1e-8
 -M0     0.012
 -parms  0.02 0.005968



#-cvode                 true




-steps 0 26 52 78 104 130 156 182 208 234 260 286 312 338 364 390 416
442 468 494 520 546 572 598 624 650 676 702 728 754 780 806 832 858 884
910 936 962 988 1014 1066 1092 1118 1144 1170 1196 1222 1248 1274 1300
1326 1353 1378 1404 1430 1456 1482 1508 1534 1560 1586 1612 1638 1664
1690 1716 1742 1768 1794 1820 1846 1872 1898 1924 1950 1976 2002 2028
2054 2080 2106 2132 2158 2184 2210 2236 2262 2288 2314 2340 2366 2392
2418 2444 2470 2496 2522 2548 2574 2600 2626 2652 2678 2704 2730 2756
2782 2808 2834 2860 2886 2912 2938 2964 2990 3016 3042 3068 3094 3120
3146 3172 3198 3224 3250 3276 3302 3328 3354 3380 3406 3432 3458 3484
3510 3536 3562 3585 3614 3640 3666 3692 3718 3744 3770 3796 3822 3848
3874 3900 3926 3952 3978 4004 4030 4056 4082 4108 4134 4160 4186 4212
4238 4264 4290 4316 4342 4368 4394 4420 4446 4472 4498 4524 4550 4676
4602 4628 4654 4680 4706 4732 4758 4784 4810 4836 4862 4888 4914 4940
4966 4992 5018 5044 5070 5096 5122 5148 5174 5200 5226 5252 5278 5304
5330 5356 5382 5408 5434 5460 5486 5512 5538 5564 5590 hour


INCREMENTAL_REACTIONS false

#------------------------------------------------------------------------
--------

RATES

Quartz

-start

1 kq = 10^-12.7

2 If (SI("Quartz")>= 0) then goto 31


#Initial values for Quartz


3 PV = 5.968     # Pore Volume...mL from expe (excel file)

4 Por1 = 0.427

5 TV = PV/Por1     #mL....the volume is for cylindrical shape pipe


#The weight composition of the sandstone sample is 75.5% Quartz, 16% K-
feldspar and 3.5% Kaolinite for a total of 21.249 g
```

```
6 QMass1 = 0.755 * 21.249   #Quartz initial mass...g

7 Qden = 2650   #Quartz Density...g/L

8 QV1 = QMass1 / Qden    #Quartz initial Volume...L

9 QPor1 = GET_POR(1)

10 QMW = 60.08      #Quartz molar weight...g/Mol

11 Qmol1 = QMass1 / QMW     #Quartz initial moles...mole

12 A0_Q = parm(1) * (((1-GET(1000)) / (1-0.427))^2/3)  #Quartz initial
surface area m2/g

13 Qmass = (Qmass1 + GET(8))

#Total reactive surface area = A0_Q * Quartz initial mass   m2


14 rate_Q = (A0_Q/(parm(2)+ GET(1002))) *  Qmass *  ((m/m0)^0.67) *
(kq) * (1 - SR("Quartz"))

15 moles = rate_Q * time
#mole

16 PUT(Qmol1,1)
17 PUT(moles,2)


#calculate new porosity:


18  Dmol_Q = GET(2)            #Quartz Dissolve moles...moles

19  DmolMass_Q = -1 * (Dmol_Q * QMW)     #Quartz Dissolve moles
mass...g

20  QMV = QMW / Qden             #Quartz molar volume...L/mole

21  DmolVol_Q = -1 * (Dmol_Q * QMV)      #Quartz Dissolve moles
volume....L

22  QPor2 = -1 * (DmolVol_Q / (TV/1000))   #Quartz extra porosity

23  Q_New_Porosity = QPor1 + QPor2


24 PUT(DmolVol_Q,3)
25 PUT(QPor1,4)
26 PUT(QPor2,5)
27 PUT(Q_New_Porosity,6)
28 PUT(A0_Q,7)
29 PUT(DmolMass_Q,8)
30 PUT(Qmass,9)
```

```
31 save moles

-end

#----------------------

Kaolinite

-start

1 PV = 5.968    # Pore Volume...mL from expe (excel file)

2 Por1 = 0.427

3 TV = PV/Por1    #mL....the volume is for cylindrical shape pipe


10 kk = 10^-12.5 #@T=50, PH=12.6

11 If (SI("Kaolinite")>= 0) then goto 270

#The weight composition of the sandstone sample is 75.5% Quartz, 16% K-
feldspar and 3.5% Kaolinite for a total of 21.249 g

20 KMass1 = 0.035 * 21.249    #Kaolinite initial mass...g

30 Kden = 2650    #kaolinite Density...g/L

40 KV1 = KMass1 / Kden    #kaolinite initial Volume...L

50 KPor1 = GET_POR(1)

60 KMW = 258.16      #Kaolinite molar weight...g/Mol

70 Kmol1 = KMass1 / KMW    #Kaolinite initial moles...mole

80 A0_K = parm(1) * (((1-GET(1000)) / (1-0.427))^2/3)  #Kaolinite
initial surface area m2/g

90 Kmass = (Kmass1 + GET(80))

#Total reactive surface area = A0_K * Kaolinite initial mass   m2

100 rate_K = (A0_K/(parm(2)+ GET(1002))) * Kmass *  ((m/m0)^0.67) *
(kk) * (1 - SR("Kaolinite"))

110 moles = rate_K * time
#mole

120 PUT(Kmol1,10)
130 PUT(moles,20)

#calculate new porosity:


140  Dmol_K = GET(20)            #kaolinite Dissolve moles...moles
```

```
150  DmolMass_K = -1 *(Dmol_K * KMW)      #kaolinite Dissolve moles
mass...g

160  KMV = KMW / Kden                #kaolinite molar volume...L/mole

170  DmolVol_K = -1 *(Dmol_K * KMV)      #Kaolinite Dissolve moles
volume....L

180  KPor2 = -1 * (DmolVol_K / (TV/1000))   #Kaolinite extra porosity

190  K_New_Porosity = KPor1 + KPor2



200 PUT(DmolVol_K,30)
210 PUT(KPor1,40)
220 PUT(KPor2,50)
230 PUT(K_New_Porosity,60)
240 PUT(A0_K,70)
250 PUT(DmolMass_K,80)
260 PUT(Kmass,90)



270 SAVE moles

-end

#----------------------------

K-feldspar


 -start

1 PV = 5.968    # Pore Volume...mL from expe (excel file)

2 Por1 = 0.427

3 TV = PV/Por1     #mL....the volume is for cylindrical shape pipe


     # find activities of inhibiting ions...

 4 a_Al = act("Al+3")
 5 BC = act("Na+") + act("K+") + act("Mg+2") + act("Ca+2")

     # temp corrected with the Arrhenius eqn, Table 8.8
     # the difference in temperature, TK gives solution temp in
Kelvin...

 10 dif_T = 1/TK - 1/281


                 # rate by H+...
 20 pk_H = 11.7 + 3500 * dif_T
 22 rate_H = 10^-pk_H * act("H+")^0.5 / ((1 + a_Al / 4e-6)^0.4 * (1 +
BC / 5e-4)^0.15)
```

```
                  # rate by hydrolysis...
 30 pk_w = 14.5 + 2000 * dif_T
 32 rate_w = 10^-pk_w / ((1 + a_Al / 4e-6)^0.14 * (1 + BC / 5e-4)^0.15)

                  # rate by OH-...
 40 pk_OH = 13.1 + 2500 * dif_T
 42 rate_OH = 10^-pk_OH * act("OH-")^0.3

                  # rate by CO2...
 50 pk_CO2 = 13.0 + 2000 * dif_T
 52 rate_CO2 = 10^-pk_CO2 * (10^SI("CO2(g)"))^0.6

                  # Sum the rate contributions...
 60 kkf = rate_H + rate_w + rate_OH + rate_CO2

 61 PUT(kkf,88)


#The weight composition of the sandstone sample is 75.5% Quartz, 16% K-
feldspar and 3.5% Kaolinite for a total of 21.249 g

 70  KfMass1 = 0.16 * 21.249   #Kfeldspar initial mass...g

 80  Kfden = 2560   #Kfeldspar Density...g/L

 90  KfV1 = KfMass1 / Kfden    #Kfeldspar initial Volume...L

100 KfPor1 = GET_POR(1)

110 KfMW = 278.33      #Kfeldspar molar weight...g/Mol

120 Kfmol1 = KfMass1 / KfMW     #Kfeldspar initial moles...mole

130 A0_Kf = parm(1) * (((1-GET(1000)) / (1-0.427))^2/3)   #Kfeldspar
initial surface area m2/g

140 Kfmass = (Kfmass1 + GET(800))

#Total reactive surface area = A0_Kf * Kfeldspar initial mass    m2

150 rate_Kf = (kkf) * (A0_Kf/(parm(2)+ GET(1002))) * Kfmass *
((m/m0)^0.67) * (1 - SR("K-feldspar"))

160 moles = rate_Kf * time

170 PUT(Kfmol1,100)
180 PUT(moles,200)

#calculate new porosity:


190  Dmol_Kf = GET(200)            #Kfeldspar Dissolve moles...moles

200  DmolMass_Kf = -1 *(Dmol_Kf * KfMW)      #Kfeldspar Dissolve moles
mass...g
```

```
210  KfMV = KfMW / Kfden                #Kfeldspar molar volume...L/mole

220  DmolVol_Kf = -1 *(Dmol_Kf * KfMV)       #Kfeldspar Dissolve moles
volume....L

230  KfPor2 = -1 *(DmolVol_Kf / (TV/1000))   #Kfeldspar extra
porosity....the (-) here is just to correct the (-) from the dissolve
mole volume equation.

240  Kf_New_Porosity = KfPor1 + KfPor2


250 PUT(DmolVol_Kf,300)
260 PUT(KfPor1,400)
270 PUT(KfPor2,500)
280 PUT(Kf_New_Porosity,600)
290 PUT(A0_Kf,700)
300 PUT(DmolMass_Kf,800)
310 PUT(Kfmass,900)

#-------------------------------

320 New_Total_V = -1 * (GET(3) + GET(30) + GET(300))

330 PUT(New_Total_V,1002)

340 Porosity_2 = GET(5) + GET(50) + GET(500)

350 PUT(Porosity_2,1001)

360 New_Porosity = GET_POR(1) + GET(1001)

370 PUT(New_Porosity,1000)

380 CHANGE_POR(New_Porosity,1)

390 save moles

 -end

#----------------------------------------------------------------------

use solution 0

 TRANSPORT

        -cells              10
        -shifts             215
        -time_step          26 hour
        -flow_direction     forward
        -boundary_conditions  flux flux
        -lengths            10*0.03
        -dispersivity       10*0.09
        -correct_disp       true
        -diffusion_coef     0.3e-9
        -initial_time       0
```

```
        -punch_cells          10
        -punch_frequency      1
        -multi_D              true
        -porosities           0.427




SELECTED_OUTPUT

 USER_PUNCH

        -headings Time Ca Na K Si CO3 Cl(-1) Mg Al U NO3 UO2(CO)3-
4_sorption UO2(CO3)2-2_sorption UO2(OH)2_sorption Q1 Q2 Q3 Q4 Q5 Q6 Q7
Q8 Q9 K1 K2 Cr3 K4 K5 K6 K7 K8 K9 Kf1 Kf2 Kf3 Kf4 Kf5 Kf6 Kf7 Kf8 Kf9
CaUO4 Na2U2O7 Soddyite Uraninite Uranophane Weeksite Becquerelite
Porosity_T Porosity_2 Volume_2 calcite CaUO4 CSHgel haiweeite kaolinite
laumontite muscovite saponite-Ca sepiolite thaumasite tobermorite-14A
UO2(OH)4-2 UO2(CO3)2-2 UO2(OH)3- UO2(OH)2 U UO2X2 Surf_alOUO2+
Surf_alO(UO2)3(OH)5 Surf_siOUO2+ Surf_siO(UO2)3(OH)5 Surf_kalOUO2OH
-start

010 PUNCH TOTAL_TIME/(60*60)
020 PUNCH tot("Ca")*40*1000
030 PUNCH tot("Na")*23*1000
040 PUNCH tot("K")*39.1*1000
050 PUNCH tot("Si")*28.09*1000
060 PUNCH tot("C(4)")*60*1000
070 PUNCH tot("Cl(-1)")*35.45*1000
080 PUNCH tot("Mg")*24.3*1000
090 PUNCH tot("Al")*27*1000
100 PUNCH tot("U")*238.03*1000
110 PUNCH tot("N(5)")*62*1000
120 PUNCH KIN("UO2(CO3)3-4_sorption")*1000*238/3570
130 PUNCH KIN("UO2(CO3)2-2_sorption")*1000*238/3570
140 PUNCH KIN("UO2(OH)2_sorption")*1000*238/3570
 150 PUNCH  GET(1)
 160 PUNCH  GET(2)
 170 PUNCH  GET(3)
 180 PUNCH  GET(4)
 190 PUNCH  GET(5)
 200 PUNCH  GET(6)
 210 PUNCH  GET(7)
 220 PUNCH  GET(8)
 230 PUNCH  GET(9)
 240 PUNCH  GET(10)
 250 PUNCH  GET(20)
 260 PUNCH  GET(30)
 270 PUNCH  GET(40)
 280 PUNCH  GET(50)
 290 PUNCH  GET(60)
 300 PUNCH  GET(70)
 310 PUNCH  GET(80)
 320 PUNCH  GET(90)
 330 PUNCH  GET(100)
 340 PUNCH  GET(200)
 350 PUNCH  GET(300)
```

```
360 PUNCH   GET(400)
370 PUNCH   GET(500)
380 PUNCH   GET(600)
390 PUNCH   GET(700)
400 PUNCH   GET(800)
410 PUNCH   GET(900)

420 PUNCH   SI("CaUO4")
430 PUNCH   SI("Na2U2O7")
440 PUNCH   SI("Soddyite")
450 PUNCH   SI("Uraninite")
460 PUNCH   SI("Uranophane")
470 PUNCH   SI("Weeksite")
480 PUNCH   SI("Becquerelite")


720 PUNCH   GET(1000)
730 PUNCH   GET(1001)
740 PUNCH   GET(1002)
750 PUNCH   SI("Calcite")
760 PUNCH   SI("CaUO4")
770 PUNCH   SI("CSHgel")
780 PUNCH   SI("Haiweeite")
790 PUNCH   SI("Kaolinite")
800 PUNCH   SI("Laumontite")
810 PUNCH   SI("Muscovite")
820 PUNCH   SI("Saponite-Ca")
830 PUNCH   SI("Sepiolite")
840 PUNCH   SI("Thaumasite")
850 PUNCH   SI("Tobermorite-14A")
860 PUNCH   MOL("UO2(OH)4-2")
870 PUNCH   MOL("UO2(CO3)2-2")
880 PUNCH   MOL("UO2(OH)3-")
890 PUNCH   MOL("UO2(OH)2")
900 PUNCH   MOL("U")
910 PUNCH   MOL("UO2X2")
920 PUNCH   MOL("Surf_alOUO2+")
930 PUNCH   MOL("Surf_alO(UO2)3(OH)5")
940 PUNCH   MOL("Surf_siOUO2+")
950 PUNCH   MOL("Surf_siO(UO2)3(OH)5")
960 PUNCH   MOL("Surf_kalOUO2OH")

970 PUNCH   GET(88)

End
```